UTS UNIVERSITY OF TECHNOLOGY SYDNEY

Dynamic Characteristics of Jointed Rocks Subjected to Cyclic Loading

by Waranga Dilanthi Habaraduwa Peellage

Thesis submitted in fulfilment of the requirements for the degree of

Doctor of Philosophy

under the supervision of A/Prof Behzad Fatahi and
Dr Haleh Rasekh

University of Technology Sydney
Faculty of Engineering and Information Technology

September 2023

Certificate of Original Authorship

I, Waranga Dilanthi Habaraduwa Peellage declare that this thesis, is submitted in fulfilment of the requirements for the award of Doctor of Philosophy, in the School of Civil and Environmental Engineering (Faculty of Engineering and Information Technology) at the University of Technology Sydney.

This thesis is wholly my own work unless otherwise referenced or acknowledged. In addition, I certify that all information sources and literature used are indicated in the thesis.

This document has not been submitted for qualifications at any other academic institution.

This research is supported by the Australian Government Research Training Program.

Signature: Production Note:
Signature removed prior to publication.

Date: 04/09/2023

To my precious ***Senumi***, with love

Acknowledgement

This PhD journey has been a life-changing experience for me, and it would not have been possible without the support and guidance I received from many people at different stages.

First and foremost, I would like to express my sincere gratitude to my principal supervisor, A/Prof. Behzad Fatahi for his invaluable and continuous advice, understanding, encouragement, support and patience during my PhD study. I am also thankful to my co-supervisor, Dr Haleh Rasekh, for her understanding, continuous guidance and support during this research work.

I am grateful to UTS for awarding me the International Research Scholarship, and Faculty of Engineering and Information Technology Scholarship, and UOW for awarding me the University Postgraduate Award and International Postgraduate Tuition Award, which provided financial support for my tuition fee and living expenses throughout my doctoral studies.

Moreover, I appreciate the support rendered by the academic and non-academic staff at UTS, especially Prof. David McGloin and my counsellor, Ms. Fiona Robertson, during the challenging periods. I would also like to thank Mr. Richard Berndt, Mr. Ritchie McLean, Mr. Duncan Best, Ms. Helen Jiang, Dr Viraj Senevirathne, A/Prof. Vinod Jayan, Prof. Cholachat Rujikiatkamjorn and Prof. Buddhima Indraratna for their support during various stages of the PhD journey.

Last but not least, I would also like to express my deepest love and gratitude to my parents, my husband, my sisters, my friends and my in-laws for their unwavering love, support and encouragement during the past few years, without which I would not have come this far.

List of Publications

1. Peellage, W.H., Fatahi, B. and Rasekh, H., 2023. Assessment of cyclic deformation and critical stress amplitude of jointed rocks via cyclic triaxial testing. Journal of Rock Mechanics and Geotechnical Engineering, 15(6), 1370-1390. https://doi.org/10.1016/j.jrmge.2023.02.001

2. Peellage, W.H., Fatahi, B. and Rasekh, H., 2022. Experimental investigation for vibration characteristics of jointed rocks using cyclic triaxial tests. Soil Dynamics and Earthquake Engineering, 160(1), 107377. https: //doi.org/10.1016/j.soildyn.2022.107377

Table of Contents

List of Figures

List of Tables

List of Symbols

A	Stress amplitude or model parameter
A_{sd}	Average dynamic axial stiffness
$A_{sd,max}$	Maximum dynamic axial stiffness
$A_{sd,min}$	Minimum dynamic axial stiffness
a	Model parameter
α	Model parameter
b	Model parameter
β	Model parameter or internal friction angle in the stress space or dip angle
c	Model parameter
γ	Model parameter
D	Damage variable
D'	Maximum strain damage
D''	Residual strain damage
D_f	Damage severity factor
ΔE	External input energy
ΔE_d	Dissipated energy
ΔE_{di}	Initial dissipated energy per load cycle
ΔE_{ds}	Steady-state dissipated energy per load cycle
ΔE_e	Elastic energy stored
$\Delta E_{e,max}$	Maximum elastic energy stored
$\Delta \varepsilon_{r_{i=n}}$	Differential residual strain after n cycles
$\Delta \varepsilon_{r_{i=N}}$	Differential residual strain at failure
Δq_{cyc}	Difference between the maximum and minimum cyclic deviatoric stresses
Δx	Sampling interval
E	Deformation modulus or elastic modulus or deformation modulus at the current state of plastic straining or actual modulus of the damaged material or instantaneous energy dissipation after some cycles
E_0	Young's modulus of undamaged material
E_{av}	Average Young's modulus
E_{avl}	Average loading Young's modulus

E_{avu}	Average unloading Young's modulus
E_{max}	Deformation modulus at the yield point
E_r	Deformation modulus at the onset of the residual state or Young's modulus
E_s	Young's modulus
E_{tot}	Total energy dissipation capacity in unit volume
ε	Axial strain at the end of a given loading cycle
$\overline{\varepsilon}$	Shear strain
ε_0	Axial strain at the beginning of cyclic loading
ε_1	Strain in the principal stress direction 1
$\varepsilon_{1,e}$	Elastic axial strain
$\varepsilon_{1,p}$	Residual axial strain
$(\varepsilon_{1,p})_{critical}$	Critical dynamic residual axial strain
$\varepsilon_{1,r}$	Residual axial strain
$\varepsilon_{1,rec}$	Recoverable axial strain during unloading
$\dot{\varepsilon}_1^{irr}$	Irreversible axial strain rate
ε_2	Strain in the principal stress direction 2
ε_3	Strain in the principal stress direction 3
ε_{cmax}	Maximum critical dynamic residual axial strain when CSR is very large
$\varepsilon_{c(f)}$	Residual strains at the final cycle
$\varepsilon_{c(n)}$	Residual strains at the current cycle
ε_d	Axial strain at the end of cyclic loading
$\varepsilon_{m(0)}$	Maximum strain at the initial cycle
$\varepsilon_{m(f)}$	Maximum strain at the final cycle
$\varepsilon_{m(n)}$	Maximum strain at the current cycle
ε_{max}^0	Initial maximum strain
ε_{max}^f	Ultimate maximum strain
ε_{max}^n	Instantaneous maximum strain after n cycles
$\overline{\varepsilon}_{max}^0$	Initial maximum shear strain before cyclic loading
$\overline{\varepsilon}_{max}^f$	Ultimate maximum shear strain
$\overline{\varepsilon}_{max}^n$	Maximum shear strain after the n^{th} cycle
ε_p	Cumulative plastic strain

ε_{p0}	Plastic strain that causes zero-cycle damage
ε_r^f	Ultimate residual strain at fatigue failure
ε_r^n	Residual strain after n cycles
ε_r^p	Total axial plastic strain accumulated at the onset of the residual state
$\left\|\varepsilon_{a,res}\right\|_i$	Residual axial strain in the i^{th} cycle
$\left\|\varepsilon_{r,res}\right\|_i$	Residual lateral strain in the i^{th} cycle
ε_v^{max}	Maximum volumetric strain,
$\varepsilon_{v,re}$	Residual volumetric strain
$\varepsilon_{v,res}^N$	Residual volumetric strain after *N* cycles
$\varepsilon_{v,res}^{N_f}$	residual volumetric strain at failure
ζ_1	Model parameter
ζ_2	Model parameter
η	Model parameter
η_1	Model parameter
η_2	Model parameter
η_d	Dynamic stress ratio
η_s	Static deviatoric stress ratio
θ	Joint inclination angle
f	Frequency
G_d	Dynamic shear modulus
$G_{d\,max}$	Maximum dynamic shear modulus
$G_{d\,min}$	Minimum dynamic shear modulus
$g(f)$	A function that assesses the impact of vibration frequency
JRC_0	Initial joint roughness coefficient
JRC_f	Final joint roughness coefficient
K	Ratio between critical dynamic deviatoric stress and peak deviatoric stress under static triaxial loading
k	Model parameter
κ	Model parameter
λ	Model parameter or Damping Ratio or Lame's constant
λ_0	Model parameter

λ_{min}	Minimum damping ratio
L_f	Damage localisation factor
L_n	Nominal length of the digitised joint profile
M	Maximum stress level
M_R	Resilient modulus
M_{R0}	Steady-state resilient modulus at very small cyclic deviatoric stress amplitude
M_{RS}	Steady-state resilient modulus
M_{RU}	Ultimate resilient modulus
m	Model parameter or maximum cycle number
μ	Loading rate or Lame's constant
n	Model parameter or number of cycles
N	Number of cycles or AE cumulative counts corresponding to a given number of cycles
N_c	Number of cycles or critical number of cycles
$N_{critical}$	Number of cycles corresponding to 85% of the maximum cumulative residual axial strain
N_f	Fatigue life or number of cycles at failure
N_i	Total number of cycles
N_m	AE cumulative counts to failure
N_p	Number of digitised points along the profile
N_q	Normalised cyclic deviatoric stress amplitude
ν	Loading frequency or Poisson's ratio
v_T^2	Origin ultrasonic wave velocity of undamaged material
$\hat{v}_{Tn}^2$	Instantaneous ultrasonic wave velocity of damaged material after n cycles
ξ	Damping ratio or a constant independent of the loading conditions
ξ_i	Initial damping ratio per load cycle
ξ_0	Steady-state damping ratio when cyclic deviatoric stress amplitude is very large
ξ_p	Hysteretic damping ratios for compressional waves
ξ_s	Steady-state damping ratio per load cycle or hysteretic damping ratios for shear waves
p_p	Mean stress at the peak deviatoric stress

ρ	Mass density of the medium
ρ_n	Density of the rock joint after *n* cycles
ρ_o	Density in the virgin state
ρ_{max}	Maximum density
ρ_{N_f}	Density at failure
σ	Stress level
σ_1	Major principal stress
σ_3	Confining pressure or minor principal stress
σ_A	Critical stress
σ_B	Critical stress
σ_c	Uniaxial compressive strength
$\bar{\sigma}^{cr}$	Equivalent stress
σ_d	Amplitude of the dynamic stress
σ_f	Static failure stress of rocks
σ_n	Normal stress on the joint plane
σ_s	Static deviator stress or critical stress
σ_t	Tensile strength
q_c	Critical dynamic deviatoric stress
q_{cyc}	Cyclic deviatoric stress
$(q_{cyc})_{avg}$	Average value of cyclic deviatoric stress
$(q_{cyc})_n$	Cyclic deviatoric stress at a given cycle n
q_{max}^{dyn}	Maximum amplitude of the cyclic stress
q_p	Peak deviatoric stress
q_{stat}	Peak deviatoric stress under static loading
$(q_s)_{max}$	Monotonic peak deviatoric stress
q_{sp}	Static peak deviatoric stress
R^2	Coefficient of determination
R_{ε_p}	Normalised residual axial strain
R_q	Dynamic deviatoric stress ratio
R_s	Stress ratio
τ_{cs}	Critical dynamic shear stress
τ_s	Monotonic Shear Strength or shear stress on the joint plane

U	Constitutive energy
U_A	Area between the first loading curve and the strain axis
U_A^d	Dissipated energy at point A
U_A^e	Area between the first unloading curve and the strain axis
u	Displacement measurement of the medium from its undisturbed state
ϕ	Friction angle of the joint
ϕ_b	Basic friction angle
W_D	Dissipated energy
w_d	Stable energy dissipation per cycle
W_d^N	Accumulative dissipated energy
W_f	Failure dissipated energy
W_I	Incident energy
x_i	Digitised x coordinate of the profile
Z_2	Root mean square of the first derivative of the profile
z_i	Digitised z coordinate of the profile

List of Abbreviations

3D	Three dimensional
AE	Acoustic Emission
ASTM	American Society for Testing and Materials
BD	Brazilian Disc
CNL	Constant Normal Load
CNS	Constant Normal Stiffness
CT	Computed Tomography
CSR	Cyclic Stress Ratio
DEM	Discrete Element Method
DIC	Digital Image Correlation
ELDYN	Entry Level Dynamic
FDM	Finite Difference Method
FEM	Finite Element Method
ISRM	International Society for Rock Mechanics
JCS	Joint wall Compressive Strength
JRC	Joint Roughness Coefficient
JR	Jointed rock

Abstract

With the rising population and demand for mobility, the expansion of the transport system has become a major necessity in many countries, including Australia. Besides, the highly populated Australian coastal belt comprises jointed rocky terrains, and to extend rail transport infrastructure across these jointed rock formations, evaluating their dynamic mechanical behaviour, especially during the design stage of projects, is vital. Nevertheless, comprehensive research studies investigating the dynamic mechanical response of jointed rock formations subjected to cyclic loads that correspond to train loading conditions are extremely scarce. This study aims to investigate the dynamic mechanical behaviour and characteristics of jointed rocks under different cyclic loading conditions, including cyclic deviatoric stress amplitude, confining pressure, number of loading cycles corresponding to train loading conditions and joint surface roughness. Moreover, empirical relationships are proposed to predict crucial dynamic mechanical properties of jointed rocks.

Firstly, a cyclic triaxial test series was performed on planar, sawtooth and natural replicated rock joints at different confining pressures and cyclic deviatoric stress amplitudes. The test results demonstrated that with increasing cyclic stress and decreasing confining pressure, the maximum residual axial strain, dissipated energy, and damping ratio increased, with smoother joints exhibiting significantly higher values than rougher joints. Meanwhile, higher confining pressure and lower cyclic deviatoric stress corresponded to higher resilient moduli. Empirical relationships to predict the steady-state resilient moduli and damping ratio were developed.

Secondly, natural replicated rock joints were subjected to incremental cyclic deviatoric stresses under different confining pressures, and the test results demonstrated that there

existed a critical dynamic deviatoric stress beyond which the yielding occurred, and this threshold increased with confining pressure. When the cyclic deviatoric stress exceeded the critical stress threshold, the accumulated residual axial strain, asperity damage, initial dissipated energy and damping ratio values were substantially higher. An empirical relationship was proposed for residual axial strain evolution under cyclic stresses surpassing the critical stress threshold. Furthermore, specimens were subjected to 500,000 loading cycles, and the test results illustrated that the resilient moduli exhibited a downward trend with cumulative residual axial strain. But resilient moduli were higher than Young's moduli under the same confining pressure. Initially, the damping ratio rapidly decreased and increased slowly with cumulative residual axial strain. There existed a critical dynamic residual axial strain at which the damping ratio was the lowest. Empirical relationships were developed for the resilient moduli degradation and critical dynamic residual axial strain.

Chapter 1: Introduction

1.1 General

Repeated loading is a common loading condition that various geomaterials, such as soils and rocks, experience in construction and infrastructure projects. Cyclic loads can result from various natural sources such as earthquakes, volcanoes, landslides, wave action and wind, and human activities, including blasting, construction operations, machine vibrations, and traffic loading (Prakash, 1981; Srbulov, 2010). Furthermore, it is widely recognised that the mechanical behaviour of rocks under cyclic loading differs substantially from that under static loading (Xiao et al., 2010; Jia et al., 2018). For instance, certain rock materials exhibit enhanced strength and ductility, whereas others display reduced strength and increased brittleness when subjected to repeated loading (Bagde and Petros, 2005a). Moreover, repeated loading has the potential to cause irreversible deformations, resulting in progressive settlements, instability, structural damage and catastrophic failure in rock structures even at stress levels considerably lower than the peak strength ascertained under static loading (Attewell and Farmer, 1973; Jia et al., 2018).

For example, Shi et al. (2014) reported that a significant number of railway tracks had been constructed on or across soft rocks due to the rapid expansion of the railway system in China. Consequently, this has led to various issues, such as accumulated plastic deformations and settlements in both the rail tracks and accompanying tunnels, which present a significant challenge to the efficiency and safety of train operations. Furthermore, according to Zhang et al. (2018b), Xu et al. (2021b) and Chai (2021), the swift development of heavy haul rail transportation on a global scale has led to increased axle loads and traffic volumes, with significant implications on the tunnel lining structure

and the underlying rock during railway operation, especially the tunnel basement structure being the most vulnerable to defects. Train vibrations, groundwater, the stability of surrounding soft rocks, and prolonged train operation can cause softening and disintegration of bedrock into fine particles, which can be eroded by groundwater, thereby causing cavities to develop over time. This process can weaken the contact between the tunnel basement structure and bedrock, resulting in the deterioration of the former and, in severe cases, rail fracture, thereby jeopardising the safety of train operations. Niu et al. (2019) reported that there were frequent rock bursts, stress-induced collapses, spalling, and cracks during the excavation of a deep-buried hard rock railway tunnel in southwest China. On the other hand, according to Aygar and Gokceoglu (2021), a shallow high-speed railway tunnel excavation in Turkey experienced a temporary halt following a collapse in a tunnel segment, which was characterised by moderately weathered rock mass with infilled joint sets. The collapse prompted a redesign of the remaining excavation, which was subsequently carried out via the open excavation procedure due to the low overburden thickness.

Moreover, the escalating population growth has led to a surge in demand for energy and resources, along with rapid urbanisation resulting in heightened traffic congestion and commuting across cities globally. Consequently, there is a pressing need for careful planning and major investments in expanding the transport system and infrastructure in many countries, including Australia (e.g. Khabbaz and Fatahi, 2014). Thus, having a comprehensive understanding of the dynamic mechanical behaviour of rock formations exposed to repeated loading becomes vital, particularly during the design and construction stages of structures on or near rock formations. Moreover, precise quantification of the dynamic characteristics of rock masses, particularly jointed rock masses exposed to various repeated loading conditions corresponding to field conditions,

is vital when predicting a more reliable dynamic response of rock formations. Such knowledge is critical for identifying potential hazards and issues, avoiding expensive mitigation measures, and, most importantly, preventing loss of lives and property damage.

As a result, numerous researchers have performed systematic experimental and theoretical investigations on the dynamic mechanical behaviour of intact rocks under various repeated loading conditions in diverse rock engineering applications. Nevertheless, there is a scarcity of comprehensive research studies that systematically investigate the dynamic mechanical response and the associated characteristics of jointed rock formations exposed to cyclic loads. In particular, research studies exploring the dynamic characteristics of rock joints exposed to train loading conditions are severely scarce, despite the growing demand for faster and heavier trains to transport bulky freight and passengers more effectively and efficiently between destinations around the world.

1.2 Research Significance

Railways are a vital component of Australia's transportation system and make a significant contribution to the country's economy. They serve as a primary mode of transportation for freight and bulk commodities between major cities and ports, as well as for carrying passengers to various destinations, particularly in urban areas. According to the Australian Bureau of Statistics (2018), the Australian population is anticipated to double by 2070, approaching nearly 50 million people. Additionally, according to the Deloitte Access Economics (2020) report, the demand for rail passenger services in Australia has consistently risen by approximately 2% per annum since 2010. Furthermore, the National Freight and Supply Chain Strategy (2019) has reported that Australia's freight task is anticipated to grow by more than 35% between 2018 and 2040,

resulting in a surge of 270 billion tonnes and the total volume transported annually reaching little over 1000 billion tonne-kilometres. In order to meet future transport demands, the implementation of faster and heavier railways, along with the expansion of relevant infrastructure, has become a critical necessity in Australia. Accordingly, the Australian government is not only upgrading the existing rail network but also undertaking new major rail infrastructure projects across the nation, including Inland Rail, METRONET, Melbourne Metro, Sydney Metro, Cross River Rail and Melbourne Airport Rail Link (Booth, 2020). For example, the Inland Rail project is the largest freight infrastructure endeavour in Australia, with the objective of addressing the rising freight demands of the nation's escalating population by establishing a 1700 km long route between Melbourne and Brisbane (Inland Rail, 2023); Sydney Metro project stands as the biggest public transport project undertaking in Australia which interconnects many regions of Sydney via a network of fully accessible stations, offering fast and reliable metro services (Sydney Metro, 2023).

Besides, many of Australia's major cities are located along the coastal belt, with approximately 67% of the Australian population centred around these cities. From a geographical point of view, the settlement and land use patterns have been greatly affected by the fact that most of Australia's interior is too dry with extreme weather conditions to sustain large cities and huge populations, as shown in Figure 1.1. Accordingly, the habitable coastal belt of Australia is characterised by a range of metamorphic, sedimentary and igneous rocky terrains primarily composed of sandstone, limestone, shale, quartzite, schist, dolomite and granite bodies. The rocky landscape may have been formed by a variety of geological processes spanning over 3.8 billion years, including metamorphism cycles, active volcanism, faulting, folding and uplift, sediment lithification, and erosional and weathering processes (Haggett, 2002; Johnson, 2009;

Blewett et al., 2012). Moreover, these rock masses are exposed to various forces, including ground stress, tectonic forces, hydrostatic forces, pore pressures and temperature stresses, during their formation process. As a result, rocks may undergo continuous deformation and form different types of structural features, such as fractures, joints, and faults, which significantly impact the strength and deformability of the rock mass. Figure 1.2 shows an example of a rock formation characterised by a significant number of joints, indicating the presence of distinct planes of weakness within the geological structure.

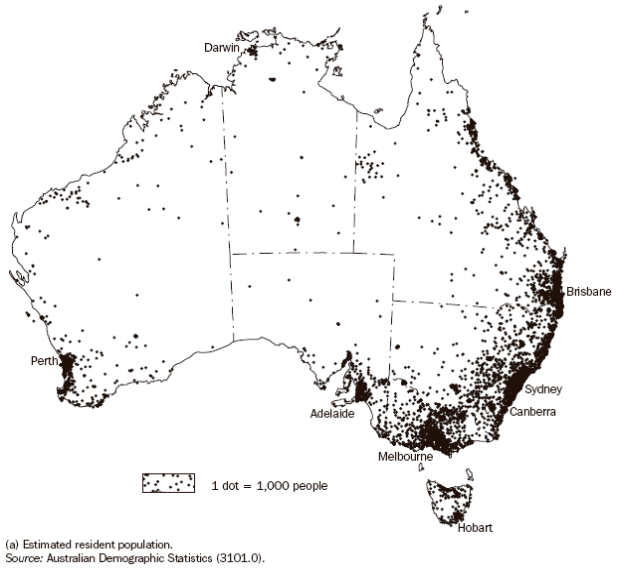

Figure 1.1. Australian map with estimated resident population distribution [Photo courtesy-Australian Demographic Statistics (https://www.abs.gov. au/statistics/people/ population/national-state-and-territory-population/latest-release)].

Figure 1.2. A heavily jointed rock formation in Mount Kosciuszko, Australia [Photo taken by the author].

Thus, it is vital to explore further and accurately quantify the dynamic characteristics of jointed rock subgrades exposed to repeated loading resulting from faster and heavier trains. Consequently, design engineers can be provided with an insight into the underlying mechanisms governing the response of jointed rocks to train loading conditions and assist them in precisely carrying out the stability and performance analysis of rail infrastructure projects during the design stage and minimising the occurrence of unforeseen issues during the construction stage. However, research studies examining the dynamic mechanical characteristics of rock subgrades, particularly jointed rock subgrades under train loading conditions, are severely scarce. Therefore, there is a distinct need for a systematic experimental investigation to determine the dynamic mechanical characteristics of jointed rocks exposed to cyclic loads corresponding to train loading conditions, assess the impact of various factors that influence the variability of these properties and develop reliable and less complicated relationships to predict associated responses reliably.

1.3 Statement of Problem

Previous research studies on rocks exposed to repeated loading conditions have primarily focused on the dynamic behaviour and properties of intact rock types, with only a few systematic research studies available on jointed rock behaviour under such conditions. It should be noted that the majority of the existing experimental studies on rock joints utilised the cyclic direct shear apparatus, with only a handful of studies exploring the dynamic response of rock joints subjected to repeated loads under cyclic uniaxial or triaxial compression test conditions. Some of these research studies have analysed the effect of various cyclic loading conditions on the dynamic mechanical properties of rock joints, such as cyclic stress-strain response, dynamic strength, fatigue life, deformation and energy characteristics, and damage and failure mechanism to some extent. However, the majority of studies conducted on rock joints under cyclic uniaxial or triaxial compression test conditions have utilised artificial or natural rock samples with intermittent joint features and systematic experimental studies on rock specimens with penetrating joints featuring joint surface roughness varying from smooth (planar) to rough (idealised sawtooth and replicated natural joint) are rather scarce.

Furthermore, when planning new surface or underground rail lines, it is vital to accurately predict the vibration levels affecting both the rail track structure as well as neighbouring structures. This requires precise quantification of the vibration characteristics like stiffness and damping parameters of railway subgrades under various field conditions. However, research studies exploring vibration characteristics of rock subgrades, particularly jointed rock masses subjected to repeated loading that are representative of train loading conditions (i.e., cyclic deviatoric stress amplitudes corresponding to different train axle loads, confining stresses reflecting different surface and underground

rail track conditions and loading frequency corresponding to the speed of the train) are very limited.

At the same time, assessing whether the maximum potential deformation of a structure complies with the safe design limits or not is a key aspect of the design stage of any construction project, including railway infrastructure projects. However, there is a substantial paucity of research studies investigating the deformation evolution process and characteristics of rock masses, particularly jointed rock masses exposed to repeated loads. Moreover, experimental investigations on the fatigue characteristics of rock joints exposed to prolonged cyclic loads (corresponding to train loading conditions) and the evolution of stiffness and damping parameters with the strain level have never been adequately explored, as per the author's knowledge.

1.4 Objectives and Scope of the Study

The main objective of this thesis is to explore the dynamic mechanical behaviour and characteristics of jointed rocks subjected to cyclic triaxial loading conditions. This study also analyses the impact of various cyclic loading conditions, including cyclic deviatoric stress amplitude, confining stress, number of loading cycles and the roughness of the joint surface on the dynamic mechanical response of rock joints subjected to repeated loading.

In particular, the following specific objectives of this study can be highlighted.

- Conducting a comprehensive review of past research studies that have explored the dynamic mechanical behaviour of both intact and jointed rocks exposed to cyclic loading and unloading conditions and identifying the research gap.
- Assessing the impact of cyclic deviatoric stress amplitude, confining stress, and joint surface roughness on the dynamic mechanical characteristics of the rock joints by conducting a cyclic triaxial experiment series on jointed rock samples

with planar, sawtooth and natural replicated joint surfaces under train loading conditions.

- Investigating the impact of cyclic deviatoric stress below or in excess of the critical cyclic deviatoric stress on the deformation response and mechanical properties of rock joints by performing a cyclic triaxial experiment series on jointed rock specimens with a natural replicated joint surface by incrementally increasing the cyclic deviatoric stress amplitude at various confining stresses.
- Exploring the impact of confining stress on the fatigue characteristics and, in particular, variation of resilient moduli and the damping ratio with the strain level by performing a cyclic triaxial experiment series on jointed rock specimens with a natural replicated joint surface under prolonged train loading conditions.
- Developing empirical relationships to predict different dynamic mechanical characteristics of jointed rocks by considering the impact of various cyclic loading parameters such as cyclic deviatoric stress, confining stress, number of cycles and joint characteristics such as joint roughness.

1.5 Organisation of the Thesis

This thesis is organised and structured into six chapters. In Chapter 1, following a general background of the project, research significance, the statement of problem, objectives and scope of this study and the organisation of the thesis are presented. The overview of the other five chapters is as follows:

Chapter 2 presents a comprehensive yet concise review of the literature on experimental studies that have investigated the dynamic mechanical response of both intact and jointed rocks subjected to repeated loading conditions. This chapter specifically focuses on the

deformation characteristics, energy dissipation, damping characteristics, strength degradation, damage evolution, failure and progressive behaviour, and the factors that influence these mechanical characteristics under cyclic uniaxial and triaxial loading conditions.

Chapter 3 investigates the vibration characteristics of jointed rocks subjected to train loading conditions. The cyclic triaxial tests are conducted on modelled rock joints with planar, sawtooth and natural replicated joint surfaces under varying confining stresses and cyclic deviatoric stress amplitudes. The cyclic stress-strain response, irreversible strains, resilient moduli degradation, dissipated energy and damping characteristics are analysed and discussed in detail while taking into account the effect of confining stress and cyclic deviatoric stress amplitude. Empirical relations for the steady-state resilient moduli and damping ratio are formulated via nonlinear regression analysis.

Chapter 4 studies the deformation response and dynamic mechanical characteristics of modelled rock joints with a natural joint surface subjected to cyclic triaxial test conditions. The tests are conducted at various confining stresses and incrementally increasing the cyclic deviatoric stress amplitudes until excessive deformation is observed. The critical cyclic deviatoric stress beyond which the rock joints yielded is identified, and the cyclic stress-strain response, yield stress, residual axial deformation evolution, stiffness degradation, dissipated energy evolution, and damping characteristics are analysed and discussed in detail. An empirical relationship to predict residual axial strain in excess of critical dynamic deviatoric stress is proposed based on nonlinear regression analysis.

Chapter 5 explores the dynamic fatigue properties of modelled rock joints with a natural joint surface subjected to prolonged train loads. The cyclic triaxial tests are performed

under a variety of confining stresses, and the static stress-strain response, cyclic stress-strain response, residual axial strain evolution, Young's moduli, resilient moduli and damping ratio variation with the strain level are analysed and discussed in detail. An empirical relationship for the resilient moduli variation with the residual axial strain was developed through nonlinear regression analysis.

Chapter 6 presents the key concluding remarks of this study and provides recommendations for further research, followed by the references list.

Chapter 2: Literature Review

2.1 General

In many rock engineering projects, the rock masses are often exposed to repeated loads resulting from diverse geological processes and rock engineering applications. Moreover, natural rock masses are heterogeneous and typically comprise discontinuities, including fractures, joints, faults and other planes of weakness. The existence of these discontinuities in a rock formation has a substantial impact on its strength and deformation properties which may affect the overall stability of rock engineering structures (Huang et al., 1993; Xie et al., 1997; Belem et al., 2007; Liu et al., 2017). Therefore, assessing the mechanical behaviour of jointed rocks exposed to cyclic loads is essential when designing and planning rock engineering projects involving jointed rock masses.

Despite several research efforts that have been devoted to exploring the dynamic characteristics of rock joints exposed to repeated loading, it is still in the initial stage and remains far from being systematically understood. However, in the past few decades, ample research works have been carried out successfully, exploring the dynamic mechanical behaviour of intact rocks exposed to cyclic loading conditions. Therefore, this chapter presents a comprehensive review of experimental and theoretical investigations that have explored the dynamic mechanical response of both intact and jointed rocks exposed to repeated loading conditions. Specifically, this chapter focuses on the deformation characteristics, energy dissipation, damping characteristics, strength degradation, damage evolution, failure and progressive behaviour, and the factors influencing these mechanical characteristics.

2.2 Overview of Cyclic Tests for Rocks

Over the past few decades, researchers have investigated the dynamic response of rock masses by conducting cyclic loading experiments on rock specimens under diverse test conditions. These cyclic experiments on rocks can be classified based on the available experimental set-up, loading conditions, rock factors and environmental conditions, which are briefly described in the following sections.

2.2.1. Various Available Cyclic Test Set-ups

Predominantly, cyclic uniaxial compression experiments are performed on rocks, and these experiments are representative of the stress state in rock structures such as mine pillars and around galleries (Attewell and Farmer, 1973; Ray et al., 1999; Bagde and Petros, 2005a; Xiao et al., 2009; Xiao et al., 2010). Moreover, Uniaxial cyclic compression tests are widely employed in advancing rock strength criteria established for rock stress-strain behaviours, and laboratory-scale uniaxial cyclic experiments are an effective approach to quantifying the deformation of rocks and their damage characteristics (Meng et al., 2016).

In most of the underground rock engineering applications such as mines, tunnels and caverns, rock masses usually exist in the three-dimensional (3D) stress state, and cyclic triaxial compression experiments are carried out to mimic the real field conditions (Zhenyu and Haihong, 1990; Fuenkajorn and Phueakphum, 2010; Liu and He, 2012; Liu et al., 2012; Ma et al., 2013; Wang et al., 2013). The influence of different confining states in the actual engineering environment on the dynamic mechanical response of rock masses is easily captured through these cyclic triaxial compression tests and is utilised to develop and calibrate constitutive models for numerical simulations (Zhang and Zhao, 2014; Cerfontaine and Collin, 2018).

To investigate the fundamental fatigue process more deeply and to estimate the tensile fatigue resistance of rocks, there are two types of cyclic tensile experiments that the ISRM and ASTM have suggested, i.e., direct tension experiments (Coviello et al., 2005; Cadoni, 2010) and indirect tension experiments (Erarslan and Williams, 2012; Erarslan et al., 2014; Wang et al., 2016). The indirect cyclic Brazilian disc (BD) testing method has been favoured over direct cyclic tensile testing for rocks, largely due to the challenges associated with the experimental operation and sample preparation. For example, during direct tension experiments, slight misalignments and gripping issues might produce unwanted stress concentrations and produce undesirable, premature failures (Zhang and Zhao, 2014).

In comparison to cyclic compressive or tensile testing of rocks, cyclic shear testing has been generally conducted on jointed rocks due to the substantial influence that joint discontinuities can have on the mechanical response of rock masses, which can result in a reduced capacity to support shear loading (Huang et al., 1993; Jing et al., 1993; Lee et al., 2001; Fathi et al., 2016; Niktabar et al., 2017; Kou et al., 2019).

Although the flexural mechanism is a crucial consideration in numerical stability analyses of rock structures, cyclic flexural experiments on rocks have rarely been performed. Nevertheless, three-point or four-point bending experiments have been conducted in the study of natural stone or the stability of historical buildings (Cattaneo and Labuz, 2001; Cardani and Meda, 2004).

A detailed review of cyclic uniaxial, triaxial and direct shear experiments done on intact and jointed rocks and their findings are presented in Sections 2.3 and 2.4, respectively.

2.2.2. Available Cyclic Loading Conditions

In many rock engineering projects, the rock masses are likely to be subjected to various forms of repeated loads. The influence of different features of cyclic loads, including waveform, stress amplitude, average stress and loading frequency, on the stability of rocks has been studied by researchers to different extents.

2.2.2.1 Loading Waveform

The repeated loads applied on rock masses may have different shapes. Inspired by Cerfontaine and Collin (2018) as well as Liu and Dai (2021), Figure 2.1 presents the regular cyclic loading waveforms, such as sinusoidal, triangular and square, most commonly used in rock testing.

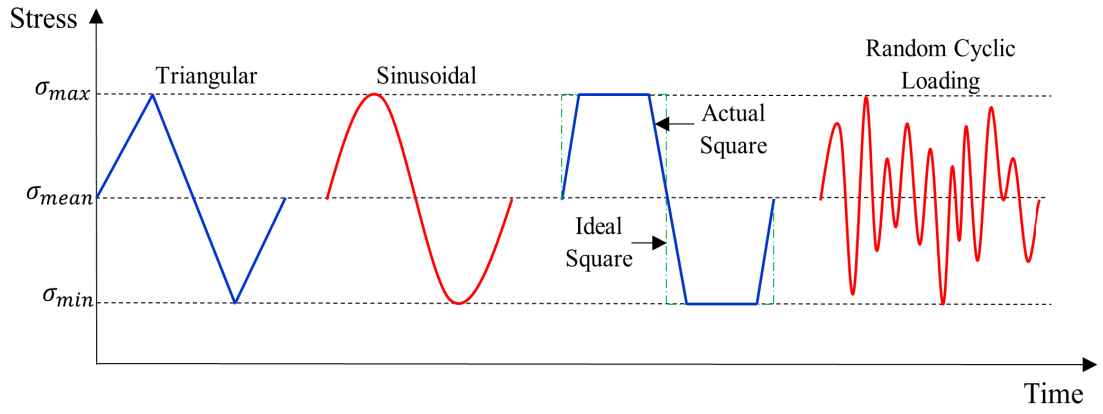

Figure 2.1. Schematics of different cyclic stress waveforms (Modified after Liu and Dai, 2021 and Cerfontaine and Collin, 2018).

The regular sinusoidal waveform has been commonly used in repeated loading experiments due to its simplicity and ease of application. On the other hand, the sinusoidal waveform is more representative of the stress waves generated during most of the dynamic loading applications on rocks. Yet, the effect of other regular and simple cyclic waveforms, such as triangular and square waveforms (Zhenyu and Haihong, 1990; Bagde and Petros,2005a), has also been considered when exploring the mechanical response of

rocks exposed to repeated loads. Zhenyu and Haihong (1990) tested sinusoidal and triangular loading waveforms and stated that the deformation resulting from the sine loading waveform was greater than that resulting from the triangular loading waveform. Moreover, Bagde and Petros (2005a) used sinusoidal, triangular and square loading waveforms and reported that the square waveform caused the most damage due to its high cyclic energy input, while the triangular waveform caused the slightest damage, as it had a lower cyclic energy input to cause the failure of the rock specimens at the same loading frequency and stress amplitude.

Meanwhile, some attempts have also been undertaken to evaluate the mechanical response of rocks subjected to random cyclic loading (Liu et al. 2018c). Figure 2.1 presents a schematic diagram of a random cyclic loading path. Liu et al. (2018c) subjected intermittent rock joints to random cyclic compression loading, and analogous to the regular cyclic loading experiments, they observed hysteresis loops in the stress-strain curves and irreversible strain in each hysteresis loop.

2.2.2.2 Loading Stress Level

Rock formations undergo repeated loading and unloading under different stress levels, requiring experimental investigations on rocks with either constant or variable stress amplitude and average stress. While most of the literature reports cyclic experiments conducted with constant amplitude and average stress conditions, alternative cyclic loading conditions have also been considered notably. These include stepwise increasing amplitude (Heap et al., 2009; Liang et al., 2012; Zhang et al., 2013; Meng et al., 2016; Li et al., 2019a), multilevel amplitude (Liu et al., 2014; Wang et al., 2013; Jia et al., 2018; Yang et al., 2018b; Peng et al., 2020) and increasing average stress with constant amplitude (Bagde and Petros, 2005a; He et al., 2016) loading. Inspired by Cerfontaine

and Collin (2018) as well as Liu and Dai (2021), Figure 2.2 presents schematic diagrams of different cyclic loading paths with variable stress levels and amplitudes commonly used in rock testing.

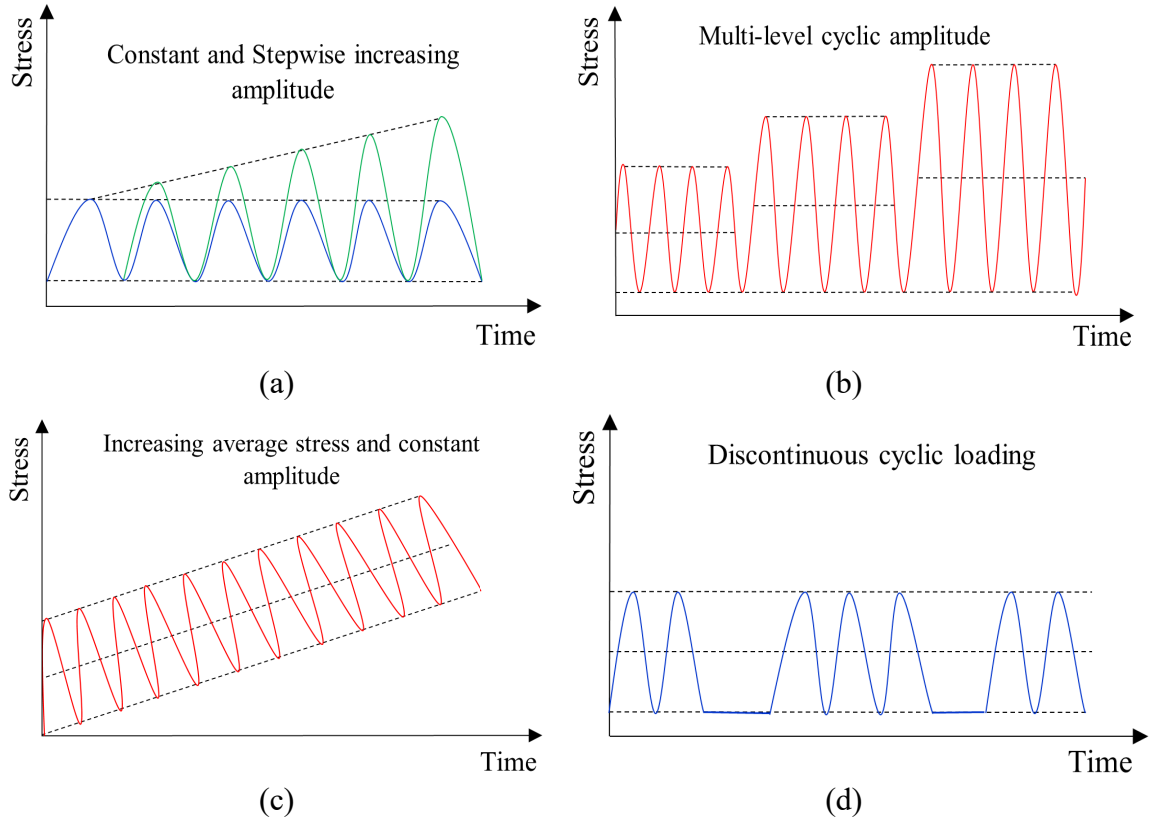

Figure 2.2. Schematics of different cyclic loading paths (Modified after Liu and Dai, 2021 and Cerfontaine and Collin, 2018).

According to Jia et al. (2018), the dynamic mechanical behaviour of rocks exposed to increasing-amplitude cyclic loading experiments differs substantially from that observed in constant-amplitude experiments. Therefore, different cyclic incremental loading tests on rocks have been performed, aiming for numerous objectives and yielding different outputs. For instance, Heap et al. (2009) and Zhang et al. (2013) investigated the degradation of elastic properties of rocks (basalt and argillite specimens, respectively) with increasing levels of maximum stress in successive cycles. Meng et al. (2016) examined the evolution of energy of red sandstone specimens during incremental cyclic loading. Liu et al. (2014) evaluated the damage progression of salt rock samples with

increasing stress levels simulating fluctuating gas pressures in gas caverns. Jia et al. (2018) studied the deformation evolution of sandstone specimens by applying a combination of constant and increasing amplitude cyclic loading, which mimics complex cyclic LOADING states encountered in hydropower stations. Yang et al. (2018b) explored the deformation and damage progression of limestone specimens under multilevel amplitude cyclic loading corresponding to repeated mining stresses.

Moreover, rock formations may be subjected to discontinuous cyclic loading with time intervals where cyclic stress levels are minimum, especially during wheel loading and oil gas mining. Therefore, cyclic experiments on rocks with discontinuous cyclic loading paths containing spaced stress cycles have also been performed to assess the impact of time intervals on the fatigue behaviour of rocks. For example, Fan et al. (2016, 2017 & 2019) carried out a comparison between conventional fatigue and interval fatigue experiments on salt rock specimens with zero-stress and low-stress intervals with different durations. They observed that the residual strain resulting from a spaced stress cycle was considerably greater than that arising from a normal stress cycle, and the accumulative rate of residual deformation increased with increasing interval duration. Further, they found out that when the intervals were shorter than a threshold value, the fatigue life of the specimens decreased, while at intervals longer than this threshold value, fatigue life slightly increased. Figure 2.2(d) illustrates a schematic diagram of a discontinuous cyclic loading path.

2.2.2.3 Loading Frequency

The cyclic loads applied on rock masses may have different loading frequencies corresponding to different cyclic loading sources. According to Liu and Dai (2021), frequencies in the range of 0-10 Hz have been extensively used for simulating seismic conditions and wheel loads, whereas rock bursts and blasting activities have been simulated using frequencies in the range of 10-100 Hz. Accordingly, some researchers have explored the impact of frequency on the dynamic mechanical response of rocks corresponding to various rock dynamic applications (Attewel and Farmer, 1973; Bagde and Petros, 2005a; Bagde and Petros, 2009; Liu et al., 2012; Zhou et al., 2015; Momeni et al., 2015; He et al., 2016; Peng et al., 2020).

The impact of loading frequency on the dynamic characteristics of rocks has been reported differently by researchers due to various reasons, including differences in the type of rock and test methods used. For instance,

- Burdine (1963) stated that the impact of frequency on the fatigue life of the tested sandstone specimens was negligible under the tested frequencies. Zhou et al. (2015) mentioned that the fatigue life of tested red sandstone specimens exhibited an initial reduction followed by an increase as the frequency was increased. Attewell and Farmer (1973), Liu et al. (2012), Momeni et al. (2015) and He et al. (2016) pointed out that the fatigue life of tested dolomite, sandstone and granite rock specimens increased at higher loading frequencies.
- Bagde and Petros (2005a & 2009) discovered that as frequency increased, there was a decrease in the fatigue strength of the tested rocks. He et al. (2016) mentioned that the fatigue strength first increased and then reduced with increasing frequency. According to Peng et al. (2020), the loading frequency had

a positive correlation with fatigue strength under a constant number of loading cycles.

- Bagde and Petros (2005a) stated that the peak axial strain reduced with increasing frequency. He et al. (2016) observed a rise in the peak axial strain with increasing loading frequency, which was then followed by a slight reduction. Liu et al. (2012), Momeni et al. (2015), and Peng et al. (2020) mentioned that at higher frequencies, the cumulative residual axial strains were also higher.
- Bagde and Petros (2005a & 2009) found that as the loading frequency increased, there was a reduction in the dynamic axial stiffness and Young's modulus of tested sandstone samples. Liu et al. (2012) stated that the initial stiffness of sandstone specimens increased at higher frequencies, and stiffness degraded more rapidly with loading cycles at lower frequencies. Momeni et al. (2015) reported that the tangent and secant moduli of granite samples showed an accelerated degradation with loading cycles at higher frequencies. Moreover, Peng et al. (2020) mentioned that the elastic moduli evolution of sandstone specimens showed an upward trend with frequency under a constant number of loading cycles.
- Bagde and Petros (2009) presented that the dissipated energy decreased while the retained elastic energy increased with increasing frequency, while Momeni et al. (2015) observed a reduction in the energy density (input energy) and hysteresis energy (dissipated energy) at higher loading frequencies.

Figure 2.3 illustrates the impact of frequency on the dynamic properties of different rocks, such as cumulative residual axial strain, dynamic axial stiffness and energy evolution adapted from Liu et al. (2012) and Momeni et al. (2015).

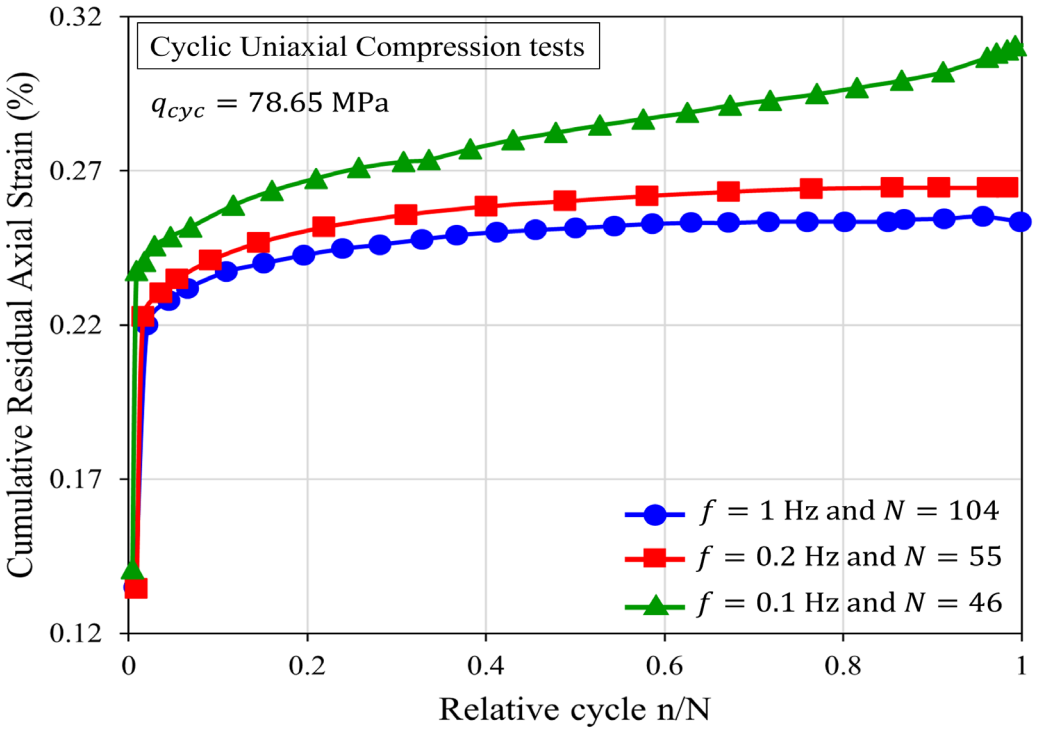
Cyclic Uniaxial Compression tests
q_{cyc} = 78.65 MPa
f = 1 Hz and N = 104
f = 0.2 Hz and N = 55
f = 0.1 Hz and N = 46
Cumulative Residual Axial Strain (%)
Relative cycle n/N
0.32
0.27
0.22
0.17
0.12
0
0.2
0.4
0.6
0.8
1

(a)

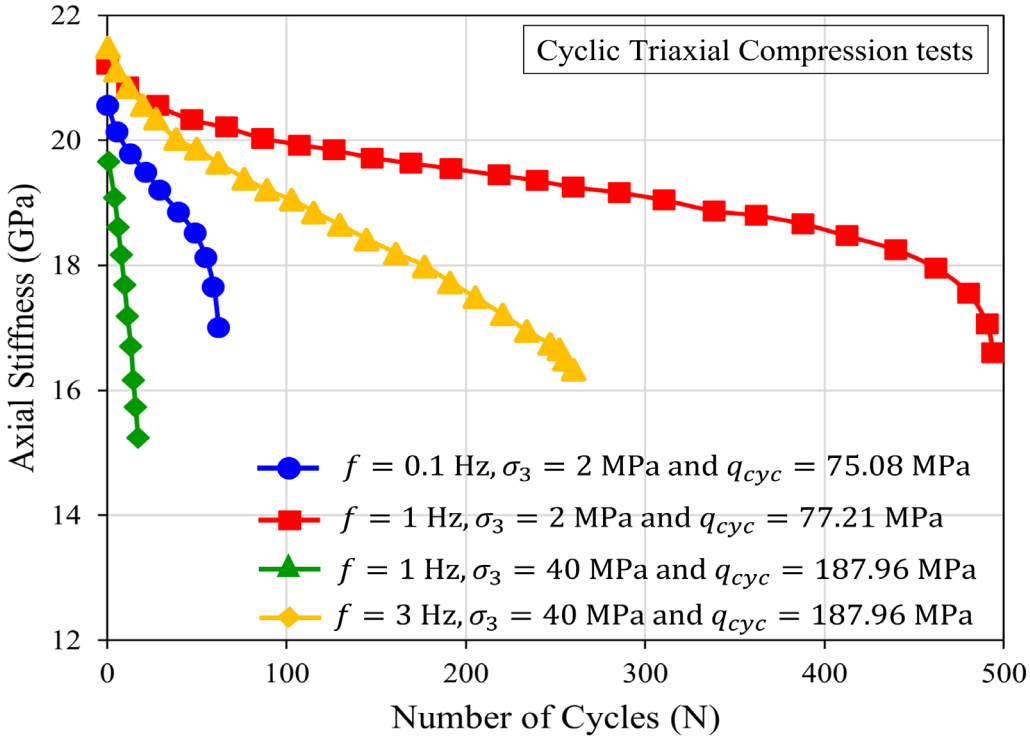
Cyclic Triaxial Compression tests
f = 0.1 Hz, σ_3 = 2 MPa and q_{cyc} = 75.08 MPa
f = 1 Hz, σ_3 = 2 MPa and q_{cyc} = 77.21 MPa
f = 1 Hz, σ_3 = 40 MPa and q_{cyc} = 187.96 MPa
f = 3 Hz, σ_3 = 40 MPa and q_{cyc} = 187.96 MPa
Axial Stiffness (GPa)
Number of Cycles (N)
22
20
18
16
14
12
0
100
200
300
400
500

(b)

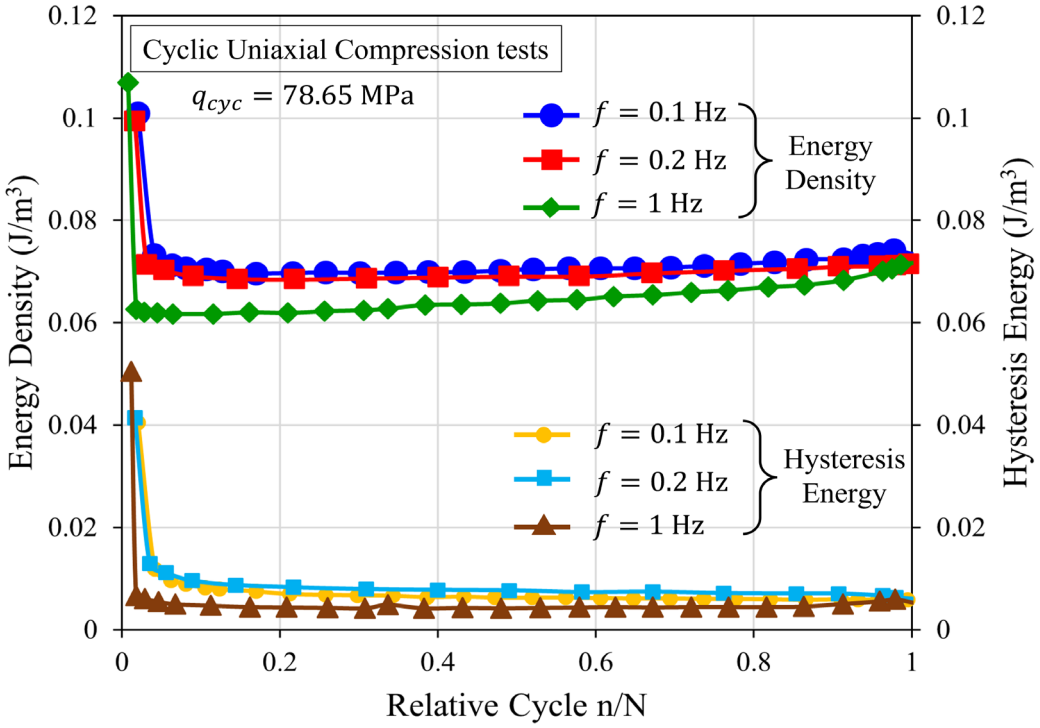

(c)

Figure 2.3. Impact of frequency on the fatigue response of different rock types in terms of (a) cumulative residual axial strain (After Momeni et al., 2015), (b) Axial stiffness (After Liu et al., 2012), and (c) Energy evolution (After Momeni et al., 2015).

2.2.3. Importance of Rock Factors for Assessing Cyclic Loading Behaviour of Rocks

Rock masses encountered in rock engineering projects can be classified into three major types based on the process that resulted in their formation: igneous, sedimentary and metamorphic. Igneous rocks originate from the cooling and solidification of magma or lava, whereas sedimentary rocks result from the accumulation and deposition of mineral and/or organic particles followed by compaction and cementation on or near the Earth's surface. Metamorphic rocks emerge from the transformation of a pre-existing rock into a novel rock type with a different mineral composition or texture as a result of changes in environmental conditions such as fluctuations in temperature, pressure, mechanical stress, chemical components or, more commonly, a combination of these factors.

Researchers have conducted cyclic loading experiments on various rock types to discover the impact of various chemical compositions, mineralogy, grain size, texture and other distinguishing characteristics on the dynamic response of these rocks exposed to various repeated loading conditions (Bagde and Petros, 2009; Heap et al., 2010; Nejati and Ghazvinian 2014; Pola et al., 2014). For example, Bagde and Petros (2009) applied cyclic uniaxial compression loading on sandstone, conglomerate and siltstone specimens obtained from various mine locations. They found out that Young's modulus, axial stiffness and fatigue strength of the rock increased as the grain size reduced and quartz content, compactness, and density increased. Further, they observed that more energy was required to cause rock fracture when the quartz content and compactness were high.

Moreover, rock formations existing in nature are usually heterogeneous and presented with discontinuities, including diaclases, joints, fractures, interbedding, foliation fissures and other planes of weaknesses. The influence of these heterogeneities and their different configurations, such as fracturing degree, orientation, aperture, roughness, presence of infill material, pore fluids and water flow on the dynamic stability and mechanical behaviour of rock masses has been considered by researchers to some extent (Li et al., 2001b; Liu et al., 2017; Liu and Liu, 2017; Zheng et al., 2020a). For example, Li et al. (2001b) and Liu et al. (2017) performed cyclic uniaxial compression experiments on intermittent rock joints to explore the effect of different joint geometries such as joint density, persistency, inclination angle and spacing on the fatigue mechanism. Li et al. (2001b) reported that the dynamic strength of the rock joints reduced as the joint density increased. Furthermore, they noted that the dynamic strength increased slightly with a rise in joint inclination angle, then decreased until it reached its lowest value and subsequently increased again. Further, they observed that the dynamic deformation modulus exhibited an upward trend with increasing joint inclination angle and decreasing

joint density. Liu et al. (2017) observed that the cumulative residual strains, Young's modulus and secant modulus increased as the joint inclination angle and spacing decreased, and joint density and persistency increased. Moreover, they stated that both the stored energy and elastic energy in each cycle reduced as the joint inclination angle, spacing, density, and persistency increased. Mirzaghorbanali et al. (2014) explored the impact of infill thickness on the shear behaviour of infilled rock joints under cyclical shearing. They found out that as the infill thickness increased, the shear mechanism of the overall joint was predominantly regulated by the infill properties. As a result, shear strength exhibited a downward trend.

A detailed review of research studies conducted to explore the dynamic mechanical response of intact and jointed rocks exposed to repeated loading conditions is presented in Sections 2.3 and 2.4.

2.2.4. Importance of Environmental Conditions in Assessing Cyclic Behaviour of Rocks

Rock formations existing in nature are exposed to diverse environmental conditions such as various humidities, temperatures, seepage and groundwater levels, and as a result, these rock masses are generally susceptible to weathering and deterioration. Cycles of wetting-drying induced by variations in rainfall, vaporisation and fluctuations in groundwater levels and reservoir water levels are key environmental conditions that weaken the rocks and accelerate the deterioration process (Yang et al., 2018a). In addition, in some cold regions, water-bearing rock masses are prone to frost pressure as well as frost-heaving forces caused by cycles of freezing and thawing of pore water within the rock mass (Liu and Dai, 2021). Moreover, deep rock formations may be exposed to repeated heating and cooling processes occurring during geothermal energy extraction, oil or gas exploitation,

and radioactive nuclear waste disposal, which can cause thermal damage to the rock microstructure (Liu et al., 2019). Despite quite distinct from mechanical loading, cyclic wetting-drying experiments (Zhang et al., 2014; Yang et al., 2018a; Chen et al., 2019c; Cai et al., 2020; Li et al., 2021), cyclic freezing-thawing experiments (Chen et al., 2004b; Takarli et al., 2008; Tan et al., 2011; Li et al., 2019b; Zhang et al., 2020) and cyclic heating-cooling experiments (Yavuz et al., 2010; Brotons et al., 2013; Liu et al., 2019) have been carried out on a variety of rock types to evaluate the impact of these processes on the mechanical behaviour of rocks.

2.3 Experimental Studies on Intact Rocks Exposed to Cyclic Loads

Rock masses present in nature may constitute unfractured rock to extremely fractured rock. In a typical rock mass, intact rock pertains to the unfractured rock located between discontinuities, which may vary in size from a few millimetres to several metres (Hudson and Harrison, 1997). The properties of intact rocks are influenced by the constituent material and the bonding mechanism between them. Therefore, intact rock properties are one of the main constituents governing rock mass behaviour. Moreover, repeated loads are commonly generated in many geological procedures and rock engineering applications, affecting the rock mass behaviour. It is well-known that the mechanical response of many materials exposed to cyclic loading significantly differs from their static loading behaviour. As a result, there has been heightened interest in exploring the behaviour of rocks exposed to repeated loading conditions over the past few decades. Therefore, numerous researchers have explored the mechanical characteristics of various types of intact rocks exposed to various repeated loading conditions. Sections 2.3.1 to 2.3.6 review existing systematic experimental studies on intact rocks under cyclic triaxial and uniaxial loading conditions.

2.3.1. Cyclic Stress-Strain Response

A stress-strain response is a measurement of how a material reacts to being loaded or deformed. Cyclic stress-strain response particularly refers to how a material behaves when subjected to repeated loading and unloading rather than a single static load. Early experimental investigations on intact rocks under repeated loading demonstrated the presence of hysteresis loops in the cyclic stress-strain curves of rocks, where the unloading curve differs from the loading curve (Burdine, 1963; Scholz and Koczynski, 1979; Zhenyu and Haihong, 1990; Tien et al.,1990). In a hysteresis loop, the axial strain during each loading and unloading cycle can be split into two components: elastic strain and plastic strain. The elastic strain refers to the reversible deformation that occurs when a material is loaded and then unloaded. The plastic strain refers to the irreversible deformation that occurs during the loading-unloading process. The plastic strain accumulation rate is not constant along the applied loading cycles, as evident from the hysteresis loop spacings (Cerfontaine and Collin, 2018; Liu and Dai, 2021).

Many researchers reported that the hysteresis loops of various intact rocks showed a sparse-dense-sparse trend when exposed to repeated loads (Wang et al., 2016; Zhao et al., 2020; Wang et al., 2022; Zhao et al., 2022b). During the initial sparse state, axial deformation develops rapidly with large hysteretic loop spacings, resulting in the accumulation of large plastic strains. As the cyclic loading continues, the strain accumulation rate stabilises, resulting in lower hysteresis loop spacings and plastic strain accumulation (i.e., dense state). However, during the final sparse state, hysteresis loop spacing and axial strain suddenly escalate, resulting in damage and failure of the rock (Wang et al., 2016; Zhao et al.,2020; Zhao et al., 2022b). Moreover, researchers observed that the hysteresis loops were quite dense at reduced levels of stress as compared to

elevated levels of stress, and the plastic strain accumulation rate escalated as the stress levels increased (Liu et al., 2014; Jia et al., 2018; Peng et al., 2019). Furthermore, when the applied cyclic stress levels are lower, the hysteresis loops presented only two phases, sparse to dense, with no signs of damage failure to the rock. Under such conditions, the hysteresis loops were wider during the initial few cycles and became tighter and tighter with increasing loading cycles (Wang et al., 2021c; Zhao et al., 2022a).

Furthermore, several researchers pointed out that under uniaxial compression loading conditions, various intact rocks exhibited a correlation between cyclic stress-strain curves and their corresponding monotonic stress-strain curves (Martin and Chandler, 1994; Xiao et al., 2009; Guo et al., 2012; Song et al., 2013).

2.3.2. Dynamic Strength and Fatigue Life

The dynamic strength of rocks refers to the stress limit a rock specimen can withstand under repeated loading without undergoing failure. However, it is noteworthy that, like most other materials, the dynamic strength of rocks is typically lower compared to their static strength (Attewell and Farmer, 1973). Therefore, having a proper understanding of the dynamic strength of rocks is crucial when designing and constructing rock engineering structures exposed to dynamic loads. Moreover, the dynamic strength of rocks can be influenced by various factors, and many researchers have explored the effect of various cyclic loading conditions on the dynamic strength of various intact rocks.

For instance, early research by Burdine (1963) revealed that with increasing confining stress, the dynamic fatigue strength of Berea sandstone specimens exposed to repeated loading increased and was in the range between 74 - 93% of the static compressive strength. Further, he observed that the dynamic strength of the wet specimens was lower than that of the dry specimens. Similarly, Haimson and Kim (1972) reported that Georgia

and Tennessee marble specimens failed at 50% and 75% of the corresponding static compressive strengths, respectively. Moreover, Singh (1989) observed that the tested Graywacke samples had a fatigue strength of 87% of the uniaxial compressive strength (UCS). At dynamic stresses of up to 29% of the UCS, specimens displayed strain-hardening behaviour. Later, Bagde and Petros (2005a) documented that the dynamic fatigue strength of tested sandstone specimens reduced with a rise in the cyclic stress and the dynamic fatigue strength of saturated specimens decreased by about 30% more than that of dry specimens. Moreover, Ma et al. (2013) performed cyclic triaxial tests on salt rock specimens and stated that the dynamic strength is approximately 80-89% of the corresponding triaxial compressive strength. Further, they pointed out that the salt rocks exhibited strain-hardening behaviour under cyclic stresses below this threshold value. Accordingly, they observed that a higher cyclic stress amplitude and confining stress corresponded to increased triaxial compressive strength values at cyclic stresses below the threshold value. Similarly, Taheri et al. (2016) observed that the fatigue strength of sandstone specimens subjected to repeated loading is around 94% of rock peak strength. Further, they noted that the peak strength obtained through post-static loading increased by 11% under lower cyclic stresses. Furthermore, Liu et al. (2021a) subjected dolomite specimens to multilevel cyclic loading and noted that the dynamic fatigue strength is in the range of 60 - 70% of the static compressive strength.

Furthermore, the fatigue life of rocks refers to the number of loading cycles a rock sample can undergo before failure occurs under repeated loading conditions. Many factors can influence the fatigue life of rocks, and various researchers have investigated the fatigue life of various intact rock types since understanding the fatigue life of rocks is essential for ensuring the safety and durability of rock engineering structures exposed to repeated loads.

Early studies by Singh (1989) on Graywacke specimens and Zhenyu and Haihong (1990) on marble and sandstone specimens established that the fatigue life of intact rocks reduces with increasing cyclic stress under both cyclic uniaxial and triaxial compression loading, respectively. Similarly, Xiao et al. (2010) stated that as the maximum applied stress and stress amplitude increase, the fatigue life decreases for granite specimens under cyclic uniaxial loading conditions. Moreover, Liu et al. (2011 & 2012) employed cyclic triaxial tests on sandstone specimens and observed that the number of cycles to reach failure diminishes as the stress ratio (defined as the maximum cyclic stress divided by the compressive strength under static triaxial testing at the same confining stress) rises. Additionally, Singh et al. (1989), Momeni et al. (2015), and Guo et al. (2018) reported that fatigue life increases exponentially as the applied cyclic stress decreases.

2.3.3. Residual Axial Deformation

Under cyclic loading, materials undergo recoverable (elastic or resilient) and residual (plastic or irrecoverable) deformation as a result of repeated loading and unloading. The elastic deformation under cyclic loading refers to the temporary deformation of the material that occurs during loading and returns to its original position and size during unloading. Plastic deformation under cyclic loading refers to the permanent deformation of the material that remains during unloading and accumulates over successive loading cycles. Figure 2.4 schematically illustrates the types of axial strains that exist during a loading cycle. Accordingly, understanding the residual axial deformation of rocks exposed to repeated loading is essential for assessing the dynamic response of rock formations and ensuring the safety as well as durability of structures built on or near them. Therefore, many researchers analysed the residual axial deformation of various intact rocks subjected to various repeated loading conditions.

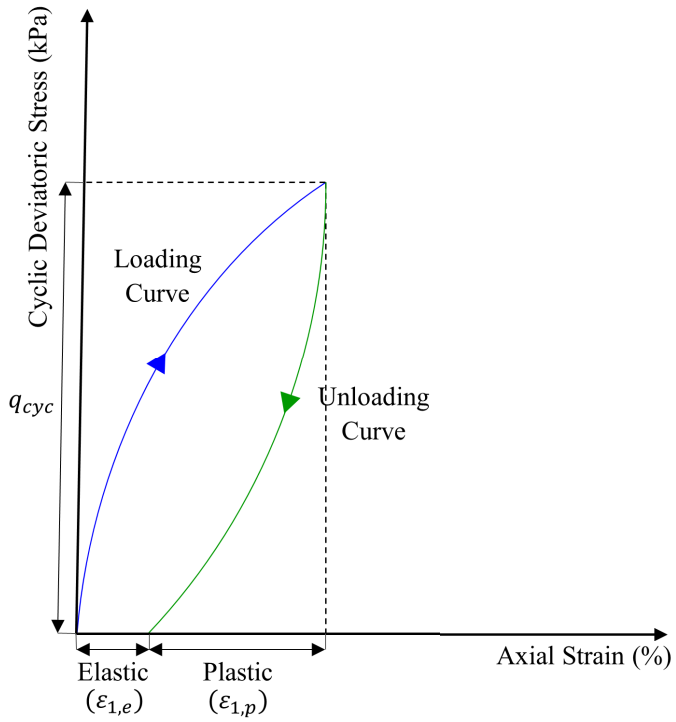

Figure 2.4. Schematic diagram of a typical hysteresis loop in a loading cycle showing elastic axial strain ($\varepsilon_{1,e}$) and residual axial strain ($\varepsilon_{1,p}$) (Modified after Zhang et al., 2017).

The residual axial strain development in rocks exposed to various repeated loading conditions can be categorised into three forms, as depicted in Figure 2.5 (Xiao et al., 2009; Liu and Dai, 2021). In many experimental studies on rocks, the development of residual axial strain follows curve b, displaying three development stages, namely, the initial, steady and accelerated stages (see Figure 2.5). During the initial stage, residual axial strain accumulates quickly and reaches a steady state, and this steady stage remains for most of the cyclic loading process. Eventually, residual axial strain accumulates sharply during the accelerated stage, finally leading to the failure of rocks. When rocks are exposed to high cyclic stresses, the accumulation of residual axial strain follows curve a. In this scenario, the residual axial strain accumulates rapidly, and the typical three-stage development law is barely evident. Consequently, these rocks experience failure within a few loading cycles, resulting in low fatigue life. When rocks are subjected to cyclic

stresses lower than the threshold for fatigue failure, the residual axial strain development follows curve c, exhibiting initial and steady phases only. Following the initial phase, the residual axial strain remains steady during the remainder cyclic loading process, with no signs of an accelerated phase occurring throughout the entire cyclic loading and unloading procedure (Xiao et al., 2009; Liu and Dai, 2021).

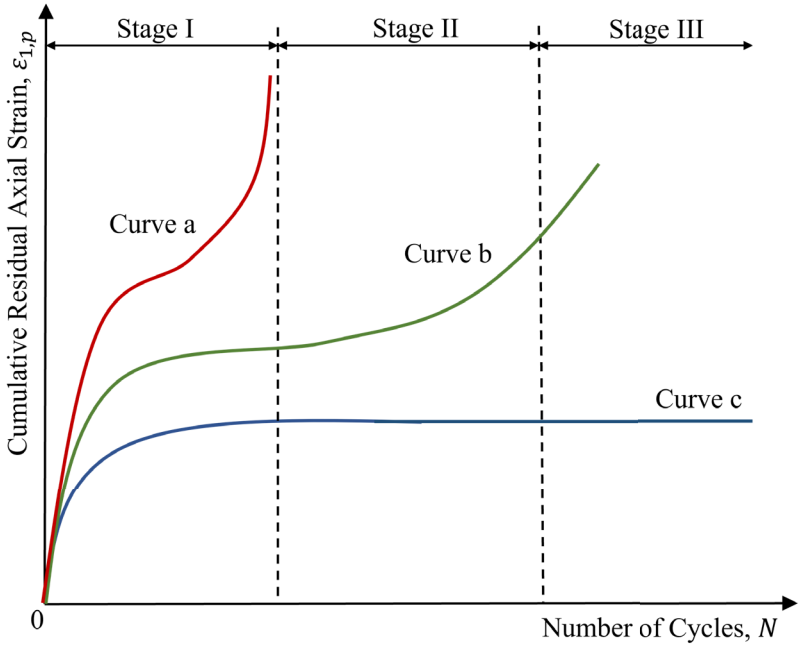

Figure 2.5. Schematics of classification of irreversible axial deformation evolution curves ($\varepsilon_{1,p}$) (Modified after Xiao et al., 2009 and Liu and Dai, 2021).

Tien et al. (1990) and Zhenyu and Haihong (1990) were pioneers who observed three distinct stages in residual axial strain development in tested rocks exposed to cyclic triaxial loading conditions similar to static creep curves. Later, Xiao et al. (2010), Liu and He (2012), Guo et al. (2018), and Zhou et al. (2020) also examined three phases (initial, steady and accelerated) in the residual axial deformation of the tested rocks under cyclic uniaxial and triaxial loading conditions. In the meantime, Ma et al. (2013) observed two stages (initial and steady) in the residual axial deformation of salt rock samples subjected to cyclic triaxial testing. Furthermore, Jia et al. (2018) and Peng et al. (2019) applied increasing amplitude cyclic loading on specimens, and within a given stress level, they

examined two stages in the residual axial strain development where residual axial strain accumulates rapidly during the initial loading cycles and reaches a steady state afterwards (similar to the well-recognised Kaiser effect observed in a variety of materials). Further, they also observed an abrupt accumulation of residual axial strain during the final stress level than the rest of the stress levels, ultimately culminating in the failure of the rock specimens. Additionally, Liu et al. (2021a) noted three phases of the residual axial deformation evolution process in tested dolomite specimens subjected to triaxial multilevel cyclic loading conditions. Besides, Wang et al. (2013) described that residual axial strain accumulation in intact rocks is affected by the volume change in rocks. They explained that within the volumetric compaction domain, the residual axial strain diminishes as the loading cycles increase, whereas, in the volumetric dilation domain, the residual axial strain rises with increasing loading cycles.

Moreover, Tien et al. (1990) stated that a critical axial strain exists beyond which failure of the sandstone samples occurred, and the value of this critical axial strain is not reliant on the applied confining stress and loading frequency. On the other hand, Liu et al. (2011 & 2012) and Liu and He (2012) conducted cyclic triaxial experiments on intact sandstone specimens and noted higher confining stresses corresponded to elevated residual axial strains at failure. In contrast, Peng et al. (2019) observed that residual axial strain development reduced under cyclic triaxial loading as the confining stress increased.

Furthermore, Zhenyu and Haihong (1990) and Ma et al. (2013) reported a positive correlation between cyclic stress and residual axial deformation. Similarly, Ma et al. (2013) and Momeni et al. (2015) stated that residual axial strain development increased as the maximum applied cyclic stress increased. Further, Zhenyu and Haihong (1990) and Jia et al. (2018) observed that the lateral deformation of the tested intact rock specimens was higher than the axial deformation under cyclic triaxial loading. Figure 2.6 presents

sample plots of residual axial strain evolution with loading cycles of intact rock specimens reported in the literature (adopted from Liu and He, 2012).

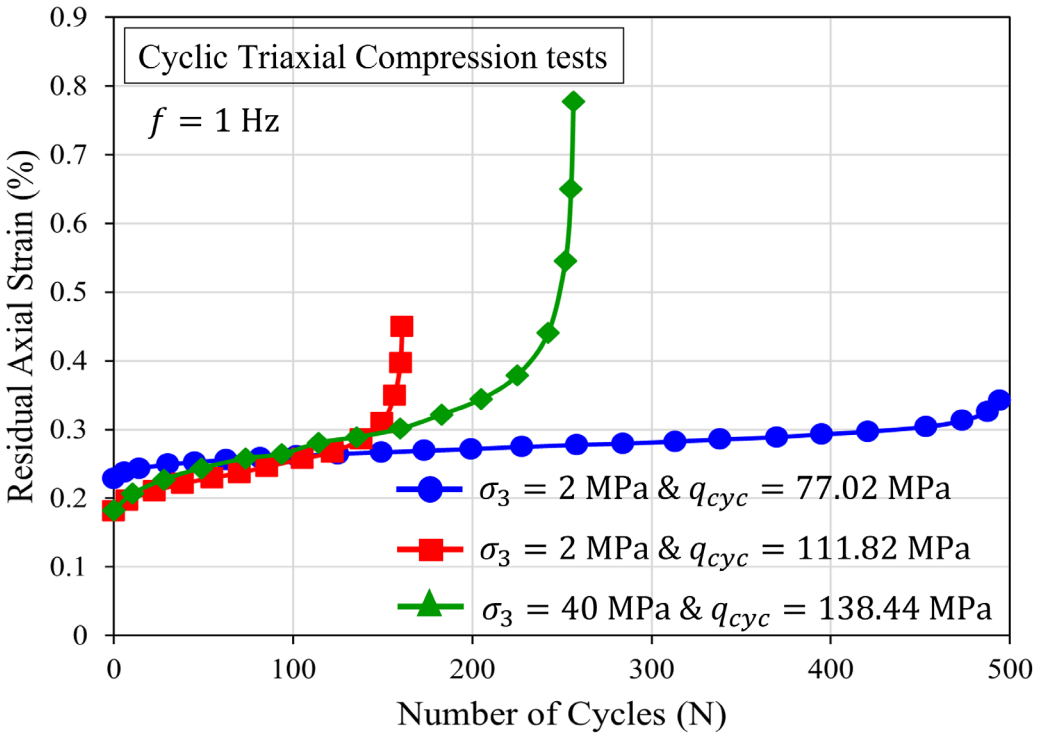

Figure 2.6. Residual axial strain evolution with loading cycles (Reproduced from Liu and He, 2012).

In addition, several researchers developed conceptual and empirical models to mathematically represent, quantify and make predictions for the residual axial deformation as a function of various factors based on observations or experimental data. Table 2.1 summarises conceptual and empirical models developed for the residual axial deformation in intact rocks under cyclic loading conditions. For instance, based on the experimental results, Shi et al. (2014) proposed an empirical equation for the cumulative plastic strain of water-rich mudstone specimens subjected to repeated loading. This model incorporates the influence of factors such as cyclic stress, number of cycles, vibration frequency, the physical state of the rock, and stress history on cumulative plastic deformation. Jia et al. (2018) developed two empirical equations based on the results obtained from cyclic triaxial tests conducted on sandstone samples: 1) to describe the

impact of stress levels on the irreversible axial strain and 2) to explain the effect of the number of loading cycles and applied stress level on the irreversible axial strain.

Table 2.1. Theoretical and empirical models developed for intact rocks under cyclic loading.

Mechanical Property	Reference	Formula	Description
Cumulative plastic strain	Shi et al. (2014)	$\varepsilon_p = a.(k\eta_s + \eta_d)^m \times g(f) \times N^b$ $\eta_d = \frac{\sigma_d}{\sigma_f}$ $\eta_s = \frac{\sigma_s}{\sigma_f}$	ε_p is the cumulative plastic strain, η_d is the dynamic stress ratio, η_s is the static deviatoric stress ratio, σ_d is the amplitude of the dynamic stress, σ_s is the static deviator stress, σ_f is the static failure stress of rocks, N is the number of cycles, $g(f)$ is a function that assesses the impact of vibration frequency, and a, b, k, m are empirical constants.
Irreversible axial strain	Jia et al. (2018)	$\dot{\varepsilon}_1^{irr} = \beta.\exp(\alpha.\sigma)$	$\dot{\varepsilon}_1^{irr}$ is the irreversible axial strain rate, σ is the stress level, α and β are material parameters.
Irreversible axial strain	Jia et al. (2018)	When $\sigma \le \sigma_s$ $\dot{\varepsilon}_1^{irr} = \frac{\sigma}{\eta_1} + \frac{\sigma}{\zeta_1}N + \frac{\sigma}{\eta_2}\left(1 - \exp\left(-\frac{\eta_2}{\zeta_2}N\right)\right)$ When $\sigma > \sigma_s$ $\dot{\varepsilon}_1^{irr} = \frac{\sigma}{\eta_1} + \frac{\sigma}{\zeta_1}N^n + \frac{\sigma}{\eta_2}\left(1 - \exp\left(-\frac{\eta_2}{\zeta_2}N\right)\right)$	$\dot{\varepsilon}_1^{irr}$ is the irreversible axial strain rate, σ is the stress level, σ_s is the critical stress, N is the number of cycles, η_1, η_2, ζ_1 and ζ_2 are material constants, and n is a parameter that reflects the rapid increase in the irreversible axial strain when the specimen reaches failure.
Deformation modulus	Yoshinaka et al. (1996)	$\frac{E}{E_{max}} = 1 - \left(1 - \frac{E_r}{E_{max}}\right)\left\{1 - \exp\left[-m\left(\frac{\varepsilon_p}{\varepsilon_r^p}\right)^n\right]\right\}$	E, E_{max} and E_r are either secant or tangential, loading or unloading deformation moduli, at the current state of plastic straining, at the yield point and at the onset of the residual state, respectively, ε_p is the current accumulated plastic

			strain, ε_r^p is the total axial plastic strain accumulated at the onset of the residual state, m and n are fitting parameters.
Deformation modulus	Wang et al. (2013)	$E = A(\bar{\sigma}^{cr})^n(\varepsilon_{1r})^m$ $\bar{\sigma}^{cr} = \frac{q_p - p_p \tan\beta}{1 - \frac{1}{3}\tan\beta}$	E is the deformation modulus, $\bar{\sigma}^{cr}$ is the equivalent stress, $q_p = \sigma_{1p} - \sigma_3$ is the peak deviatoric stress, $p_p = \frac{(\sigma_{1p}+2\sigma_3)}{3}$ is the mean stress at the peak deviatoric stress, β is the internal friction angle in the stress space, ε_{1r} is the residual axial strain and A, n and m are material parameters.
Dissipated energy	He et al. (2018)	$w_d = c(\mu v)^a \exp[b(A - \sigma_3)]$	w_d is the stable energy dissipation per cycle, μ is the loading rate, v is the loading frequency, A is the stress amplitude, σ_3 is the confining stress, a, b and c are fitting coefficients.
Fatigue life (based on energy evolution)	He et al. (2018)	$N_f = \xi \frac{W_f}{c(\mu v)^a \exp[b(A - \sigma_3)]}$ $W_d^N = \frac{Nc(\mu v)^a \exp[b(A - \sigma_3)]}{\xi}$	N_f is the fatigue life, W_f is the accumulative dissipated energy when the specimen fractures, defined as the failure dissipated energy, W_d^N is the accumulative dissipated energy, N is the cycle number, μ is the loading rate, v is the loading frequency, A is the stress amplitude, σ_3 is the confining stress, ξ is a constant independent of the loading conditions, a, b and c are fitting coefficients.
Damping ratio	He et al. (2021b)	For different stress levels: $\lambda = \lambda_{min} + \frac{\lambda_0}{b}\left(1 - \frac{G_d}{G_{d\,min}}\right)$ For different stress amplitudes: $\lambda = \lambda_{min} + \frac{\lambda_0}{b}\left(1 - \frac{G_d}{G_{d\,max}}\right)$	λ is the damping ratio, λ_{min} is the minimum damping ratio, λ_0 is an empirical parameter that can be experimentally determined, G_d is the dynamic shear modulus, $G_{d\,min}$ is the minimum dynamic shear modulus, $G_{d\,max}$ is the maximum dynamic shear modulus at a prescribed stress and b is a material constant.

2.3.4. Dynamic Elastic Modulus

In accordance with the description provided in Section 2.3.3, the deformation of materials exposed to repetitive loading and unloading conditions can be categorised into two portions: elastic and plastic deformation. Over the years, various forms of dynamic elastic moduli have been employed to assess the elastic deformation characteristics of various materials during repeated loading and unloading processes. For instance, Young's modulus, secant modulus, tangent modulus, resilient modulus and axial stiffness are commonly utilised forms of dynamic elastic moduli, particularly in the design and analysis of rock engineering structures that are exposed to cyclic and dynamic loads. According to Bagde and Petros (2005a), the dynamic Young's modulus is determined from the average gradients of the approximately linear section of the stress-strain loop. The dynamic secant modulus is calculated from the gradient of the straight line joining origin and the point corresponding to 50% of the maximum load in the stress-strain loop. The dynamic tangent modulus is measured as the gradient at a point on the stress-strain loop, usually at 50% of the maximum load. Further, the dynamic axial stiffness can be expressed as the ratio between stress difference and strain difference obtained from the corresponding peak-valley data in a cyclic stress-strain loop (Bagde and Petros, 2005a; Liu et al., 2011). Moreover, the dynamic elastic moduli of rocks can be affected by a variety of factors, and many researchers have investigated how various cyclic loading conditions can impact the dynamic elastic moduli of various intact rock types.

According to Cerfontaine and Collin (2018), the evolution of the dynamic elastic moduli of various rock types under repeated loading conditions remains unclear, given the divergent findings reported by various researchers. Attewell and Farmer (1973) and Eberhardt et al. (1999) were pioneers who observed the trend of dynamic elastic moduli

degradation with loading cycles of rocks exposed to cyclic uniaxial compression loading. Similarly, Heap et al. (2009 & 2010) and Xiao et al. (2010) applied cyclic uniaxial loading on various intact rock types and examined the deterioration of the dynamic Young's moduli with increasing loading cycles. Moreover, Momeni et al. (2015) described that the dynamic tangent modulus of granite specimens subjected to cyclic uniaxial loading displayed a downward trend with a scattered pattern, while the dynamic secant modulus exhibited three stages of accumulative damage during the fatigue process. Furthermore, Fuenkajorn and Phueakphum (2010) and Ma et al. (2013) noticed that the dynamic elastic moduli of salt rocks exposed to cyclic triaxial loading decreased rapidly during the initial loading cycles and then reached a steady state with further loading cycles. In the meantime, Wang et al. (2013) conducted cyclic compression experiments on granite specimens and reported that the progression of dynamic elastic moduli with loading cycles is affected by the volume change in the rock. They observed that in the volumetric compaction domain, dynamic elastic moduli showed an upward trend, and in the volumetric dilation domain, dynamic elastic moduli showed a downward trend with increasing loading cycles. Moreover, Yang et al. (2015 & 2017) stated that the dynamic elastic moduli evolution with respect to the number of loading cycles can be characterised by four stages, namely, material strengthening, material degradation, shear failure and structural slippage. They noted that the dynamic elastic modulus rises noticeably in the material strengthening stage, whereas in both the material degradation and shear failure stages, the dynamic elastic modulus decreases. However, they did not observe any variation in the dynamic elastic modulus during the structural slippage stage. Furthermore, Jia et al. (2018) applied increasing amplitude cyclic loading on sandstone specimens and identified that there are two levels of critical stresses, namely, σ_A and σ_B. They observed that the dynamic elastic modulus exhibited an upward trend with loading

cycles when the applied stress was less than σ_A. When the applied stress was between σ_A and σ_B, the dynamic elastic modulus was almost constant with a slow decrement. However, dynamic elastic modulus degraded rapidly when the applied stress was higher than σ_B. Liu et al. (2021a) made a similar observation for dolomite specimens subjected to multilevel cyclic loading.

Further, Heap et al. (2009 & 2010) reported a 10-30% decrease, while Ma et al. (2013) noted a 25-35% reduction in dynamic elastic moduli of tested intact rock specimens over the complete cyclic loading procedure. Bagde and Petros (2005a), Momeni et al. (2015) and Liu et al. (2021a) stated that elevated cyclic stresses corresponded to lower dynamic elastic moduli under cyclic uniaxial and triaxial loading conditions. Liu et al. (2011) applied cyclic triaxial loading on intact sandstone specimens and examined that higher confining stresses resulted in higher dynamic axial stiffness, and degradation of stiffness at lower confining stresses was more rapid. Yang et al. (2017) made a similar observation for marble specimens exposed to cyclic triaxial loading. Arora et al. (2019) applied cyclic uniaxial compression loading on several intact rock types and concluded that the rate of degradation of dynamic secant moduli is dependent on the type of rock. Figure 2.7 presents a sample of dynamic elastic moduli versus the number of loading cycle plots of intact rock specimens reported in the literature (adopted from Xiao et al., 2010).

Additionally, based on the observations or experimental data, some researchers proposed theoretical and empirical models for the fatigue behaviour of intact rocks subjected to repeated loading. Table 2.1 provides a summary of such models developed for the dynamic elastic moduli of intact rocks subjected to repeated loading conditions. For example, Yoshinaka et al. (1996) performed cyclic triaxial tests on four types of soft rock specimens and proposed an exponential equation to explain the relationship between deformation modulus and axial plastic strain. Wang et al. (2013) developed a constitutive

model to describe the fatigue behaviour of rocks when subjected to cyclic loading. This model incorporated residual axial strain as an internal state variable and also accounted for the effects of peak deviatoric stress and confining stress on the deformation modulus.

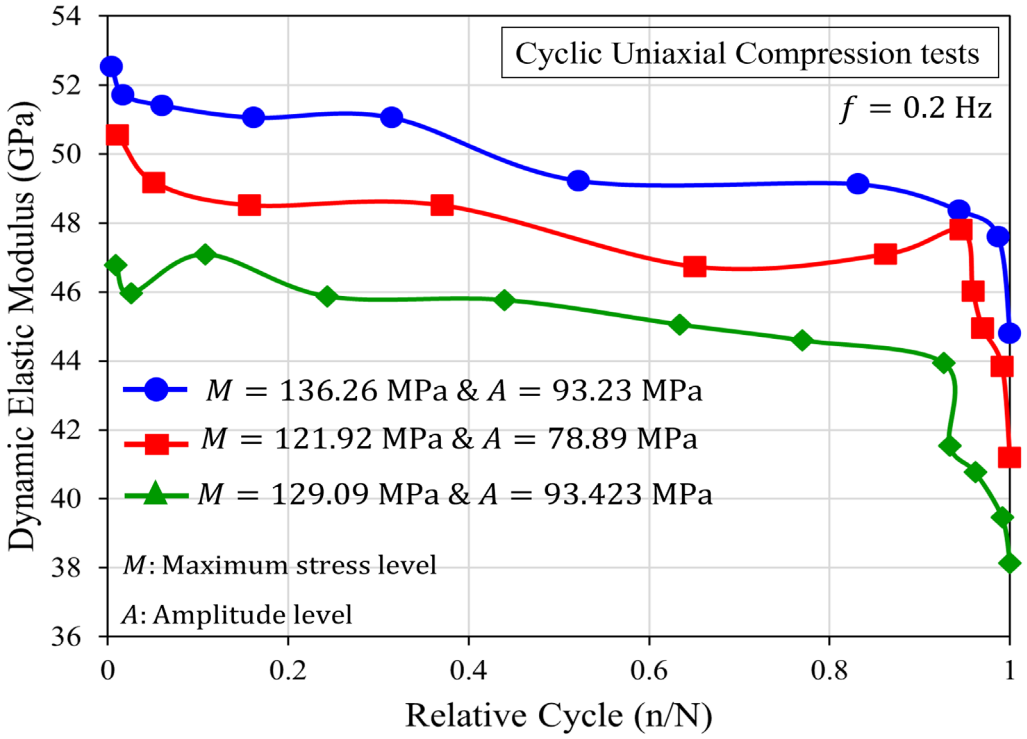

Figure 2.7. Variation of dynamic elastic moduli with the number of loading cycles (Reproduced from Xiao et al., 2010).

2.3.5. Dissipated Energy Evolution and Damping Properties

Due to the limitations inherent in classical mechanical theories, energy-based theories and principles have been applied to obtain a more comprehensive understanding of the mechanical behaviour of different materials, including rocks. A comprehensive study of the energy characteristics of rocks provides researchers with valuable insights into the underlying mechanisms of the deformation and failure of rocks. These insights can be instrumental in developing more effective and sustainable solutions to address challenges

encountered in the design and analysis of rock engineering structures subjected to dynamic loads.

Many researchers have reported that the rock deformation and failure process can be considered a process of energy input, storage, dissipation and release (Wasantha et al., 2014; Zhang et al., 2017; Gong et al., 2018a; Gong et al., 2019). The external world typically inputs energy to rock masses in the form of mechanical energy. A portion of this input mechanical energy will be accumulated within the rock as elastic energy, and the remaining portion will be dissipated, causing micro-crack development and plastic deformation in the rock mass. Upon reaching a critical strength threshold, the elastic energy stored in the rock mass will be released, causing ultimate failure (Wasantha et al., 2014; Zhang et al., 2017). Moreover, Zhang et al. (2017) and Song et al. (2020) suggested that a similar energy evolution process can also be anticipated during laboratory conditions.

During triaxial loading, the loading actuator applies an axial load on the rock specimen, which is the external energy input to the rock specimen. In the absence of accounting for other forms of energy losses, a portion of this input energy will be stored as elastic deformation energy which will cause the elastic deformation in the rock specimen, which is subsequently released upon unloading. The remaining portion of the input energy will be dissipated in the form of dissipation energy, which will cause plastic deformation in the rock specimen. The relationship among external input energy (ΔE), elastic energy stored in the rock (ΔE_e) and the energy dissipated by the rock (ΔE_d) during the loading-unloading process can be expressed as follows:

$$\Delta E = \Delta E_e + \Delta E_d \tag{2.1}$$

Under triaxial loading conditions, these energies can be determined from the cyclic stress-strain response of the rock specimen. A schematic diagram of a loading-unloading cycle at a given stress level, which portrays these energies, is presented in Figure 2.8. Referring to Figure 2.8, the area under the loading curve represents the energy absorbed by the rock (i.e., input energy) during the given cycle. The area under the unloading curve represents the elastic energy stored by the rock specimen, which is also released during unloading in the given cycle. The area of the hysteresis loop reflects the energy dissipated from the rock specimen in the given cycle. Therefore, numerous researchers have experimentally investigated the energy characteristics of various intact rock types under repeated loading conditions.

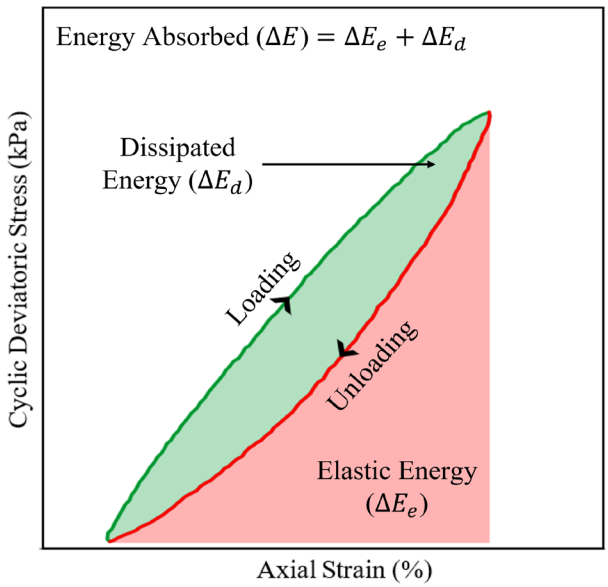

Figure 2.8. Schematic diagram of a typical hysteresis loop showing dissipated energy (ΔE_d), elastic energy (ΔE_e) and energy absorbed (ΔE).

Attewell and Farmer (1973) proposed that the rock fatigue mechanism can be explained in terms of strain energy-dependent crack propagation. They stated that the rock specimens would fail during repeated loading when the strain energy stored in the sample surpassed a critical energy threshold equivalent to the failure under non-cyclic loading. Moreover, Momeni et al. (2015) reported that the energy density, as well as hysteresis

energy of granite specimens subjected to cyclic uniaxial loading, exhibited a sharp decrease during the initial few cycles, followed by a gradual increase that eventually became rapid. Accordingly, they concluded that both forms of energy demonstrate three phases: an initial brief decreasing phase, followed by a prolonged uniform increasing phase, leading to a short and rapid increasing phase. Yang et al. (2018b) applied cyclic triaxial loading on the limestone specimens and discovered that at lower cyclic stress levels, the dissipated energy curve follows an L-shaped pattern, and the specimens did not exhibit any indications of failure. However, at higher cyclic stress levels, they observed that the dissipated energy curve follows a U-shaped pattern and is characterised by three phases of dissipated energy evolution, namely, primary, steady and acceleration phases. Similarly, He et al. (2018) reported that the energy dissipation evolution of salt rock samples under cyclic uniaxial loading could be divided into three stages. Initially, they observed that the dissipated energy decreased slowly over a few cycles, and then it tended to stabilise after a certain number of cycles. In the final stage, the dissipated energy escalated swiftly until the salt rock specimen experienced fractures.

On the other hand, Meng et al. (2016) suggested that the energy evolution in rocks is more closely associated with axial stress than the rate of axial loading, based on the cyclic uniaxial compression experiments conducted on sandstone specimens. Moreover, they examined that the rate of change of stored energy was the highest while the rate of change of dissipated energy was the lowest before reaching the peak strength. They also observed that energy accumulation predominates before attaining the peak strength, whereas energy dissipation takes over afterwards. Similarly, Zhang et al. (2017) performed cyclic triaxial experiments on sandstone specimens and observed that prior to reaching the peak, elastic energy increased gradually at the beginning and then swiftly, indicating higher energy accumulation. As the point of failure was approached, the dissipated energy

growth rate was higher, and after reaching the peak, they noted a sharp decrease in elastic energy and a substantial rise in the dissipated energy, which primarily manifested as energy dissipation and release. Moreover, they reported that the percentage of elastic energy prior to reaching the peak was consistently greater than that of dissipated energy. Conversely, after reaching the peak, the percentage of dissipated energy surpassed that of elastic energy. Further, Yang et al. (2020c) stated that the dissipated energy of sandstone samples under cyclic triaxial loading exhibited different behaviours under different levels of cyclic stresses. Accordingly, the dissipated energy increased linearly with increasing cyclic stress when the applied stress was below 50% of the failure stress. However, when the applied stress was greater than 50% of the failure stress, the dissipated energy increased nonlinearly and exhibited a rapid increase near the peak strength.

Moreover, Bagde and Petros (2005a & 2009) applied cyclic uniaxial loading on several intact rock specimens and observed that as the cyclic stress increased, the sustained dynamic energy, as well as the released stress energy increased. They also stated that the released stress-energy was dependent on the rock type. Momeni et al. (2015) and Meng et al. (2016) made similar observations for the energy density of granite specimens and stored energy, elastic energy and dissipated energy of the sandstone samples subjected to cyclic uniaxial loading, respectively. Moreover, Zhang et al. (2017) reported that a rise in the applied confining stress resulted in a corresponding rise in the characteristic energy density parameters of the specimens, suggesting an expansion in the rock energy storage limit. Furthermore, with an increase in the confining stress, they noted a decline in the proportion of elastic energy reduction during the peak failure, and as a result, they suggested that confining stress exerted a repressive influence on the energy release process. Further, Zhang et al. (2017) also observed that after the peak failure, upon returning to a stable state, the rock specimens regained their capacity to accumulate

energy, which resulted in an increase in the percentage of elastic energy. Nevertheless, owing to the decrease in energy storage capacity induced by fracturing, the percentage of elastic energy could not be reinstated to its initial level. Figure 2.9 presents a sample of variation of dissipated energy versus the number of loading cycles plots of intact rock specimens reported in the literature (adopted from Momeni et al., 2015).

Furthermore, some researchers developed conceptual and empirical models for the energy characteristics of intact rocks exposed to repeated loading conditions based on observations or experimental data. A summary of these models is provided in Table 2.1. For instance, He et al. (2018) performed cyclic triaxial experiments on salt rock specimens and proposed an exponential function for the stable energy dissipation per cycle by considering the influence of loading rate, loading frequency, applied stress amplitude and confining stress. Further, they also proposed an equation to predict the fatigue life of rocks subjected to repeated loading by considering the evolution law of the dissipated energy.

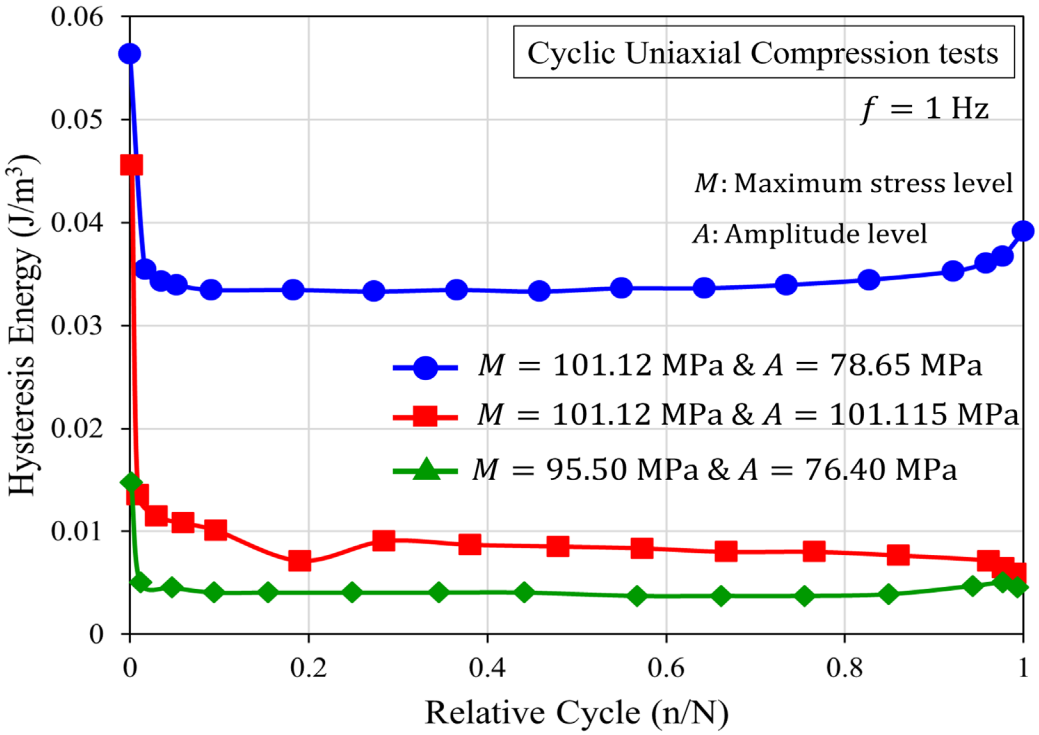

Figure 2.9. Variation of hysteresis energy with the number of loading cycles (Reproduced from Momeni et al., 2015).

The energy dissipation phenomenon in rocks subjected to cyclic loading conditions plays a vital role in evaluating the response of ground-structure systems in many rock engineering applications. Damping is a measure of energy dissipation in a vibrating or cyclically loaded system, which is a crucial aspect of designing and constructing stable and safe structures on/in or near the rock masses. Researchers have employed various parameters as a measure of damping or energy dissipation in various fields; however, the damping ratio is the most widely utilised parameter in the field of geotechnical engineering. The damping ratio is defined as the ratio between energy dissipated and the maximum elastic energy stored during a load cycle. During cyclic loading and deformation, energy loss is evident from the hysteretic behaviour of rocks, as explained in the previous section. In accordance with ASTM D3999-91 (2013), for sinusoidal waveform loading, the damping ratio for a given hysteresis loop can be determined as,

$$\xi = \frac{\Delta E_D}{\pi \, \Delta E_{e,max}} \tag{2.2}$$

where ΔE_D is the inner area of the hysteresis loop, which indicates the energy dissipated during one loading cycle while $\Delta E_{e,max}$ is the maximum elastic energy stored during one loading cycle approximated by the area of the shaded triangle, as shown in Figure 2.10. Accordingly, considerable investigations have been carried out to explore the damping characteristics of various intact rocks exposed to repeated loading conditions.

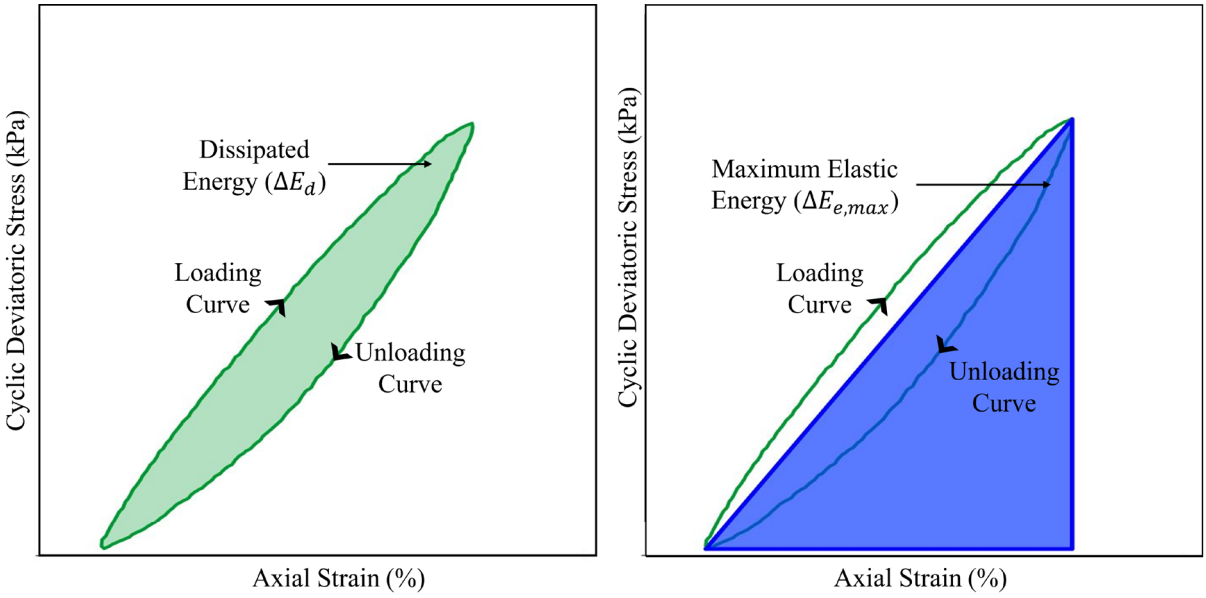

Figure 2.10. Schematic diagram of a typical hysteresis loop showing dissipated energy (ΔE_d) and maximum elastic energy ($\Delta E_{e,max}$).

Tien et al. (2020) performed cyclic triaxial tests on sandstone specimens and observed a gradual decrease in the damping ratio alongside apparent fluctuations as the number of cycles increased. Bie and Liu (2020) reported that at the same stress level, the damping ratio of phyllite specimens increased during the initial loading cycles. However, during the later stages, the damping ratio of phyllite specimens either stabilised or reduced, and this behaviour was not detected during high-stress levels. Liu et al. (2021a) stated that the damping ratio of dolomite specimens subjected to multilevel cyclic loading demonstrated a three-phase process, where the damping ratio exhibited a rapid decrease during phase I,

followed by a slower reduction during phase II and a slight increase during phase III as the number of cycles increased. Further, they observed that the damping ratio exhibited a slight increase when the cyclic stress approached around 60% of the static compressive strength.

Yang et al. (2020a) reported that for sandstone and granite specimens subjected to the same stress level, the damping ratios exhibited a downward trend as the strain ratio increased, followed by a stabilisation phase. However, the damping ratios began to rise again with a further increase in the strain ratio. They also observed that as the stress ratios increased, the damping ratios of both sandstone and granite specimens initially reduced and then increased. Furthermore, Bie and Liu (2020) stated that as the stress amplitude increased, the damping ratio of phyllite specimens subjected to triaxial multi-stage cyclic loading displayed a two-phase evolution law. During phase I, the damping ratio showed a rapid decline with increasing stress amplitude, whereas, during phase II, the change in the damping ratio was slight. He et al. (2021b) applied multi-stage cyclic loading on glutenite, sandstone and conglomerate specimens and examined that the damping ratio showed an upward trend with rising stress amplitude and shear strain. Furthermore, they also reported that at a fixed stress level and stress amplitude, the damping ratio of the tested specimens was higher for different stress level paths than the stress amplitude paths. Similarly, Wang et al. (2021a) observed that the damping ratio of granite and red sandstone specimens decreased linearly as the stress level increased, while it increased with rising strain amplitude.

Additionally, Yang et al. (2020a) noted a gradual rise in the damping ratio as the confining stress was increased. However, He et al. (2021b) noted that under the same stress amplitude, the variation in the damping ratios of tested glutenite, sandstone and conglomerate specimens was strongly influenced by the type of rock rather than the

applied confining pressure. Similarly, Wang et al. (2021a) reported that the damping ratio of granite is approximately 80% of that of sandstone, leading to the conclusion that the damping properties of sandstone are notably superior to those of granite, possibly due to the lithological disparities.

Moreover, certain researchers formulated empirical models to describe the damping characteristics of intact rocks subjected to repeated loading conditions based on the experiment results. A summary of these models is provided in Table 2.1. As an example, He et al. (2021b) formulated a model to correlate the dynamic shear modulus with the damping ratio for soft rock at different stress levels and stress amplitudes based on the results of multistage cyclic loading experiments conducted on sandstone, conglomerate and glutenite rock specimens.

2.3.6. Damage Evolution and Failure

Many rock engineering structures are often subjected to repeated loads, and it often leads to the weakening of these structures as a consequence of damage evolution occurring within the rock mass. As explained by Martin and Chandler (1994), the application of external loading to rocks often leads to the formation of micro-cracks or micro-voids within the rock mass, which precedes the development of macro-fractures. The formation and propagation of these micro-cracks and micro-voids are typically considered as damage. Precisely understanding the mechanisms of damage evolution in rocks exposed to repeated loading is crucial for predicting and mitigating the risk of natural disasters and designing safe and reliable rock engineering structures.

The damage evolution process leads to significant changes in material properties, and damage variables have been commonly utilised to physically quantify and characterise this process. Therefore, researchers have proposed a variety of definitions for damage

variables using residual strain, maximum strain, elastic modulus, residual strength, density, acoustic emission (AE) accumulative counts and ultrasonic wave velocity characteristics. According to Eberhardt et al. (1999), irrespective of the chosen method, the fatigue damage evolution process should align with the formation, propagation and coalescence of micro-cracks. Consequently, a reasonable damage variable must fulfil several fundamental requirements, such as possessing distinct physical meaning; being easily measurable and applicable in engineering; having an evolution law that aligns with the actual degradation process of the material and taking the initial damage into account (Xiao et al., 2010). The commonly utilised damage variable definitions are summarised in Table 2.2. Moreover, some researchers employed pre-defined damage variables to describe the damage evolution in various intact rocks subjected to repeated loading conditions.

Table 2.2. Fatigue damage variables defined for intact rocks under cyclic loading.

Definition	Reference	Formula	Description
Residual strain method	Xiao et al. (2010)	$D = \frac{\varepsilon_r^n}{\varepsilon_r^f}$	ε_r^n is the residual strain after n cycles and ε_r^f is the ultimate residual strain at fatigue failure.
Irreversible deformation method	Yang et al. (2017)	$D = \frac{(\varepsilon_p)_N}{\sum_{N=1}^{m}(\varepsilon_p)_N}$	ε_p is the irreversible deformation of rock, m denotes the maximum cycle number, and N is the cycle number.
Residual strain method	Yang et al. (2018b)	$D = \frac{\varepsilon - \varepsilon_0 + \varepsilon_{p0}}{\varepsilon_d - \varepsilon_0 + \varepsilon_{p0}}$	ε is the axial strain at the end of a given loading cycle, ε_0 is the axial strain at the beginning of cyclic loading when $D = 0$ and ε_d is the axial strain at the end of cyclic loading when $D = 1$ and ε_{p0} is the plastic strain that causes zero-cycle damage

Residual strain method	Vaneghi et al. (2020)	$D_i = \frac{\Delta\varepsilon_{r_{i=n}}}{\Delta\varepsilon_{r_{i=N}}}$	$\Delta\varepsilon_{r_{i=n}}$ is the differential residual strain after n cycles and $\Delta\varepsilon_{r_{i=N}}$ is the differential residual strain at failure.
Maximum strain method	Xiao et al. (2010)	$D = \frac{(\varepsilon_{max}^{n} - \varepsilon_{max}^{0})}{(\varepsilon_{max}^{f} - \varepsilon_{max}^{0})}$	ε_{max}^{0}, ε_{max}^{f} and ε_{max}^{n} are the initial maximum strain, ultimate maximum strain and instantaneous maximum strain after n cycles.
Volumetric strain method	Liu et al. (2012)	$D_N = \frac{\sum_{j=1}^{N}\lvert\varepsilon_{v,re}\rvert_j}{\sum_{j=1}^{N_f}\lvert\varepsilon_{v,re}\rvert_j}$	$\varepsilon_{v,re}$ is the residual volumetric strain, N is the number of cycles and N_f is the number of cycles at failure
Elastic modulus method	Xiao et al. (2010)	$D = 1 - \frac{E}{E_0}$	E is the actual modulus of the damaged material and E_0 is the Young's modulus of undamaged material.
Axial secant modulus method	Liu and He (2012)	$D = \frac{(A_{sd,max} - A_{sd})}{(A_{sd,max} - A_{sd,min})}$	A_{sd} is the average dynamic axial stiffness, $A_{sd,max}$ and $A_{sd,min}$ are the maximum and minimum dynamic axial stiffness, respectively.
Energy dissipation method	Xiao et al. (2010)	$D = \frac{E}{E_{tot}}$	E is the instantaneous energy dissipation after some cycles and E_{tot} is the total energy dissipation capacity in unit volume.
Energy dissipation method	Liu et al. (2016)	$D_A = \frac{U_A^d}{U} = \frac{U_A - U_A^e}{U}$	U is the constitutive energy, U_A^d is the dissipated energy at point A, U_A is the area between the first loading curve and the strain axis and U_A^e is the area between the first unloading curve and the strain axis.
Energy dissipation method	Chen et al. (2020)	$D = \frac{W_D}{W_I}$	W_D is the dissipated energy and W_I is the incident energy.
Ultrasonic wave velocity method	Xiao et al. (2010)	$D = 1 - \frac{\hat{v}_{Tn}^2}{v_T^2}$	v_T^2 is the origin ultrasonic wave velocity of undamaged material and $\hat{v}_{Tn}^2$ is the instantaneous ultrasonic wave velocity of damaged material after n cycles

Acoustic emission cumulative counts method	Xiao et al. (2010)	$D = \frac{N}{N_m}$	N_m is the AE cumulative counts to failure and N is the AE cumulative counts corresponding to a given number of cycles

Xiao et al. (2010) analysed six frequently used damage variable definitions (i.e., residual strain, maximum strain, elastic modulus, energy dissipation, ultrasonic wave velocity and acoustic emission cumulative counts methods) using test data obtained from granite specimens subjected to cyclic uniaxial loading and found that these definitions effectively depict the actual fatigue damage evolution process. However, they noted that the residual strain method was the ideal definition, given its clear physical interpretation, descriptive representation of the degradation behaviour, and incorporation of the initial fatigue damage. Similarly, Liu and He (2012) stated that the residual strain approach, as well as the newly proposed axial secant modulus approach, could precisely explain the fatigue damage evolution of sandstone specimens under cyclic triaxial loading.

Furthermore, Xiao et al. (2010) observed the three-stage evolution process of fatigue damage in granite specimens exposed to cyclic uniaxial loading across most of the defined damage variables. The formation of fatigue cracks occurred in the initiation phase I, followed by the propagation of stable cracks during the uniform velocity phase II, and ultimately, the propagation of unstable cracks leading to sudden failure in the accelerated phase III. Liu et al. (2012), Liu and He (2012) and Momeni et al. (2015) reported similar observations for the damage progression in sandstone and granite specimens exposed to cyclic triaxial and uniaxial loading conditions, respectively, using different damage variables. Furthermore, Song et al. (2016) defined two parameters, namely, the damage severity factor (D_f) and the damage localisation factor (L_f) to characterise the progression and localisation of damage in sandstone specimens subjected to cyclic uniaxial loading.

Their observations revealed that during the initial loading stage, D_f increased gradually and L_f decreased at a nearly constant rate as the load increased. They also noted that D_f underwent a sudden increase, while L_f decreased significantly as the number of loading cycles increased.

Yang et al. (2015) performed cyclic triaxial experiments on sandstone specimens and proposed axial and radial damage variables. At the same confining stress, they observed that the axial damage surpassed the radial damage prior to the peak strength, while after the peak strength, the radial damage exceeded the axial damage. Further, Yang et al. (2015) noted that the axial and radial damage value of sandstone specimens exhibited a slight increase initially prior to reaching the peak strength. Subsequently, a dramatic escalation in damage was observed with the increasing number of cycles after peak strength was attained. Moreover, Yang et al. (2015) discovered that during the initial cycles, the evolution rate of radial damage was slower compared to that of axial damage. However, in the subsequent cycles, the rate of radial damage evolution increased substantially compared to that of axial damage. Furthermore, Momeni et al. (2015) compared axial and lateral strain damages in granite specimens subjected to cyclic uniaxial loading and observed that crack propagation and crack opening took place in the loading and lateral directions, respectively.

Moreover, Yang et al. (2015) discovered that the confining stress substantially impacts the progression of axial and radial damage in sandstone specimens exposed to repeated loading. They noted that a rise in confining stress resulted in a reduction in both axial and radial damage evolution. Contradictorily, Yang et al. (2017) subjected marble specimens to repeated loading, and their findings indicated that the impact of confining stress on the progression of damage in marble specimens was insignificant. Nevertheless, they also

noted that the damage variable increased with the cycle number at the same confining stress.

The study of failure characteristics of rocks exposed to repeated loading has gained considerable attention in recent years due to the distinct mechanical behaviours exhibited by rocks under dynamic loading conditions, which differ from those observed under monotonic loading conditions. Understanding the underlying mechanism of rock failure under dynamic loading conditions is essential when developing effective strategies for mitigating and managing the risks associated with rock engineering structures susceptible to dynamic loads. Consequently, researchers have employed various approaches such as visual inspection, X-ray micro-computed tomography (micro-CT) observations, non-destructive AE monitoring, high-speed photography and digital image correlation (DIC) techniques to characterise failure properties of various intact rock types exposed to repeated loading conditions. Additionally, many researchers have utilised numerical simulation procedures, including the finite element method (FEM), finite difference method (FDM) and discrete element method (DEM), to provide further insights into the progressive failure behaviour of rocks exposed to repeated loading (Liu and Dai, 2021).

Based on the peak fatigue strength and dynamic energy results of dry and saturated sandstone specimens exposed to cyclic uniaxial loading, Bagde and Petros (2005a) concluded that micro-fracturing was the principal mechanism of fatigue failure in the rock specimens. Later, Bagde and Petros (2009) mentioned that the occurrence of fatigue failure in rocks was significantly linked to their physical, mechanical and petro-graphical properties, and micro-fracturing was identified as the primary contributor to fatigue failure. Liu et al. (2011 & 2012) reported that the failure mode of the sandstone specimens under cyclic triaxial loading was a shear failure. Furthermore, Liu et al. (2011) observed that under higher confining stresses and dynamic loading conditions, the localised failure

bands were wider than those observed during static loading. Moreover, Liu et al. (2012) noted that a rise in confining stresses resulted in an elevated angle between the maximum principal stress plane and the failure plane. Similarly, Yang et al. (2017) observed that marble specimens subjected to cyclic triaxial loading experienced a single shear fracture, and the fracture angle reduced gradually with a rise in the confining stress.

Moreover, Song et al. (2013) utilised the DIC technique to examine the damage progression and crack development of sandstone specimens under repeated loading. They observed that the damage in the rock specimens initially displayed homogeneous distribution, but as loading cycles progressed, damage gradually developed and localised, ultimately leading to crack nucleation. Furthermore, Yang et al. (2015) subjected sandstone specimens to cyclic compression loading and an X-ray micro-CT scanning system was utilised to analyse the failed samples. They noted that the specimens subjected to repeated loading exhibited a greater number of axial and lateral tensile cracks compared to monotonic loading. Yang et al. (2020b) analysed the cross-sectional and 3D reconstructed images of CT scans of sandstone specimens that were subjected to cyclic triaxial loading and noted that the crack patterns developed under cyclic loading were more intricate compared to that observed under static loading. Additionally, Meng et al. (2016) explored the process of rock failure, which involves fracture development and compression to structural adjustment and eventual instability, by applying AE activity on red sandstone specimens under cyclic uniaxial compression loading. They observed that the AE activity reflected the strain deformation in the rock specimens, while the density and intensity of AE events provided an indication of the degree of damage present in the specimens. Further, based on the rock AE response, they concluded that the evolution of internal defects induced the macro-fractures in the rock specimens.

2.4 Experimental Studies on Jointed Rocks Exposed to Cyclic Loads

Rock masses are heterogeneous in nature and often comprise discontinuities such as joints, bedding planes, faults, shear zones and other planes of weakness. Among these discontinuities, joints are the most common and geotechnically most significant discontinuity type encountered in rock masses. They are cracks formed in rock masses due to the single or combined effect of different stresses such as ground stress, tectonic forces, hydrostatic forces, pore pressures and temperature stresses. According to Gamage (2000), joints found in rock masses can range from minor cracks having a length of only a few centimetres to more prominent and well-developed major fractures extending to several kilometres. The presence of such discontinuities and their unique features significantly influence the strength, deformability and overall stability of the rock mass as well as the structures associated with it (Huang et al., 1993; Xie et al., 1997; Belem et al., 2007).

Most of the existing experimental studies on rock joints have focussed on their mechanical properties under static loading conditions. Researchers have performed static uniaxial compression experiments (Kulatilake et al., 1997; Singh et al., 2002; Chen et al., 2012; Asadizadeh et al., 2019), triaxial compression experiments (Ramamurthy, 2001; Yu et al., 2016; Duan et al., 2019; Xiang et al., 2020) and direct shear experiments (Hossaini et al., 2014; Li et al., 2015; Bahaaddini et al., 2016; Ge et al., 2017) using physical rock models containing various joints to explore their static properties and mechanical behaviour under static loading. Despite the notable discrepancies in the mechanical response of rock materials between cyclic loading and static loading (Attewell and Farmer, 1973; Tien et al., 1990; Xiao et al., 2010; Jia et al., 2018), efforts to investigate the mechanical characteristics and the behaviour of rock joints under cyclic loading conditions are generally scarce. Yet, Sections 2.4.1 and 2.4.2 comprehensively

review the existing systematic experimental studies conducted on rock joints under repeated loading conditions.

2.4.1. Cyclic Shear Tests on Rock Joints

Over the past decades, some researchers have performed experimental studies to investigate rock joint behaviour subjected to cyclic shear loading conditions. The majority of these studies have primarily concentrated on exploring the cyclic shear mechanism, shear strength parameters and asperity degradation experimentally under either constant normal load (CNL) or constant normal stiffness (CNS) conditions. Additionally, researchers have proposed theoretical and empirical models to predict the cyclic shear behaviour and asperity degradation mechanism of rock joints.

2.4.1.1 Asperity Degradation and Failure Mechanism

Hutson and Dowding (1990) was a pioneer who contributed to comprehending the intricate degradation process of real rock joint asperities during cyclic shear loading. They applied cyclic shear loading on granite and limestone specimens under CNL conditions and discovered that the asperity degradation is dependent on various factors such as work, normal stress, unconfined compressive strength and initial joint roughness. Huang et al. (1993) conducted cyclic direct shear experiments on both artificial sawtooth joints and natural dolomite joints under CNL conditions. Their findings showed that at low normal stresses, the surface damage of the joints was predominantly caused by wear, which can be mainly attributed to gradual asperity degradation. However, when subjected to high normal stresses, joint damage occurred more swiftly and disastrously, with asperities being sheared off. Under moderate normal stresses, the initial damage mode was wear, which subsequently transitioned to asperity shearing. Furthermore, they examined that the damaged asperity material remained in the joint, forming a new contact

surface and altering the joint surface shape, subsequently influencing the joint behaviour. Later, Lee et al. (2001) applied cyclic shear loading on saw-cut granite joints and split tensile marble joints under CNS conditions. They noted that the degradation of asperities under cyclic shear loading was dependent on numerous factors, such as the type of asperities, shearing direction and strength of the rock material. Moreover, Jafari et al. (2003) carried out cyclic shear experiments on artificial sawtooth and natural replicated joints under CNL conditions. Their observations indicated that the cyclic shear displacement and the magnitude of the applied normal stress have a significant impact on the first and second-order asperity degradation.

Furthermore, Fathi et al. (2016) applied pre-peak cyclic shear loading on mortar replicas made from a natural unweathered granite joint, and they identified that the impact of pre-peak cyclic loading on the joint shear mechanism could be classified into two processes: contraction and degradation. During the initial shear cycles, they observed that the steepest asperities began to ride over each other, leading to a rapid increase in the joint contact area which can be attributed to the contraction of the joint. However, this contraction effect diminished with increasing loading cycles, after which degradation began to increase. The contact area remained relatively constant throughout the middle cycles, which can be attributed to the asperity riding over each other without considerable degradation. However, with further increase in loading cycles, they observed degradation on the steepest in-contact asperities, which were identified as second-order asperities. Similarly, Liu et al. (2018a) conducted cyclic shear tests on rock joints with first and second-order triangular asperities under pre-peak cyclic loading conditions. They found that under a lower number of cycles, fatigue damage occurred at the second-order asperities in the upper and lower blocks of the joint. However, as the number of cycles

increased, the fatigue cracks began to form in the first-order asperities in the upper and lower blocks, which led to rock fragmentation.

He et al. (2022) performed pre-peak cyclic shear loading experiments on artificial jointed rock specimens and studied the impact of various factors such as initial joint roughness, joint wall compressive strength (JCS), normal stress, loading frequency, cyclic stress amplitude and the number of cycles on the asperity degradation process. Their results revealed a positive correlation between the coefficient of joint surface degradation and the joint surface degradation thickness with the loading frequency, cyclic stress amplitude and cycle number, while a negative correlation was observed with the JCS. Furthermore, they observed that the joint surface degradation thickness increased while the joint surface degradation coefficient decreased as the initial joint roughness and normal stress increased. Additionally, they noted that a higher loading frequency, cyclic stress amplitude, initial joint roughness, normal stress and cycle number and a lower JCS corresponded to a lower joint roughness parameter at any given cycle. Further, the rate of reduction in joint roughness parameter at any given angle shifted from a rapid decline to a gradual decline, with the increasing number of loading cycles. The process of joint degradation was observed to be characterised by two distinct stages: a stage of rapid decline followed by a stage of gradual decline.

Kou et al. (2019) reported the presence of three distinct shear failure modes, namely, climbing shear failure mode, mixed climbing-gnawing failure modes and gnawing shear failure mode in jointed rock samples subjected to cyclic direct shear tests. They stated that the climbing shear failure mode was caused by the coalescence of tensile cracks at the primary and secondary asperities, while the combined climbing-gnawing failure mode resulted from the coalescence of shear cracks at secondary asperities and mixed tensile-shear crack coalescence at primary asperities. The gnawing failure mode was observed

due to the coalescence of tensile cracks at primary asperities and shear cracks at secondary asperities.

Based on the experimental findings, several researchers proposed theoretical and empirical models to predict and capture the asperity degradation mechanism in rock joints subjected to cyclic shear loading. For instance, Hutson and Dowding (1990) were among the pioneers who formulated a basic exponential wear equation to describe the joint asperity degradation in cyclic shear. Later, Lee et al. (2001) developed an elastoplastic constitutive model incorporating the degradation of second-order asperities. Belem et al. (2007) developed two asperity degradation models to explain the degradation of initial surface roughness, considering both first and second-order asperities during cyclic shearing. Moreover, He et al. (2022) also formulated an empirical model to predict the joint roughness parameter at any given cycle as a function of loading frequency, cyclic stress amplitude, number of loading cycles, JCS, initial joint roughness parameter and normal stress.

2.4.1.2 Cyclic Shear Strength

Huang et al. (1993) observed that the shear behaviour of both artificial and natural joints under cyclic shear loading conditions was generally consistent. However, in the case of natural rock joints, they examined that the peak shear strength during the first cycle was typically higher than that of the subsequent cycles, and the stress softening behaviour was clearly evident. This behaviour could be ascribed to the presence of second-order asperity roughness in natural joints, which was not present in the artificial joints. Furthermore, Jing et al. (1993) conducted cyclic shear experiments on replicas of granite joints under CNS conditions, and they determined that the shear strength and deformability of jointed rock were both anisotropic and stress-dependent. Additionally, Jafari et al. (2003)

analysed the results of cyclic direct shear experiments performed on artificial sawtooth and natural replicated joints, and they concluded that the shear strength of rock joints was affected by various factors such as the dilation angle, asperity degradation and wearing process.

Mirzaghorbanali et al. (2014) performed cyclic direct shear experiments on infilled rock joints with triangular asperities under CNS conditions. They discovered that, at a certain normal stiffness, the cyclic shear strength of an infilled rock joint could be described as a function of several factors, including the initial normal stress, joint surface friction angle, initial asperity angle, infill friction angle, infill thickness, loading direction and the number of loading cycles. Similarly, Han et al. (2019) performed cyclic shear experiments on clean and infilled natural rough joints under CNS conditions. Their findings indicated that the filling materials have a greater influence on the shearing process due to their lower density and UCS compared to rock-like materials.

Moreover, Fathi et al. (2016) applied pre-peak cyclic loading on jointed rocks, and they noted that the peak shear stress increased under a lower number of cycles, possibly due to contraction of the joint surfaces (i.e., negative dilation). However, at a higher number of cycles, they observed that the peak shear stress reduced, despite the increase in the contact area, which can be attributed to the deterioration of the second-order asperities. Similarly, when the number of cycles was lesser than 200, Liu et al. (2018a) observed that the peak shear strength of rock joints increased gradually as the number of cycles increased, and the peak shear strength (under cyclic shear loads) was higher than that observed under monotonic shear loads. However, when the number of cycles exceeded 200, the peak shear strength of rock joints reduced gradually with the increasing number of cycles, and the peak shear strength under cyclic shear loads was lower than that under monotonic shear loads. A similar observation was made by Kou et al. (2019) for artificial

rock joints with multiscale asperities subjected to pre-peak cyclic shear loading. Nevertheless, when the applied cyclic shear load was approximately 80% of the maximum monotonic peak shear strength, Liu et al. (2018a) and Kou et al. (2019) reported that there is no considerable impact on the peak strength of the rock joints as the number of cycles increased. On the other hand, Han et al. (2019) observed that normal displacement, shear stress and normal stress of clean and infilled jointed rock samples exhibited a downward trend with the increasing number of loading cycles.

Moreover, Liu et al. (2018a) noted that as the cyclic loading rate increased, the rate of increase in peak shear strength of rock joints under a lower number of cycles demonstrated a downward trend, while at a higher number of cycles, the degradation of the peak shear strength showed an upward trend. Kou et al. (2019) reported a similar behaviour for artificial rock joints with multiscale asperities that were subjected to pre-peak cyclic shear loading. Conversely, Han et al. (2019) reported that the initial normal stress exerts a more substantial impact on the shearing process of both clean and infilled joints compared to the shear stiffness and shear velocity. Furthermore, Fathi et al. (2016) performed an evaluation of the residual stage of shearing and observed that the residual shear strength of the joints remained altered by a lower number of cycles. Nevertheless, when the number of cycles surpassed 100 cycles, a minor reduction in residual shear strength was noticed.

Based on the experimental findings, various researchers have developed theoretical and empirical models aimed at predicting and characterising the shear strength criterion of jointed rocks under cyclic shear loading. For example, Mirzaghorbanali et al. (2014) developed a mathematical model for the shear strength of infilled rock joints subjected to cyclic shear loading. The proposed model incorporates various factors, including the initial normal stress and infill thickness to asperity height ratio and initial asperity angles.

Hou et al. (2016) conducted cyclic shear experiments on rock specimens with tensile joints and proposed an empirical relationship to predict the peak shear strength of jointed rocks under cyclic shear loading.

2.4.2. Cyclic Uniaxial and Triaxial Tests on Rock Joints

A few researchers have carried out experimental investigations to study the rock joint behaviour under cyclic uniaxial and triaxial loading conditions.

Brown and Hudson (1973) and Prost (1988) were pioneers who investigated the fatigue mechanism of rock joints under cyclic uniaxial and triaxial loading conditions, respectively. Brown and Hudson (1973) utilised idealised models of block-jointed specimens prepared from a gypsum plaster mixture, while Prost (1988) used sandstone-granite composite samples with a saw cut at different angles in the granite portion. Later, Gatelier et al. (2002) subjected sandstone specimens with structural anisotropy planes oriented to varying inclinations to both cyclic uniaxial and triaxial loading. Li et al. (2001b) and Liu et al. (2018b) conducted cyclic uniaxial compression experiments on intermittent rock joints made with a gypsum plaster mixture and cement mixture, respectively, while Lin et al. (2020) tested yellow sandstone specimens with a pre-cut semi-elliptical surface cut under cyclic uniaxial compression loading. Moreover, Jafari et al. (2004) performed cyclic triaxial compression tests on artificial jointed rock specimens made with a special cement-based mortar mixture with triangular sawtooth asperities, while Ding et al. (2014) tested soft rock-concrete composite specimens under cyclic triaxial loading. Later, Liu and Liu (2017) and Zheng et al. (2020a) tested artificial rock joints with a planar penetrating joint surface made with a cement mixture under cyclic triaxial loading, while Zheng et al. (2020b) and Yu et al. (2021) used mudstone samples with a half through cut. The findings of the investigations on the dynamic response of

rock joints exposed to cyclic loading and unloading conditions can be categorised and summarised under the following aspects:

2.4.2.1 Cyclic Stress-Strain Response

Similar to the cyclic stress-strain curves of intact rocks, previous researchers have reported the presence of hysteresis loops in the cyclic stress-strain curves of the rock joints subjected to repeated loading. For example, Gaterlier et al. (2002) examined hysteresis in unloading-reloading cycles and irreversible strain upon complete unloading in the stratified sandstone samples. Ding et al. (2014) and Lin et al. (2020) observed that the hysteresis loops of the tested rock joints transitioned from sparse to dense as the number of loading cycles increased. Furthermore, Yu et al. (2021) stated that the hysteresis loops of jointed mudstone samples appeared to be dense and narrow during the initial cycles. Subsequently, their density and width exhibited negligible changes or advanced slowly in the following cycles, and hysteresis loops became sparse and widened when approaching failure. Moreover, Liu and Liu (2017), Liu et al. (2018b), and Zheng et al. (2020a & b) observed that the hysteresis loops of rock joints transitioned from sparse to dense and subsequently back to sparse as the cyclic loading progressed.

Furthermore, Liu and Liu (2017) stated that sparse and dense hysteresis loops indicated elastoplastic and nearly elastic behaviour in rock joints, respectively. Likewise, Zheng et al. (2020a) mentioned that sparse-dense-sparse hysteresis loops indicated that the rock joints experienced cyclic softening, hardening and subsequent cyclic softening prior to ultimate failure, respectively. Also, Liu and Liu (2017) stated that the variation pattern of the spacing of hysteresis loops is controlled by the stress ratio (which was defined as the maximum cyclic stress divided by the compressive strength under static triaxial loading

at the same confining stress). Additionally, Zheng et al. (2020a) reported that a higher frequency corresponded to denser hysteresis loops.

Moreover, some researchers noted a close correlation between the cyclic stress-strain curve of jointed rocks under cyclic uniaxial loading and the corresponding static stress-strain curve. For instance, Brown and Hudson (1973) reported that the jointed rock samples under pre-peak cyclic loading underwent progressive deformation until failure took place at the intersection of the residual strength locus. Liu et al. (2018b) observed that the axial strain corresponding to the point of fatigue failure in the cyclic stress-strain curve was roughly equivalent to the axial strain observed at the point of maximum cyclic stress in the post-failure section of the associated static stress-strain curve.

2.4.2.2 Dynamic Strength and Fatigue Life

Early experimental investigations revealed that when jointed rocks are cyclically loaded, the samples fail after a few loading cycles, and the applied maximum cyclic load is lower than the UCS of the rock. For instance, Brown and Hudson (1973) stated that failure of the block-jointed rock models occurred when subjected to pre-peak cyclic loads, which were less than 80% of the static mean peak load sustained by the specimens. Prost (1988) observed that the rock joints exposed to cyclic axial loads greater than 64% of the static compressive strength failed in the cyclic compression-tension experiments. Moreover, Li et al. (2001b) observed that a higher frequency resulted in an increased dynamic strength of the intermittently jointed samples, and a dynamic residual strength value existed, unlike the static residual strength under uniaxial loading conditions. Moreover, Jafari et al. (2004) conducted cyclic triaxial tests on artificial saw-toothed rock joints followed by static triaxial loading to examine the effect of varied cyclic loading parameters on the

maximum and residual shear strengths. The results exhibited a reduction in shear strength caused by increased loading cycles, loading frequency and cyclic stress amplitude.

Previous researchers explored the influence of various cyclic loading parameters on the fatigue life of jointed rocks exposed to repeated loading. For instance, Prost (1988) conducted cyclic triaxial compression-tension experiments on jointed rocks and observed that the specimens experienced failure at a lesser number of cycles under higher applied cyclic axial loads. Similarly, Liu and Liu (2017) and Zheng et al. (2020a) reported that the number of loading cycles to attain failure of rock joints diminished as the stress ratio (which was defined as the maximum cyclic stress divided by the compressive strength under static triaxial testing at the same confining stress) increased as demonstrated in Figure 2.11. Later, Yu et al. (2021) also observed that the fatigue life of jointed mudstone samples attenuated with a rise in the stress ratio (defined as the ratio between dynamic stress and the difference between static strength and dynamic average stress). Moreover, Zheng et al. (2020a & b) observed that the rock joints subjected to cyclic triaxial loading required more loading cycles to reach failure as the loading frequency increased.

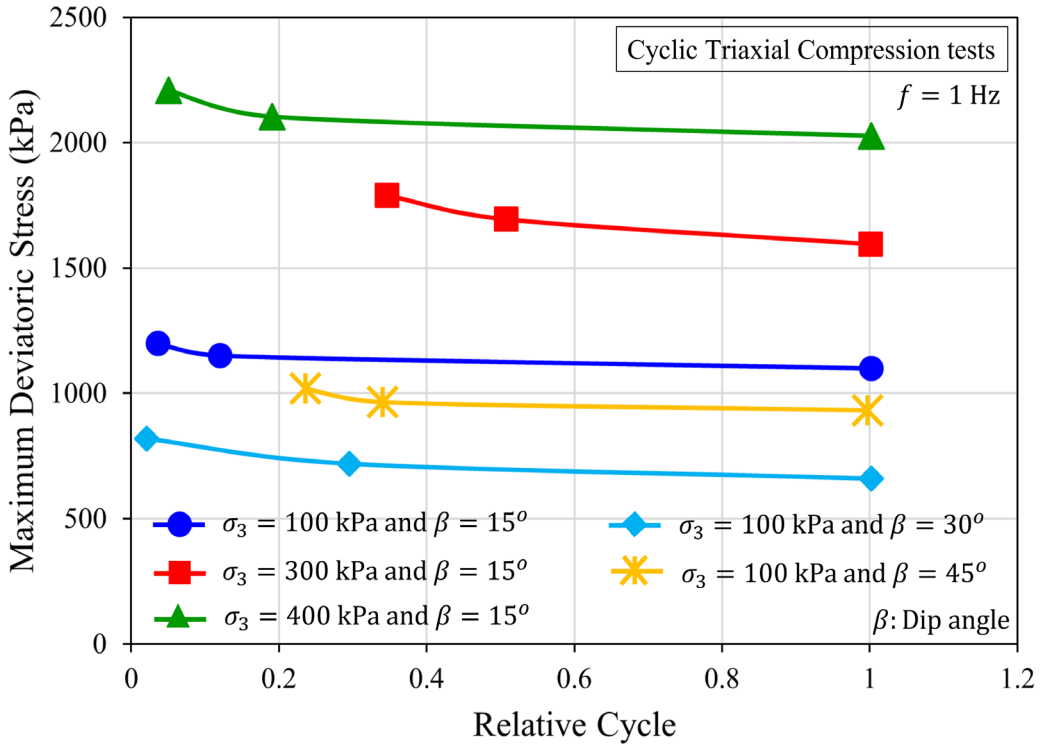

(a)

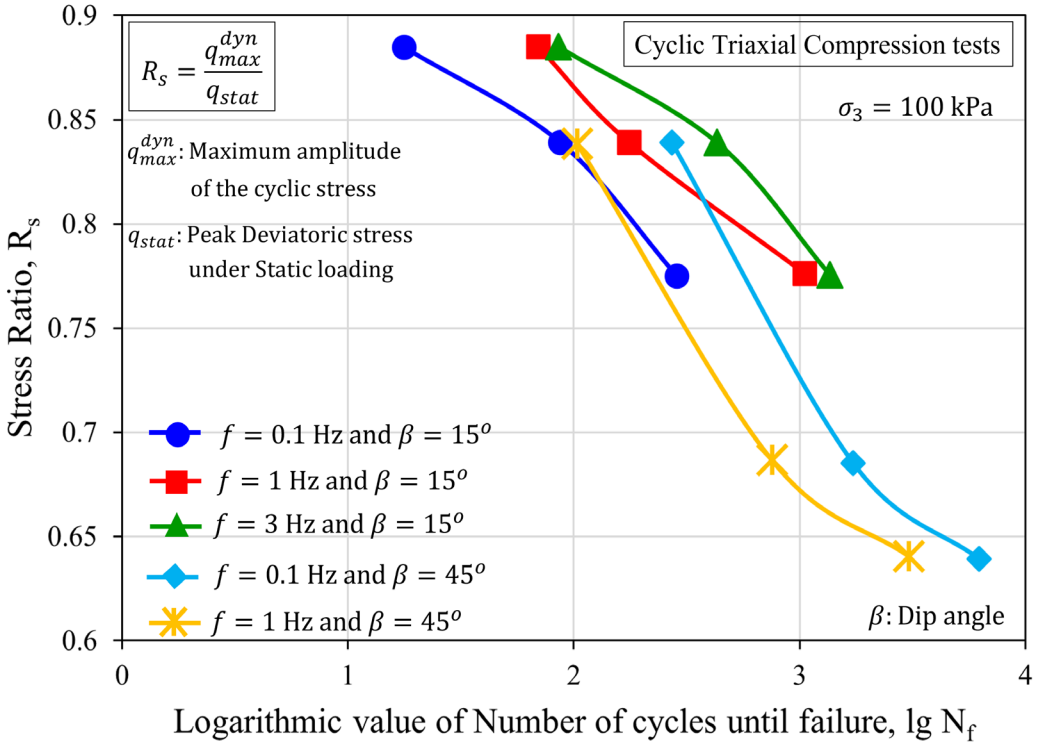

(b)

Figure 2.11. Variation of fatigue life with maximum deviatoric stress and stress ratio, reproduced from a) Liu and Liu (2017) and b) Zheng et al. (2020a).

2.4.2.3 Residual Axial Deformation

Previous researchers investigated the residual axial deformation evolution in jointed rocks subjected to repeated loads. Brown and Hudson (1973) observed a substantial rise in the axial displacement within the initial 1500 cycles, followed by a considerable reduction in the axial displacement accumulation rate. Subsequently, after 2500 cycles, the axial displacement escalated at an accelerating rate until block-jointed rock samples failed. Further, they mentioned that these three stages of displacement development were similar to primary, secondary and tertiary stages of creep. Similarly, Liu and Liu (2017) and Liu et al. (2018b) observed three stages in residual axial strain development in jointed rock samples (i.e., initial, uniform, and accelerated deformation stages). During the initial loading cycles, the residual axial strain accumulated rapidly, after which it stabilised during the uniform deformation stage. Then residual axial strain escalated at an accelerated rate, ultimately leading to the failure of the jointed rocks when subjected to cyclic triaxial and uniaxial loading, respectively. Besides, Ding et al. (2014) reported that the residual axial strain development in jointed rock samples proceeded through two stages (i.e., initial and uniform deformation stages). During the initial loading cycles, the residual axial strain accumulated rapidly and eventually reached a steady state. Moreover, Yu et al. (2021) examined two stages in residual axial strain evolution (i.e., uniform and accelerated deformation stages). During the uniform stage, the residual axial strain accumulated steadily, followed by a swift escalation, ultimately leading to failure. Figure 2.12 displays sample plots of cumulative residual axial strain versus the number of loading cycles rock joints reported in the literature (adopted after Liu and Liu, 2017 and Liu et al., 2018b).

Moreover, Li et al. (2001b) and Liu et al. (2018b) observed that higher stress levels and lower frequencies resulted in higher residual strain development in jointed rock under cyclic uniaxial loading. Moreover, Lin et al. (2020) reported that higher cyclic stresses resulted in an increase in the residual strain of the initial as well as final cycles and the cumulative difference in the strains of sandstone rock joints. Similarly, Liu and Liu (2017) stated that the initial residual axial strain of rock joints subjected to cyclic triaxial loading displayed an upward trend with rising maximum cyclic stress and confining stress. Furthermore, Ding et al. (2014) observed an increase in the accumulated residual strain in soft rock-concrete combined samples increased as the frequency decreased. Contradictorily, Zheng et al. (2020a & b) reported that the residual axial strain in the rock joints under cyclic triaxial loading increased with increasing frequency.

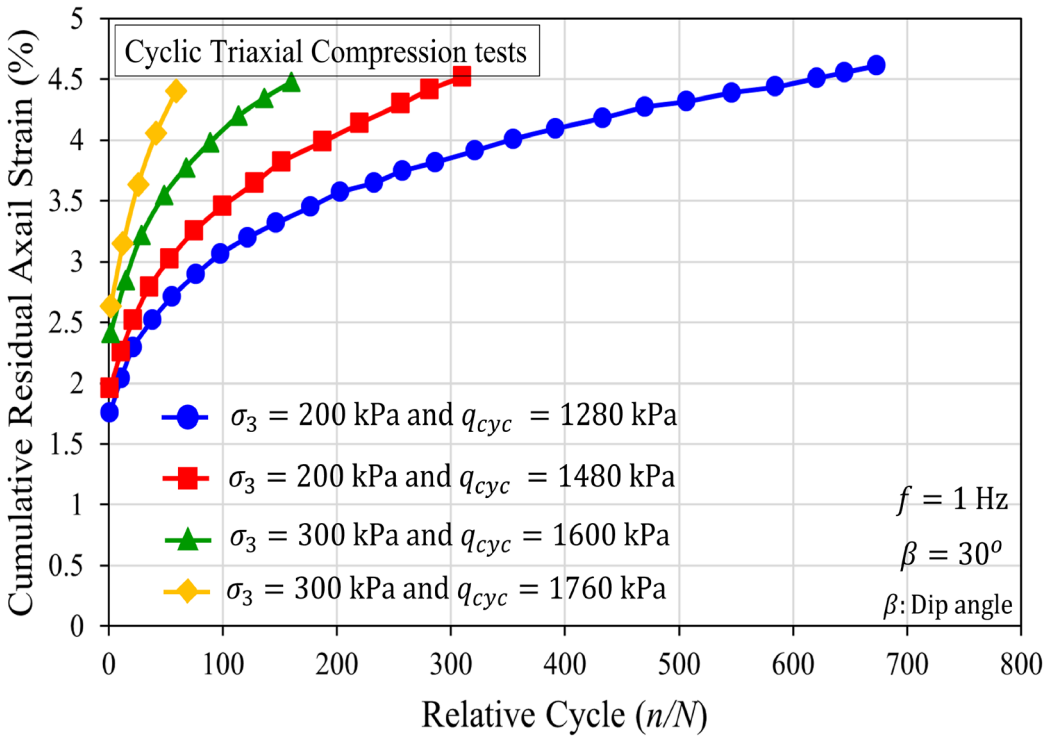

(a)

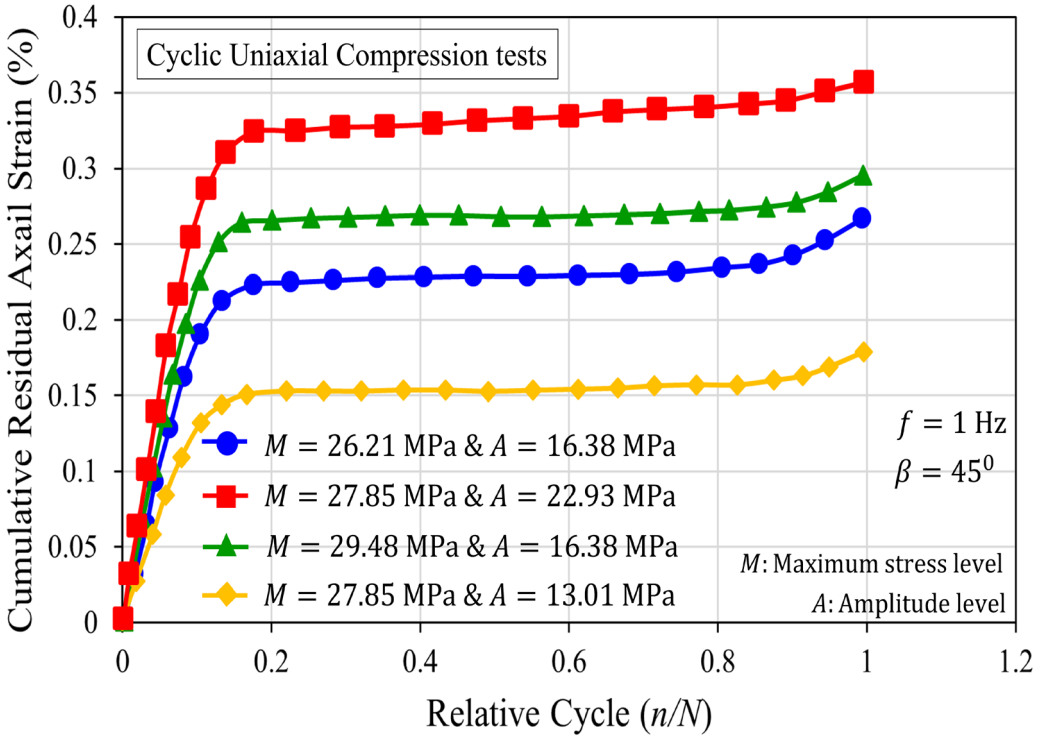

(b)

Figure 2.12. Variation of cumulative residual axial strain with the number of loading cycles, reproduced from a) Liu and Liu (2017) and b) Liu et al. (2018).

The residual volumetric strain is an important measure used by past researchers to explain the dilatant behaviour of jointed rocks exposed to cyclic triaxial compression loading. For example, Gatelier et al. (2002) observed positive incremental residual volumetric strains during the initial loading cycles, which progressively became negative during the subsequent loading steps. Hence, they stated that the irreversible volumetric strain was initially contracting and then became dilatant. Liu and Liu (2017) stated that the rock joints exposed to repeated loading underwent compaction characterised by comparatively low volumetric strains during the initial cycles, followed by subsequent dilation culminating in failure, accompanied by relatively high-volume expansions. Further, they observed that a higher volumetric strain is developed when the stress ratio (which was defined as the maximum cyclic stress divided by the compressive strength under static triaxial testing at the same confining stress) is higher. Similarly, Zheng et al. (2020a)

observed that the volume deformation trend of the jointed rock samples under cyclic triaxial loading was contraction followed by expansion. Further, they found out that as the frequency increased, the contractive volumetric strain increased while the volume expansion diminished.

2.4.2.4 Dynamic Elastic Modulus

Previous researchers have investigated the elastic deformation properties of jointed rocks exposed to repeated loads through deformation moduli such as Young's modulus, tangent modulus, secant modulus and axial stiffness. Gaterlier et al. (2002) measured the axial, transverse and shear moduli of the stratified specimens from the slope of the initial linear unloading portion of the stress-strain curves and observed that the axial modulus is higher when the loading is parallel to the strata. Moreover, they observed that all three moduli increased with rising confining stress. Moreover, Li et al. (2001b) calculated the deformation modulus of intermittent rock joints and observed a rise in the modulus with increasing loading frequency and decreasing stress level. Similarly, Zheng et al. (2020a & b) observed that the initial average axial stiffness and average Young's moduli during loading and unloading were greater at a higher frequency. Contradictorily, Liu et al. (2018b) and Lin et al. (2020) reported a rise in both Young's and secant moduli of jointed rock samples with increasing maximum stress and amplitude and a decrease in loading frequency. Figure 2.13 presents sample plots of variation of deformation moduli of rock joints with the number of loading cycles reported in the literature adopted from Zheng et al. (2020b) and Lin et al. (2020).

Moreover, Liu et al. (2018b) and Lin et al. (2020) stated that both Young's and secant moduli exhibited a non-linear decrease with increasing loading cycles. Furthermore, Zheng et al. (2020a) observed a swift reduction in the average axial stiffness during the

initial loading cycles, followed by a gradual increase, ultimately leading to a reduction again with successive loading cycles. Besides, Lin et al. (2020) noted that Young's moduli increased rapidly in the early stage of loading and then stabilised while the secant modulus gradually decreased with the progression of cyclic loading.

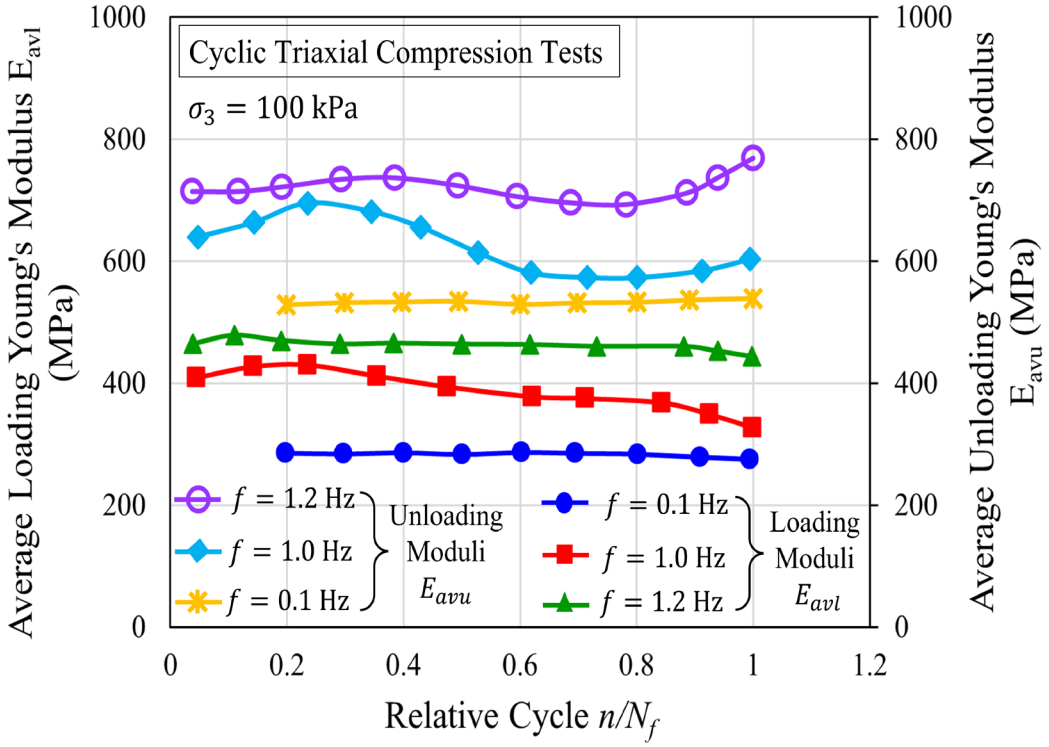

(a)

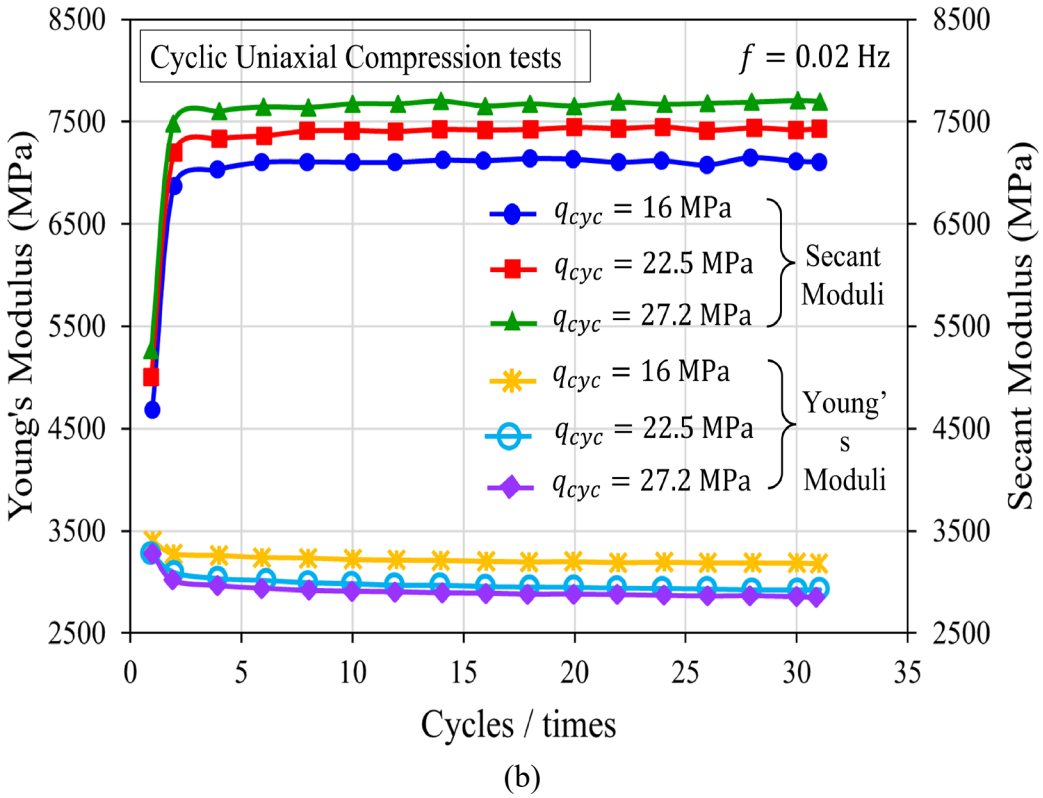

(b)

Figure 2.13. Variation of deformation moduli with the number of loading cycles, reproduced from a) Zheng et al. (2020b) and b) Lin et al. (2020).

2.4.2.5 Dissipated Energy Evolution and Damping Properties

Few researchers analysed the energy properties of jointed rocks exposed to repeated loads where the energy density parameters were calculated via the integration of the pertinent cyclic-stress strain curves. Li et al. (2001b) calculated dissipated energy during the application of cyclic uniaxial compression loading on intermittently jointed samples and observed a rise in the dissipated energy with increasing stress levels and decreasing loading frequency. Lin et al. (2020) calculated elastic energy and hysteresis energy densities from the cyclic stress-strain plots and observed that both energies were greater at higher cyclic stresses. Similarly, Liu et al. (2018b) quantified the total energy, elastic energy and hysteresis energy densities from the cyclic uniaxial compression tests on the intermittent rock joints and reported that all three energy densities increased with

increasing maximum stress and decreasing frequency. Contradictorily, Zheng et al. (2020a) observed that a higher frequency resulted in increased dissipated energy of the rock joints under cyclic triaxial loading.

Moreover, Liu et al. (2018b) reported a reduction in total energy density during the initial cycles, followed by a period of steadiness and then an increase again. In contrast, elastic energy density exhibited the opposite behaviour. Further, they observed a dramatic increasing and decreasing transition in the hysteresis energy density during the initial cycles, which gradually increased again during the subsequent loading cycles. Furthermore, Lin et al. (2020) observed a linear decrease in elastic energy density with loading cycles, while hysteretic energy density exhibited a nonlinear decrease, which gradually stabilised. Figure 2.14 presents sample plots of variation of dissipated energy and elastic energy of rock joints with loading cycles reported in the literature adopted from Liu et al. (2018b) and Zheng et al. (2020a).

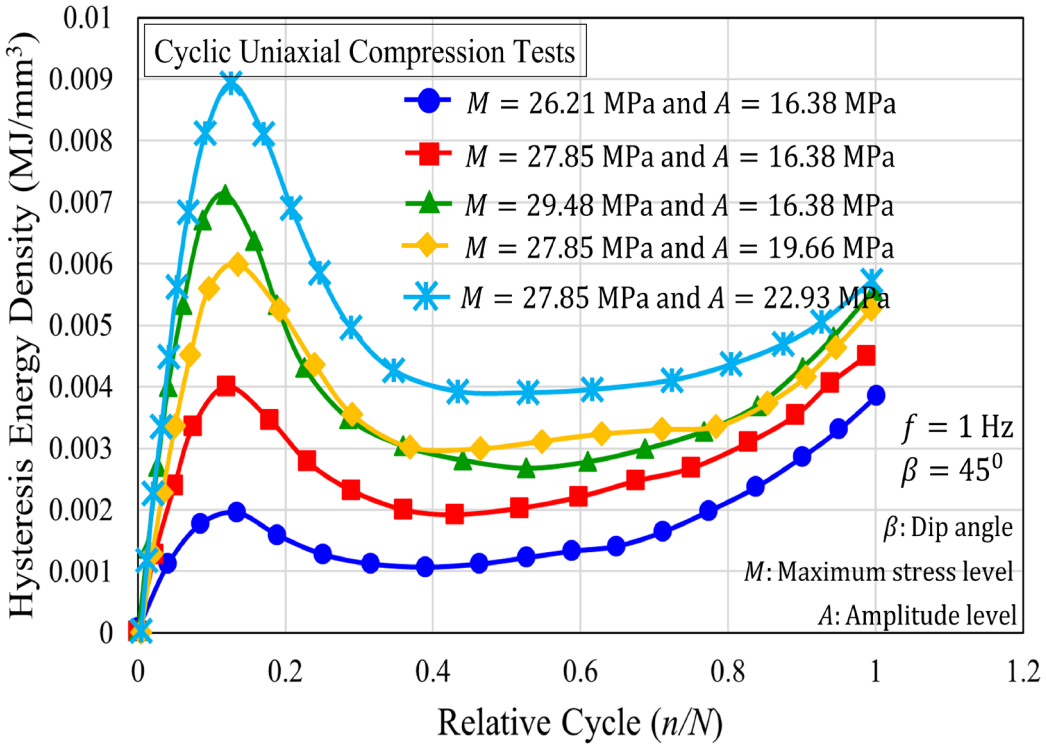

(a)

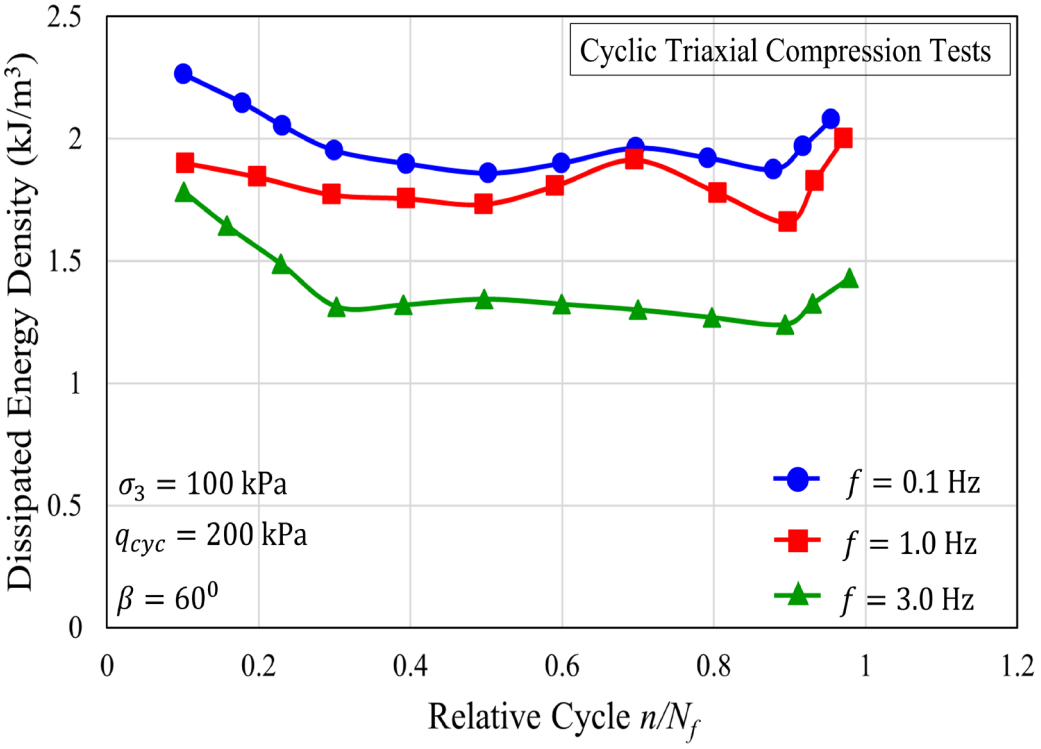

(b)

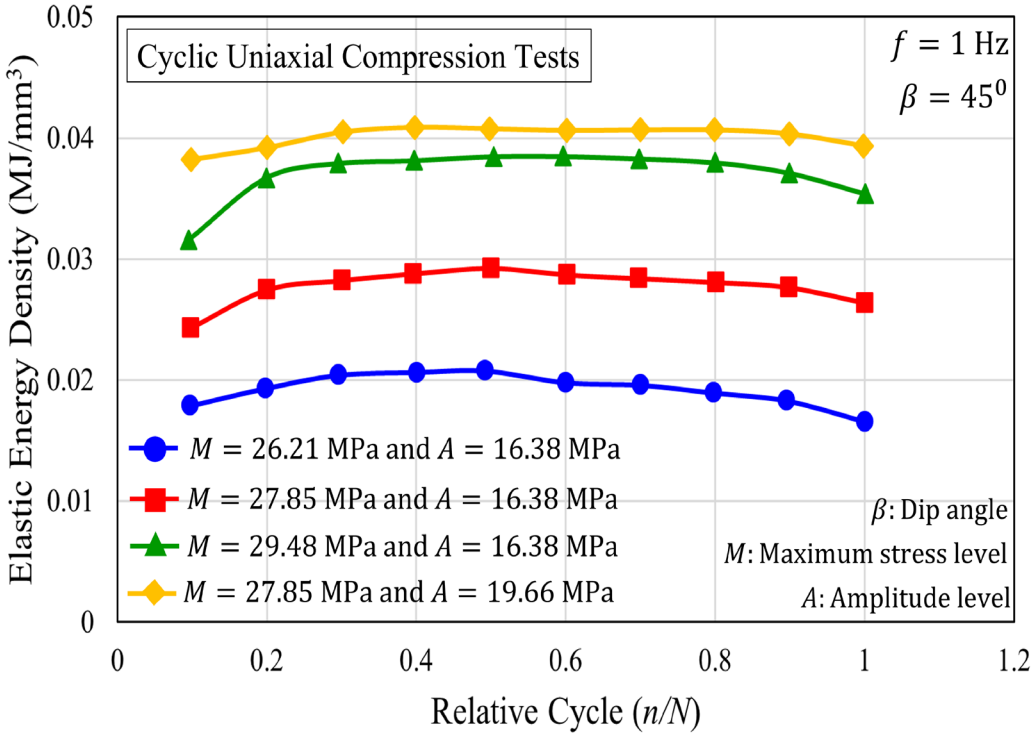

(c)

Figure 2.14. Variation of dissipated energy and elastic energy with the number of loading cycles, reproduced from a) Liu et al. (2018b), b) Zheng et al. (2020a) and c) Liu et al. (2018b).

2.4.2.6 Damage Evolution and Failure

Some researchers explored the damage evolution and failure mechanism of jointed rocks exposed to repeated loading using approaches such as visual inspection and defining damage variables. For example, through visual inspections, Brown and Hudson (1973) stated that the progressive accumulation of damage occurred in the block-jointed rock models where the cracking density increased, and existing cracks and joints progressively advanced as the cyclic loading progressed. They stated that the damage sustained during the primary and secondary creep stages was minimum, but the major structural breakdown occurred during the short tertiary stage of repeated loading. Moreover, Gatelier et al. (2002) identified two damage mechanisms, namely compaction and microcracking, throughout the loading process based on the evolution of moduli and irreversible volumetric strain. They suggested that compaction occurred as a result of the pore collapse and readjustment of grains into a denser packing pattern in the direction of axial stress, as evident from increased axial modulus and contracting residual volumetric strains. In contrast, they pointed out that dilatancy occurred due to the intergranular cracking and subsequent movement of grains, as evident from reduced transverse moduli and dilating residual volumetric strains. Further, they discovered that both these mechanisms were influenced by the initial anisotropy and the effect of anisotropy substantially reduced with an increase in confining stress.

Some researchers proposed new damage variables to quantify the accumulative damage and explain the fatigue damage progression of jointed rocks under repeated loading (Liu and Liu, 2017; Zheng et al., 2020a & b; Lin et al., 2020). The corresponding formulae are summarised in Table 2.3. Moreover, some researchers utilised existing fatigue damage variables (defined for intact rocks) to describe the fatigue damage of jointed rocks under

repeated loading (Liu et al., 2018b). Based on the damage evolution curves, Liu et al. (2018b), Lin et al. (2020), and Zheng et al. (2020a & b) stated that the damage developed in three stages (i.e., initial, uniform velocity and accelerated stages). During the initial stage, the damage increased swiftly, followed by a gradual increase at a steady rate, and finally, culminated in a rapid escalation until failure occurred. According to Zheng et al. (2020a), closure of the joint surface and micro-crack initiation took place during the initial damage stage, followed by stable growth of micro-cracks in the second stage. In the last stage, accelerated growth of micro cracks or their coalescence led to ultimate failure. Moreover, Liu and Liu (2017) and Liu et al. (2018b) observed that the damage progressed more rapidly at higher maximum stress levels. Furthermore, Liu and Liu (2017) found a positive correlation between the initial damage and confining stress, while Liu et al. (2018b) stated that damage increased as the loading frequency decreased.

Table 2.3. Fatigue damage variables defined for jointed rock under cyclic loading.

Definition	Reference	Formula	Description
Residual volumetric strain method	Liu and Liu (2017)	$D = \frac{(2\varepsilon_v^{max} - \varepsilon_{v,res}^{N})}{(2\varepsilon_v^{max} - \varepsilon_{v,res}^{N_f})}$	ε_v^{max} is the maximum volumetric strain, $\varepsilon_{v,res}^{N}$ and $\varepsilon_{v,res}^{N_f}$ are the residual volumetric strain after N cycles and at failure, respectively.
Density method	Zheng et al. (2020a)	When $\frac{\partial_{\rho_n}}{\partial_n} \geq 0$ $D = \frac{\rho_n - \rho_0}{2\rho_{max} - \rho_0 - \rho_{N_f}}$ When $\frac{\partial_{\rho_n}}{\partial_n} < 0$ $D = \frac{2\rho_{max} - \rho_0 - \rho_n}{2\rho_{max} - \rho_0 - \rho_{N_f}}$	ρ_n is the density of the rock joint after n cycles, ρ_0 is the density in the virgin state, ρ_{max} is the maximum density and ρ_{N_f} is the density at failure.
Residual strain method	Zheng et al. (2020a)	When $\frac{\partial_{\rho_n}}{\partial_n} < 0$	$\lvert\varepsilon_{r,res}\rvert_i$ is the residual lateral strain in the i^{th} cycle and $\lvert\varepsilon_{a,res}\rvert_i$ is the residual axial strain in the i^{th} cycle.

		$D = \frac{\sum_{i=1}^{n} 2\left\|\varepsilon_{r,res}\right\|_i + \left\|\varepsilon_{a,res}\right\|_i}{\sum_{i=1}^{N_f} 2\left\|\varepsilon_{r,res}\right\|_i + \left\|\varepsilon_{a,res}\right\|_i}$	
Shear strain method	Zheng et al. (2020b)	$D = \frac{(\overline{\varepsilon}_{max}^{n} - \overline{\varepsilon}_{max}^{0})}{(\overline{\varepsilon}_{max}^{f} - \overline{\varepsilon}_{max}^{0})}$	$\overline{\varepsilon}$ is the shear strain defined as, $\overline{\varepsilon} = \frac{\sqrt{2}}{3}[(\varepsilon_1 - \varepsilon_2)^2 + (\varepsilon_1 - \varepsilon_3)^2 + (\varepsilon_2 - \varepsilon_3)^2]^{\frac{1}{2}}$ where ε_1, ε_2 and ε_3 are the strains in three principal stress directions, respectively, $\overline{\varepsilon}_{max}^{0}$ is the initial maximum shear strain before cyclic loading, $\overline{\varepsilon}_{max}^{n}$ is the maximum shear strain after the n^{th} cycle and $\overline{\varepsilon}_{max}^{f}$ is the ultimate maximum shear strain.
Maximum strain method	Lin et al. (2020)	$D' = \frac{(\varepsilon_{m(n)} - \varepsilon_{m(0)})}{(\varepsilon_{m(f)} - \varepsilon_{m(0)})}$	D' is the maximum strain damage, $\varepsilon_{m(n)}$, $\varepsilon_{m(f)}$ and $\varepsilon_{m(0)}$ denote the maximum strains at the current cycle, final cycle and initial cycle, respectively.
Residual strain method	Lin et al. (2020)	$D'' = \frac{\varepsilon_{c(n)}}{\varepsilon_{c(f)}}$	D'' is the residual strain damage, $\varepsilon_{c(n)}$ and $\varepsilon_{c(f)}$ denote the residual strains at the current cycle and final cycle, respectively.

Moreover, previous researchers have also explored fatigue failure properties of jointed rocks exposed to repeated loads. For instance, Brown and Hudson (1973) pointed out that the failure of block-jointed rock models under repeated loading was catastrophic rather than controlled. Similarly, Liu et al. (2018b) stated that in contrast to the progressive failure behaviour of rock joints subjected to static loading, the fatigue failure of the jointed rocks exposed to repeated loading was more abrupt and did not exhibit any prior indications. Furthermore, Prost (1988) suggested that when the jointed rocks were

subjected to cyclic triaxial compression-tension loading, they experienced failure due to the gradual development and coalescence of perpendicular cracks, leading to alternating axial and lateral extension. This ultimately resulted in the specimens failing at stresses lower than the corresponding static triaxial compressive strengths.

Liu and Liu (2017) and Zheng et al. (2020a) reported that when cyclically loaded, slip and dislocation along the joint plane were evident in failed rock specimens with larger joint inclination angles. Moreover, Liu and Liu (2017) stated that the ballooning effect was evident in the failed rock specimens with lower joint inclination angles, while Zheng et al. (2020a) stated that specimens with lower joint inclination angles primarily experienced shear failure as the main failure mode. Furthermore, Liu and Liu (2017) observed that the ballooning effect was more evident at higher confining stresses. Zheng et al. (2020a & b) reported that more cracks were evident at lower frequencies. Furthermore, Zheng et al. (2020b) reported that there were no noticeable shear fracture planes in cyclically loaded semi-through joined mudstone samples. Instead, they observed cracks initiated from the tip of the joint and progressed, ultimately resulting in failure. Additionally, they noted cyclic loading led to a greater number of cracks compared to static triaxial compressive loading. Furthermore, Liu et al. (2018b) stated that the tensile wing cracks are the main cracks observed in the rock joints that failed under repeated loading.

2.5 Summary

Over the past few decades, there have been numerous experimental and theoretical investigations into the dynamic mechanical behaviour of various intact rocks exposed to repeated loads. This chapter comprehensively reviews experimental studies conducted on intact rocks under various cyclic loading conditions. Previous researchers have employed diverse laboratory conditions to simulate various field and environmental conditions when carrying out these experimental investigations on various intact rocks that exhibit distinct features. Moreover, past researchers have explored the influence of various cyclic loading factors, such as stress level, loading waveform, loading frequency and the number of loading cycles on the dynamic mechanical characteristics of intact rocks to a greater extent. These characteristics include cyclic stress-strain response, dynamic strength, fatigue life, residual deformation and dynamic elastic modulus evolution. Furthermore, researchers have employed energy theories and principles to analyse the energy dissipation mechanism that governs the deformation, damage and failure of intact rocks exposed to repeated loads. They have also defined numerous damage parameters to describe the damage evolution and failure mechanism of various intact rocks exposed to cyclic loading conditions.

Yet, a limited number of researchers have investigated the dynamic mechanical behaviour of jointed rocks when exposed to cyclic loading conditions. However, most of these experimental studies on jointed rocks have also been conducted utilising the cyclic direct shear apparatus. They have focussed on exploring the shearing mechanism, shear strength parameters, dilation and asperity degradation behaviour of jointed rocks under cyclic shear loading conditions. Moreover, some of these studies have also analysed the impact of various joint asperity characteristics, joint infill properties, shearing rate, applied

normal stress and number of shear cycles on the cyclic shear behaviour of jointed rocks to some extent.

According to the literature review presented in this chapter, only a handful of researchers have systematically investigated the dynamic mechanical response of rock joints exposed to repeated loads under cyclic uniaxial or triaxial compression test conditions. Some of these research studies have analysed the effect of various cyclic loading factors such as loading waveform, loading frequency, applied cyclic stress level and confining stress on the dynamic characteristics of rock joints to some extent. Yet, the majority of studies conducted on jointed rocks under cyclic uniaxial or triaxial compression test conditions have utilised artificial and natural rock specimens with intermittent joint features. However, systematic experimental studies investigating the dynamic characteristics of rock specimens with penetrating joints featuring different joint surface roughness subjected to various cyclic stresses and confining stresses are rather scarce. Therefore, this study attempts to experimentally evaluate the dynamic mechanical characteristics of rock samples with smooth (planar) and rough (natural replicated and ideal sawtooth) penetrating joint surfaces under various cyclic triaxial loading conditions. Specifically, the influence of various factors, including cyclic stress and confining stress conditions, number of loading cycles and joint surface roughness on the dynamic characteristics of jointed rocks such as cyclic stress-strain response, dynamic strength, residual axial deformation and dynamic elastic modulus evolution, dissipated energy and damping characteristics are analysed and discussed in detail.

Chapter 3: Experimental Investigation for Vibration Characteristics of Jointed Rocks Using Cyclic Triaxial Tests

3.1 General

Vibration assessment has always been crucial in civil engineering design and construction. Vibrations can be caused by road vehicles, trains, construction activities, and industrial machinery or naturally generated by earthquakes, wave action, landslides, volcanic eruptions and other actions (Srbulov, 2010). Among these, railways are one of the primary sources of vibration, whether underground or surface railways (Jamal-Eddine, 2017). Due to the rapid growth in population, urbanisation, growing congestion in major cities, and rising demand for energy, the introduction of high-speed trains and heavy axle freight trains has become a significant necessity in Australia (Khabbaz and Fatahi, 2014). One of the biggest challenges with high-speed heavy trains is the excessive levels of vibration generated. These excessive vibrations can cause significant adverse effects on the surrounding environment, such as distressing nearby inhabitants and damaging the close by buildings and sensitive equipment (Costa et al., 2012; Connolly, 2013; Dos Santos et al., 2017; Arcos et al., 2021). For example, according to Stiebel et al. (2012), Switzerland's national railway company had to incur an immense expense to fix vibration problems across the country's railway network. Holm et al. (2002) also reported that speed restrictions and other counter measures had to be imposed on a newly built high-speed line in Sweden due to excessively elevated vibration levels monitored. A detailed investigation carried out by Rainer et al. (1988) showed that elevated levels of vibrations had caused architectural damage and vibration-induced settlement of the foundations of homes near a track in Canada. Similarly, when high-speed rail lines are exposed to excessive vibrations, the passenger comfort and stability of the freight

transported can be impacted adversely. At the same time, the degradation of the track components and rolling stock would increase, requiring more frequent repairs and replacements (Connolly, 2013).

The effect of vibrations on human beings can vary from annoyance to severe illness (Srbulov, 2010). Experimental work conducted by Duarte and Filho (2003) illustrated that human beings are more sensitive to low-frequency vibrations in the ranges of 20 - 40 Hz and 50 - 100 Hz since these frequencies correspond with the resonant frequencies of the human head and chest wall-ocular globe, respectively. Moreover, according to Dai et al. (2019), there are safety concerns over freight trains carrying cargo in liquid form. Since these containers are usually partially filled, the liquid cargo may experience sloshing under dynamic excitations. Substantial sloshing forces and overturning moments could intensify the dynamic response of the vehicle and diminish its stability. In the meantime, when coal is transported from coal mines to their final destinations on uncovered rail cars, plumes of coal dust with harmful substances like Mercury, lead and cadmium may be generated. When the dust settles, there can be railroad safety concerns on top of the extensive environmental consequences, which can be expedited by excessive railway vibrations (Trimming, 2012). Therefore, accurately predicting the vibration levels is vital, especially when planning new surface or underground railway lines. This is necessary to avoid extensive financial expenditures that may be associated with unexpected abatement measures, speed restrictions and legal action arising from real estate losses (Connolly, 2013).

Railway vibrations are generated primarily through quasi-static and dynamic excitations and are transferred to the track, underlying subgrade and surrounding environment. These quasi-static excitations are caused by the weight of the vehicle, whereas dynamic excitations are generated by the irregularities and discontinuities at the wheel-rail

interface. The forces generated due to these excitations propagate to the railway subgrade and nearby structures as waves. Rayleigh, shear and compressional waves are the most common wave types that cause vibration effects (Connolly, 2013).

The fundamental equation for wave propagation through an elastic medium is given by:

$$\rho \frac{\partial^2 u}{\partial t^2} = (\lambda + 2\mu)\nabla(\nabla . u) - \mu\nabla \times (\nabla \times u) \tag{3.1}$$

where, ρ is the mass density of the medium, u is the displacement measurement of the medium from its undisturbed state, λ and μ are Lamé's constants. The Lamé's constants are related to elastic modulus (E) and Poisson's ratio (ν) as:

$$\mu = \frac{E}{2(1+\nu)} \tag{3.2}$$

$$\lambda = \frac{E\nu}{(1+\nu)(1-2\nu)} \tag{3.3}$$

Referring to previous research studies (Connolly, 2013; Jones, 2010; Kouroussis et al., 2014), the propagation of vibration in a medium depends on its elastic properties as well as the geometric and material damping of the medium. According to Graff (2012), to capture the impacts of medium damping on vibration characteristics and wave propagation, modified Lamé's constants can be used as below:

$$\lambda^* + 2\mu^* = (\lambda + 2\mu)\left(1 + 2i\xi_p\right) \tag{3.4}$$

$$\mu^* = \mu(1 + 2i\xi_s) \tag{3.5}$$

where, ξ_p and ξ_s are the hysteretic damping ratios for compressional and shear waves, respectively. These modified Lamé's constants can be used in Equation (3.1) to determine vibration amplitudes with the effect of damping of the medium considered.

On the other hand, most of the Australian population is located around the coastal belt with an extensive railway network. Geographically, the coastal belt of Australia is

comprised of rocky terrains (Clark and Johnston, 2017), which naturally consists of discontinuities such as fractures, joints and other planes of weaknesses. Therefore, exploring the vibration characteristics of rock joints exposed to repeated loading from high-speed heavy haul trains is essential. Therefore, in order to accurately quantify railway-induced vibration levels, precise quantification of vibration characteristics like stiffness and damping parameters of the railway subgrades under various field conditions is vital. Research studies on vibration characteristics of rock subgrades, particularly jointed rock subgrades exposed to cyclic loads from train loads, are rather scarce. According to the field studies conducted by Volberg (1983) on railways, Jayasinghe et al. (2019) on a rock blast and Chen et al. (2019a) on a vibrating roller compactor, the vibration amplitudes are generally higher with slower attenuation in a rock mass in comparison to a soil mass.

Numerous researchers have conducted experimental and theoretical investigations to explore the dynamic behaviour of various types of intact rocks under cyclic uniaxial or triaxial loading conditions. Strength and deformational characteristics of various intact rocks exposed to cyclic loading conditions have been studied, and the impact of stress amplitude, frequency, maximum cyclic stress and cyclic waveform have been analysed (Attewell and Farmer, 1973; Zhenyu and Haihong, 1990; Yoshinaka et al., 1996; Bagde and Petroš, 2005a; Fuenkajorn and Phueakphum, 2010; Liu et al., 2011; Liu and He, 2012; Liu et al., 2012; Ma et al., 2013; Wang et al., 2013; Taheri et al., 2016; Zhou et al., 2019). Dynamic damage evolution and failure characteristics of various types of intact rocks under cyclic loading have also been studied, defining damage variables (Liu and He, 2012; Liu et al., 2012; Xiao et al., 2009; Xiao et al., 2010; Liu et al., 2016). Moreover, dynamic energy characteristics of intact rocks subjected to repeated loading have been investigated through energy parameters determined through the integration of cyclic

stress-strain curves (Bagde and Petros, 2009; Momeni et al., 2015; Zhang et al., 2017; Yang et al., 2016; Yang et al., 2018b).

Besides, some researchers have investigated the jointed rock behaviour under cyclic loads, and most of them have conducted cyclic shear experiments. These studies investigated the shear mechanism, dilation and asperity degradation behaviour under cyclic shear loading, as well as the impact of loading rate, number of shear cycles and normal stress have been analysed (Hutson and Dowding, 1990; Huang et al., 1993; Jing et al., 1993; Armand et al., 1998; Lee et al., 2001; Jafari et al., 2003; Belem et al., 2007; Fathi et al., 2016; Liu et al., 2018a; Kou et al., 2019; Xu et al., 2021a).

In addition, a handful of research studies have been carried out on rock joints under cyclic uniaxial or triaxial loading conditions. Early Studies on intermittently jointed rock samples subjected to cyclic uniaxial (Brown and Hudson, 1973; Li et al., 2001a & b) and triaxial (Prost, 1988) loading conditions analysed the impact of repeated loading on the dynamic strength and deformation behaviour of intermittent joints. Studies by Liu et al. (2017, 2018b & c) further analysed deformation characteristics, energy and fatigue damage and failure mode of intermittent joints under cyclic uniaxial compression. Jafari et al. (2003 & 2004) investigated the effect of repeated loading on the shear strength of jointed rocks under triaxial conditions. Ding et al. (2014) studied the impact of contact state on dynamic deformation behaviour. Studies by Liu and Liu (2017) and Zheng et al. (2020a & b) investigated the deformation characteristics, dynamic damage and failure mechanism of prefabricated jointed rock under cyclic triaxial conditions.

As indicated by the aforementioned research studies, most of the previous researchers have focussed on intact rock behaviour, and investigations on dynamic mechanical properties and deformation response of jointed rocks exposed to repeated loading are

rather limited. Indeed, most of the previous studies on rock joints utilised either cyclic direct shear tests for testing penetrating joints or cyclic uniaxial and triaxial tests for intermittent joints. However, studies on the cyclic response of jointed rock with penetrating joints subjected to various confining stresses and considering different joint surface roughness are scarce. Meanwhile, analysis of rock joint behaviour from the perspective of deformation, energy and damping characteristics is limited. This study presents the vibration characteristics of rock joints subjected to cyclic triaxial tests under train loads. The experiments are carried out on artificial rock joints with planar, sawtooth and natural replicated joint surfaces under various cyclic deviatoric stress amplitudes, which correspond to different train axle loads and confining stresses representing different vertical depths from the rail track bed. The stress-strain response, irreversible strains, the effect of cyclic deviatoric stress amplitude and confining stress on deformation characteristics, dissipated energy and damping characteristics are analysed and discussed in detail.

3.2 Laboratory Investigation

3.2.1 Sample Preparation

In order to carry out an experimental study to investigate the impact of load characteristics on rock joints, it is necessary to have a set of identical specimens. However, the use of natural rock joints is quite difficult due to the probable irregularities and heterogeneities. To produce rather identical specimens with controlled conditions, many researchers proposed the use of various materials and mixtures to create artificially jointed rocks (Hobbs, 1966; Saucier, 1967; Rosenblad, 1970; Stimpson, 1970; Johnston and Choi, 1986; Huang and Doong, 1990; Indraratna, 1990; Mostyn and Bagheripour, 1998; Kusumi et al., 1998; Kulatilake et al., 2001). Among the available materials, gypsum

plaster has been used widely to model weak rocks, and Hobbs (1966) was one of the pioneers who proposed the use of gypsum plaster to model sedimentary rocks. This material is readily available, relatively inexpensive, can be moulded into any shape when mixed with water, and its long-term strength is independent of time once the chemical hydration is complete. Therefore, model rock joints with idealised joint surfaces (planar and saw-toothed) and a natural imprinted rock (sandstone) surface were cast using gypsum plaster ($CaSO_4.H_2O$ hemihydrates, 98%).

All the jointed specimens were cast with a mean dip angle of 60^o since Goodman (1989) stated that when the joint has a dip angle between 50^o and 65^o, the shearing of the joint will occur before the failure of the rock. This also agrees with the Mohr-Coulomb criterion, where the critical joint dip angle is given by $(45° + \phi/2)$, in which ϕ is the friction angle of the rock joint (Abdellah et al., 2016). The jointed specimen had a diameter of 50 mm, and when the halves of the specimen were fully mated, the overall height was 100 mm, which maintained a height-to-diameter ratio of two. The idealised sawtooth joints had 2 mm high asperities with an initial asperity angle of 18^o, whereas planar joints had no asperities. It should be noted that many researchers have used initial asperity angles between 5^o and 30^o to represent low to high levels of roughness in sawtooth joint surfaces (Jafari et al., 2003; Sinha and Singh, 2000; Mirzaghorbanali et al., 2014).

Cylindrical hollow moulds of 50 mm diameter and 100 mm height (see Figures 3.1a & b) and cylindrical moulds of each side of the planar and sawtooth joints surfaces (see Figure 3.1c) were created using acetal plastic. A block of sandstone was split to obtain a naturally rough rock surface, and the split sandstone surface was copied onto a mould using a mould-making silicon rubber Dalchem SRT 30. These cylindrical rubber moulds with an imprinted natural joint surface were used to prepare replicated natural joint specimens.

For all the rock joints, each side of the joint surface was created separately to ensure that the joint was fully mated after assembly. The moulds of the joint surfaces were placed inside the cylindrical hollow moulds, and a silicon-based lubricant was applied. In line with previous research studies (Atapour and Moosavi, 2014; Jahanian and Sadaghiani, 2015; Gong et al., 2018b), gypsum plaster mixed with water in a ratio of 3.5:1 by mass was used in this study to prepare the model rock joints. Gypsum and water were mixed uniformly and poured into the cylindrical moulds. A mild vibration was then applied to the cylindrical moulds externally to release any air bubbles trapped in the gypsum mixture. The specimens were allowed to harden for about 30 minutes and were then removed from the moulds. Subsequently, the specimens were cured in an oven at the controlled temperature of 40 ºC for two weeks and were used for testing once they reached room temperature. Details of the cylindrical hollow moulds, the moulds of one side of the joint surfaces and the casted samples with sawtooth, planar and natural replicated joint surfaces are shown in Figure 3.1. Moreover, three additional samples without a joint (50 mm diameter and 100 mm height) were also prepared to determine the uniaxial compressive and tensile strengths and the relevant values of intact samples are reported in Table 3.1.

Table 3.1. Mechanical properties of the hardened gypsum plaster mixture used to cast the rock samples.

Uniaxial Compressive Strength, σ_c (MPa)	62.1
Young's Modulus, E_r (GPa)	19.1
Tensile Strength, σ_t (MPa)	15.4
Basic friction angle, ϕ_b (degrees)	30

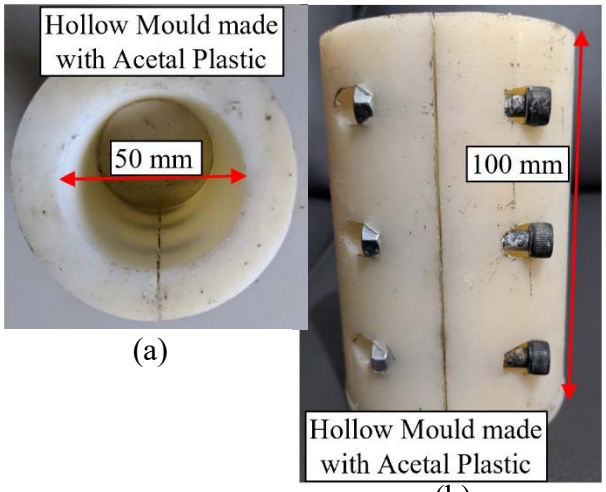

(a) (b)

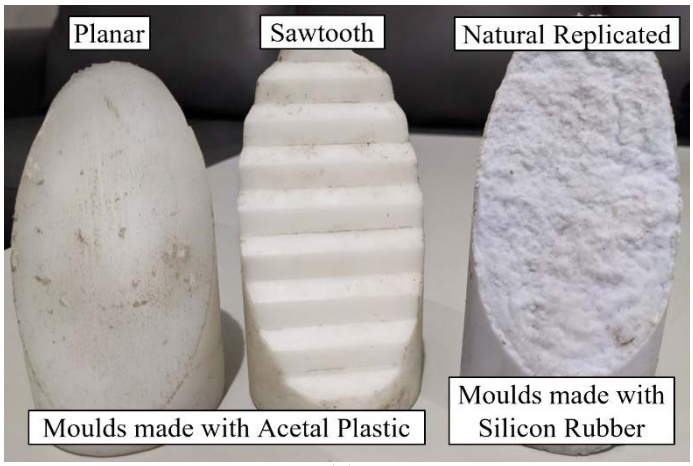

(c)

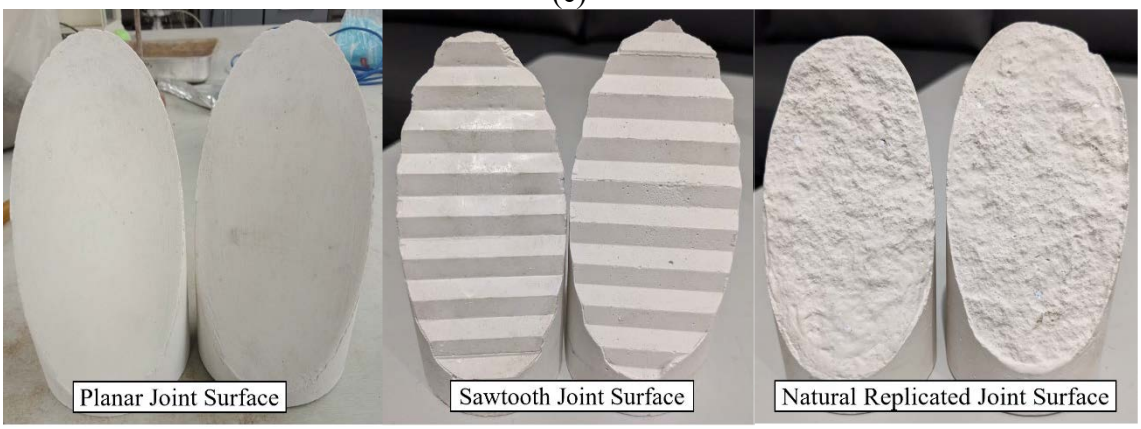

(d) (e) (f)

Figure 3.1. (a) The top view of the circular mould with one-half of the sawtooth joint mould inside it (b) The transverse view of the circular mould; (c) One-half of the joint moulds with planar, sawtooth and natural replicated joint surfaces; (d) The two opposite surfaces of a planar jointed sample; (e) The two opposite surfaces of a sawtooth jointed sample and (f) The two opposite surfaces of a natural replicated jointed sample.

3.2.2 Testing Procedure

Although direct shear apparatus has been commonly used for testing of rock joints by many researchers due to its ease of operation, inspired by Jafari et al. (2004), the cyclic triaxial apparatus was selected in this study since it can allow investigation of the jointed rock in a state similar to actual underground conditions. As shown in Figure 3.2, the GDS Entry Level Dynamic (ELDYN) triaxial apparatus was used to conduct the cyclic triaxial experiments in this study. The adopted cyclic triaxial set-up had a load frame with a beam-mounted electro-mechanical actuator which had a load capacity of 10 kN and a maximum achievable loading frequency of 10 Hz. The cell pressure was pneumatically controlled, and de-aired water was used as the cell liquid. After necessary checks and calibrations, the jointed sample was placed in the triaxial cell, covered with a membrane and O-rings to seal the sample. After applying the target cell pressure, the cyclic loading was applied continuously for up to 10000 cycles under undrained conditions. The jointed rock samples were kept dried throughout the tests, and as a result, the saturation of the sample was not required.

The samples tested captured three joint types, namely planar, saw-toothed and natural replicated joints, with a mean dip angle of 60^{o}. Three levels of confining stresses (i.e., 20 kPa, 90 kPa and 150 kPa) and three levels of cyclic stress amplitudes (i.e., 220 kPa, 260 kPa and 300 kPa) were selected. The confining stresses were calculated by considering both surface and underground railway tracks resting on a rock subgrade and compared with those used by Ding et al. (2014), Nie et al. (2020) and Wang and Zhuang (2021). The adopted cyclic deviatoric stress amplitudes were calculated by conducting an elastic stress analysis of a moving train (i.e., a beam on an elastic foundation approach coupled with Boussinesq's solution) corresponding to 30-ton, 35-ton and 40-ton axle loads. It

should be noted that vertical stresses in the range of 100 kPa to 300 kPa were measured or utilised by previous researchers for cyclic testing, field measurements and numerical simulations of the formation layer of heavy haul train lines (Rose et al., 2004; Suiker et al., 2005; Leshchinsky and Ling, 2013; Chen et al., 2019b; Arulrajah et al., Arulrajah et al., 2020). The cyclic loading was applied up to 10,000 cycles (beyond which no considerable change in axial strains was observed) with a frequency of 8 Hz (corresponding to a train speed of 90 km/h) for all the tests. Frequencies in the range of 5- 10 Hz have been used by many researchers in the past for cyclic experiments subjected to a load of heavy haul or rather high-speed train lines (Suiker et al., 2005; Zhang et al., 2018a; Mohammadinia et al., 2020; Touqan et al., 2020; Naeini et al., 2021). The cyclic load was applied in the form of a sinusoidal wave where minimum deviatoric stress was maintained constant (20kPa or 40kPa) while the maximum deviatoric stress was adjusted to apply the target cyclic deviatoric stress amplitudes.

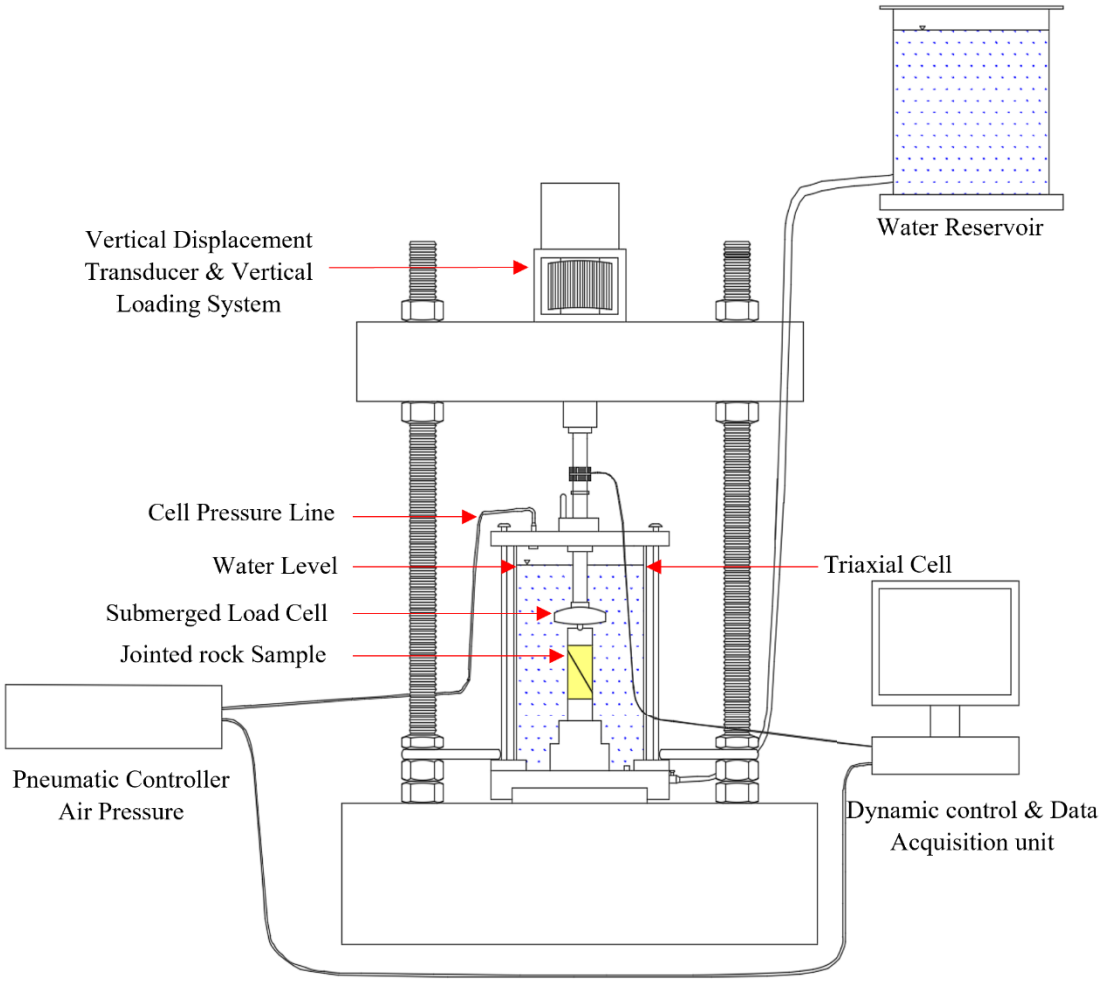
Vertical Displacement
Transducer & Vertical
Loading System
Water Reservoir
Cell Pressure Line
Water Level
Triaxial Cell
Submerged Load Cell
Jointed rock Sample
Pneumatic Controller
Air Pressure
Dynamic control & Data
Acquisition unit

(a)

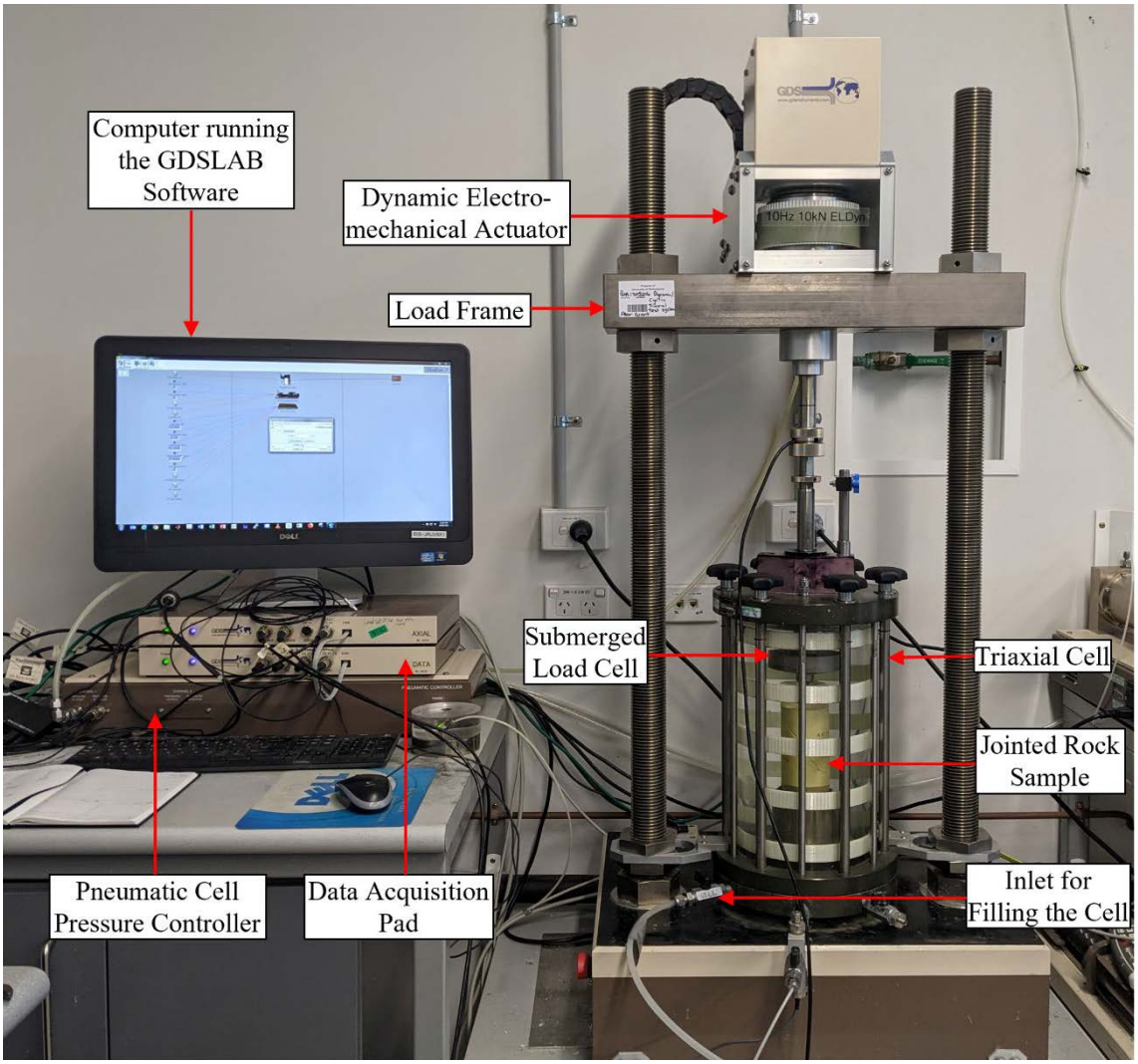

(b)

Figure 3.2. (a) Schematic diagram of the experimental setup; and (b) GDS 10 Hz cyclic triaxial equipment used in this study.

3.3 Results and Discussion

3.3.1 Cyclic Stress-Strain Response

Figures 3.3 and 3.4 present examples of the dynamic stress-strain curves obtained for different joint types. Under the tested conditions, the hysteresis loops transitioned from sparse to dense with increasing loading cycles. This could be clearly observed under the lowest confining stress of 20 kPa (Figures 3.3a, 3.4a & b) irrespective of the joint type. The hysteresis loops at lower deviatoric stress amplitudes were considerably denser than

that under higher deviatoric stress amplitudes (Figures 3.4a & b). A similar trend was also observed in the dynamic stress-strain curves reported by Ding et al. (2014) for the rock-concrete composite samples and Taheri et al. (2016) for the Hawkesbury sandstone samples subjected to lower pre-peak cyclic loads.

Moreover, the samples with sawtooth joint surfaces developed the lowest axial deformations, whereas the samples with planar joint surfaces developed much elevated axial deformations. Furthermore, Referring to Figures 3.3 and 3.4, as the confining stress increased or cyclic deviatoric stress decreased, the maximum axial strain attained by the samples decreased across all three adopted joint types.

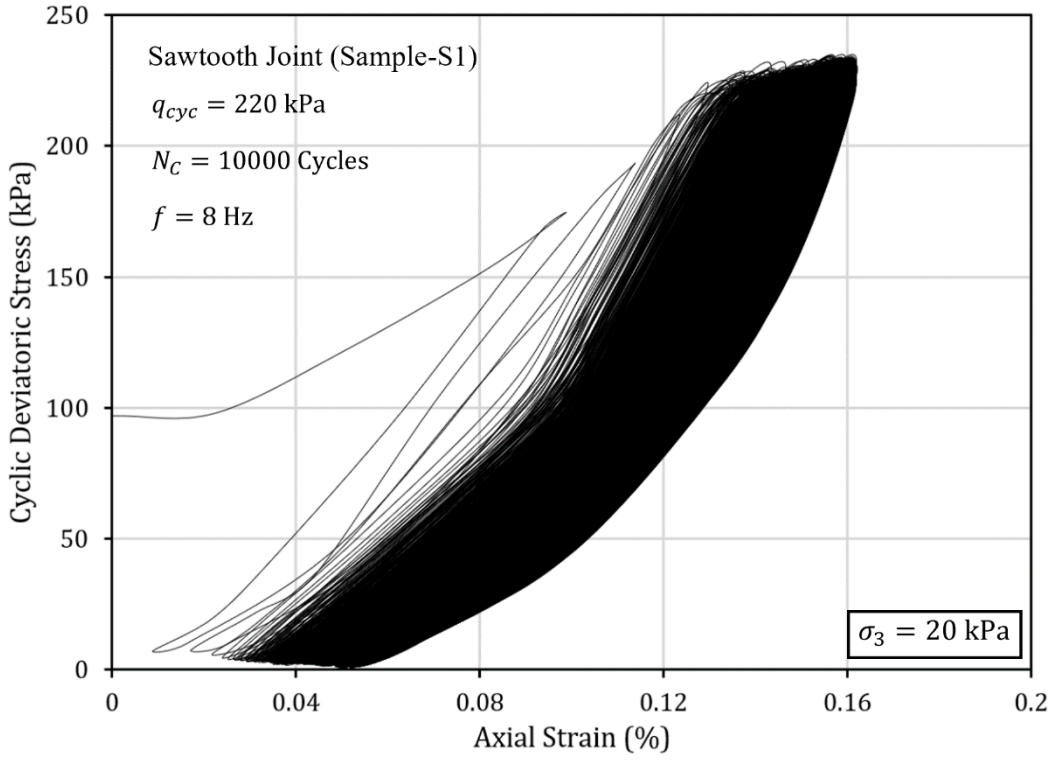

(a)

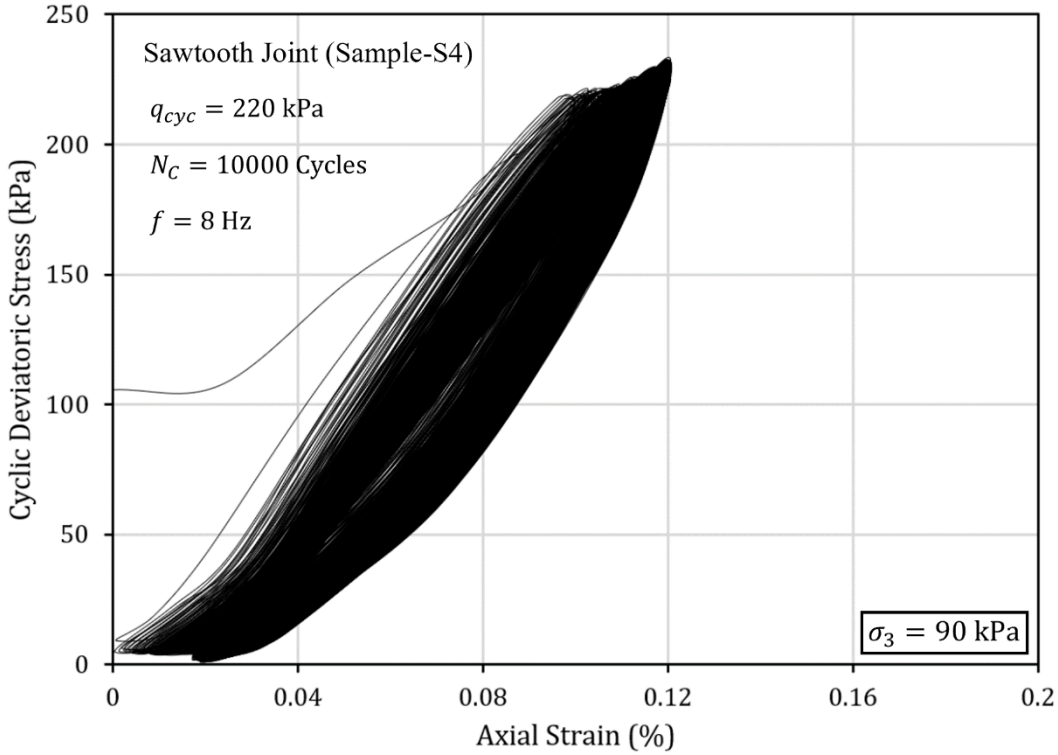

(b)

Figure 3.3. The dynamic stress-strain curves for sawtooth joints with cyclic deviatoric stress amplitude (q_{cyc}) of 220 kPa: (a) Confining pressure (σ_3) = 20 kPa, (b) Confining pressure (σ_3) = 90 kPa.

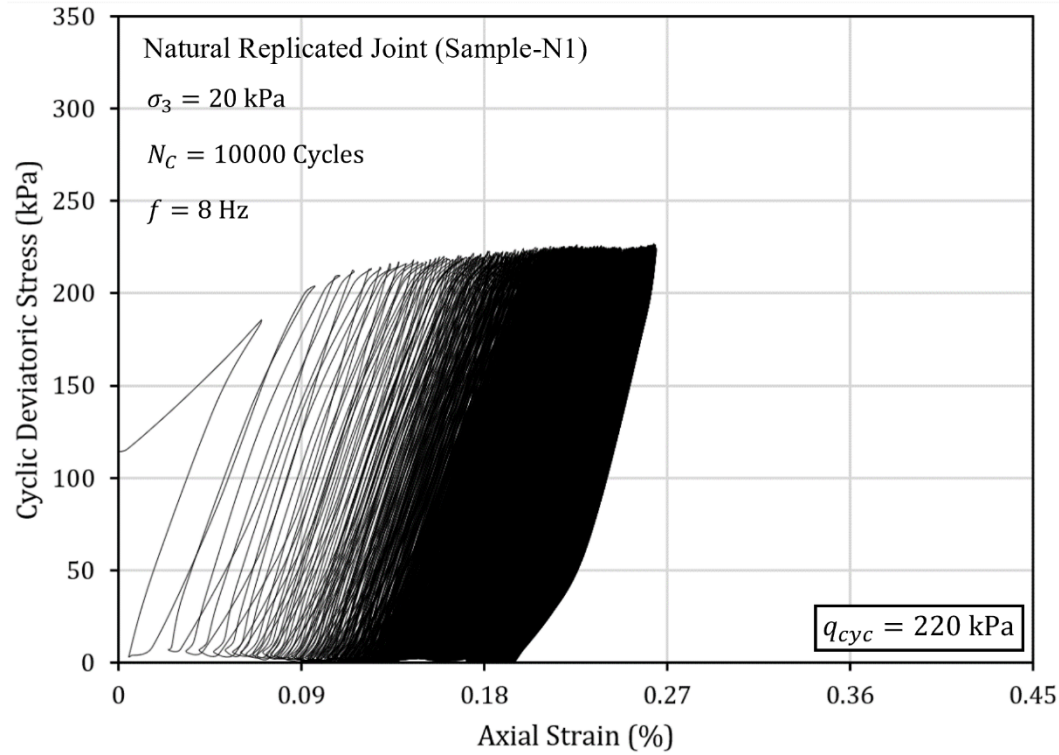

(a)

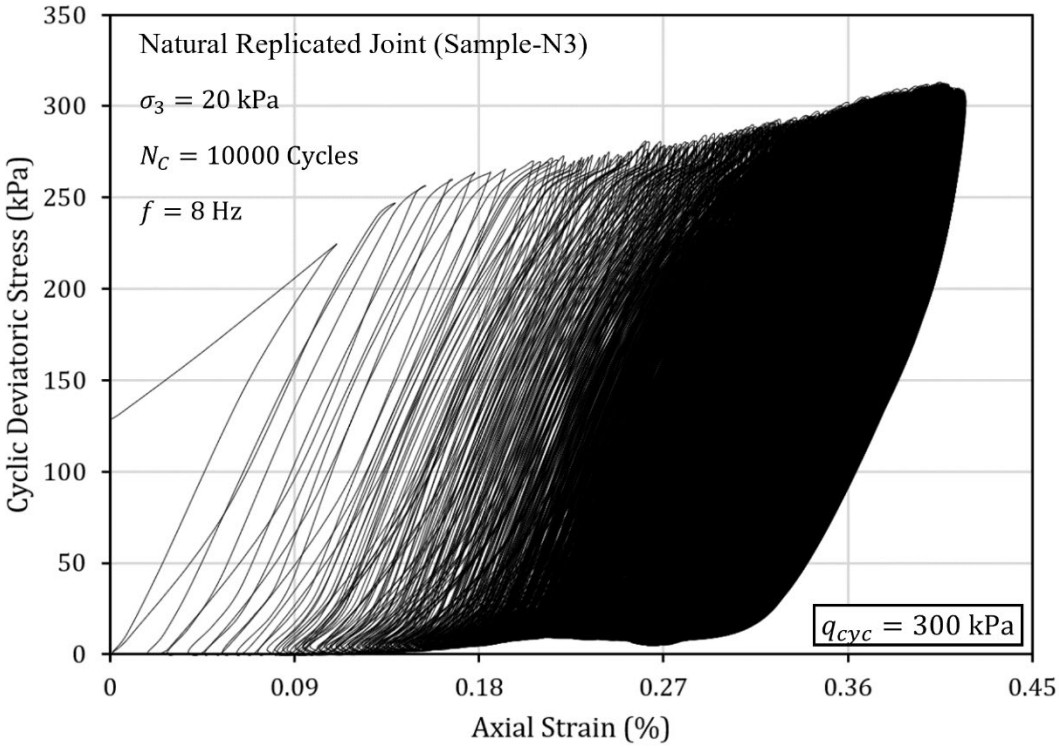
Natural Replicated Joint (Sample-N3)
σ_3 = 20 kPa
N_C = 10000 Cycles
f = 8 Hz
q_{cyc} = 300 kPa
Cyclic Deviatoric Stress (kPa)
Axial Strain (%)
0
50
100
150
200
250
300
350
0
0.09
0.18
0.27
0.36
0.45

(b)

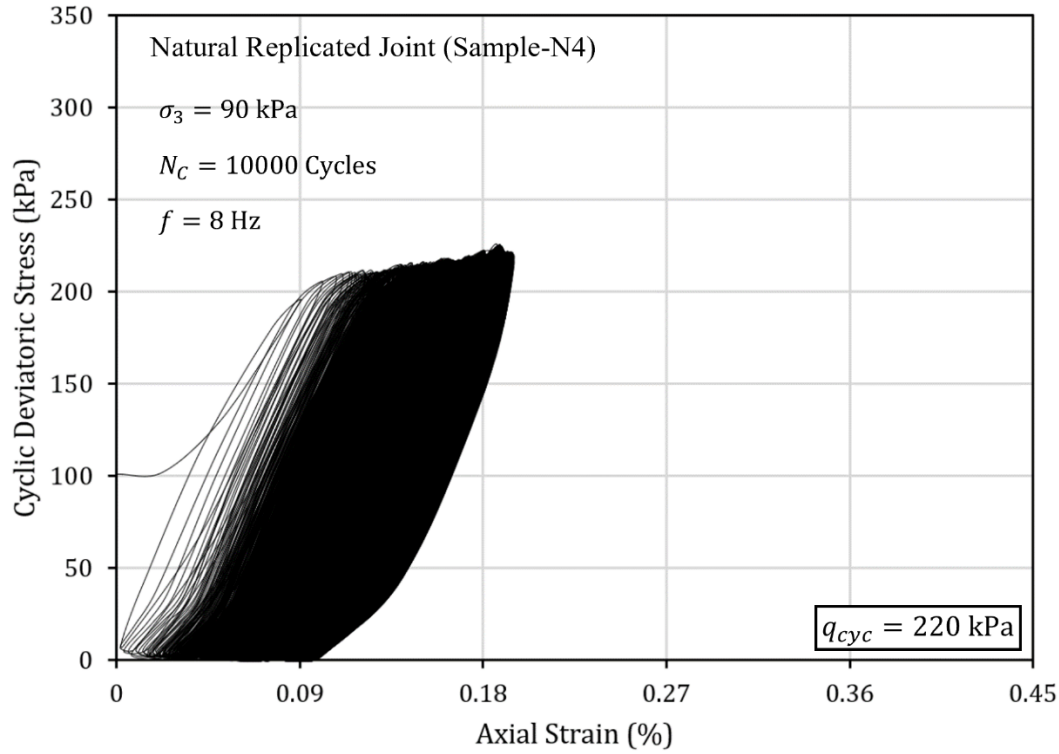
Natural Replicated Joint (Sample-N4)
σ_3 = 90 kPa
N_C = 10000 Cycles
f = 8 Hz
q_{cyc} = 220 kPa
Cyclic Deviatoric Stress (kPa)
Axial Strain (%)
0
50
100
150
200
250
300
350
0
0.09
0.18
0.27
0.36
0.45

(c)

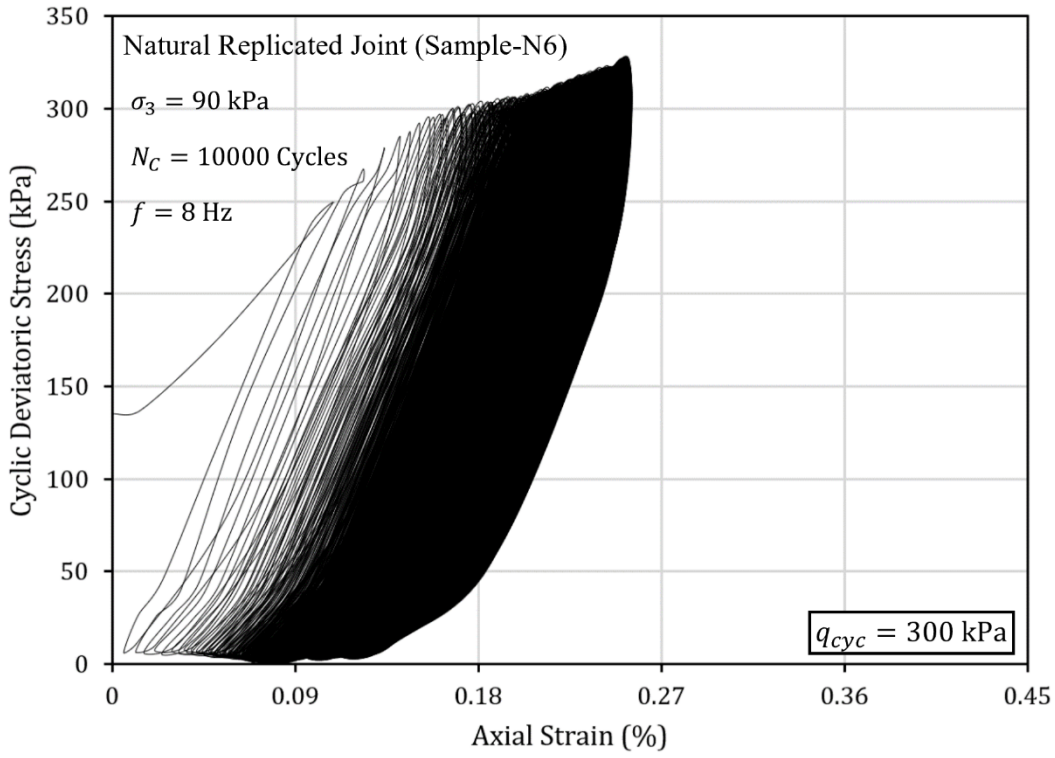

(d)

Figure 3.4. The dynamic stress-strain curves for natural replicated joints varying confining pressures (σ_3) of 20 kPa and 90 kPa and cyclic deviatoric stress amplitudes (q_{cyc}) of 220 kPa and 300 kPa: (a) σ_3 = 20 kPa and q_{cyc} = 220 kPa, (b) σ_3 = 20 kPa and q_{cyc} = 300 kPa, (c) σ_3 = 90 kPa and q_{cyc} = 220 kPa and (d) σ_3 = 90 kPa and q_{cyc} = 300 kPa.

3.3.2 Residual Axial Strain

Figure 3.5 shows how cumulative residual axial strain varied with the number of cycles for all three joint types under various confining stresses and cyclic deviatoric stress amplitudes. As the number of cycles increased, the cumulative residual axial strain rapidly increased during the initial loading cycles and then tended to stabilise during the subsequent loading cycles. Accordingly, the cumulative residual axial strain curves exhibited two phases in terms of axial deformation response: (i) the initial phase, where residual axial deformation increases rapidly, followed by phase (II), the steady phase, where after some loading cycles, the rate of residual axial deformation development tended to stabilise for the rest of the loading cycles.

According to Gatelier et al. (2002), the residual axial deformation behaviour of rough joints, i.e., sawtooth and natural replicated joint types, could be explained by the Kaiser effect observed in a wide range of materials. i.e., once a rock mass is loaded to a certain stress level, it would not produce any AE upon reloading until the previous maximum stress level has been exceeded (especially when the applied stress level is below the critical threshold, which can cause extensive irreversible deformations) (Dexing et al., 2019). Referring to Figure 3.5a, compared with the samples with sawtooth and natural replicated joint surfaces, the cumulative irreversible deformations of the samples with planar joint surfaces were significantly higher. This significant amplification in cumulative irreversible axial deformations in planar joint surfaces is attributed to the smoothness of the joint surface, allowing easier sliding along the joint plane. Natural replicated and sawtooth joints possess rough joint surfaces, and according to Ladanyi and Archambault (1969), deformation of a jointed rock mass with a rough joint surface occurs due to the asperity overriding and damage. Further, Barton and Choubey (1977) stated that the joint material strength also contributes to the asperity overriding and breaking mechanism of the rock joint. Hence, lower cumulative irreversible deformations of natural replicated and sawtooth joints can be attributed to the inadequacy of the applied cyclic load to cause significant asperity overriding or breakage to generate higher irreversible deformations of the jointed samples. Indeed, sawtooth joints exhibited the lowest cumulative irreversible axial deformations (see Figure 3.5b). As evident in Figure 3.5, all the considered joint types demonstrated a negative correlation between the applied confining pressure and the cumulative residual axial strain, while higher cyclic stress amplitudes corresponded to higher cumulative residual axial strains at the same confining stress. This behaviour can be due to higher confining stresses providing higher resistance, while higher cyclic stress amplitudes provide higher aid to joint asperity overriding and

damage. This attests that the potential irreversible deformation of the jointed rock subgrades caused by train loads reduces when progressing to deeper levels of the jointed rock subgrade, while irreversible deformation at any depth amplifies when heavily loaded trains pass.

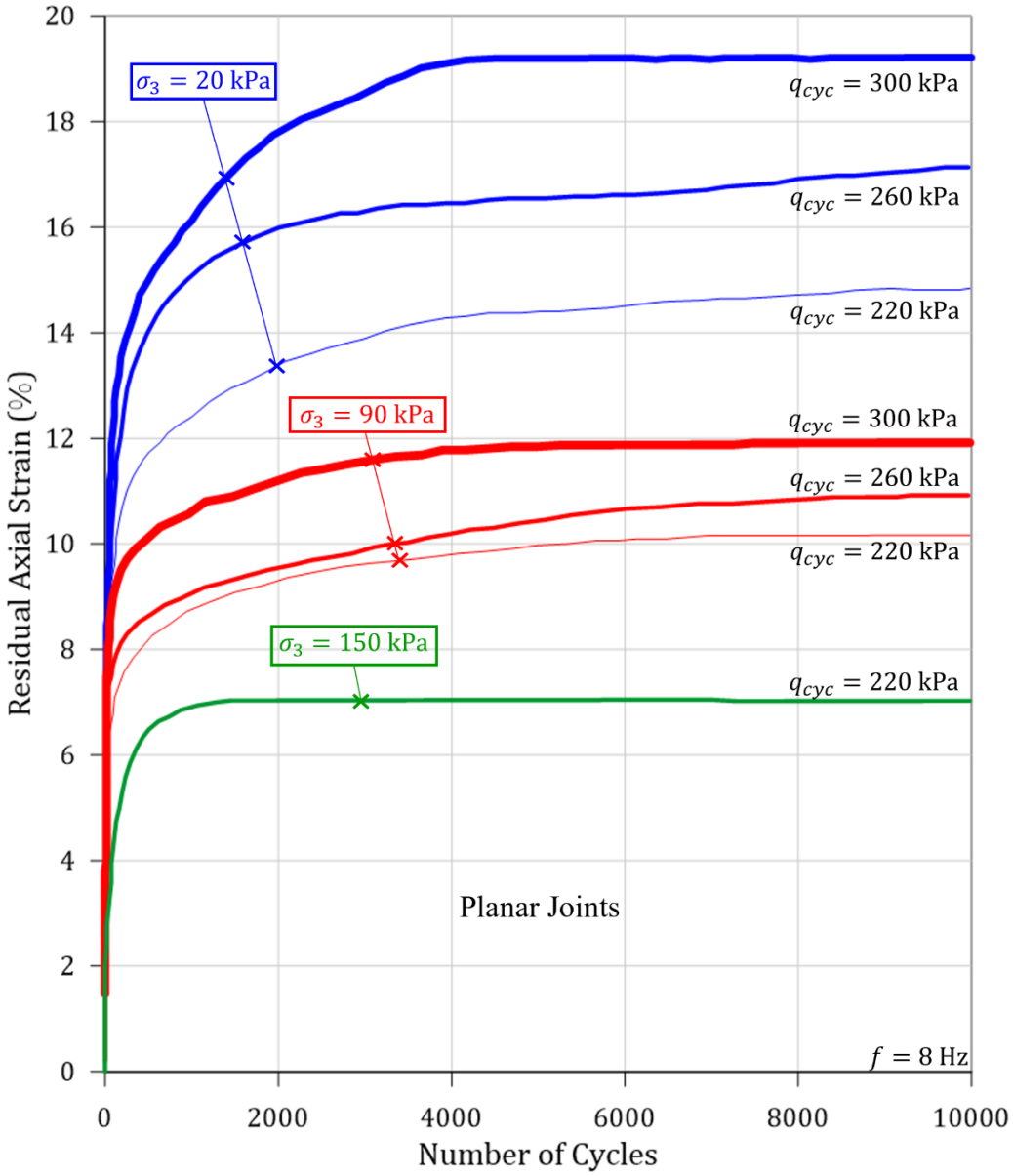

(a)

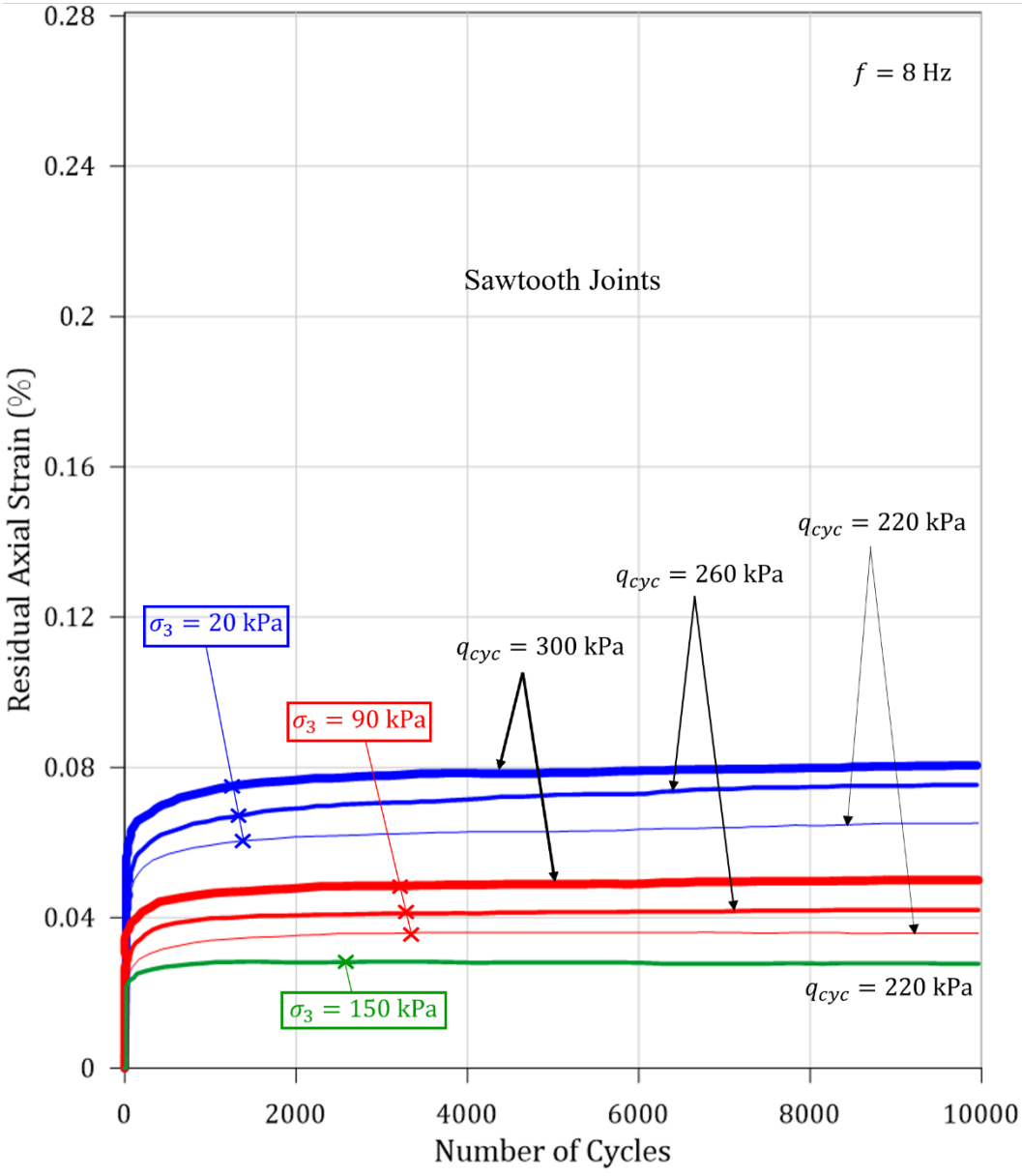
0.28
0.24
0.2
0.16
0.12
0.08
0.04
0
Residual Axial Strain (%)
f = 8 Hz
Sawtooth Joints
q_{cyc} = 220 kPa
q_{cyc} = 260 kPa
q_{cyc} = 300 kPa
σ_3 = 20 kPa
σ_3 = 90 kPa
σ_3 = 150 kPa
q_{cyc} = 220 kPa
0
2000
4000
6000
8000
10000
Number of Cycles

(b)

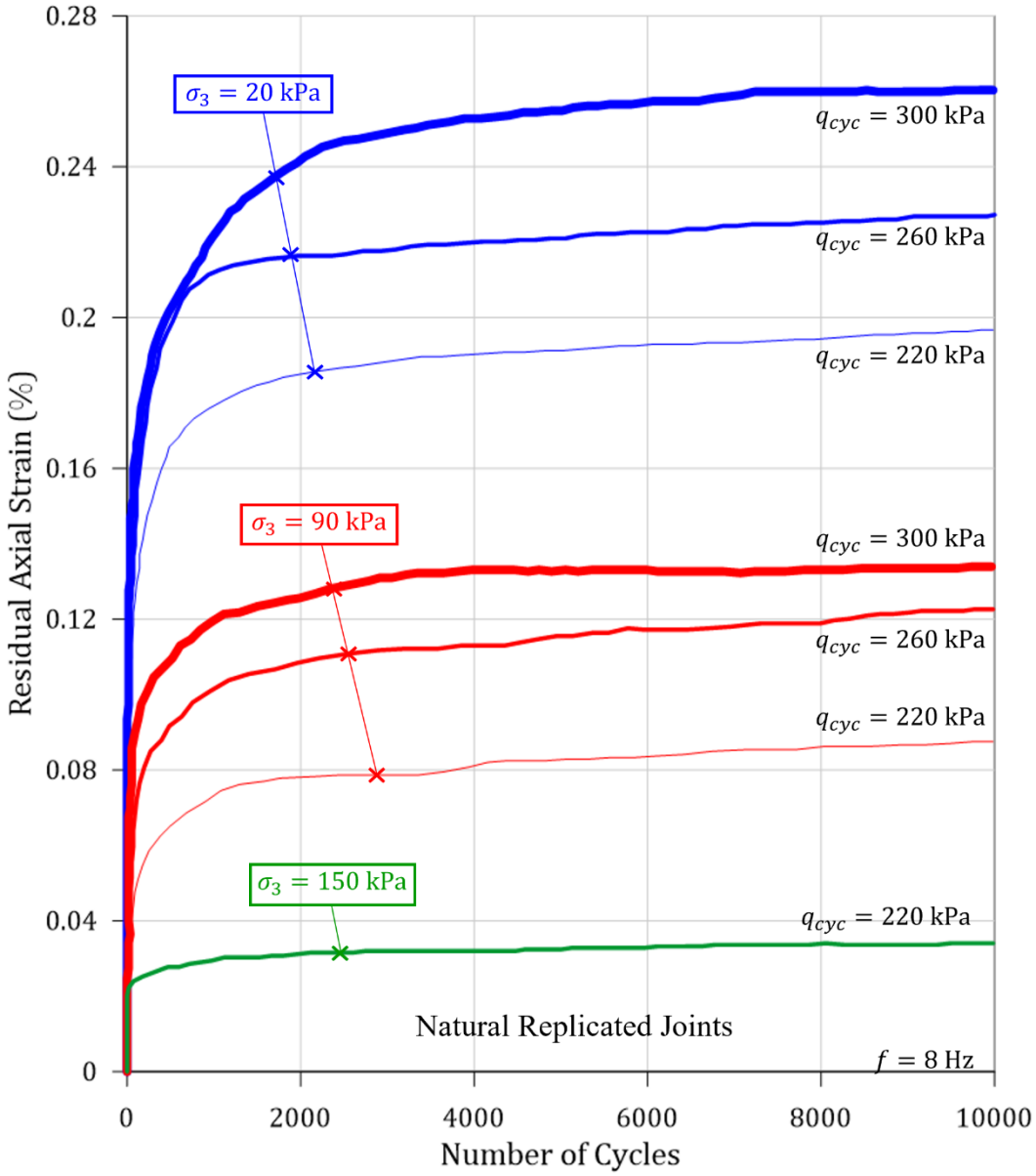

(c)

Figure 3.5. The evolution of residual axial strain with loading cycles at various confining pressures (σ_3) of 20 kPa, 90 kPa and 150 kPa and cyclic deviatoric stress amplitudes (q_{cyc}) of 220 kPa, 260 kPa and 300 kPa for (a) Planar Joints, (b) Sawtooth Joints and (c) Natural Replicated Joints.

The number of cycles corresponding to 85% of the maximum cumulative residual axial strain ($N_{critical}$) attained by all three types of joints at various confining stresses, and cyclic deviatoric stress amplitudes were determined and presented in Figures 3.6 and 3.7. These figures show how $N_{critical}$ varied with the confining stress and the cyclic deviatoric stress amplitude. It should be noted that as recommended by ASTM D5311-13 (2013),

since the value of cyclic deviatoric stress for each loading cycle slightly deviated from the target input value, a weighted average value of cyclic deviatoric stress was calculated using Equation (3.6) and used in the plots of Figures 3.6 and 3.7.

$$(q_{cyc})_{avg} = \frac{1}{N_i}\sum_{n=1}^{N_i}(q_{cyc})_n \tag{3.6}$$

where, $(q_{cyc})_{avg}$ is the average value of cyclic deviatoric stress, $(q_{cyc})_n$ is the cyclic deviatoric stress at a given cycle n, and N_i is the total number of cycles for a particular test.

According to Figure 3.6, with rising cyclic deviatoric stress, $N_{critical}$ gradually increased for a given confining stress, and Figure 3.7 illustrates that a rise in the confining stress resulted in reduction of $N_{critical}$ for a given cyclic deviatoric stress for all three adopted joint types. On the other hand, this observation suggests that with increased train loads, in order to reach the corresponding maximum irreversible settlement of the jointed rock subgrade, a higher number of train passes would be required. Whilst at deeper levels of the subgrade, the potential maximum irreversible settlement will be attained within a lesser number of train passes, and further settlement of the jointed rock foundation will not take place.

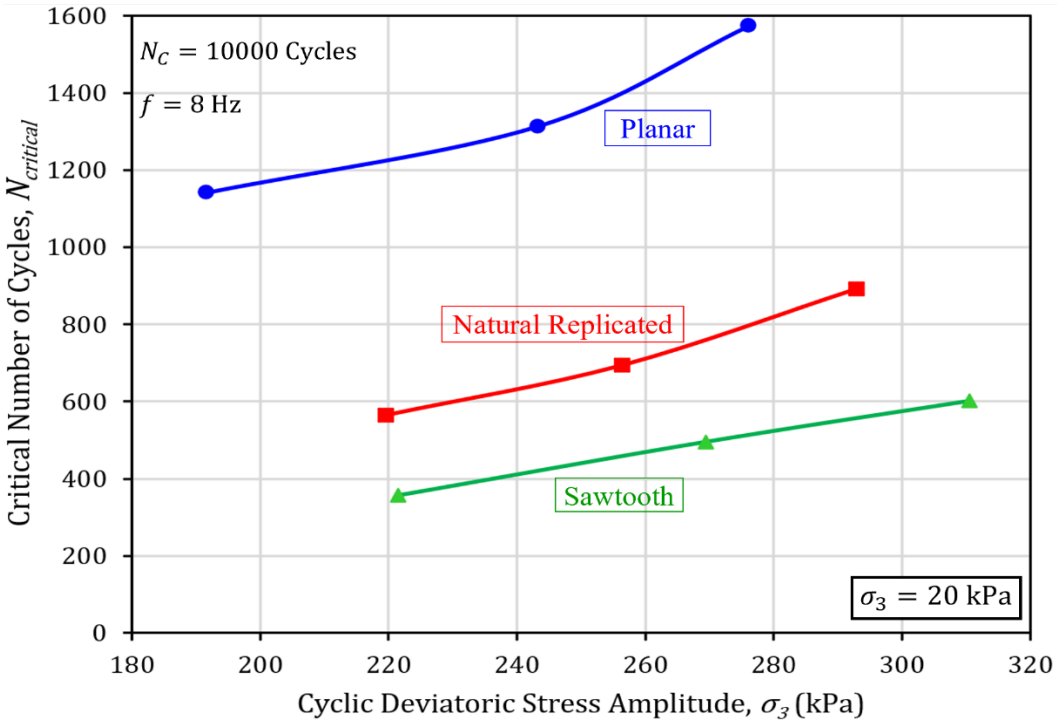

(a)

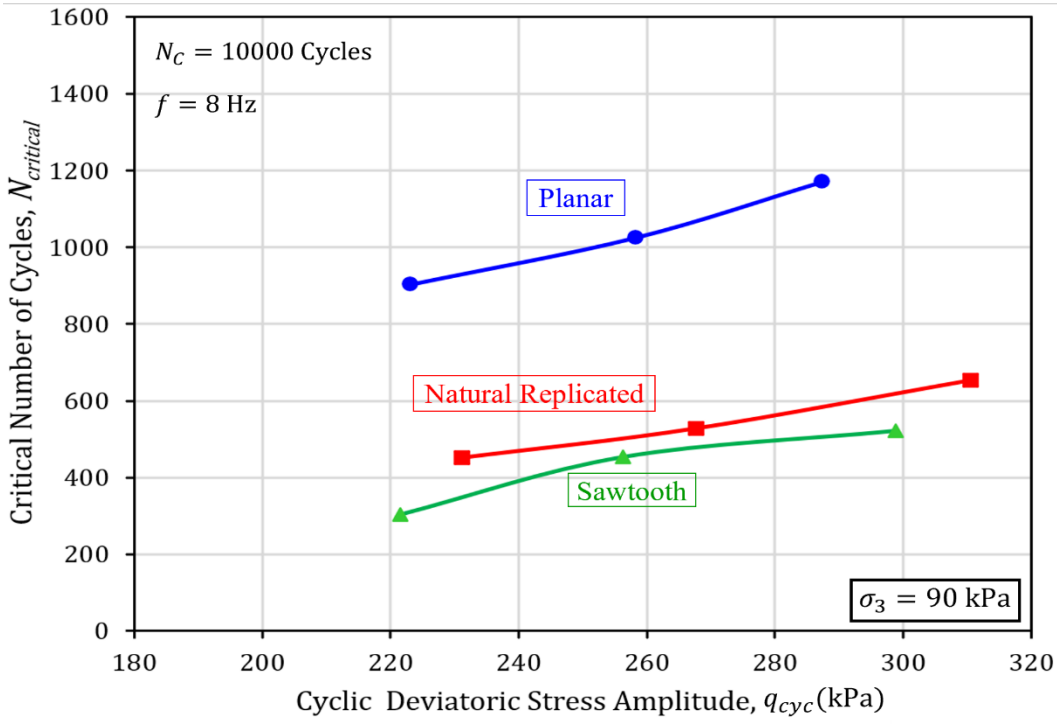

(b)

Figure 3.6. The number of Cycles ($N_{critical}$) corresponding to 85% of the maximum residual axial strain vs cyclic deviatoric stress amplitude (q_{cyc}) at confining pressures (σ_3) of 20 kPa and 90 kPa for the three types of joints: (a) At $\sigma_3 = 20$ kPa and (b) At $\sigma_3 = 90$ kPa.

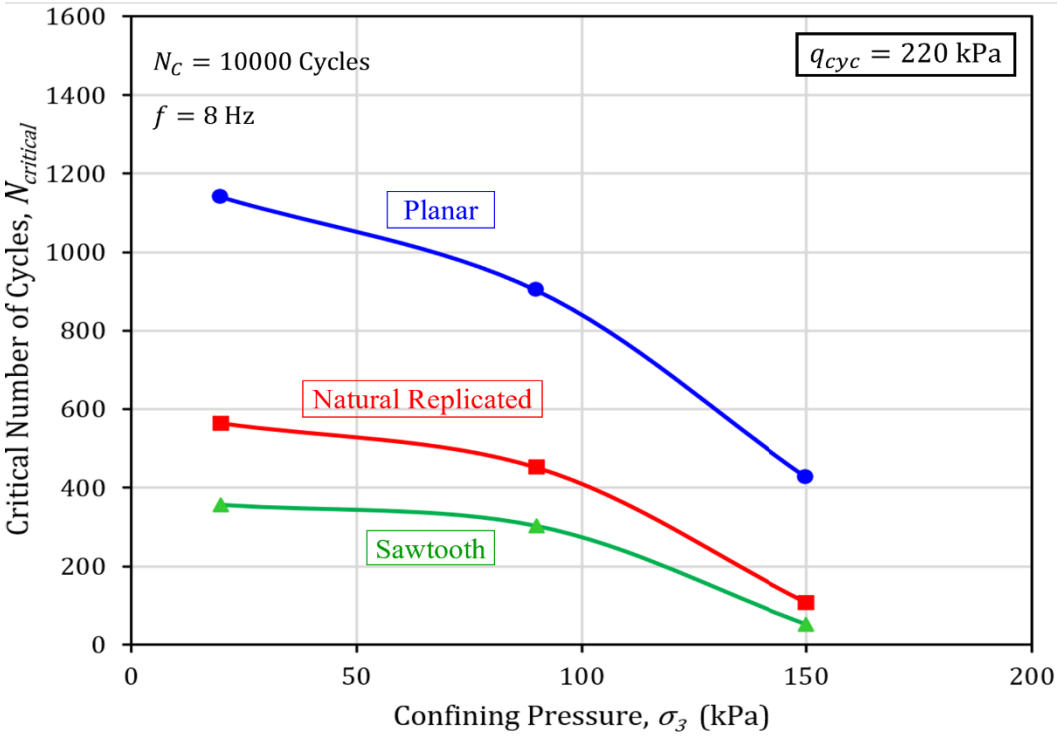

Figure 3.7. The number of Cycles ($N_{critical}$) corresponding to 85% of the maximum residual axial strain vs confining pressure (σ_3) at cyclic deviatoric stress (q_{cyc}) of 220 kPa for the three types of joints.

3.3.3 Resilient Modulus

The unloading characteristics of the sample, which depend on the reversible axial strains recovered during unloading, can be captured by the Resilient Modulus (M_R) defined as follows:

$$M_R = \frac{\Delta q_{cyc}}{\varepsilon_{1,rec}} \tag{3.7}$$

where Δq_{cyc} is the difference between the maximum and minimum cyclic deviatoric stresses (i.e., from the unloading point to the beginning of the reloading) and $\varepsilon_{1,rec}$ is the recoverable axial strain during unloading. The calculated values of resilient moduli using Equation (3.7) are plotted against the number of cycles, as shown in Figures 3.8 and 3.9. The resilient modulus degraded with increasing loading cycles, especially during the initial loading cycles in all three joint types. For planar joints (Figures 3.8a and 3.9), the

downward trend of resilient moduli was very evident compared to the other joint types. However, the resilient moduli of sawtooth and natural replicated joint types (Figures 3.8b & c and Figure 3.9) stabilised after the initial few cycles, whereas the number of loading cycles consumed by planar joints to establish stabilised resilient moduli was quite large. This is also evident from the cumulative residual axial strain curves of planar joints (Figure 3.5a), where cumulative residual axial strain stabilises after consuming a larger number of cycles.

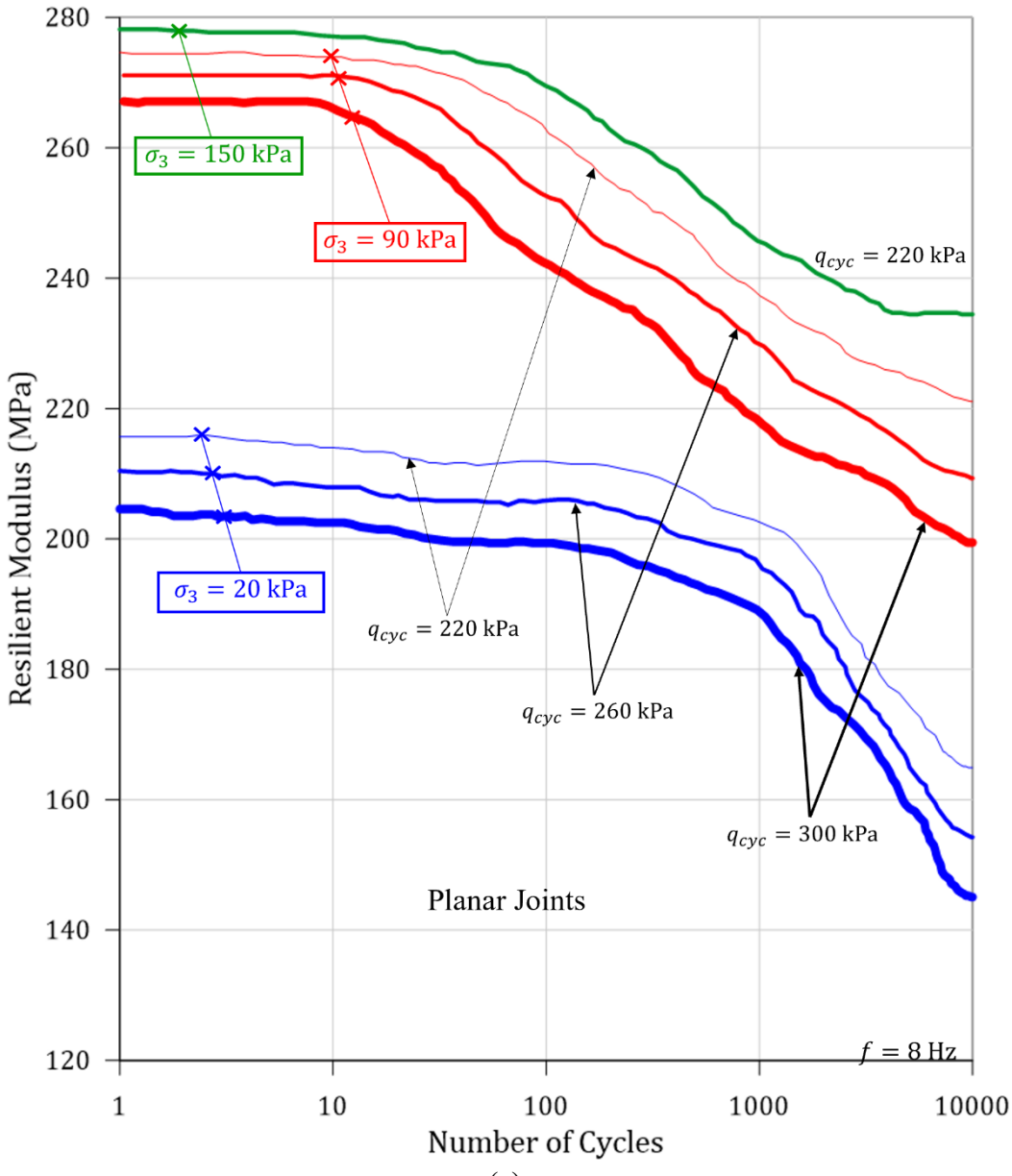

(a)

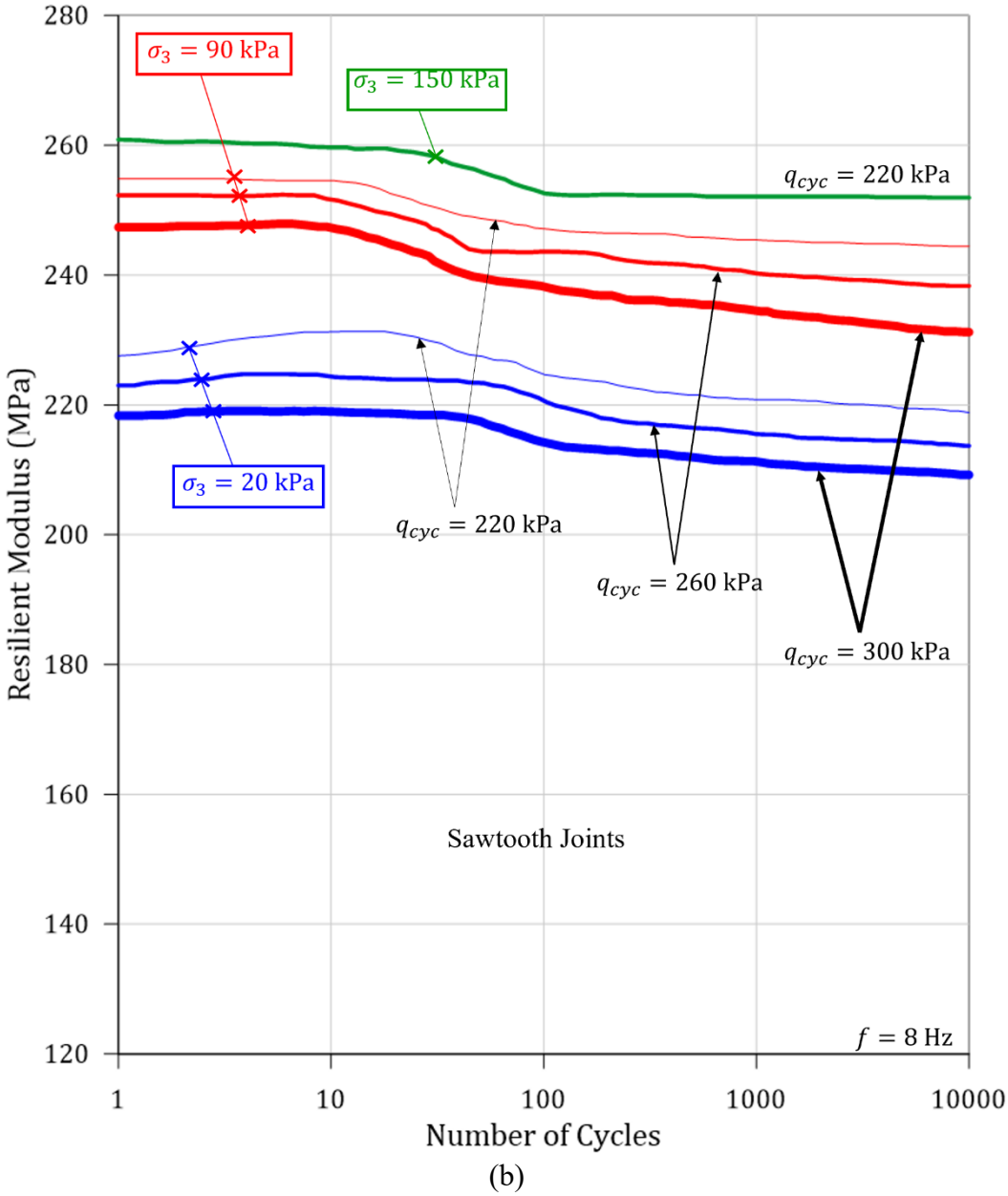
280
260
240
220
200
180
160
140
120
Resilient Modulus (MPa)
σ_3 = 90 kPa
σ_3 = 150 kPa
σ_3 = 20 kPa
q_{cyc} = 220 kPa
q_{cyc} = 220 kPa
q_{cyc} = 260 kPa
q_{cyc} = 300 kPa
Sawtooth Joints
f = 8 Hz
1
10
100
1000
10000
Number of Cycles

(b)

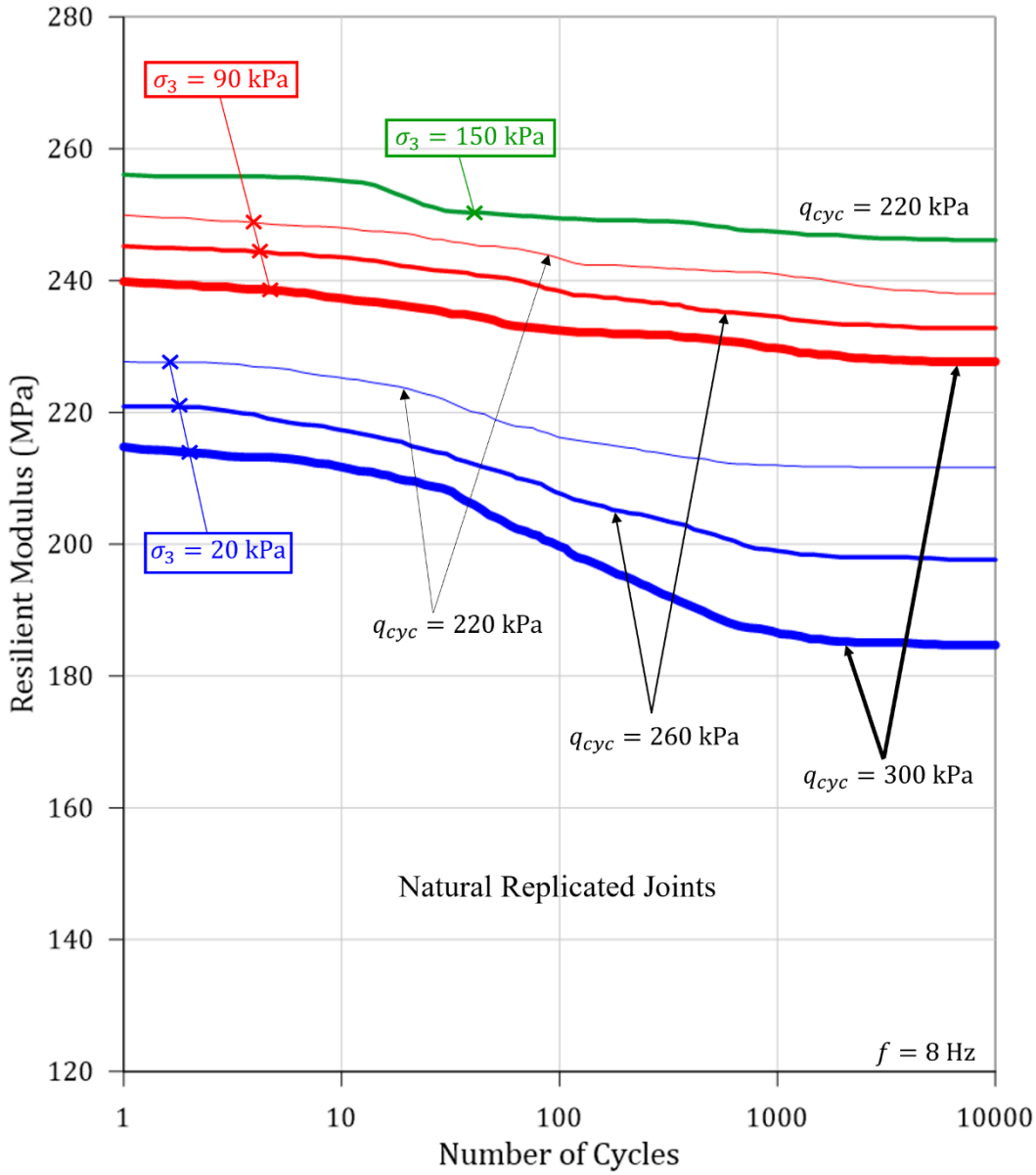

(c)

Figure 3.8. The resilient modulus vs number of cycles curves under different confining pressures (σ_3) of 20 kPa, 90 kPa and 150 kPa and cyclic deviatoric stress amplitudes (q_{cyc}) of 220 kPa, 260 kPa and 300 kPa for (a) Planar Joints, (b) Sawtooth Joints and (c) Natural Replicated Joints.

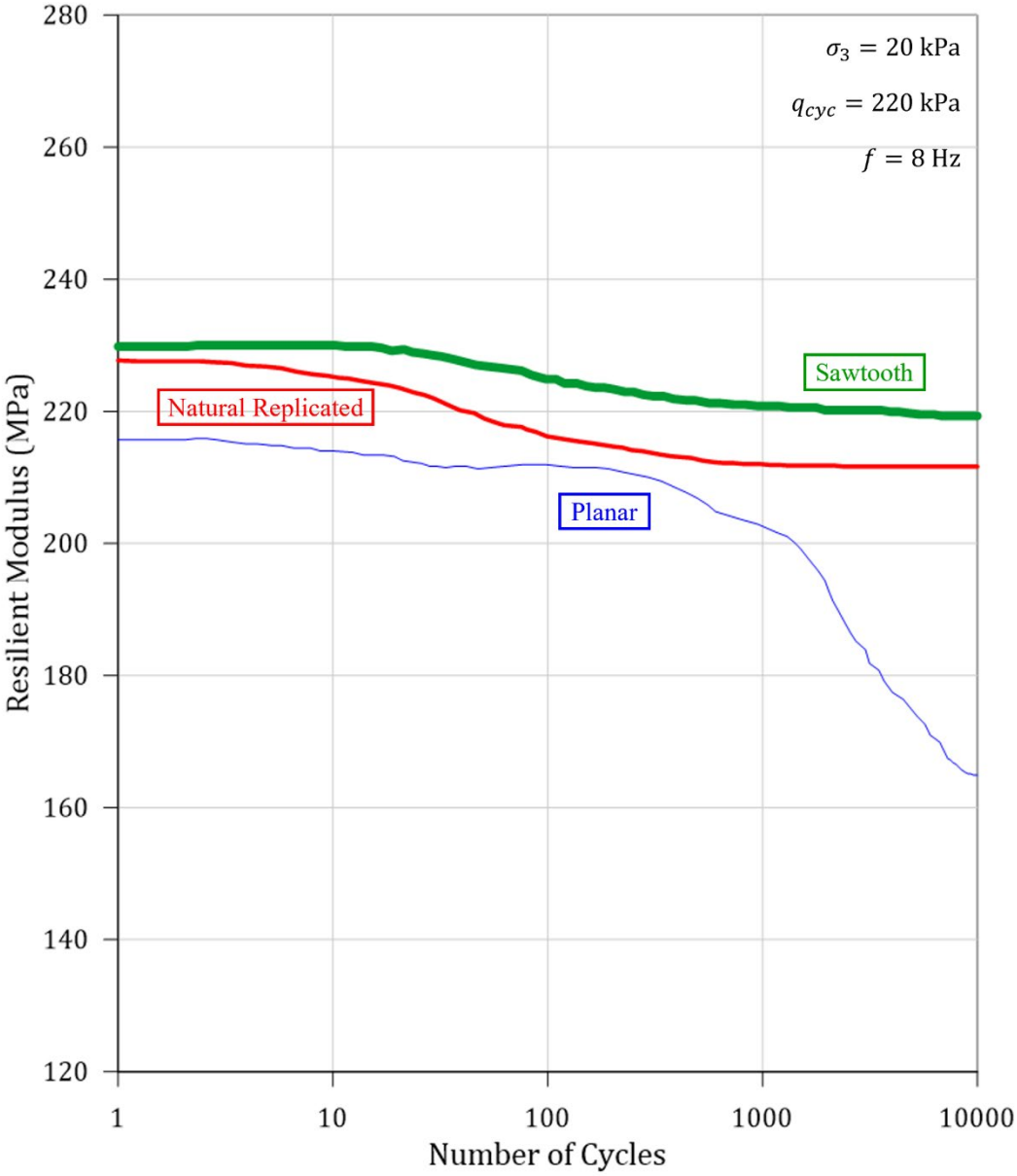
σ_3 = 20 kPa
q_{cyc} = 220 kPa
f = 8 Hz
Sawtooth
Natural Replicated
Planar
Resilient Modulus (MPa)
280
260
240
220
200
180
160
140
120
1
10
100
1000
10000
Number of Cycles

(a)

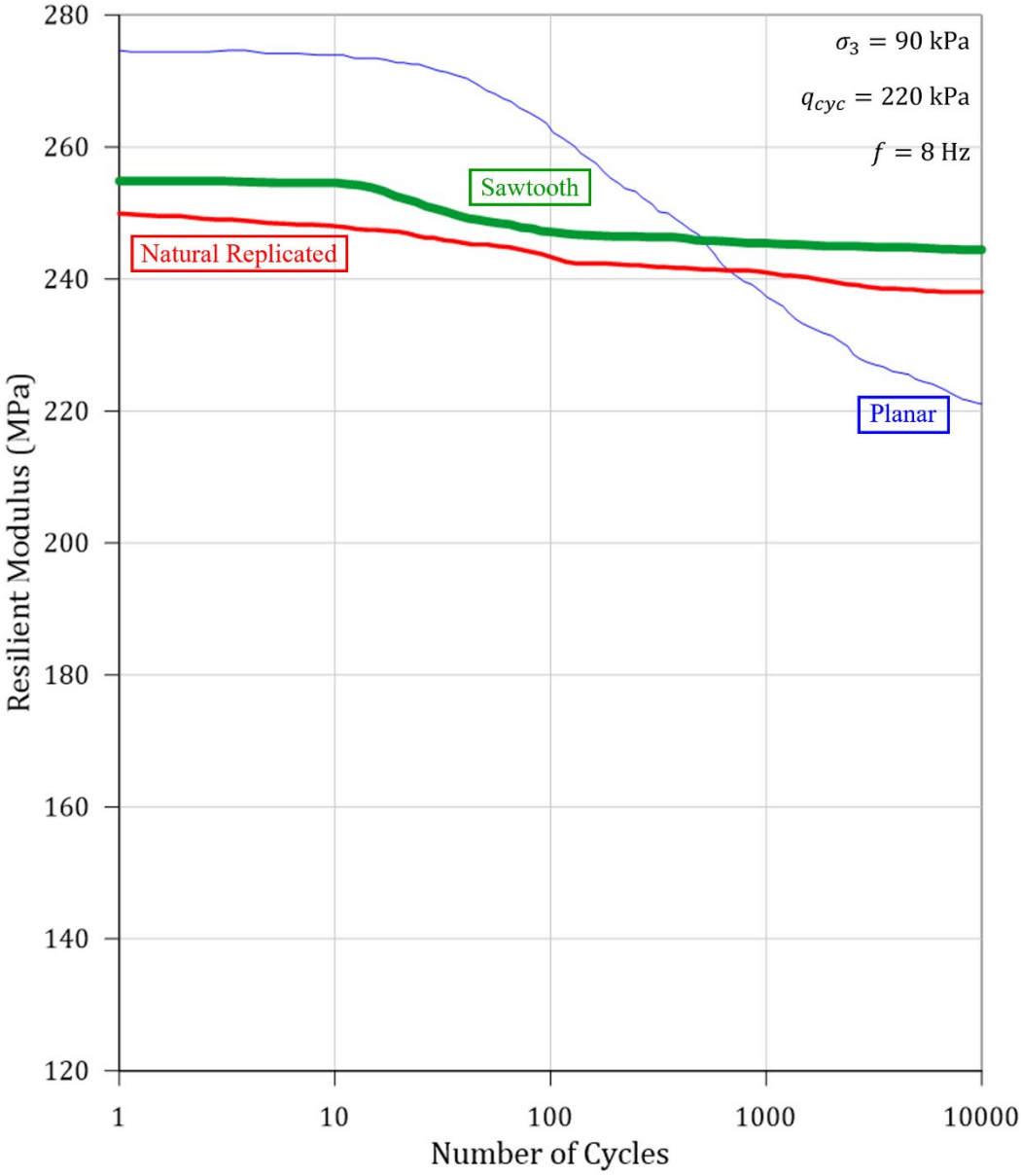

(b)

Figure 3.9. The resilient modulus vs number of cycles curves by changing the joint type for confining pressures (σ_3) of 20 kPa and 90 kPa and cyclic deviatoric stress amplitude (q_{cyc}) of 220 kPa: (a) σ_3 = 20 kPa and q_{cyc} = 220 kPa and (b) σ_3 = 90 kPa and q_{cyc} = 220 kPa.

Accordingly, the resilient moduli of all three joint types exhibited two phases of evolution similar to the development of residual axial deformation, (i) the initial phase, where resilient moduli degrade rapidly, and (ii) the steady phase, where after some loading cycles, the resilient moduli degradation tended to stabilise for the rest of the loading cycles. In other words, joint elasticity reduced rapidly during the initial loading cycles

(i.e., initial phase) and became rather constant during the steady phase, comparable to observations made by Ma et al. (2013). According to Bagde and Petros (2009) and Ma et al. (2013), the downward trend of the resilient modulus (i.e., stiffness degradation) with increasing loading cycles indicates the progressive development of irreversible deformation of the rock joints exposed to repeated loading. This observation is also supported by Wang et al. (2013), who found that there is a direct relationship between the deformation modulus and axial residual strain of rocks exposed to repeated loading.

Accordingly, in planar joints, the observed considerable degradation of resilient moduli with the number of cycles in Figure 3.8a can be attributed to the generation of excessive irreversible deformations smoothening the joint surface and reducing its shear stiffness. Similarly, slight degradation of the resilient moduli of natural replicated and sawtooth joints during the initial loading cycles (Figures 3.8b & c) can be attributed to the changes in the joint stiffness due to slight build-up of residual axial strains during the first few loading cycles. After the initial loading cycles, resilient moduli reaching a steady state (see Figure 3.9) can be due to the cumulative residual axial strains reaching a steady state indicating no more irreversible deformation in the rock joints (see Figure 3.5). Comparable trends for variations of the resilient moduli with the number of cycles were also reported by Zheng et al. (2020a) for artificial jointed rock samples, Liu et al. (2012) for sandstone samples, Wang et al. (2013) for granite specimens, Fuenkajorn and Phueakphum (2010) for Maha Sarakham rock salt samples and Liu et al. (2017) on intermittent rock joints subjected to repeated loading.

Referring to Figures 3.8 and 3.9, the rock joints subjected to repeated loading exhibited greater initial resilient moduli under higher confining stresses for all three joint types. In planar joints, the resilient modulus decreased more rapidly at lower confining stresses. Similarly, referring to Figure 3.8, rock joints subjected to higher cyclic deviatoric stresses

exhibited relatively lower initial resilient moduli. The above-mentioned observation can be affiliated with the higher irreversible deformations generated at lower confining stresses and higher cyclic deviatoric stresses, as evident in Figure 3.5. Indeed, lower resistance to deformation provided by lower confining pressure and higher aid to deformation provided by higher cyclic deviatoric stresses contribute to lower joint stiffness.

According to Figures 3.8 and 3.9, the steady-state resilient moduli attained by samples at the end of cyclic loading experiments (M_{RS}) showed an upward trend with confining stress and a downward trend with cyclic deviatoric stress for the adopted joint types. According to Figure 3.8, M_{RS} showed an upward trend at higher joint roughness. In order to quantify the joint roughness, corresponding joint friction angles were calculated through conventional static triaxial testing, as reported in Figure 3.10. Equation (3.8) presents the proposed empirical relationship for variation of the steady-state resilient modulus (M_{RS}) with confining pressure (σ_3) and cyclic deviatoric stress (q_{cyc}) based on the experimental results reported in Figure 3.8.

$$M_{RS} = M_{RO} \tanh\left[\left(1 + \left(\frac{1}{CSR}\right)^{\alpha}\right) \times \left(\frac{\tan\phi}{N_q}\right)^{\beta}\right] \quad (3.8a)$$

$$N_q = \frac{q_{cyc}}{\tau_s} \quad 3.(8b)$$

$$CSR = \frac{q_{cyc}}{2\sigma_3} \quad (3.8c)$$

where, N_q is the normalised cyclic deviatoric stress amplitude, CSR is the cyclic stress ratio and ϕ is the friction angle of the joint representing the joint roughness. It should be noted that M_{RO} refers to the steady-state resilient modulus at very small cyclic deviatoric stress amplitude (i.e., $q_n \rightarrow 0$), while α and β are empirical constants obtained based on data fitting exercise, which depends on the joint characteristics such as joint inclination

and JCS. In this study, the values of M_{RO}, α and β obtained through nonlinear regression analysis were 245.56 MPa, 1.37 and 0.14, respectively. A MATLAB code was developed to extract data, and the custom equation fit with nonlinear combinations of the variables was utilised to obtain the best-fit surface for the M_{RS}. Custom equation fit uses the nonlinear least squares fitting procedure and provides the option to define the equation with linear and/or nonlinear combinations of the parameters. Figure 3.10 presents the predicted resilient moduli via Equation (3.8) versus the laboratory measurements in the 3D space; it is evident that the proposed empirical equation gives reasonable predictions.

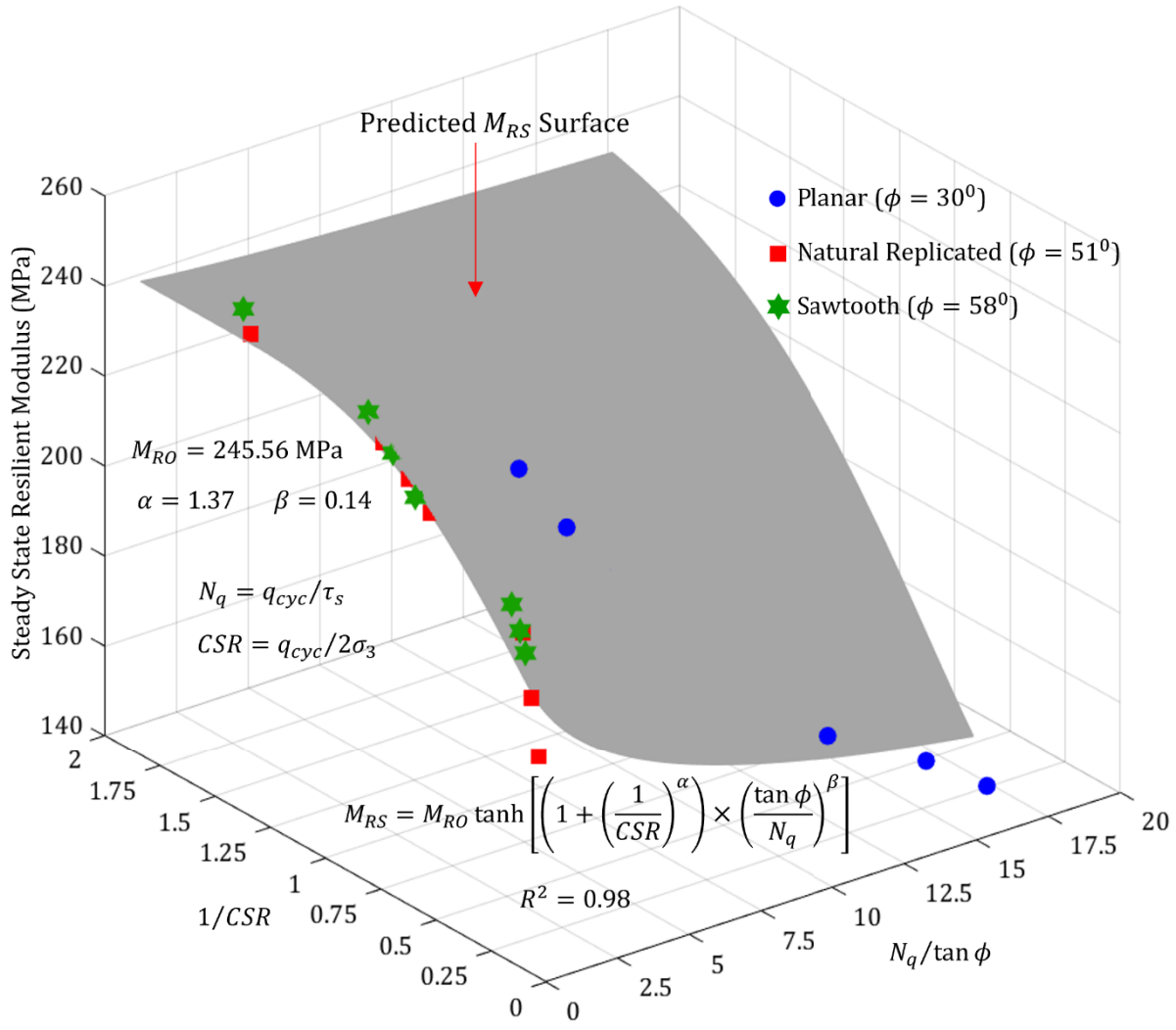

Figure 3.10. Variation of actual and predicted steady-state resilient modulus (M_{RS}) in the 3D space.

3.3.4 Dissipated Energy

The dynamic characteristics of the jointed rock specimen were further analysed using energy dissipation. In the cyclic triaxial experiments, the dissipated energy can be determined from the stress-strain response records of the samples during loading-unloading cycles (i.e., Figures 3.3 and 3.4). Samples of the hysteresis loops formed at different test conditions and different cycle numbers are illustrated in Figure 3.11. In this study, a MATLAB code was developed to calculate the area within the hysteresis loop from the data collected to quantify the energy dissipated during loading and unloading cycles. Figure 3.12 shows the variation of energy dissipated per load cycle with the

number of cycles for various confining stresses and cyclic deviatoric stress amplitudes for the three types of joint surfaces adopted.

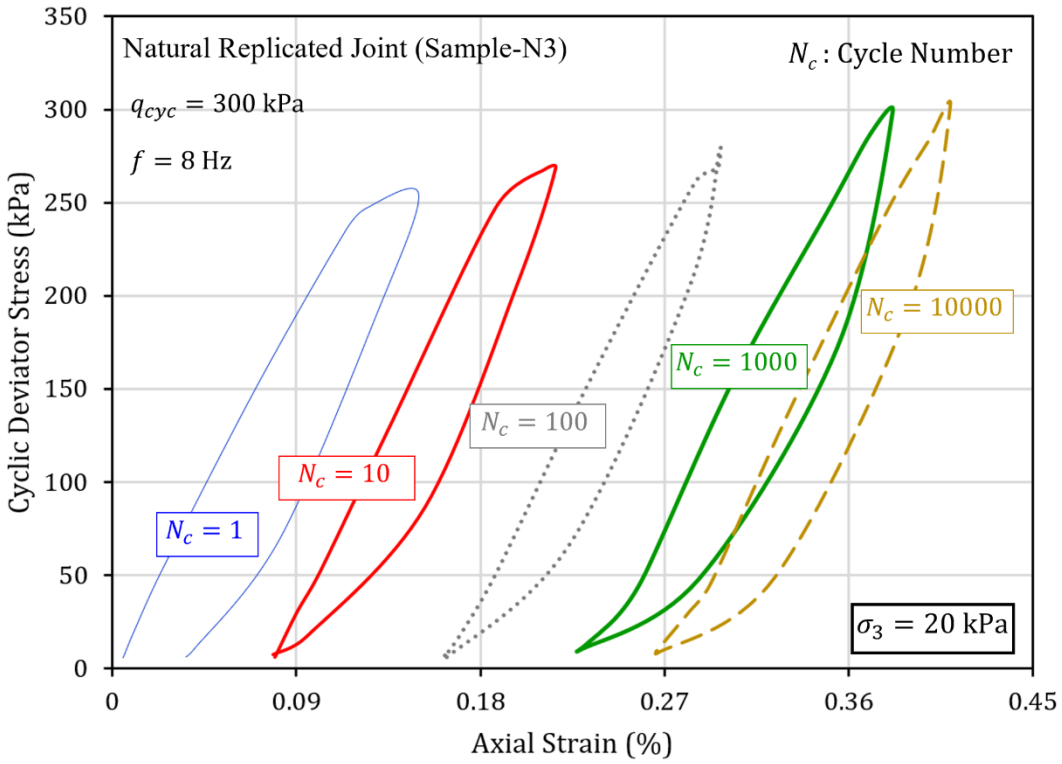

(a)

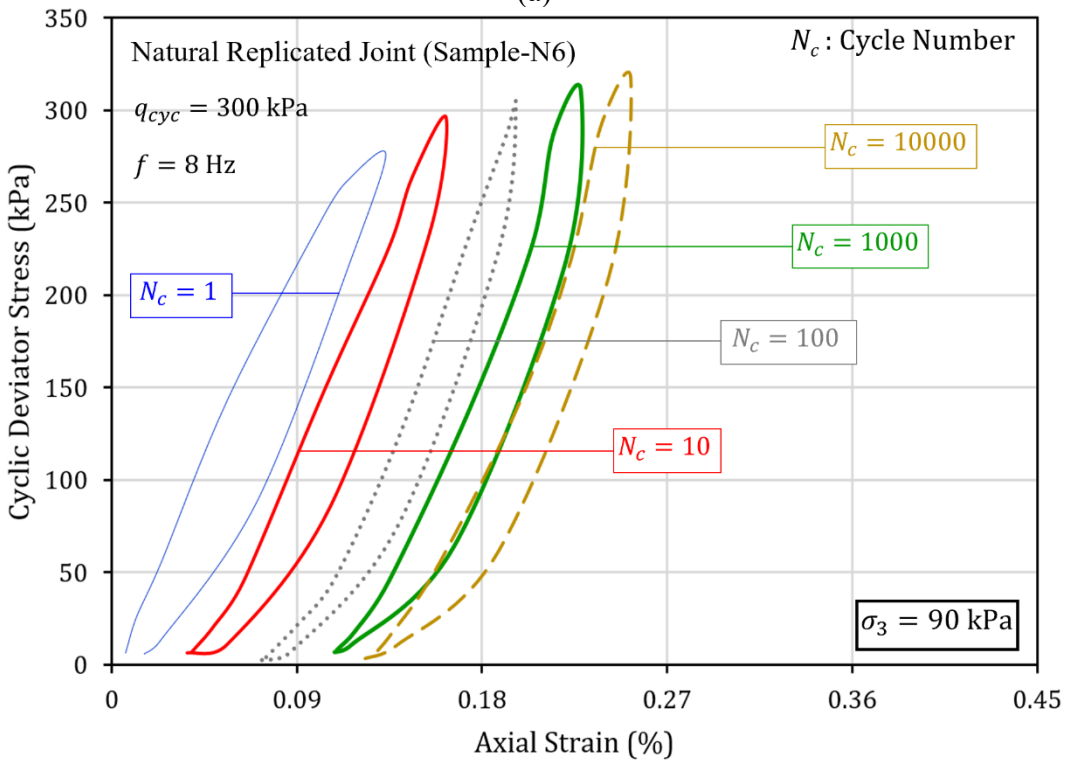

(b)

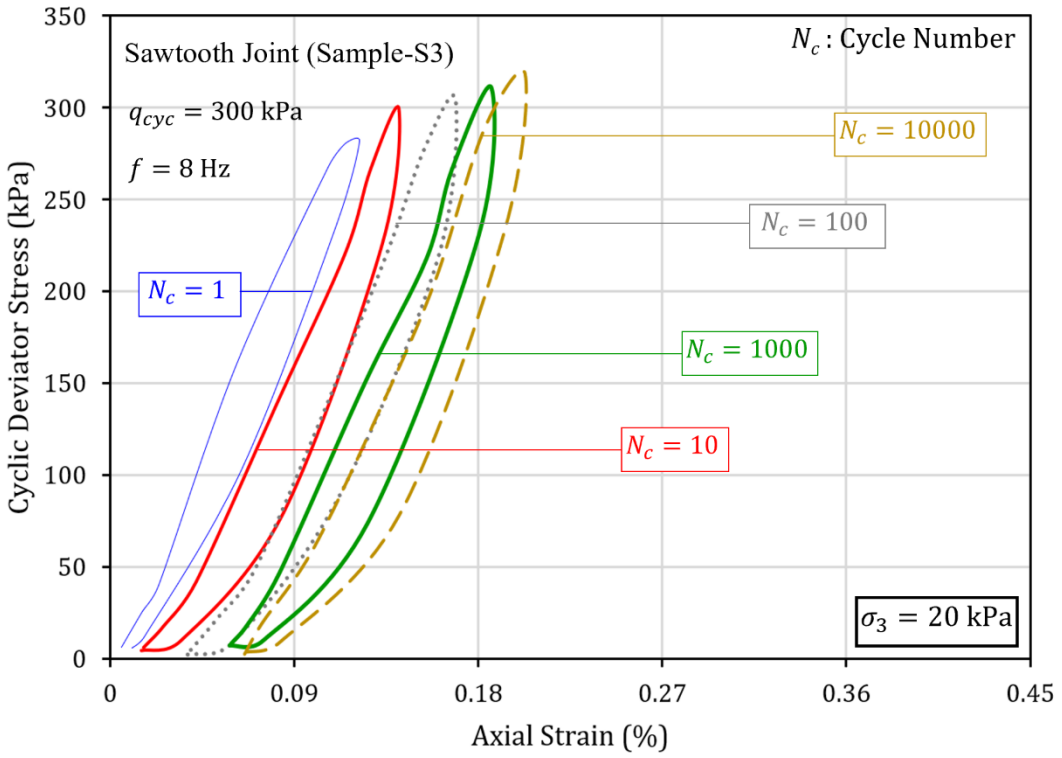

(c)

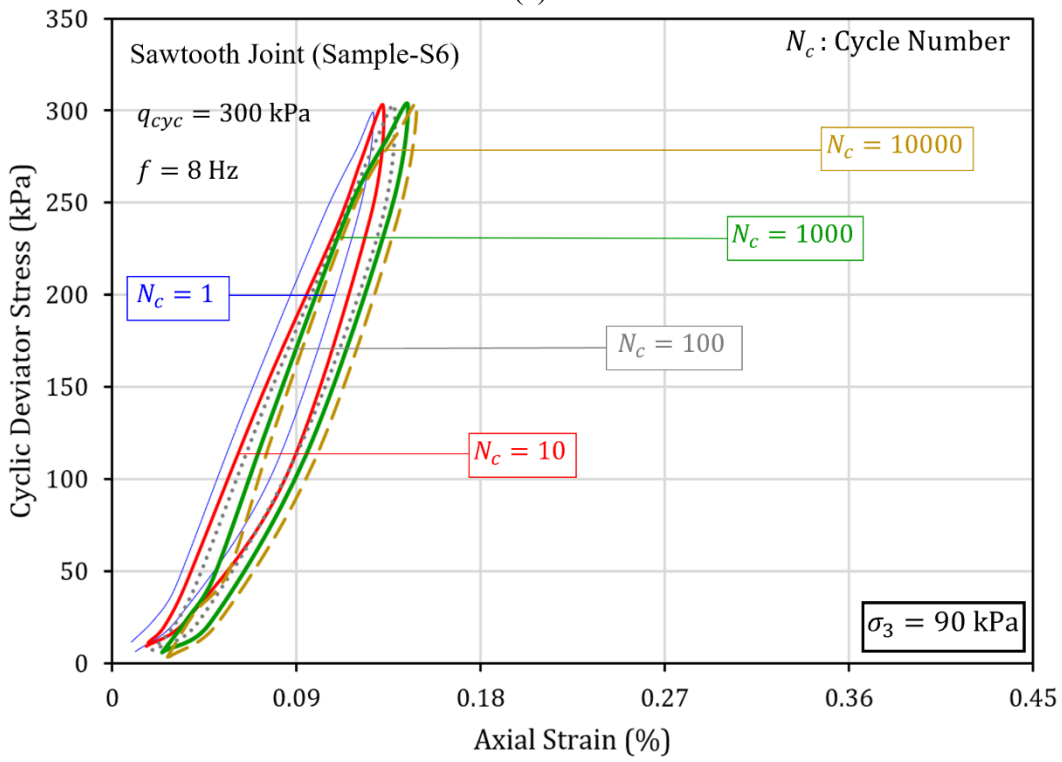

(d)

Figure 3.11. Stress-Strain hysteresis loops at various cycle numbers at confining pressures (σ_3) of 20 kPa and 90 kPa and cyclic deviatoric stress amplitude (q_{cyc}) of 300 kPa: for (a) Natural replicated joints (σ_3=20 kPa), (b) Natural replicated joints (σ_3=90 kPa), (c) Sawtooth joints (σ_3=20 kPa) and Sawtooth joints (σ_3=90 kPa).

As evident in Figure 3.12, when the number of cycles increased, the dissipated energy per load cycle promptly decreased and then slightly recovered and gradually stabilised for all three types of joint surfaces used for testing. In the case of natural replicated and sawtooth joint types, referring to Figures 3.12a & b, dissipated energy stabilised within a few cycles and remained almost constant during the rest of the loading cycles, especially at higher confining stresses (i.e., 90 kPa and 150 kPa). According to Yang et al. (2016), developing irreversible strains during the first few cycles was a consequence of the jointed rock samples producing substantial dissipated hysteresis energy. As the irreversible strains gradually stabilised, the dissipated hysteresis energy promptly decreased, followed by a slight rise during the subsequent cycles and then stabilised for the rest of the loading cycles. Similar trends were also observed by Momeni et al. (2015) for granite specimens, Liu et al. (2017 & 2018b) for intermittent jointed rock samples, Yang et al. (2018b) for limestone samples, and Zheng et al. (2020a) for artificial jointed rock samples subjected to repeated loading.

Furthermore, as demonstrated in Figure 3.12, higher confining stress led to reduced dissipated energy, whereas higher cyclic deviatoric stress contributed to increased dissipated energy. Referring to Yang et al. (2016), these results demonstrate that at lower confining stresses, lower resistance to deformation is provided, and as a result, a larger portion of absorbed energy induced by the external load is dissipated by the jointed rock sample to generate higher irreversible deformation of the joint during loading. Similarly, at higher cyclic deviatoric stresses, a larger portion of the energy is absorbed by the jointed rock sample that will dissipate during unloading, developing higher irreversible deformation. It should also be noted that according to Figure 3.12, the energy dissipated in rock joints with planar joint surfaces was rather higher than that in the specimens with sawtooth and natural replicated joint surfaces. This can be attributed to a larger portion

of absorbed energy being dissipated by planar joints to generate higher irreversible deformations due to the smoothness of the joint surface. However, a lower portion of absorbed energy was dissipated by sawtooth and natural replicated joint types, generating less irreversible deformations due to resistance to deformation provided by the roughness of the joint surface. These observations demonstrate that the energy evolution of the loaded jointed rock subgrades is heavily affected by diverse field conditions such as depths from the rail track, train loads, and the number of train passes along with the surface geometry of the joints.

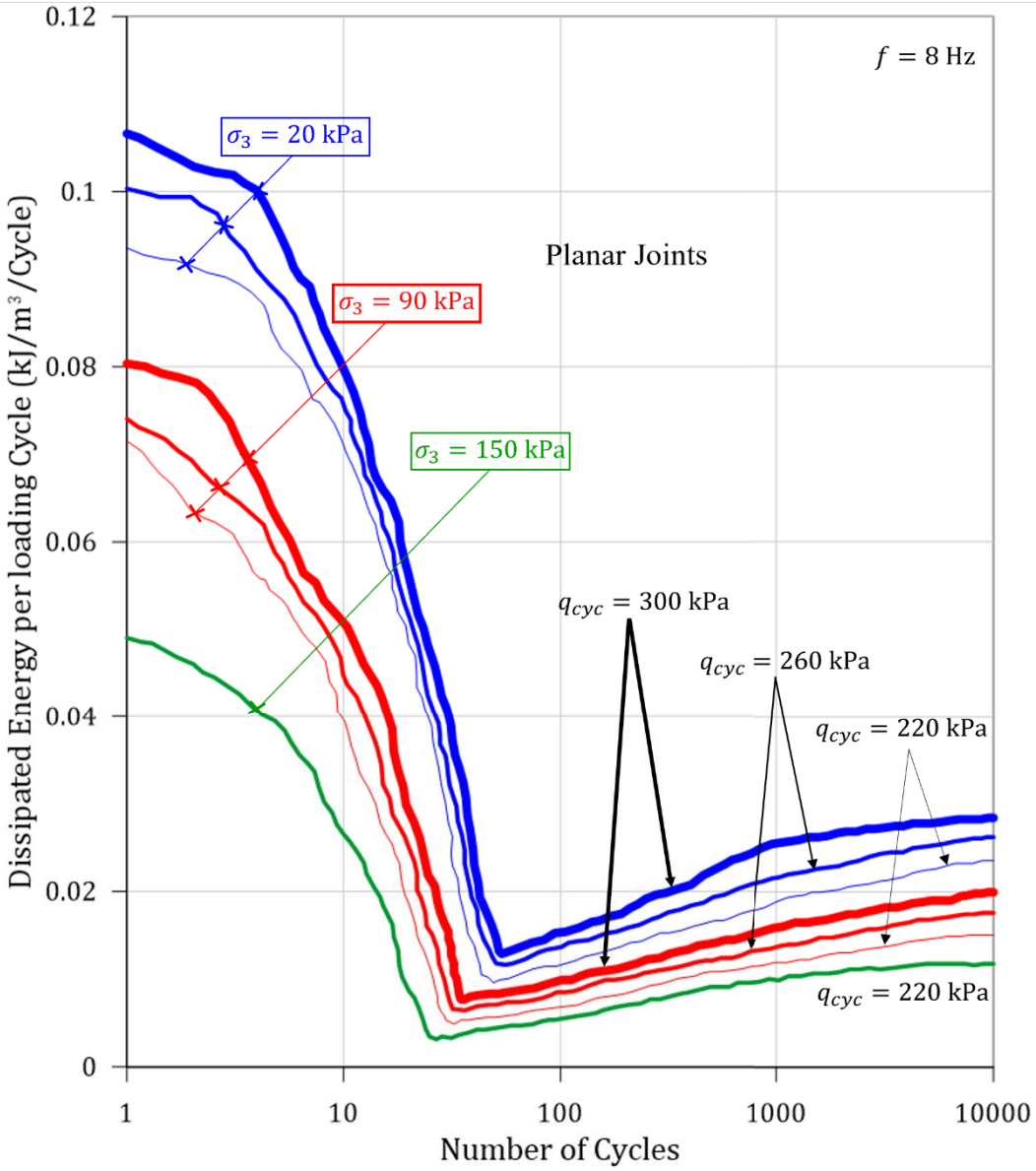
f = 8 Hz
σ_3 = 20 kPa
σ_3 = 90 kPa
σ_3 = 150 kPa
Planar Joints
q_{cyc} = 300 kPa
q_{cyc} = 260 kPa
q_{cyc} = 220 kPa
q_{cyc} = 220 kPa
Dissipated Energy per loading Cycle (kJ/m³/Cycle)
Number of Cycles
0.12
0.1
0.08
0.06
0.04
0.02
0
1
10
100
1000
10000

(a)

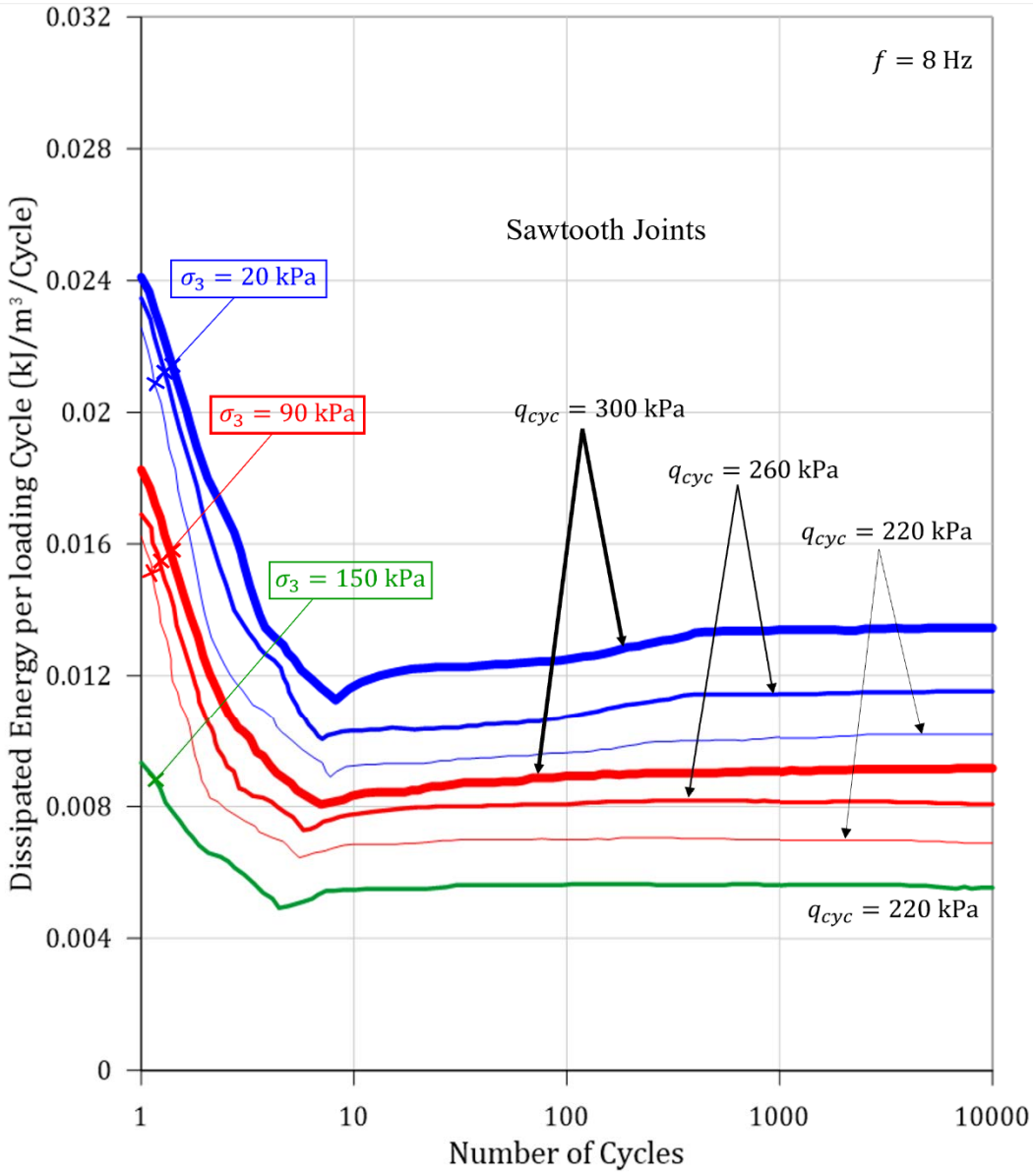
f = 8 Hz
Sawtooth Joints
σ_3 = 20 kPa
σ_3 = 90 kPa
σ_3 = 150 kPa
q_{cyc} = 300 kPa
q_{cyc} = 260 kPa
q_{cyc} = 220 kPa
q_{cyc} = 220 kPa
Dissipated Energy per loading Cycle (kJ/m^3/Cycle)
Number of Cycles
0.032
0.028
0.024
0.02
0.016
0.012
0.008
0.004
0
1
10
100
1000
10000

(b)

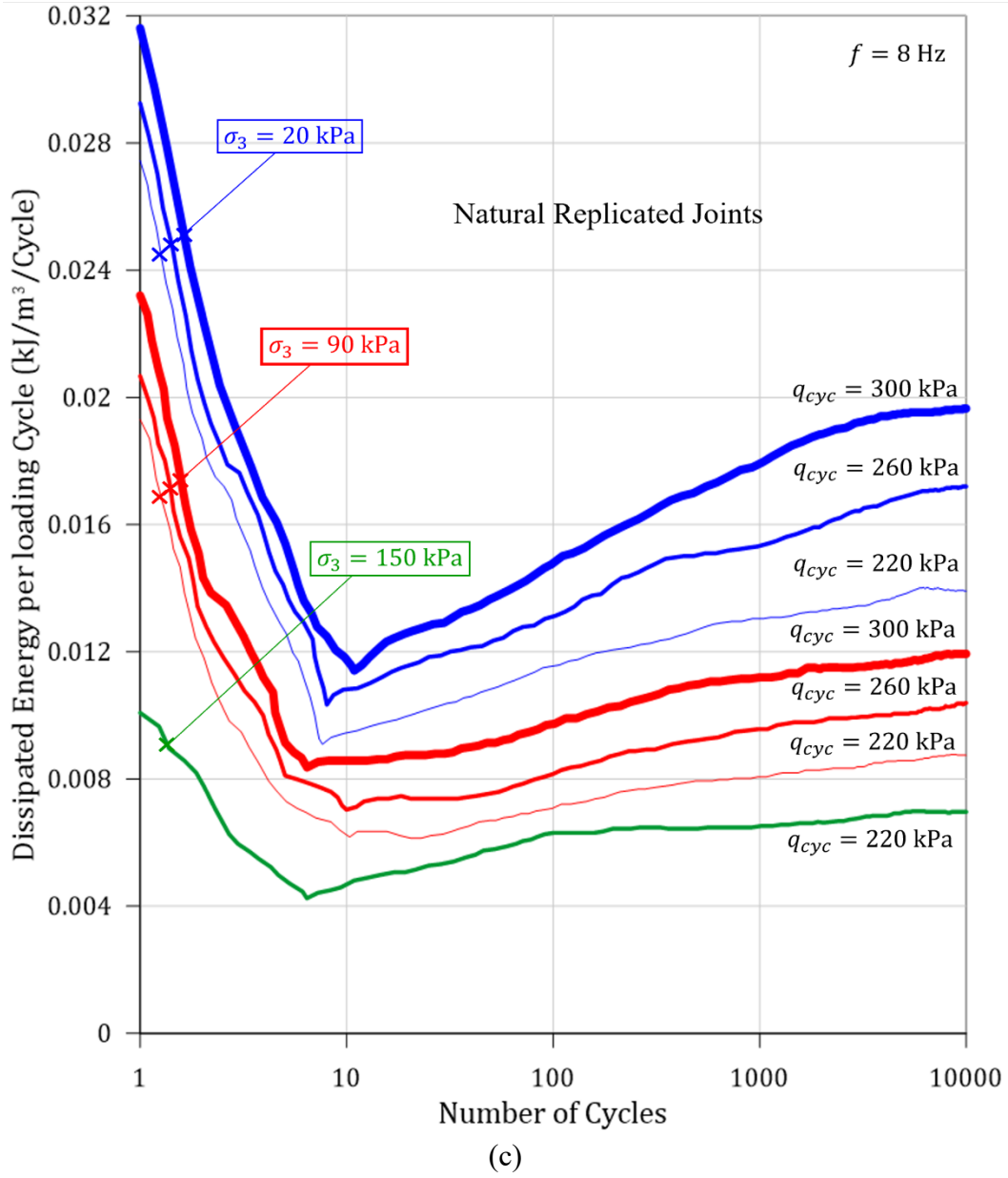

(c)

Figure 3.12. The dissipated energy per load cycle vs number of cycles curves under confining pressures (σ_3) of 20 kPa, 90 kPa and 150 kPa and cyclic deviatoric stress amplitudes (q_{cyc}) of 220 kPa, 260 kPa and 300 kPa for: (a) Planar joints, (b) Sawtooth joints and (c) Natural replicated joints.

3.3.5 Damping Ratio

Damping is one of the important dynamic characteristics of rock masses, which is an inherent property of the rock material, corresponding to the extent of energy dissipation in rock elements. The damping ratio is one of the most commonly used measures of energy dissipation. Referring to ASTM D3999-91 (2003), for sinusoidal waveform loading, the damping ratio (ξ) of jointed rock within a single load cycle was calculated from the hysteresis loop using Equation 2.2.

Figures 3.13 and 3.14 show how the damping ratio per cycle evolved with increasing load cycles at various confining stresses and cyclic deviatoric stresses for the three joint types utilised. As shown in Figures 3.13 and 3.14, all three joint types showed similar responses where the damping ratio decreased promptly during the initial loading cycles and then slightly increased, followed by a gradual stabilisation during the subsequent loading cycles, as also observed in dissipated energy curves in Figure 3.12. According to Liu et al. (2017) and Wang et al. (2021), due to the generation of irreversible strains during the first few cycles, a higher level of energy is dissipated along with lower levels of elastic energy being stored, which cause higher damping ratios observed during the first few cycles. With irreversible strains being stabilised after a few cycles, the dissipated energy decreased and stabilised while stored elastic energy increased and stabilised for the rest of the loading cycles resulting in stabilisation of the damping ratio values.

Furthermore, when the confining stresses were higher, the initial damping ratios were lower, whereas when the cyclic deviatoric stresses were higher, the initial damping ratios were also higher (see Figure 3.13). This observation can be related to lower irreversible strains developed at higher confining stresses (due to higher resistance to deformation provided by higher confining pressures), resulting in lower dissipated energy, higher

elastic energy stored and lower damping ratios. Similarly, at higher cyclic deviatoric stresses, generated irreversible strains were higher (due to higher aid provided for deformation by higher cyclic stresses) (see Figure 3.5), which resulted in higher dissipated energy, lower elastic energy and higher damping ratios, as also explained in the previous section. It should be noted that the damping ratios of planar joints were relatively higher than that of sawtooth and natural replicated joints (see Figures 3.13 and 3.14). This observation can be attributed to the development of elevated levels of irreversible strains in planar joints due to the smoothness of the joint surface, resulting in higher dissipated energy and damping ratios. In the case of natural replicated and sawtooth joints, the generation of higher levels of irreversible strains was interrupted by the joint surface roughness under the applied loads, and it resulted in lower levels of dissipated energy and damping ratios.

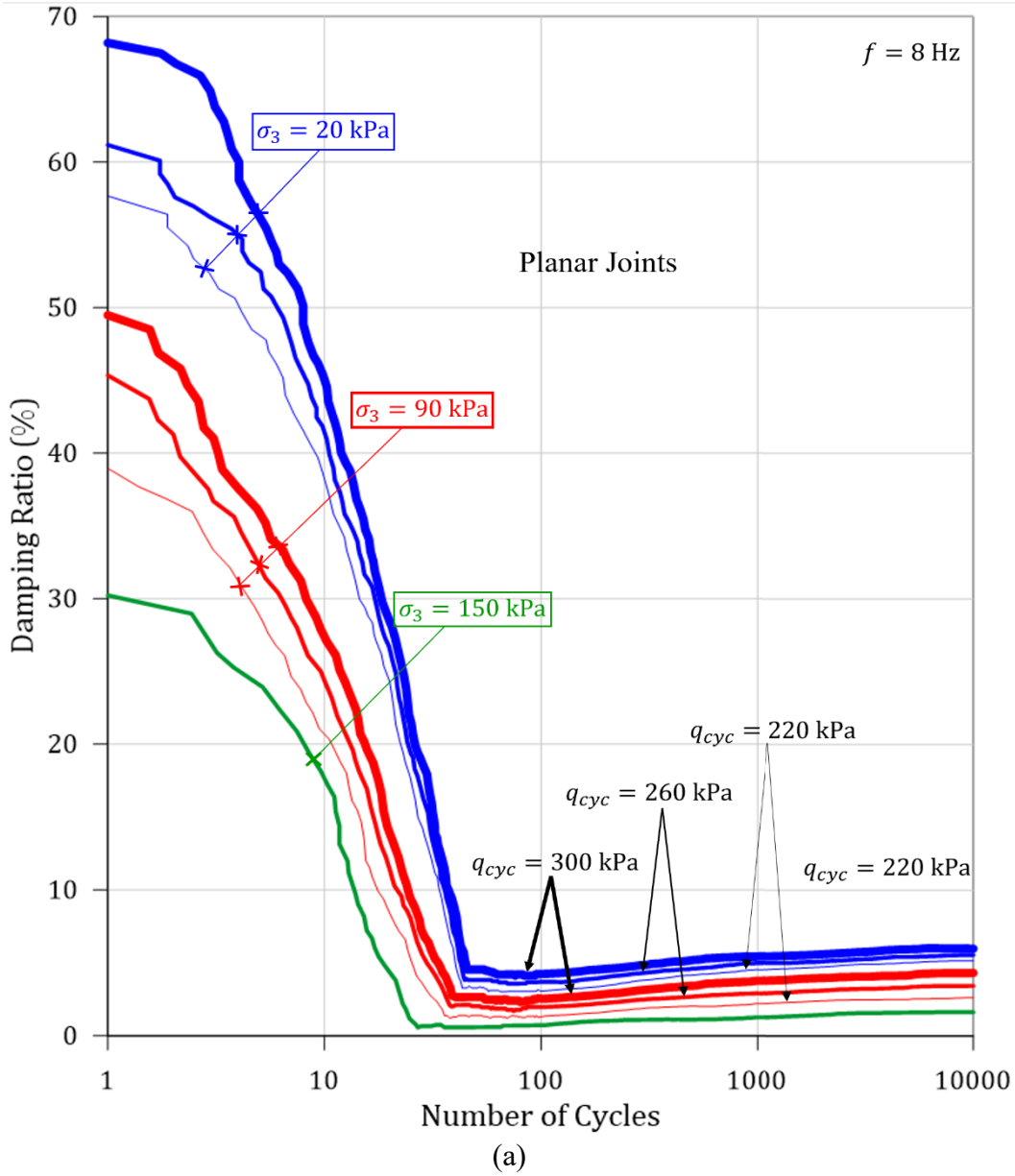
f = 8 Hz
σ_3 = 20 kPa
Planar Joints
σ_3 = 90 kPa
σ_3 = 150 kPa
q_{cyc} = 220 kPa
q_{cyc} = 260 kPa
q_{cyc} = 300 kPa
q_{cyc} = 220 kPa
Damping Ratio (%)
Number of Cycles
70
60
50
40
30
20
10
0
1
10
100
1000
10000
(a)

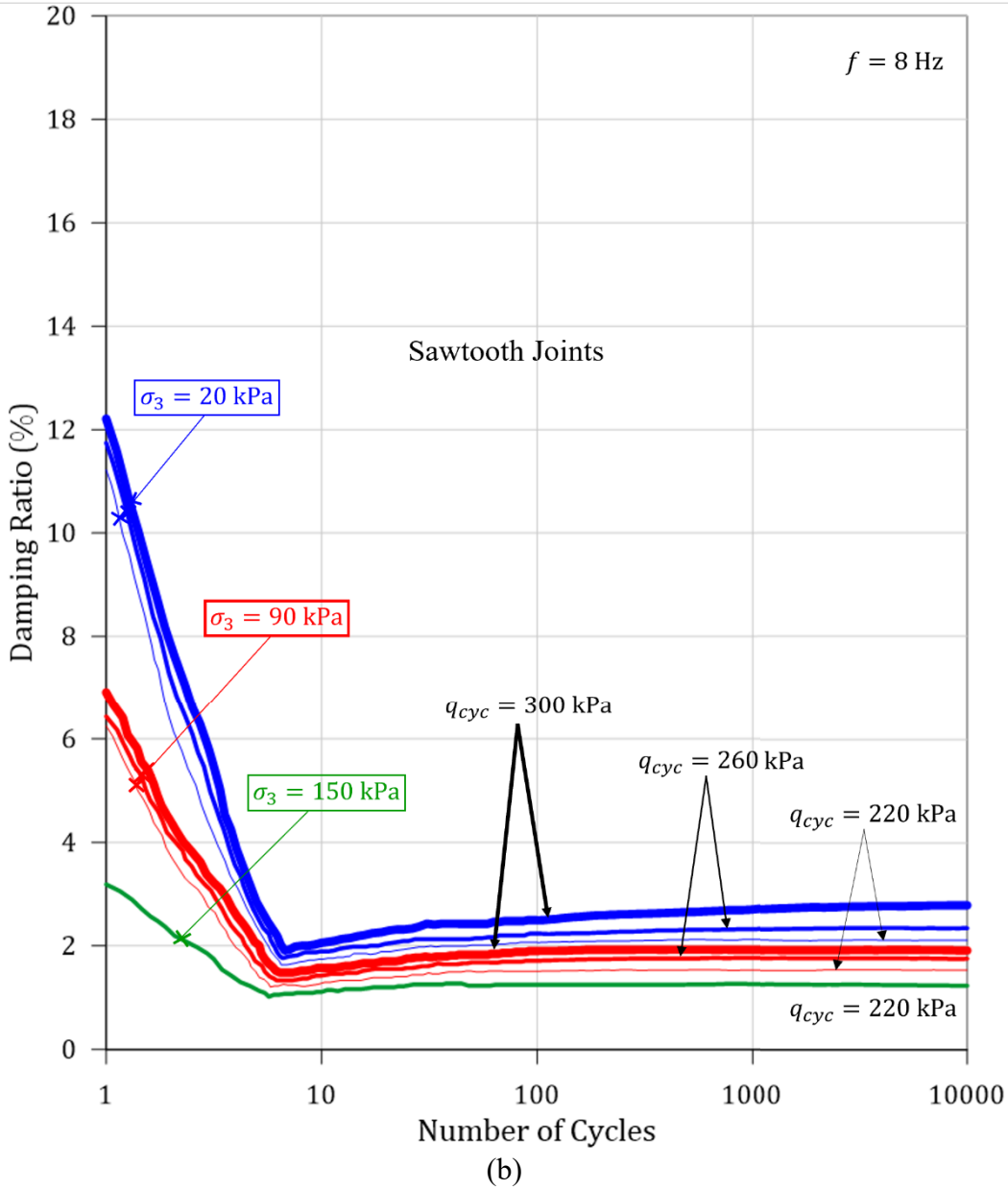
f = 8 Hz
Sawtooth Joints
σ_3 = 20 kPa
σ_3 = 90 kPa
σ_3 = 150 kPa
q_{cyc} = 300 kPa
q_{cyc} = 260 kPa
q_{cyc} = 220 kPa
q_{cyc} = 220 kPa
Damping Ratio (%)
Number of Cycles
0
2
4
6
8
10
12
14
16
18
20
1
10
100
1000
10000

(b)

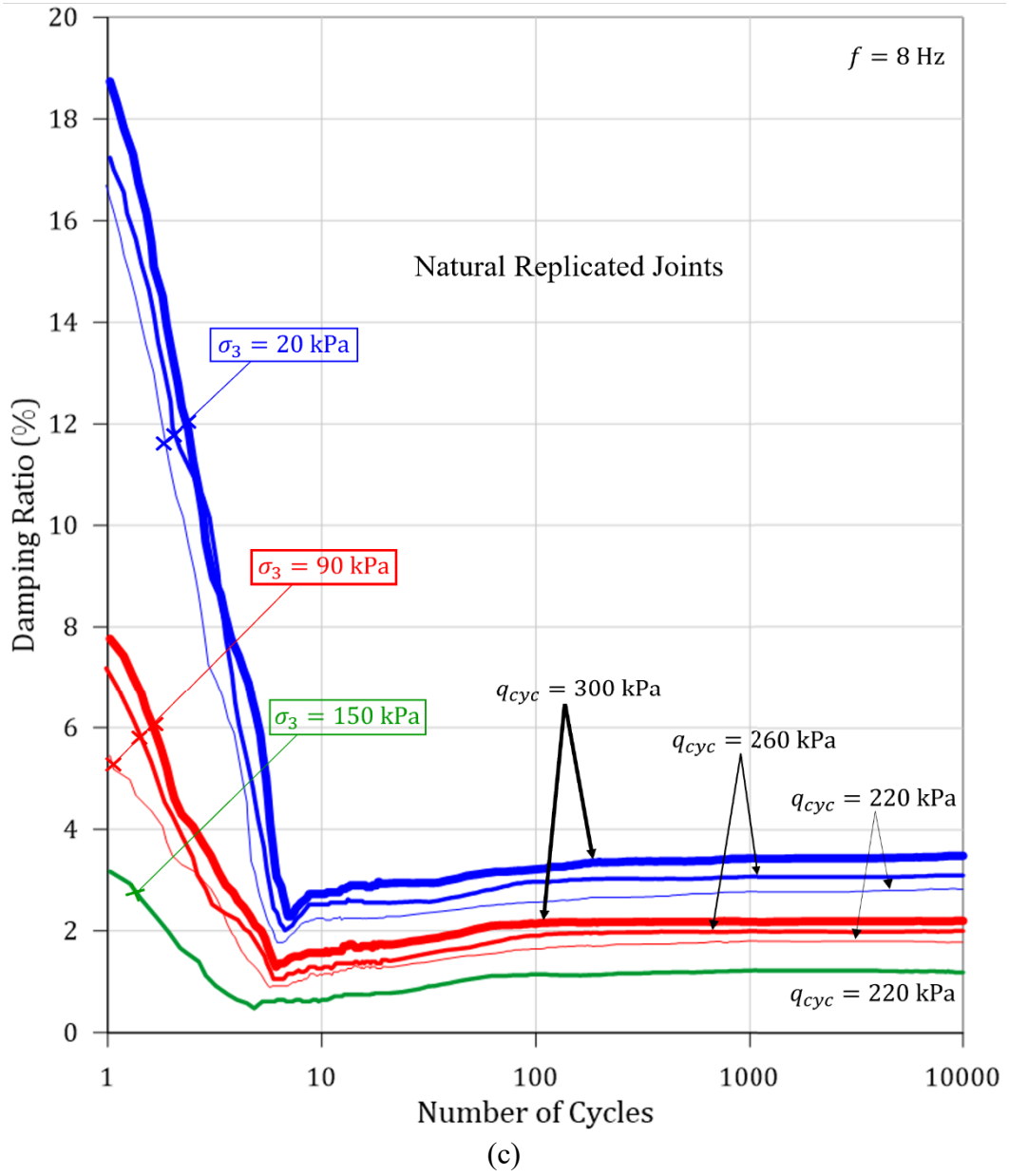

Figure 3.13. The damping ratio per load cycle vs number of cycles curves under confining pressures (σ_3) of 20 kPa, 90 kPa and 150 kPa and cyclic deviatoric stress amplitudes (q_{cyc}) of 220 kPa, 260 kPa and 300 kPa for: (a) Planar joints, (b) Sawtooth joints and (c) Natural replicated joints.

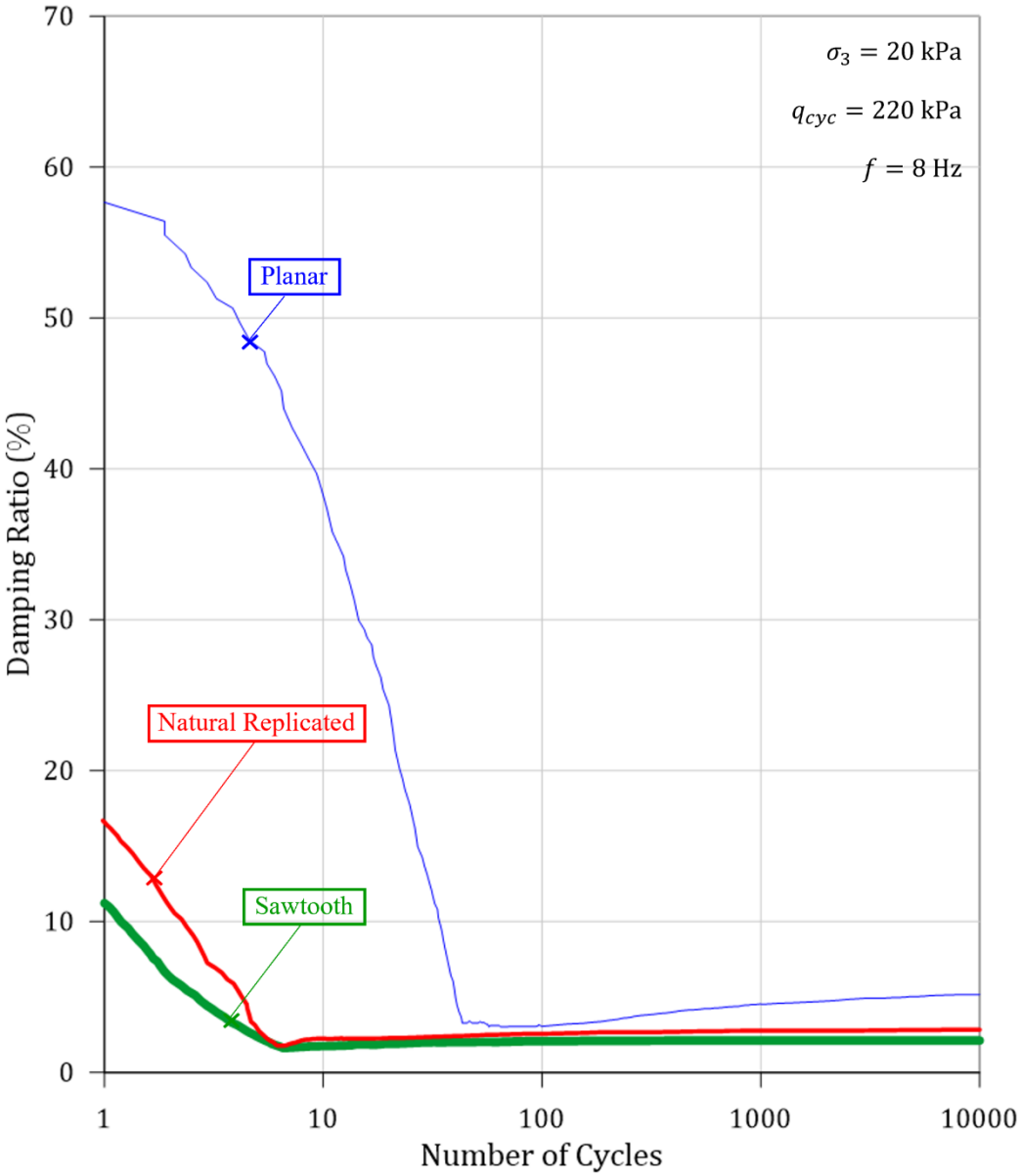
σ_3 = 20 kPa
q_{cyc} = 220 kPa
f = 8 Hz
Planar
Natural Replicated
Sawtooth
Damping Ratio (%)
Number of Cycles
0
10
20
30
40
50
60
70
1
10
100
1000
10000

(a)

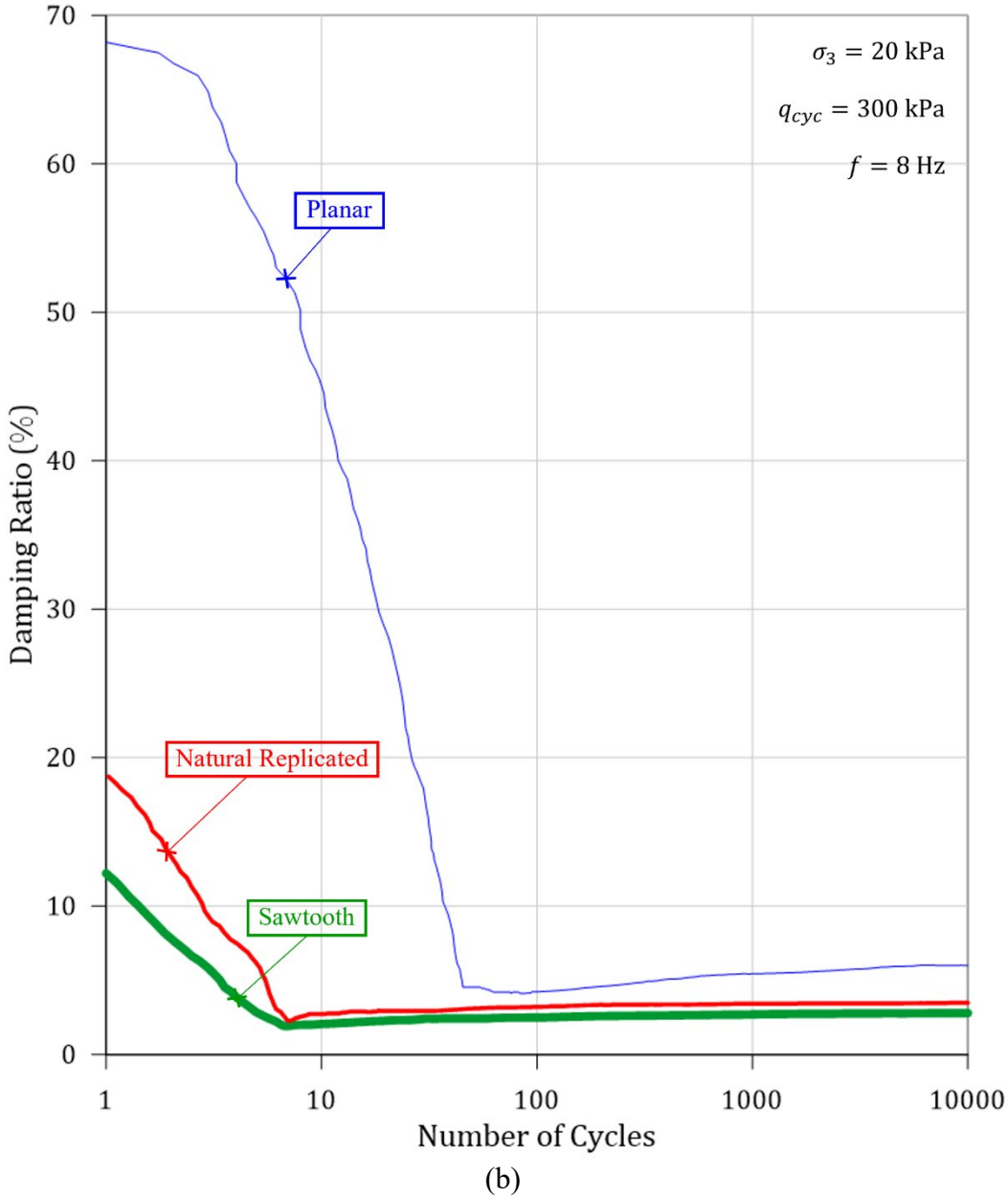

Figure 3.14. The damping ratio per load cycle vs number of cycles curves by changing the joint type at confining pressure (σ_3) of 20 kPa and cyclic deviatoric stress amplitude (q_{cyc}) of 220 kPa and 300 kPa: (a) σ_3 = 20 kPa and q_{cyc} = 220 kPa and (b) σ_3 = 20 kPa and q_{cyc} = 300 kPa.

Furthermore, under all the tested conditions, the damping ratios tended to stabilise after some initial loading cycles and remained rather constant until the end of cyclic loading. Referring to Figure 3.13, the steady-state damping ratio (ξ_S) showed an upward trend with cyclic deviatoric stress amplitude and a downward trend with the confining stress for the joint types tested. According to Figures 3.13 and 3.14, the steady-state damping ratio

showed a downward trend with the increasing roughness of the joint surface. The joint roughness was quantified through the joint friction angle determined from conventional static triaxial testing (undrained condition) of the jointed rock samples, as in Figure 3.15. An empirical relationship correlating the steady-state damping ratio (ξ_S) to confining stress (σ_3) and cyclic deviatoric stress amplitude (q_{cyc}) is developed based on the experimental results reported in Figure 3.13 below:

$$\xi_S = \xi_O \tanh\left[\frac{\left(\frac{N_q}{\tan\phi}\right)^{\kappa}}{1+\left(\frac{1}{CSR}\right)^{\eta}}\right] \tag{3.9}$$

where, CSR and N_q are as defined in Equations (3.8b) and (3.8c), ϕ is the joint friction angle representing joint roughness. ξ_O captures the steady-state damping ratio when cyclic deviatoric stress amplitude is very large (i.e., $q_n \rightarrow \infty$). κ and η are empirical constants depending on the joint properties such as joint inclination and JCS. The values of ξ_O, κ and η obtained through regression analysis were 5.18 %, 0.27 and 0.92, respectively. Figure 3.15 presents the comparison between the predictions adopting the empirical model for damping ratio in Equation (3.9) and laboratory measurements in the 3D space, and they are in reasonable agreement.

The results shown in Figures 3.13 – 3.15 suggest that utilising a single constant damping value to represent the damping response of the jointed rock mass in vibration analyses is not accurate since the damping of jointed rocks varies significantly with confining stress and cyclic stress. Therefore, empirical relations like Equation (3.9) can be used by practising engineers to predict more precise damping responses for a jointed rock foundation under various field conditions when conducting vibration analyses.

Indeed, the results of this experimental research can assist practising engineers in understanding the nonlinearities involved in wave propagation analysis due to vibration

from sources such as railways impacting nearby structures. It should be noted that the prediction of vibration levels accurately during the design phase of infrastructure projects can expedite allocating suitable vibration mitigation processes before complaints are made because of vibration levels exceeding the acceptable thresholds. For example, for railway lines, it would be much more efficient and cost-effective to design and build vibration mitigation elements during the actual construction rather than retrofitting or adding new mitigation strategies post-construction while the railway line would be in service.

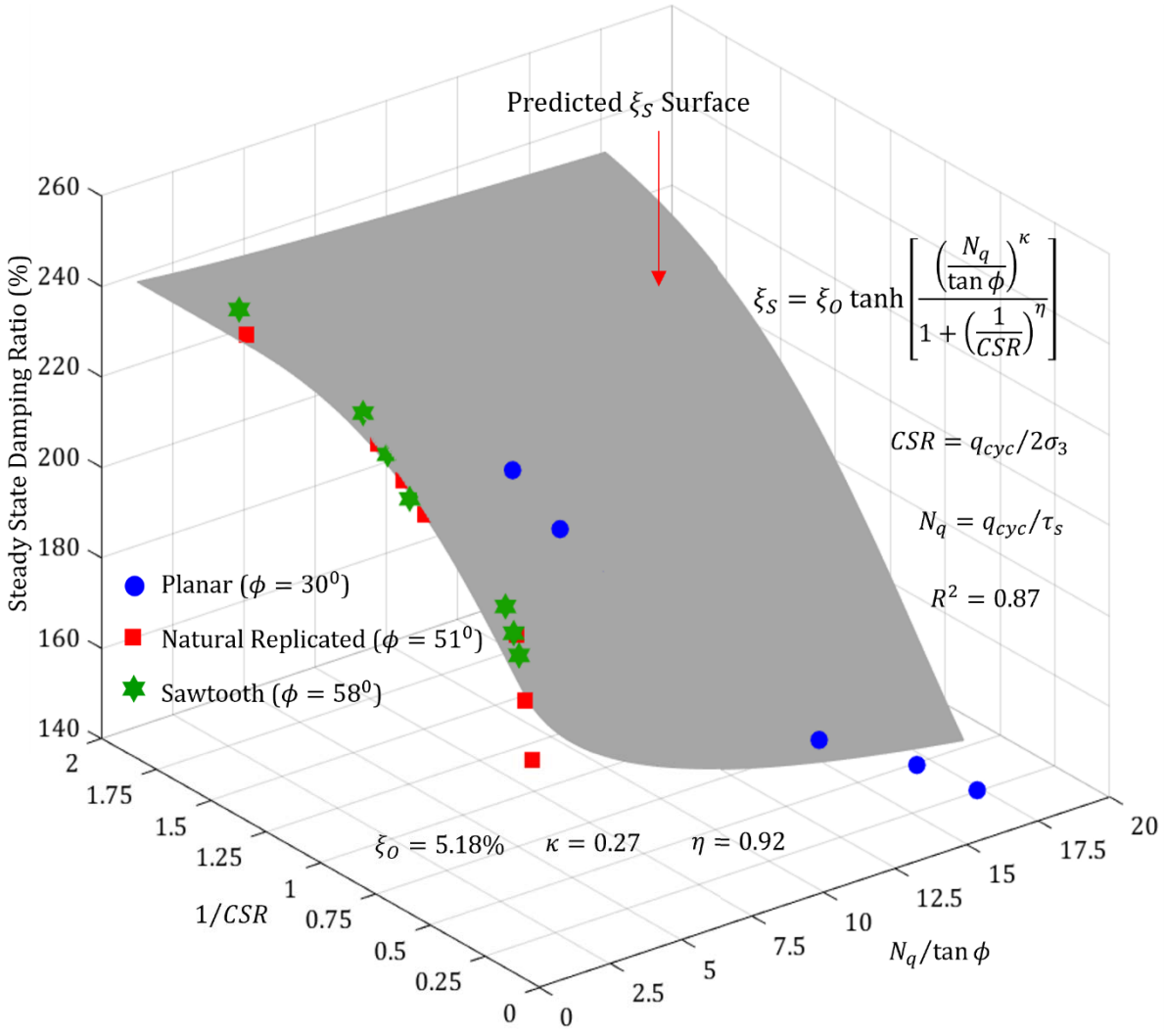

Figure 3.15. Variation of actual and predicted steady-state damping ratio (ξ_s) in the 3D space.

3.4 Summary

This study investigated the effect of cyclic deviatoric stress amplitude, confining stress and roughness of the joint surface on the dynamic characteristics of rock joints under cyclic triaxial loading conditions. The results showed that the cyclic stress-strain hysteresis loops of the jointed rock transitioned from sparse to dense with increasing loading cycles. The maximum residual axial strain gained by the rock joints increased with increasing cyclic deviatoric stress and decreasing confining stress, with smoother joints exhibiting significantly greater values than rougher joints. The resilient modulus demonstrated a downward trend with increasing loading cycles, with lower confining stress and higher cyclic deviatoric stress leading to decreased resilient moduli values. The dissipated energy and damping ratio decreased rapidly during the initial loading cycles and reached a steady state during the subsequent loading cycles. Higher cyclic deviatoric stress and lower confining stress resulted in higher dissipated energy and damping ratio values, while smoother joints exhibited considerably greater dissipated energy and damping ratio values than rougher joints. Empirical relationships were proposed for the steady-state resilient modulus and steady-state damping ratio values.

Chapter 4: Assessment of Cyclic Deformation and Critical Stress Amplitude of Jointed Rocks via Cyclic Triaxial Testing

4.1 General

In foundation design, avoiding excessive deformation under the applied loads is one of the key performance requirements evaluated by engineers (Craig, 2014). The Leaning Tower of Pisa is a classic example that points out the significance of evaluating the deformational characteristics of the ground precisely at the design phase. The deformation response of the ground under static loading conditions has been extensively investigated and reported in the literature. However, soil and rock formations are often exposed to repeated loads generated through natural causes such as earthquakes, wave actions, landslides and volcanic eruptions and human activities such as construction and demolition activities, traffic loads and machine vibrations (Sheng et al., 2006; Huang et al., 2007). It is well established that the material behaviour under cyclic loading is highly different from that under static loading. Under extreme conditions, cyclic loading may induce instantaneous settlements, leading to instability, damage and even disastrous failures in structures (Prakash, 1981; Yasuhara et al., 2001; Das and Ramana, 2011).

According to Ng et al. (2013), cyclic loading due to running trains was considered one of the possible causes of excessive long-term tunnel settlements observed along several metro lines in Shanghai. Shi et al. (2014) reported that a large number of rail tracks had been built on or across soft rocks in China, which had resulted in problems such as accumulated deformation and settlements in the tracks jeopardising the safety and efficiency of train operations. Rainer (1982) reported that foundation settlements were observed even in buildings far from railway lines inducing continuous vibrations over extended periods of loading. Lacy and Gould (1985) analysed cases of damage to nearby

structures caused by settlement from pile driving and concluded that increased cyclic loading induced by pile driving could lead to damaging levels of settlements. According to Yasuhara et al. (2001), extreme destructions were experienced in the 1957 and 1985 earthquakes in Mexico and the 1964 earthquake in Alaska due to seismically induced differential settlements. Massive land and rock slides triggered by the 1999 earthquake in central Taiwan (Chen et al., 2004a), the 2002 Alaska earthquake (Jibson et al., 2006) and the 2008 Wenchuan earthquake (Qi et al., 2011) can be considered as well documented case histories for catastrophic events due to seismically induced deformations of fractured and weak rock blocks.

Therefore, it is of utmost significance to evaluate the deformation behaviour of grounds exposed to dynamic loads during the design phase of structures rigorously. Yet, research studies on deformation characteristics and the evolution process of deformation of rock masses, particularly jointed rock masses subjected to repeated loading, are scarce. Rock masses present in nature generally consist of discontinuities such as joints, fractures, and other planes of weakness. The presence of such discontinuities significantly influences the strength and deformability of rock masses (Huang et al., 1993; Xie et al., 1997; Belem et al., 2006). According to Hungr and Coates (1978), settlement predictions are of paramount importance for structures founded on the jointed rock since joint deformation can constitute a significant portion of the settlement of the rock stratum. Huang et al. (1993) stated that during excavations and constructions at shallow depths of rock formations, the deformation of the rock mass is primarily controlled by the joint behaviour. Therefore, exploring the deformation behaviour of rock joints exposed to repeated loads is vital.

Over the past few decades, numerous researchers have conducted experimental and theoretical investigations to explore the deformation response of various intact rock types

under cyclic uniaxial or triaxial conditions. The dynamic strength and deformation characteristics of various intact rocks under repeated loading, as well as their evolution in relation to stress amplitude (Attewel and Farmer, 1973; Zhenyu and Haihong, 1990; Bagde and Petros, 2005a; Bagde and Petros, 2009; Ma et al., 2013; Momeni et al., 2015), frequency (Attewel and Farmer, 1973; Bagde and Petros, 2005a; Bagde and Petros, 2009; Liu et al., 2012; Ma et al., 2013) and waveform (Zhenyu and Haihong, 1990; Bagde and Petros, 2005b), were also studied. Apart from the studies mentioned above, which were carried out under constant cyclic loading amplitude, some experimental investigations were also conducted with variable cyclic loading amplitudes (i.e., stepwise increasing amplitudes, multi-level cyclic loading and random cyclic loading) (Liang et al., 2012; Jia et al., 2018; Vaneghi et al., 2018; Peng et al.,2019; Liu et al., 2021a). Researchers also defined numerous damage parameters to describe the dynamic damage progression and failure of various intact rocks subjected to repeated loading conditions (Xiao et al., 2009; Xiao et al., 2010; Liu et al., 2011; Liu and He, 2012; Li et al., 2019c). In addition, researchers employed energy theories and principles to analyse the energy dissipation mechanism that governs the deformation and failure of various intact rock types exposed to repeated loads (Bagde and Petros, 2009; Yang et al., 2016; Zhang et al., 2017; Song et al., 2020; He et al., 2021b).

Moreover, several researchers executed systematic experimental and theoretical studies to investigate the rock joint behaviour under repeated loading conditions. Most of these scholars conducted cyclic direct shear experiments to investigate the shearing mechanism, dilation and asperity degradation behaviour under cyclic shearing. They also analysed the influence of joint asperity characteristics, loading rate, number of shear cycles and normal stress on the jointed rock behaviour under cyclic direct shear loading (Hutson and Dowding, 1990; Huang et al., 1993; Lee et al., 2001; Jafari et al., 2003;

Belem et al., 2007; Zheng et al., 2016; Fathi et al., 2016; Niktabar et al., 2017; Kou et al., 2019).

In addition, a few researchers carried out experimental and theoretical investigations to examine the response of jointed rocks subjected to cyclic uniaxial or triaxial loading conditions. Early studies on intermittently jointed rock samples conducted by Brown and Hudson (1973) and Li et al. (2001a & b) under cyclic uniaxial loading and Prost (1988) under cyclic triaxial loading assessed the impact of repeated loading on the dynamic strength and deformation of intermittent joints. Later, Liu et al. (2017, 2018a & b) conducted cyclic uniaxial compression experiments on intermittently jointed rock samples and further analysed deformation characteristics, energy evolution, fatigue damage and failure of the specimens. Jafari et al. (2003 & 2004) investigated the impact of repeated loading (i.e., number of cycles and cyclic stress amplitude) on the shear strength of sawtoothed rock joints under triaxial conditions. Ding et al. (2014) studied the effect of the contact condition of joints on the deformation behaviour of rocks under cyclic triaxial loading. Studies by Liu and Liu (2017) and Zheng et al. (2020a & b) investigated the deformation characteristics, dynamic damage and failure mechanism of prefabricated jointed rock with a planar joint surface under cyclic triaxial conditions. They also defined damage variables capturing the evolution of dynamic damage of the rock joints.

Indeed, most of the previous research studies on rocks under cyclic loading conditions had focused on the deformation response and dynamic properties of intact rocks. However, only a few research studies are available related to the rock joint behaviour under repeated loading conditions. The majority of studies investigating the cyclic behaviour of jointed rocks have employed cyclic direct shear apparatus for continuous penetrating joints and cyclic triaxial or uniaxial apparatus for prefabricated intermittent

joints. Experimental studies on jointed rocks with continuous penetrating joints replicating a natural rough joint surface under cyclic triaxial conditions are rather scarce. To date, there has been a lack of thorough investigation into the deformation behaviour and dynamic properties of rock joints subjected to repeated loading in relation to their deformation characteristics, yielding, energy and damage evolution, and damping properties. Therefore, this study experimentally investigates the deformation response and dynamic mechanical characteristics of rock joints with a natural joint surface subjected to cyclic triaxial test conditions. Indeed, this study provides an important reference and quantifies variation of parameters such as permanent deformation, yielding stress, stiffness and damping ratio with field conditions. Design engineers can use the results of this study for more reliable prediction of the response of jointed rocks exposed to repeated loading and propose efficient and cost-effective solutions to curtail excessive deformations of structures built on or near jointed rock foundations exposed to repeated loading from machine foundations, railway, road traffic loads and rock cutting. A cyclic triaxial experiments series was performed on rock samples with a natural replicated joint surface oriented at a mean dip angle of 60^{o} under various confining stresses and cyclic deviatoric stresses. The cyclic stress-strain response, yield stress, residual axial deformation evolution, stiffness degradation, dissipated energy evolution, and damping characteristics were analysed and discussed in detail.

4.2 Laboratory Investigation

4.2.1 Sample Preparation

The deformation behaviour of jointed rock was explored through a thorough laboratory experiment series conducted on a set of modelled rock joints having a natural joint surface. Due to the difficulty of obtaining a set of natural rock joints with the same morphology, replicas of jointed rock specimens can be cast with natural and synthetic materials. Stimpson (1970) provided a comprehensive summary of various types of model material used to simulate rock during a variety of investigations. Gypsum plaster is one such material most commonly used to model various rock types, including sedimentary rocks (Hobbs, 1966; Rosenblad, 1971; Indraratna, 1990; Waltham and Swift, 2004; Atapour and Moosavi, 2014; Jahanian and Sadaghiani, 2015; Gong et al., 2018b). It can also be moulded into various shapes and dries quickly with minimum apparent long-term changes in strength. In this study, gypsum plaster ($CaSO_4.H_2O$ hemihydrates, 98%) was used to make replicas of rock joints with a natural joint surface.

The cylindrical jointed rock specimens had a diameter of 50 mm and an overall height of 100 mm when the two halves of the specimen were fully mated. Hence, the jointed rock specimen maintained a height-to-diameter ratio of two, as required for triaxial testing. According to Goodman (1989), when the joint is oriented at an angle 50^o - 65^o with the direction of minor principal stress, the joint will slip before fracturing the rock, allowing determination of the joint characteristics. According to Jafari et al. (2004) and Abdellah et al. (2016), the critical orientation of the joint can also be determined from the Mohr-Coulomb criterion given by $45^o + \phi/2$, where, ϕ is the friction angle of the joint. Accordingly, in this study, the joint surface was oriented at 60^o with the direction of minor principal stress.

Each side of the joint surface was cast separately to ensure that the joint was fully mated after assembly. To cast replicas of cylindrical modelled rock joints, a cylindrical hollow mould and cylindrical moulds with each side of the natural joint surface were required. As reported in Section 3.2.1, cylindrical hollow moulds, 50 mm in diameter and 100 mm in height (see Figure 4.1a), were created using acetal plastic since this material could be machined to obtain the desired shape. An actual block of sandstone taken from Kangaroo Valley, New South Wales, Australia, was split to obtain a naturally rough rock surface, and Dlachem SRT30 mould-making silicon rubber (in the liquid form) was used to copy the split sandstone rough surface to prepare moulds of each side of the joint surface (see Figure 4.1b). This material consisted of a base component and a catalyst which were mixed in a ratio of 20:1 and poured over the split sandstone surface, and allowed to harden. The rubber moulds were taken out after a setting time of 72 hours and were used to cast the 50 mm diameter jointed cylindrical specimens.

The rubber moulds of the joint profiles were placed separately in cylindrical hollow moulds (Figure 4.1a), and a silicon-based lubricant was sprayed on the joint surface and the interior wall of the hollow moulds to prevent the gypsum plaster mixture from adhering to the moulds. Gypsum cement was then mixed with water in a ratio of 3.5:1 by weight and stirred until it became a uniform mixture. The uniform mixture was then poured into the hollow moulds, and a mild vibration was applied to the moulds externally to release any air bubbles trapped in the gypsum plaster mixture. After completion of the initial setting time of 30 minutes, the specimens (Figure 4.1c) were removed from the moulds and cured for two weeks at a controlled temperature of 40 ^{o}C. After the completion of curing time, the modelled rock joints were used for testing after reaching room temperature. A comparable sample preparation procedure was also reported in Section 3.2.1.

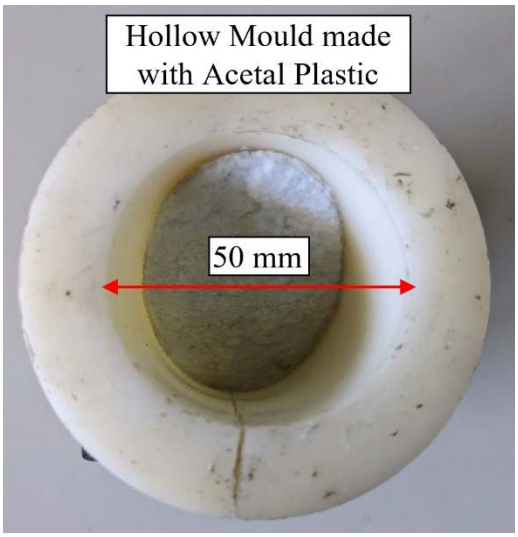

(a)

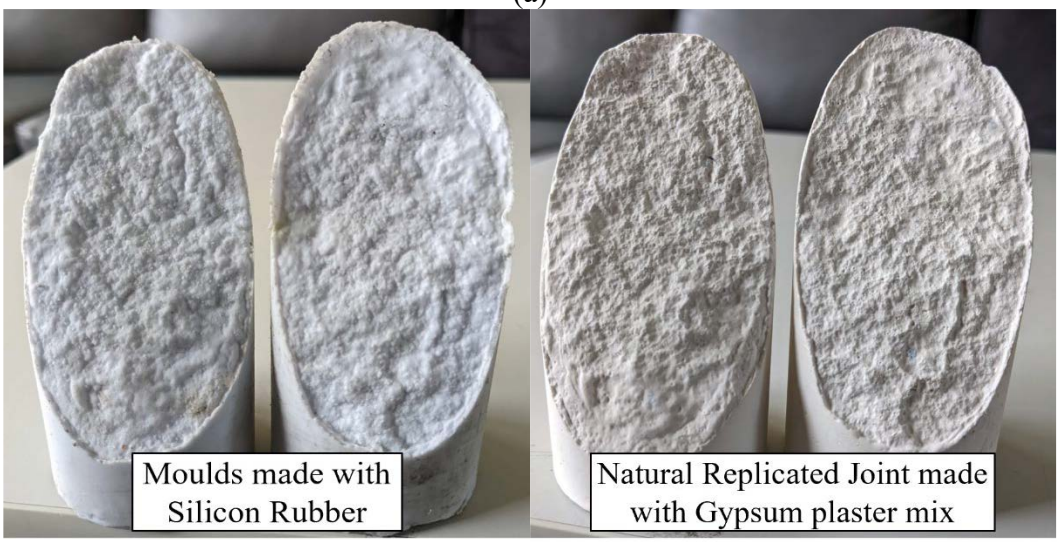

(b) (c)

Figure 4.1. (a) The top view of the cylindrical hollow mould with one-half of the joint mould inside it; (b) Rubber moulds of the two opposite sides of the natural replicated joint surface; and (c) The two opposite surfaces of a natural replicated jointed sample.

4.2.2 Testing Procedure

In this study, the triaxial setup was employed to perform all the tests to explore the joint behaviour under repeated loading conditions similar to those encountered in an underground setting (Jafari et al., 2004). In order to carry out the experimental work, the GDS ELDYN triaxial apparatus, as shown in Figure 4.2a, was used when testing rock joints under lower cyclic deviatoric stresses (q_{cyc} < 400 kPa). On the other hand, a triaxial

condition set up using the CMA electro-hydraulic actuator (Figure 4.2b) was employed when testing rock joints under higher cyclic deviatoric stresses (q_{cyc} > 400 kPa). In the ELDYN triaxial apparatus, the axial load was applied via the electro-mechanical actuator, which had a load capacity of 10 kN and a maximum frequency of 10 Hz could be applied. The CMA electro-hydraulic actuator had a load capacity of 40 kN, and a maximum frequency of 40 Hz could be applied. In both experimental setups, the confining pressure was applied by pressurising the cell with de-aired water, controlled by air through the air pressure controller. After thorough checks and calibrations of the apparatus, the jointed rock specimen was placed on the triaxial base and then covered with a membrane and O-rings to seal the sample.

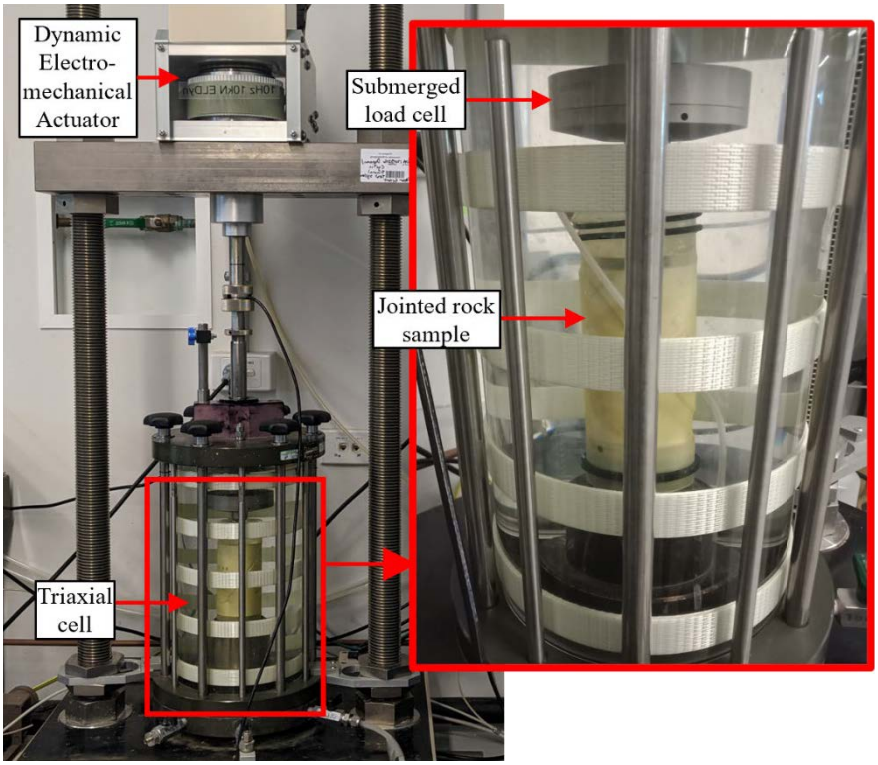

(a)

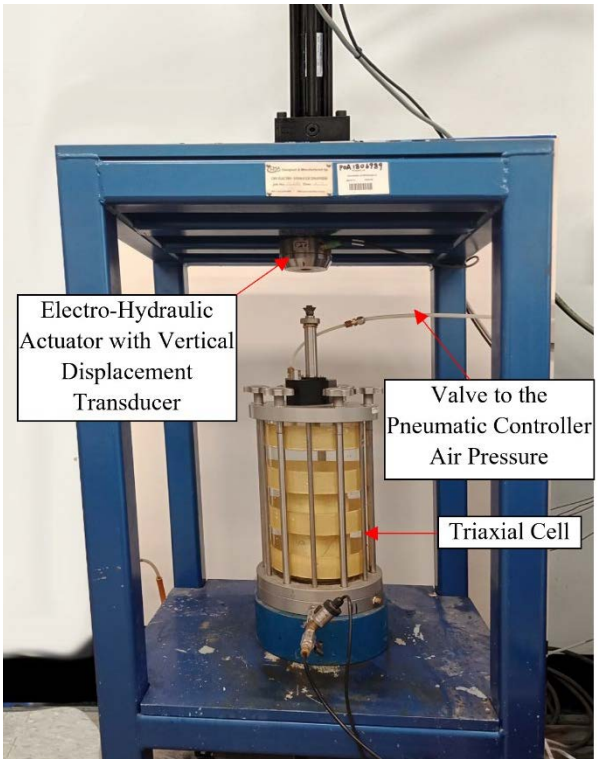

(b)

Figure 4.2. (a) GDS 10 Hz cyclic triaxial equipment used in this study; and (b) Triaxial condition set up using the CMA electro-hydraulic actuator.

The tested samples had a natural replicated joint surface with a Joint Roughness Coefficient (JRC) of 11.51. It should be noted that the JRC value of the joint surface was calculated using the relationships proposed by Tse and Cruden (1979) as follows.

$$JRC = 32.2 + 32.47 \log Z_2 \tag{4.1}$$

where Z_2 is the root mean square of the first derivative of the profile which is given by Equation (4.2).

$$Z_2 = \sqrt{\left(\frac{1}{L_n}\sum_{i=1}^{N_p-1}\frac{(z_{i+1}-z_i)^2}{(x_{i+1}-x_i)}\right)} \tag{4.2}$$

where, the values (x_i, z_i) and (x_{i+1}, z_{i+1}) represent the adjacent digitised coordinates of the profile separated by the sampling interval Δx, N_p is the number of digitised points along the profile, and L_n is the nominal length of the digitised joint profile. A non-contact

3D digitiser (MINOLTA VIVID 910) was used for digitising the joint surface (Figure 4.3). The digitised coordinates of 10 joint profiles along the shear direction of the joint surface were used to determine the weighted average JRC based on the coverage area to describe the roughness of the joint surface. Moreover, conventional static triaxial experiments were conducted with a shearing rate of 0.05 mm/min to measure the friction angle of the joint ($\phi = 51^0$).

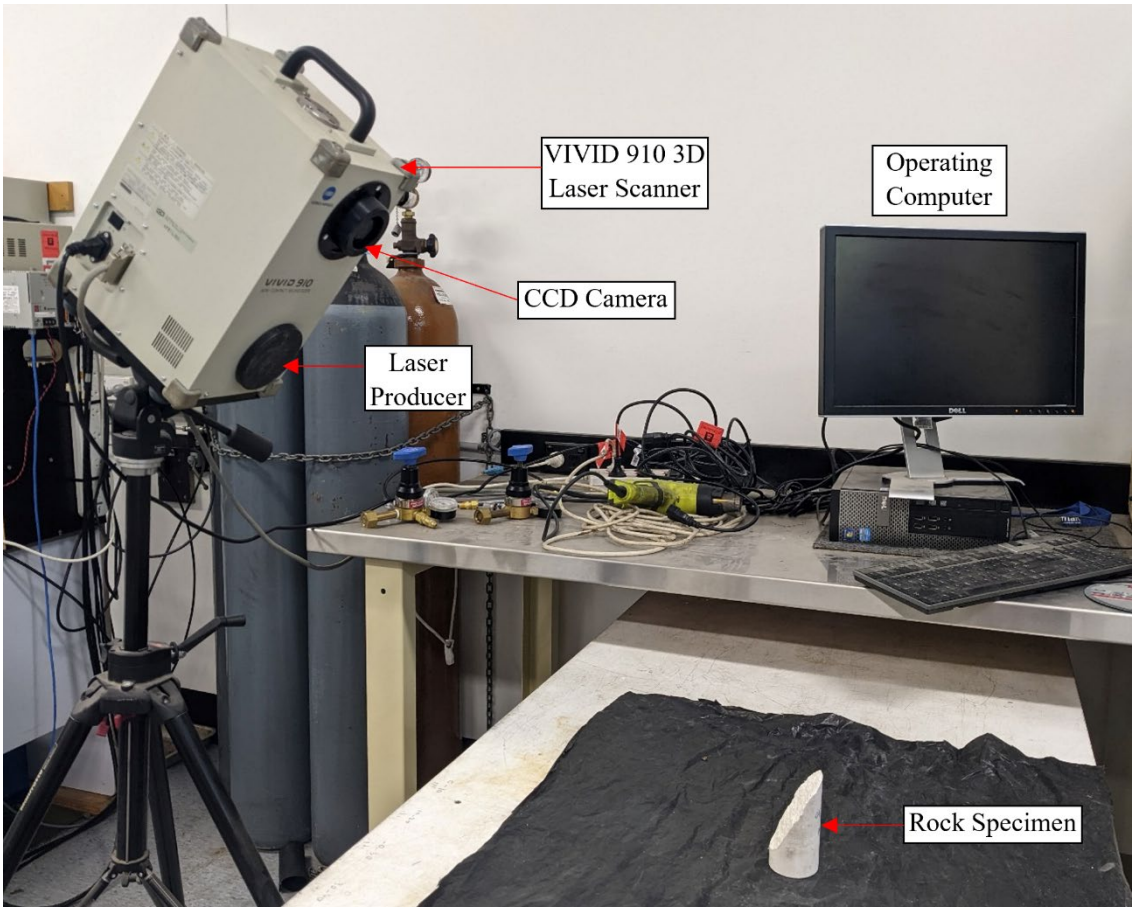

(a)

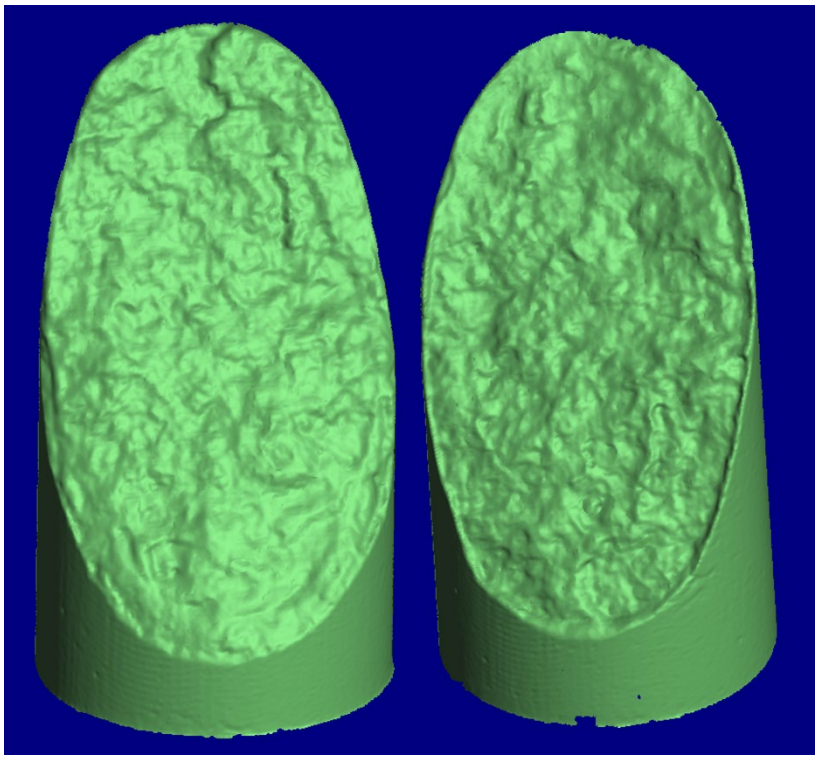

(b)

Figure 4.3. (a) The non-contact 3D Laser Scanner (MINOLTA VIVID 910); and (b) Scanned 3D opposite surfaces of the jointed rock specimen.

Six levels of confining stresses (i.e., 15 kPa, 20 kPa, 25 kPa, 90 kPa, 120 kPa and 150 kPa) were selected for the testing, in line with previous research studies by other researchers for laboratory testing, field measurements and numerical simulations of shallow rock formations for various applications. For example, Sinha and Sinha (2000) used an effective confining pressure of 125 kPa when simulating rock joints filled along the surface of the discontinuity in a rock mass prone to landslides; Liu and Liu (2017) simulated jointed rocks exposed to repeated loads, including seismic loads, train loads and blasting loads, using confining stresses in the range of 100 - 400 kPa; Ding et al. (2014) conducted cyclic triaxial experiments with confining stress of 200 kPa when analysing the stability of tunnel bed under high-speed train operation; Nie et al. (2020) and Wang and Zhuang (2021) used confining stresses in the range of 20 - 150 kPa when simulating railway subgrades under train loads. In line with previous research studies, various cyclic deviatoric stress amplitudes were used for each confining pressure to

identify the critical dynamic deviatoric stress clearly. It should be noted that for each case with different cyclic deviatoric stress amplitudes, a new sample was used to ensure micro-cracking from the previous loading stresses would not accumulate and impact the accurate determination of the critical dynamic stress.

In this study, the tests were terminated when 10000 loading cycles were applied. The minimum deviatoric stress was maintained constant, while the maximum deviatoric stress was adjusted to apply the target cyclic deviatoric stress amplitudes. The sinusoidal waveform was utilised to apply the cyclic load on the jointed rock samples. Frequencies in the range of 0.1 - 20 Hz were utilised in the past by previous researchers for cyclic experiments simulating rock formations under dynamic loads such as earthquakes, construction and demolition activities, traffic loads and machine vibrations (Liu and Dai, 2021). For example, Attewell and Farmer (1973) simulated rock engineering operations such as drilling for explosive blasting and cutting during tunnel boring, using frequencies in the range of 0.3 - 20 Hz; Bagde and Petros (2005a) used frequencies in the range of 0.1 - 10 Hz stimulating rock bursts; Liu et al. (2018a & b) simulated earthquake, quarrying and rock bursts using frequencies in the range of 1 - 10 Hz. Referring to previous studies (Bian et al., 2014; Zhang et al., 2018a), frequencies in the range of 1 - 12 Hz have been utilised for subgrades of heavy haul or rather high-speed train lines. Therefore, a loading frequency of 8 Hz was used for the experiments in this study.

4.3 Results and Discussion

4.3.1 Static Stress-Strain Response

The conventional triaxial compression experiments were performed at various confining stresses to obtain the peak deviatoric stresses and the corresponding shear strength values of the rock joints under static loading. Figure 4.4 illustrates the static deviatoric stress vs axial strain curves obtained from the static triaxial tests, and the corresponding peak deviatoric stress and shear strength values are reported in Table 4.1. The normal and shear stress components along the joint surface were determined from the principal stresses and the inclination angle of the joint as per the stress state on the joint surface, as shown in Figure 4.5 and using Equation (4.3).

$$\tau_s = \frac{(\sigma_1 - \sigma_3)\sin 2\theta}{2} \tag{4.3a}$$

$$\sigma_n = \frac{(\sigma_1 + \sigma_3)}{2} + \frac{(\sigma_1 - \sigma_3)\cos 2\theta}{2} \tag{4.3b}$$

where, σ_1 is the major principal stress, σ_3 is the minor principal stress, τ_s is the shear stress on the joint plane, σ_n is the normal stress on the joint plane, and θ is the joint inclination angle.

The stress-strain plots in Figure 4.4 indicated stick-slip behaviour possibly due to local sliding, over-riding and degradation of asperities accompanied by relocking of the broken and/or unbroken asperities during shearing (Byerlee, 1970). As shown in Figure 4.4, with increased confining stress, the rock joints exhibited a rise in the peak deviatoric stress as expected. At low confining stresses (i.e. 15 kPa, 20 kPa and 25 kPa), a higher axial strain was necessary to attain the peak deviatoric stress when compared to higher confining stresses (i.e. 90 kPa, 120 kPa and 150 kPa). The peak deviatoric stress and confining stress are used in the Mohr-Coulomb analysis to obtain the corresponding shear strength,

and the friction angle of the joint was determined to be 51^0, and comparable results were reported by other researchers (e.g. Premadasa, 2013).

Table 4.1. Test conditions and results of jointed rock samples at static and dynamic failure.

Confining Pressure, σ_3 (kPa)	Static Peak Deviator Stress, q_{sp} (kPa)	Static Shear Strength, τ_s (kPa)	Critical Dynamic Stress, q_c (kPa)	Critical Dynamic Shear Strength, τ_{cs} (kPa)	Ratio between q_c and q_{sp}	Ultimate Residual Axial Strain (%)
15	601	260	400	173	0.66	9.48
20	687	298	450	195	0.65	8.96
25	801	347	500	217	0.62	8.39
90	1276	553	900	390	0.70	5.29
120	1439	623	1000	433	0.69	4.76
150	1627	705	1100	476	0.67	4.04

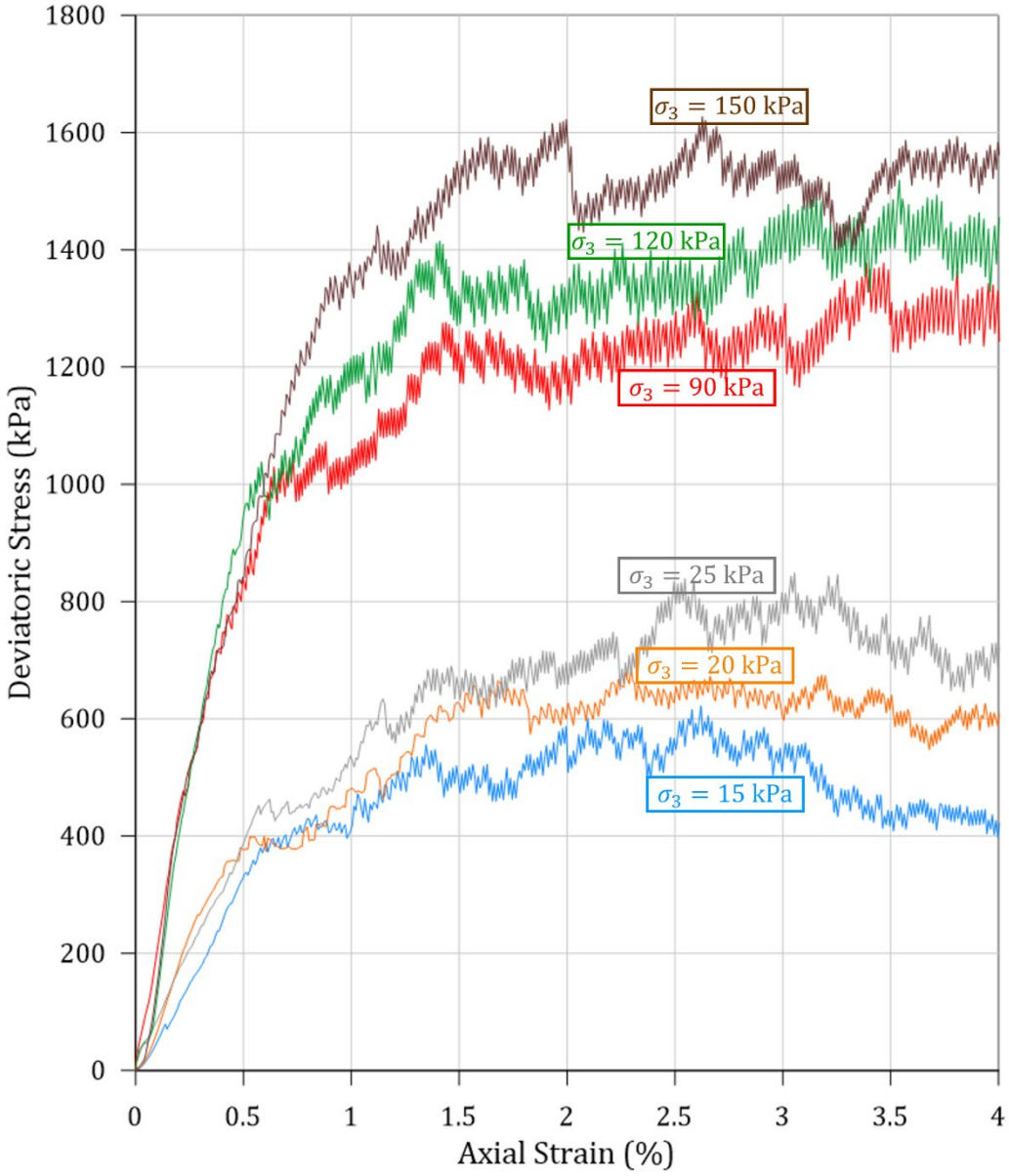

Figure 4.4. The static stress-strain curves for jointed rock samples under confining pressures (σ_3) of 15 kPa, 20 kPa, 25 kPa, 90 kPa, 120 kPa and 150 kPa.

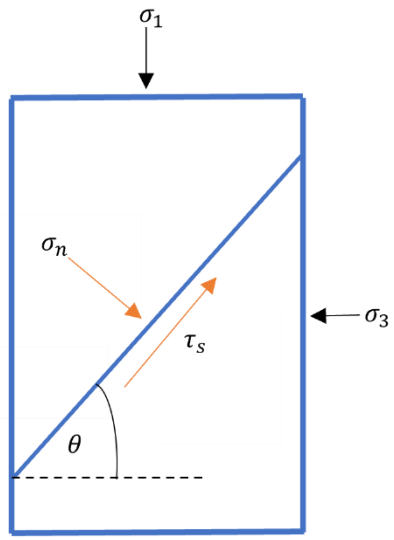

Figure 4.5. Schematic diagram of the stress state at the joint surface.

4.3.2 Cyclic Stress-Strain Response

Samples of cyclic stress-strain curves of the rock joints under the confining stresses of 20 kPa, 90 kPa and 150 kPa are presented in figures 4.6 – 4.8, respectively. Figures 4.6 – 4.8 demonstrate that the stress-strain curves in the loading-unloading process formed a hysteresis loop in each loading cycle. Under all the adopted confining stresses, the hysteresis loops transitioned from sparse to dense with the progression of cyclic loading. This transition from sparse to dense hysteresis loops was more evident at lower confining stresses such as 20 kPa (Figure 4.6) and higher cyclic deviatoric stresses (Figures 4.7c and 4.8c).

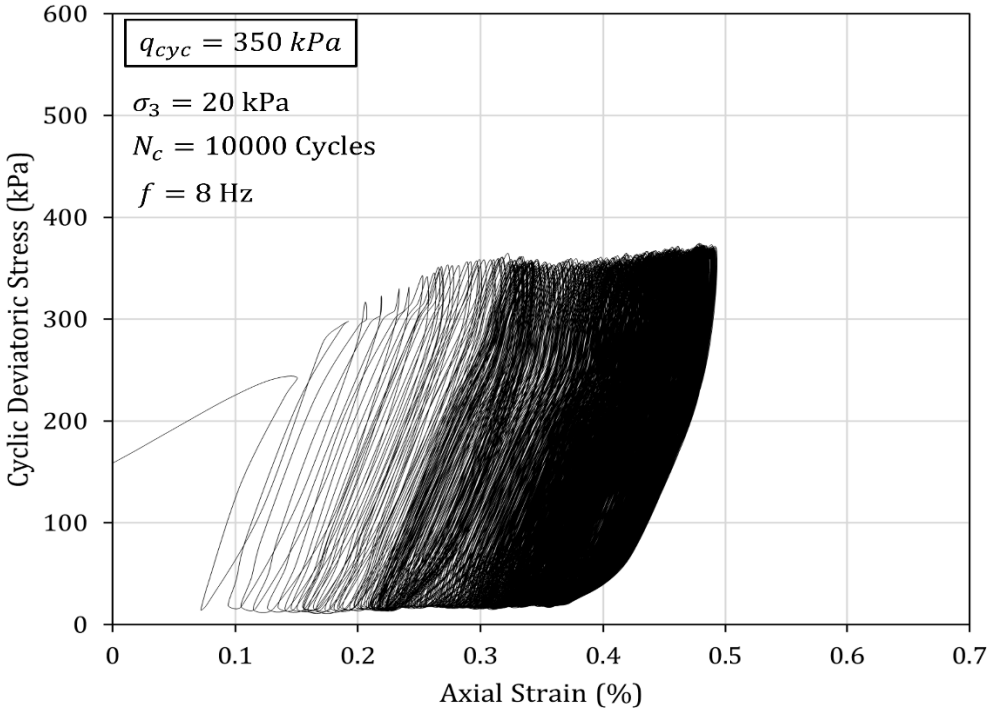
$q_{cyc} = 350\ kPa$
$\sigma_3 = 20$ kPa
$N_c = 10000$ Cycles
$f = 8$ Hz
Cyclic Deviatoric Stress (kPa)
Axial Strain (%)
0
100
200
300
400
500
600
0
0.1
0.2
0.3
0.4
0.5
0.6
0.7

(a)

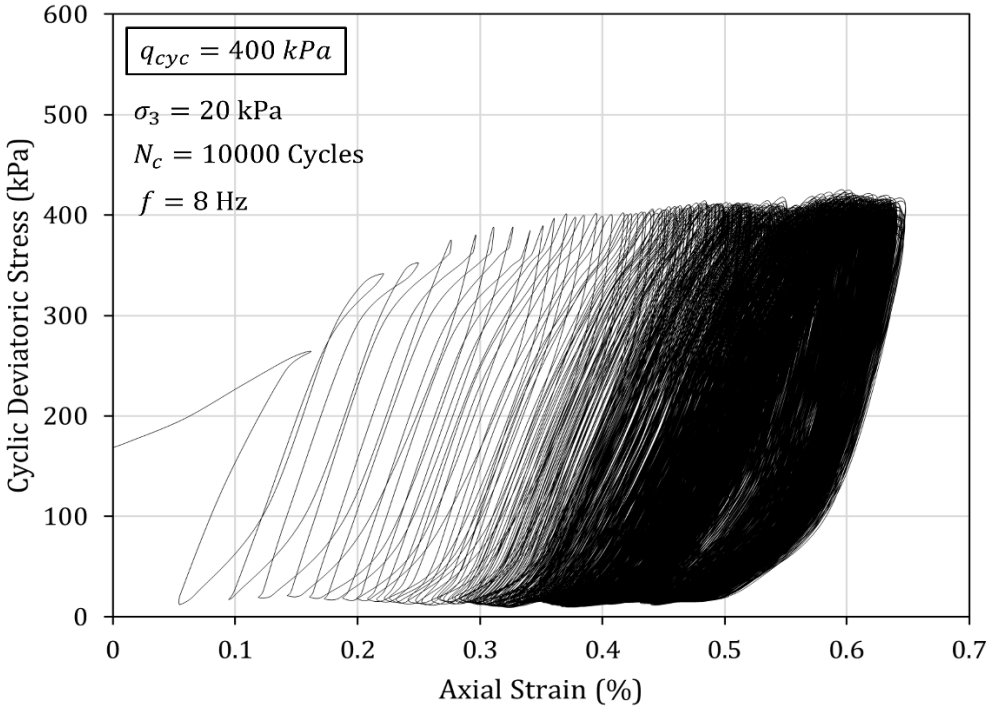
$q_{cyc} = 400\ kPa$
$\sigma_3 = 20$ kPa
$N_c = 10000$ Cycles
$f = 8$ Hz
Cyclic Deviatoric Stress (kPa)
Axial Strain (%)
0
100
200
300
400
500
600
0
0.1
0.2
0.3
0.4
0.5
0.6
0.7

(b)

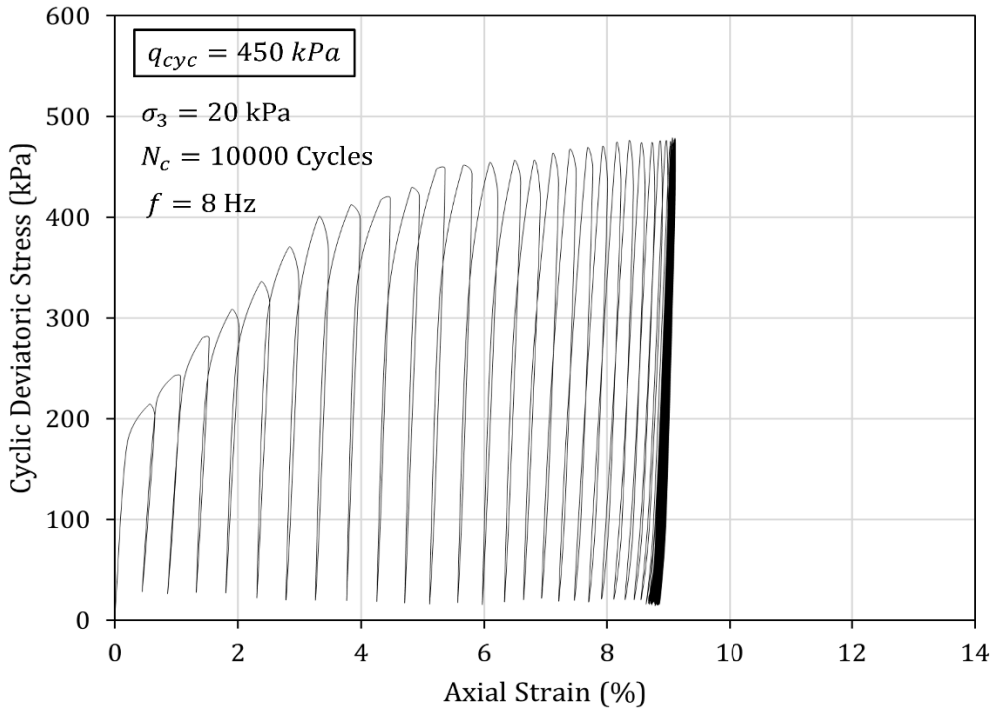

(c)

Figure 4.6. The Cyclic stress-strain curves for jointed rock samples under confining pressure (σ_3) of 20 kPa and cyclic deviatoric stress amplitudes (q_{cyc}) of: (a) 350 kPa; (b) 400 kPa and (c) 450 kPa.

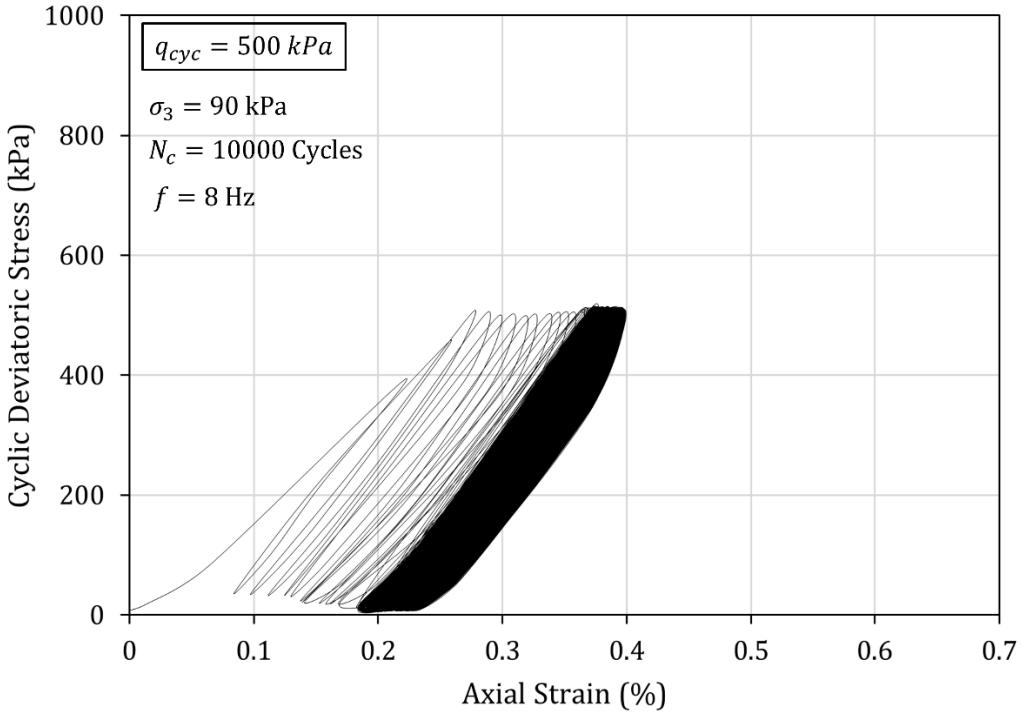

(a)

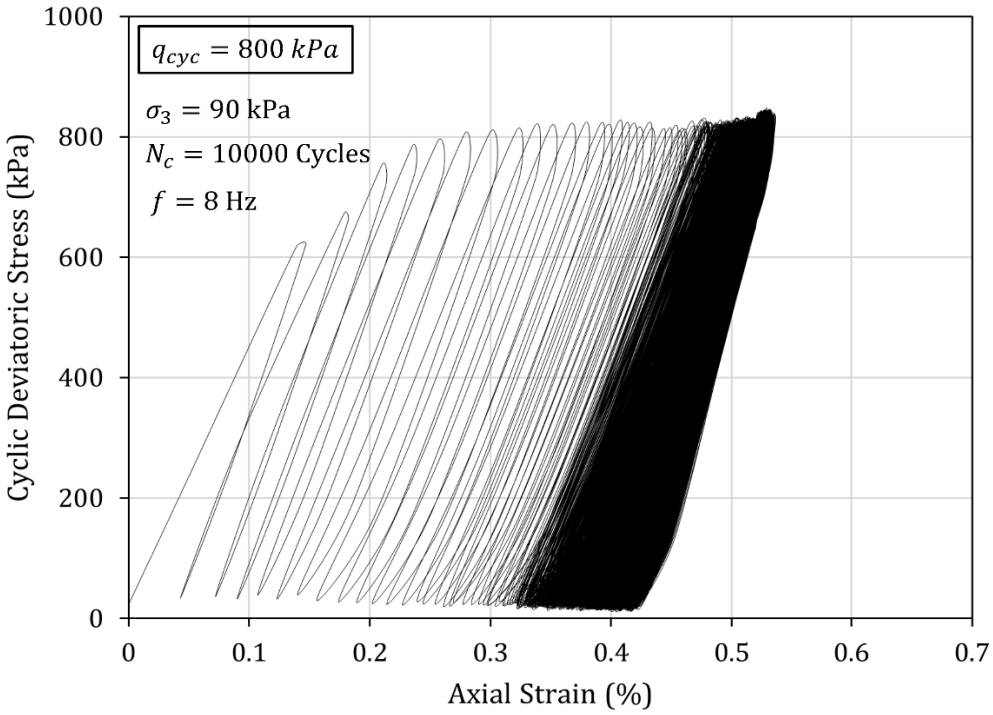

(b)

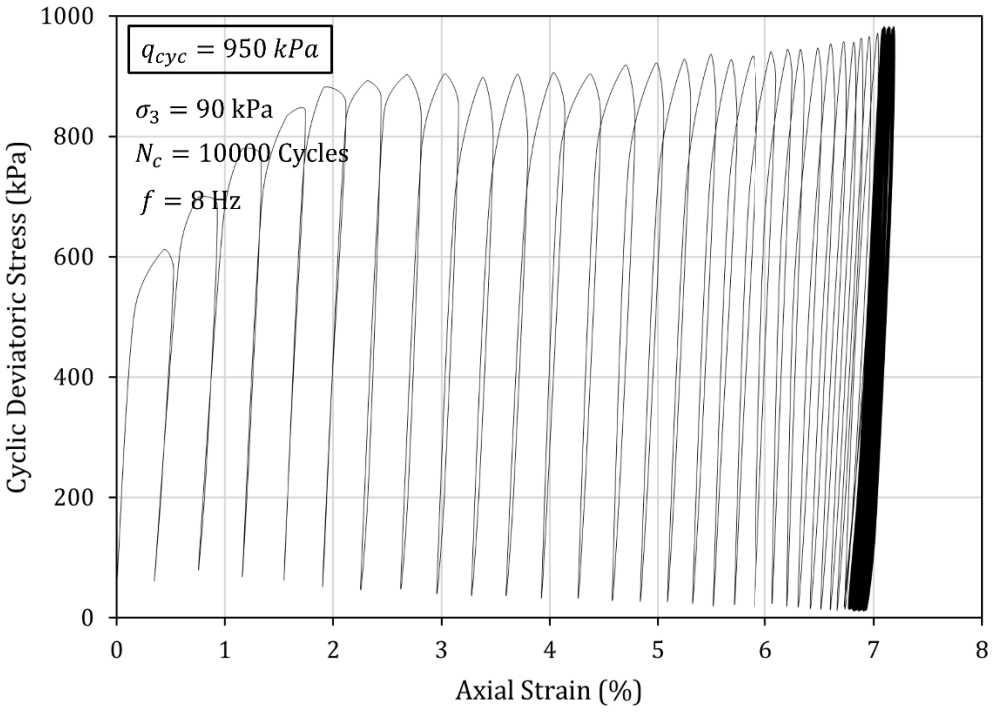

(c)

Figure 4.7. The Cyclic stress-strain curves for jointed rock samples under confining pressure (σ_3) of 90 kPa and cyclic deviatoric stress amplitudes (q_{cyc}) of: (a) 500 kPa; (b) 800 kPa and (c) 950 kPa.

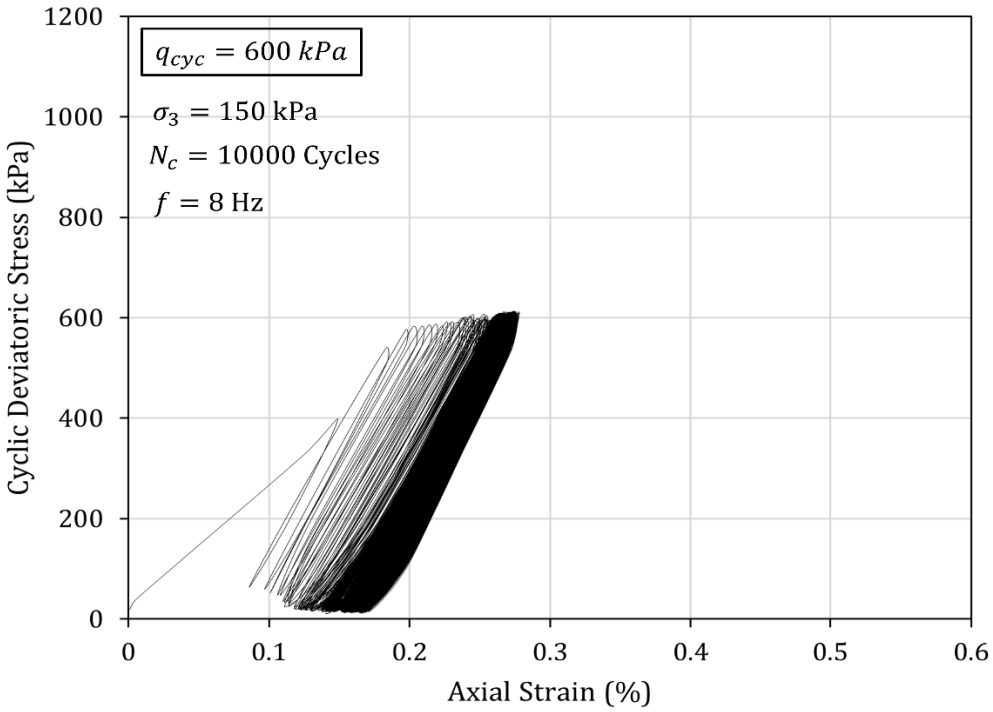
$q_{cyc} = 600\ kPa$
$\sigma_3 = 150$ kPa
$N_c = 10000$ Cycles
$f = 8$ Hz
Cyclic Deviatoric Stress (kPa)
Axial Strain (%)
0
200
400
600
800
1000
1200
0
0.1
0.2
0.3
0.4
0.5
0.6

(a)

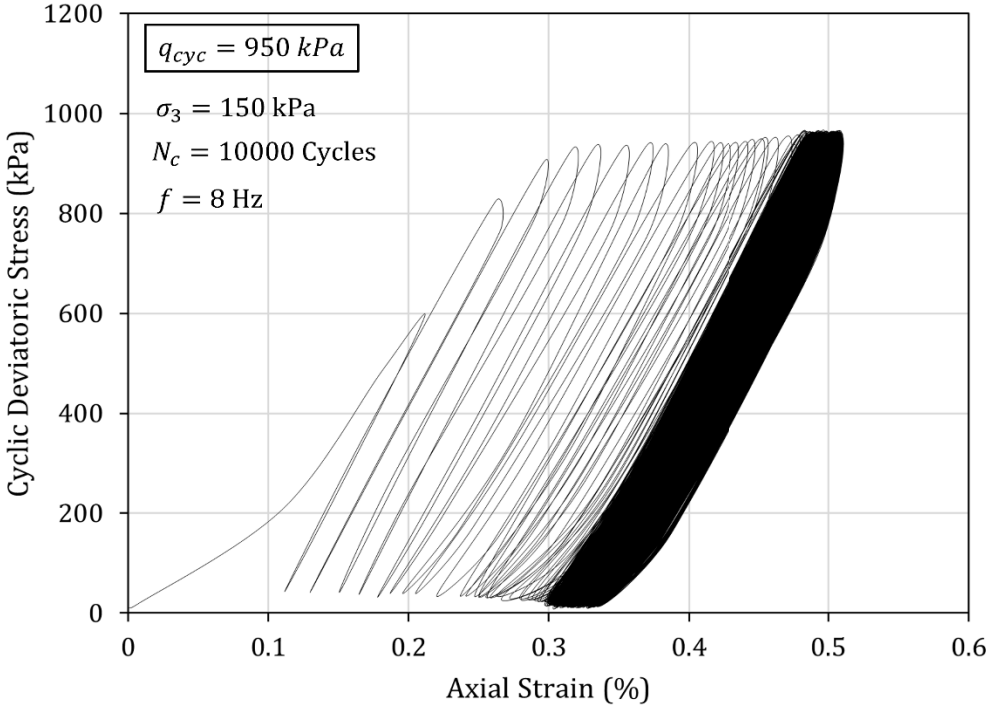
$q_{cyc} = 950\ kPa$
$\sigma_3 = 150$ kPa
$N_c = 10000$ Cycles
$f = 8$ Hz
Cyclic Deviatoric Stress (kPa)
Axial Strain (%)
0
200
400
600
800
1000
1200
0
0.1
0.2
0.3
0.4
0.5
0.6

(b)

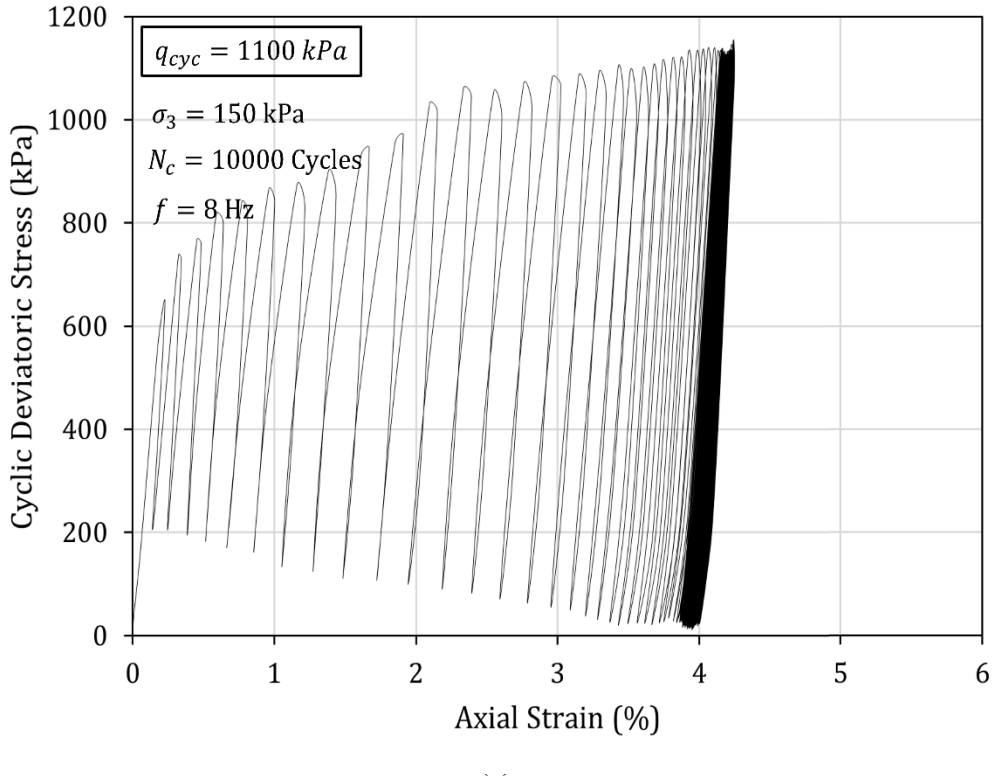

Figure 4.8. The Cyclic stress-strain curves for jointed rock samples under confining pressure (σ_3) of 150 kPa and cyclic deviatoric stress amplitudes (q_{cyc}) of: (a) 600 kPa; (b) 950 kPa and (c) 1100 kPa.

Figure 4.9 shows samples of the hysteresis loops formed at different test conditions and cycle numbers. Referring to Figures 4.6 – 4.9, at lower cyclic deviatoric stress amplitudes (i.e. $q_{cyc} < q_c$), the hysteresis loops nearly overlapped, and the loops were almost closed with a small residual axial strain. In addition, only slight variations in the shape and area of the loops were observed. However, as the cyclic deviatoric stress amplitude exceeded the critical dynamic deviatoric stress (i.e. $q_{cyc} \geq q_c$) as evident in Figures 4.6c, 4.7c and 4.8c, significant changes in the hysteresis loops were observed, characterised by a rise in the height, breadth and area of the loops. During the initial loading cycles, the loops hardly overlapped, and the loading-unloading curves were no longer closed, indicating a significant accumulation of plastic strains and energy dissipation. However, during the subsequent loading cycles, the loops gradually overlapped, and closed loops were formed with the indication of no further notable accumulation of residual axial strain until the

end of the test. This observation is also evident from Figures 4.6 - 4.9, where the accumulated residual axial strain increased with the number of loading cycles and then stabilised.

It should be noted that the amplitude of residual axial strain increment in each cycle became progressively lower. Accordingly, during the initial loading cycles, the rock joints exhibited viscoelastic plastic behaviour with increasing irreversible axial strains, which is also reflected in the sparse hysteresis loops. During the subsequent loading cycles, nearly viscoelastic behaviour was illustrated.

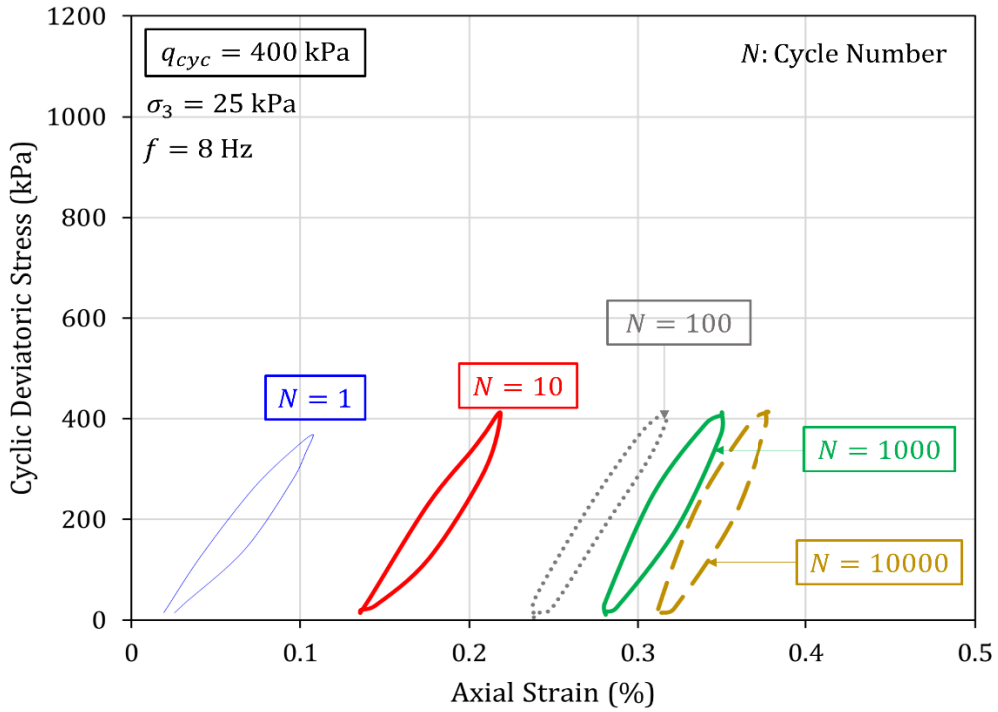

(a)

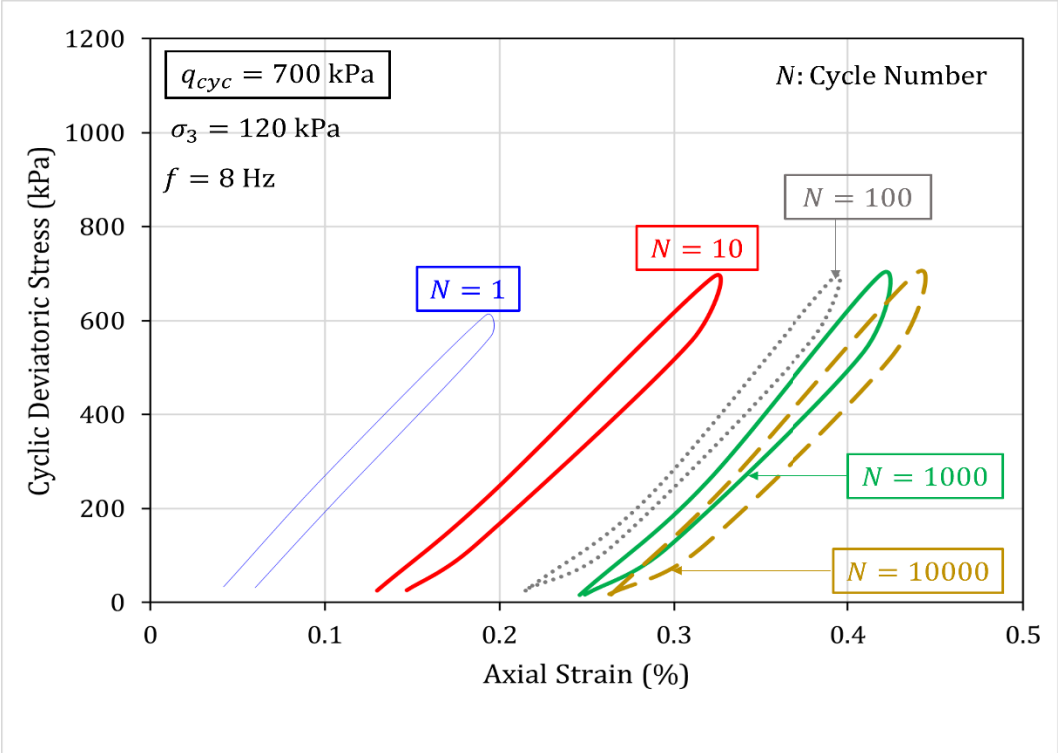
q_{cyc} = 700 kPa
σ_3 = 120 kPa
f = 8 Hz
N: Cycle Number
N = 1
N = 10
N = 100
N = 1000
N = 10000
Cyclic Deviatoric Stress (kPa)
Axial Strain (%)
0
200
400
600
800
1000
1200
0
0.1
0.2
0.3
0.4
0.5

(b)

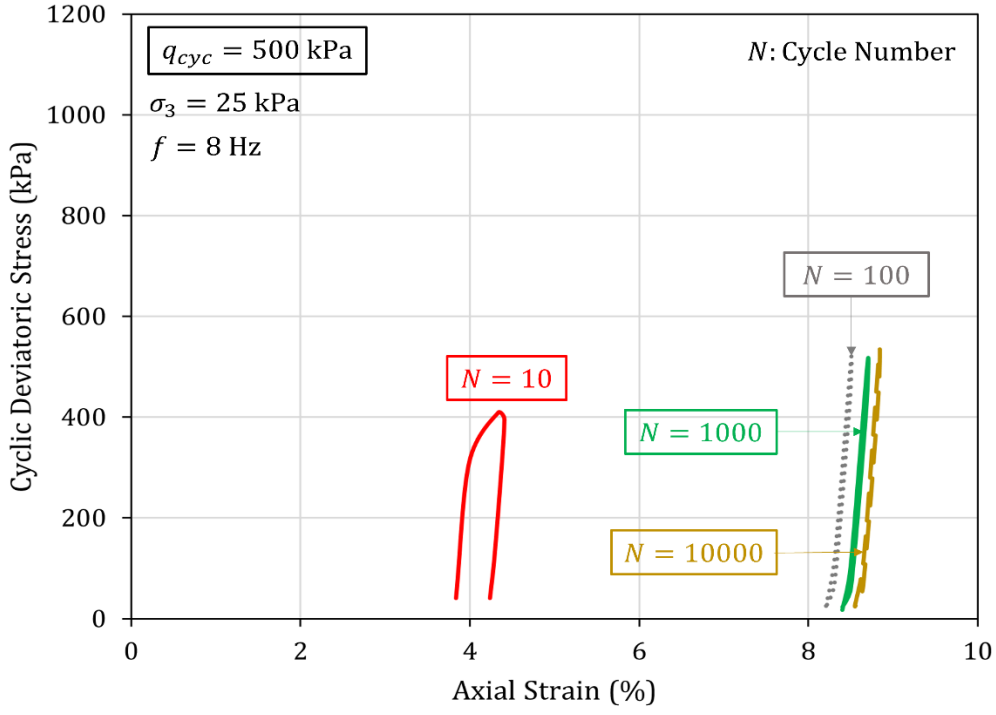
q_{cyc} = 500 kPa
σ_3 = 25 kPa
f = 8 Hz
N: Cycle Number
N = 10
N = 100
N = 1000
N = 10000
Cyclic Deviatoric Stress (kPa)
Axial Strain (%)
0
200
400
600
800
1000
1200
0
2
4
6
8
10

(c)

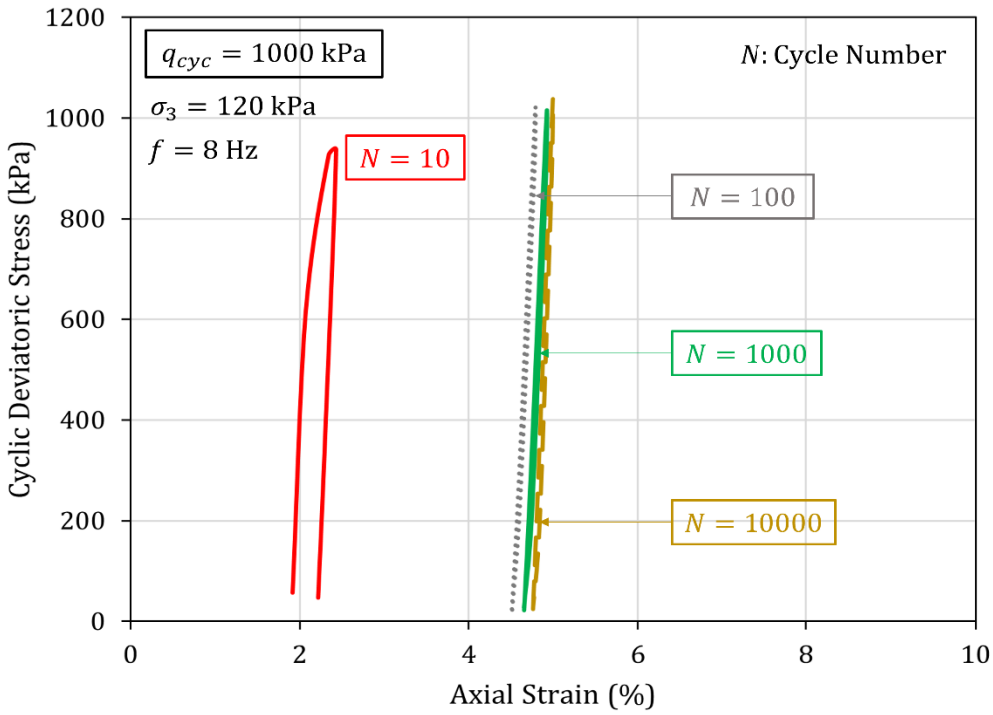

(d)

Figure 4.9. Stress-strain hysteresis loops at various number of cycles at confining pressures (σ_3) and cyclic deviatoric stress amplitudes (q_{cyc}) of: (a) σ_3= 25 kPa and q_{cyc}= 400 kPa; (b) σ_3= 120 kPa and q_{cyc}= 700 kPa; (c) σ_3=25 kPa and q_{cyc}= 500 kPa; and (d) σ_3=120 kPa and q_{cyc}= 1000 kPa.

Moreover, a numerical analysis was conducted using the finite element software PLAXIS 3D to compare the experimental results with the numerical predictions. A 3D model of a jointed rock with a 50 mm diameter and 100 mm height was created. The JR (Jointed Rock) model, which is available in PLAXIS 3D software capturing the joint direction and plasticity, was used as the constitutive model (PLAXIS 3D Material Models Manual, 2022). Shear strength parameters obtained from the stress-strain plots were used for the numerical analysis, while a unit weight of 24 kN/m^3 and a Poisson's ratio of 0.2 was adopted. Young's moduli in the range of 80 MPa - 120 MPa were used in the numerical analysis. It should be noted that since continuum-based modelling was used in this study, the elastic response of the jointed rock was regulated by the elastic characteristics of the joint, which is more deformable than the intact rock due to the absence of cementation in

the joint and reduced stiffness. With respect to displacement boundary conditions, the bottom boundary was fixed in the normal direction, while the side and top boundaries were kept free to simulate the cylindrical triaxial experiment. Dynamic analysis was conducted, allowing the application of cyclic loading with a cyclic deviatoric stress amplitude (q_{cyc}) of 400 kPa, and confining stress (σ_3) of 20 kPa. Figure 4.10 shows the overview of the 3D finite element model and its characteristics.

Figure 4.11 presents a comparison of the dynamic stress-strain response of the rock joint in numerical modelling and experimental results for the first loading cycle. As evident in Figure 4.11, when the sample was loaded to a certain stress level, the numerical predictions display that the unloading curve was below the original loading curve, forming plastic hysteresis cycles, as also observed in the experimental results. Moreover, in both numerical and experimental results, the axial strain produced during the loading process did not recover completely during the unloading process, resulting in a residual axial strain at the end of the cycle.

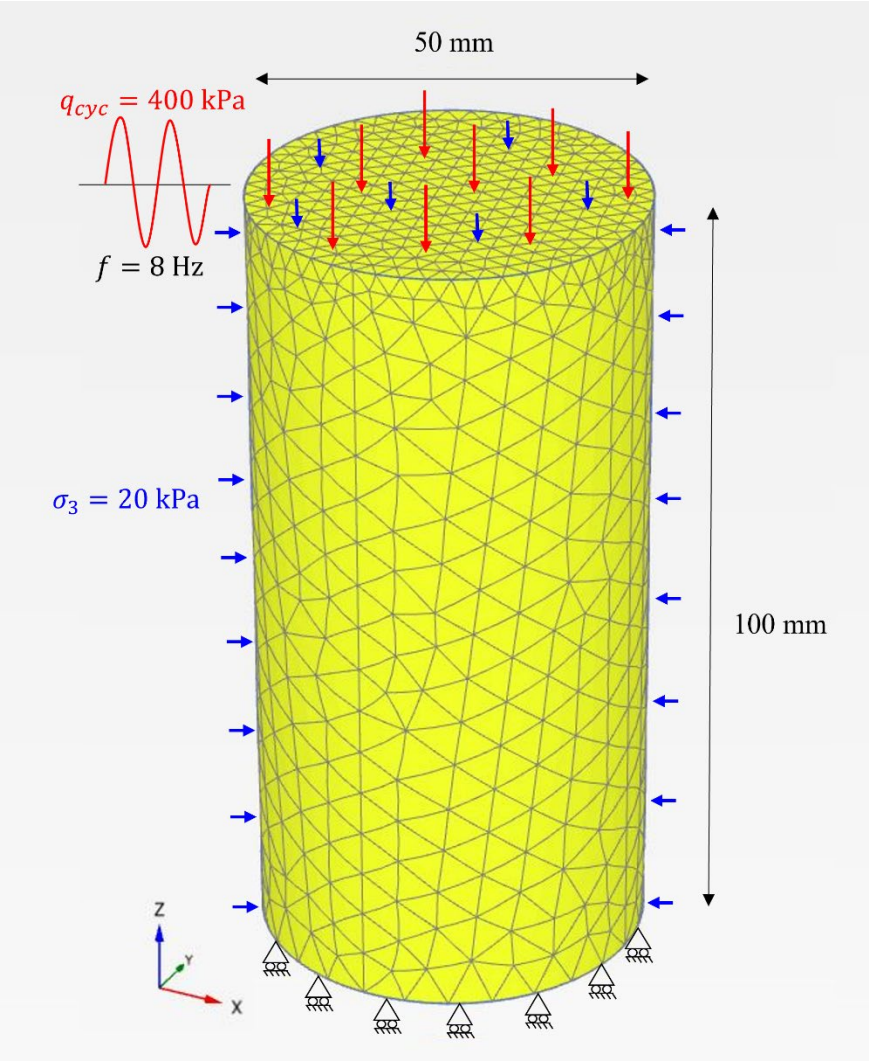

Figure 4.10. Overview of the 3D finite element model.

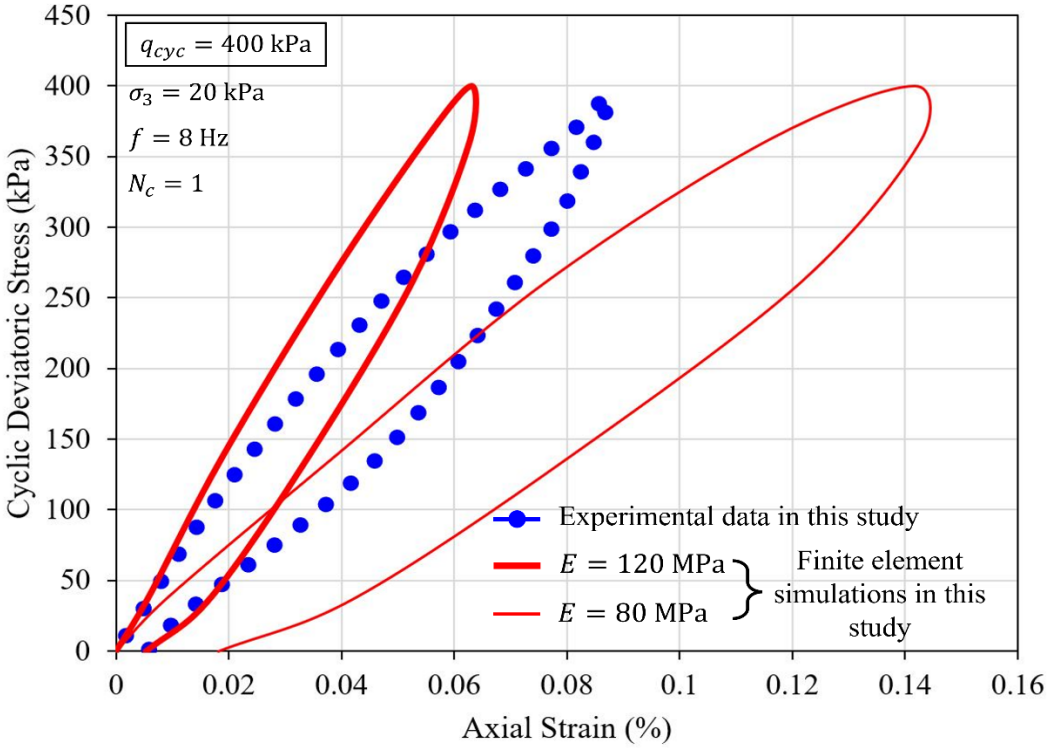

Figure 4.11. Comparison of numerical predictions and laboratory measurements of cyclic stress-strain relationship for $q_{cyc} = 400$ kPa and $\sigma_3 = 20$ kPa.

4.3.3 Critical Dynamic Deviatoric Stress

The critical dynamic deviatoric stress (q_c) reported here is the cyclic deviatoric stress amplitude at which the yielding of the rock joint is initiated under repeated loading. Figure 4.12 presents how critical dynamic deviatoric stress and the corresponding peak deviatoric stress under static loading (q_s) varied with confining stress. Table 4.1 reports the critical dynamic deviatoric stress values and the corresponding critical dynamic shear strength value calculated along the joint plane using Equation (4.3). As shown in Table 4.1 and Figure 4.12, the critical dynamic deviatoric stress was always below the corresponding peak static deviatoric stress. According to Xiao et al. (2009), Momeni et al. (2015) and Jia et al. (2018), cyclic loading often causes rock masses to fail prematurely, i.e., at stress levels lower than the peak strength determined under static

loading conditions. According to Table 4.1, the ratio between critical dynamic deviatoric stress and the corresponding peak deviatoric stress under static loading was in the range of 0.6 – 0.7. It should be noted that the failure of intact rock samples under reduced dynamic stresses with reduction factors in the range of 0.7 - 0.9 was reported in the past by Bieniawski (1967) and Ma et al. (2013). Moreover, as evident in Figure 4.12, the determined critical dynamic deviatoric stresses increased with the confining stress. This behaviour could be due to the slower damage evolution of the jointed rock samples under higher confining stresses.

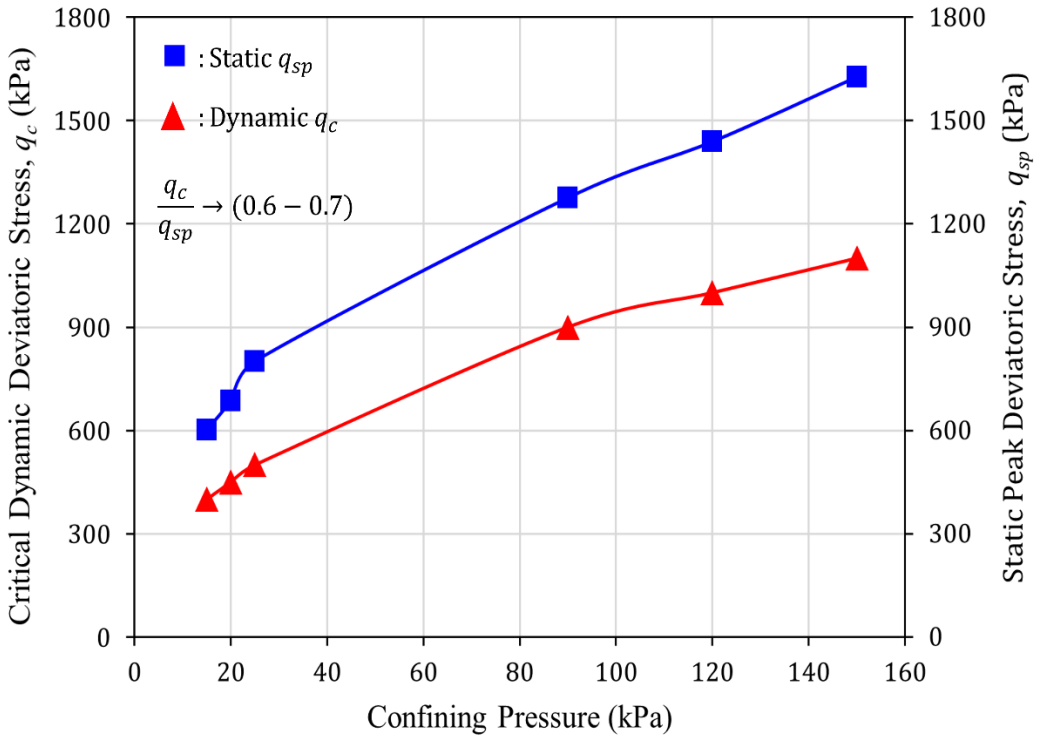

Figure 4.12. Variation of critical dynamic stress and peak deviatoric stress under static loading with confining pressure.

The critical number of cycles (N_c), defined as the cycle number at which the maximum residual axial strain per cycle would occur, were obtained from the results of cyclic triaxial experiments with stress levels in excess of the critical dynamic deviatoric stress. The variation of the critical number of cycles with cyclic stress ratio (CSR) (i.e. cyclic deviatoric stress divided by two times the applied confining pressure) is presented in

Figure 4.13. It is evident that the critical number of cycles was in the range of N_c = 10 - 20. Yet, with the rising CSR, the critical number of cycles showed a slight reduction. This behaviour could be due to the accelerated damage progression of the rock joint when subjected to higher cyclic deviatoric stress or lower confining stress, resulting in an elevated CSR.

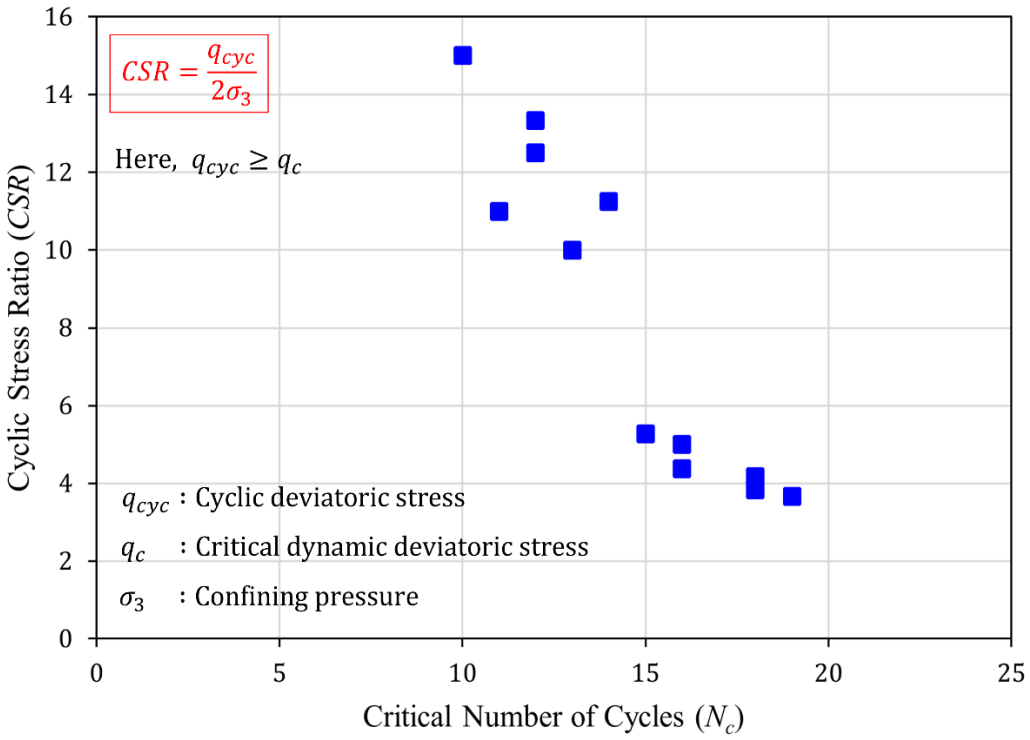

Figure 4.13. Variation of the Critical number of cycles with Cyclic stress ratio.

4.3.4 Residual Axial Strain and Damage Evolution

Figure 4.14 illustrates how cumulative residual axial strain varied with the number of cycles for various confining stresses (i.e. 15 kPa, 25 kPa, 90 kPa and 120 kPa) and increasing cyclic deviatoric stress amplitudes. According to Figure 4.14, at lower cyclic deviatoric stress amplitudes (i.e. $q_{cyc} < q_c$), the cumulative residual axial strain exhibited a gradual increase and eventually tended to stabilise with the progression of cyclic loading. Under such circumstances, the accumulated axial strains were minor, and they

built up very slowly with cyclic loading, such that even after being subjected to thousands of loading cycles, the growth of residual deformation was still so slow, exhibiting no signs of yielding. Nevertheless, when the cyclic deviatoric stress amplitude exceeded the critical dynamic deviatoric stress (i.e. $q_{cyc} \geq q_c$), the residual axial strain rapidly increased during the initial loading cycles and then gradually increased for a few more cycles and tended to stabilise until the end of cyclic loading. Under such conditions, the yielding of the joint was observed only after a few cycles, and the accumulated ultimate residual axial strains were extensive (Figure 4.14). Therefore, the results of this study suggest the existence of a critical cyclic deviatoric stress amplitude (i.e. the critical dynamic deviatoric stress (q_c)) beyond which the yielding of the rock joint progressed remarkably. Comparable observations were also reported by Bagde and Petros (2005a) for intact sandstone specimens and Liu et al. (2021b) for jointed soft rock samples.

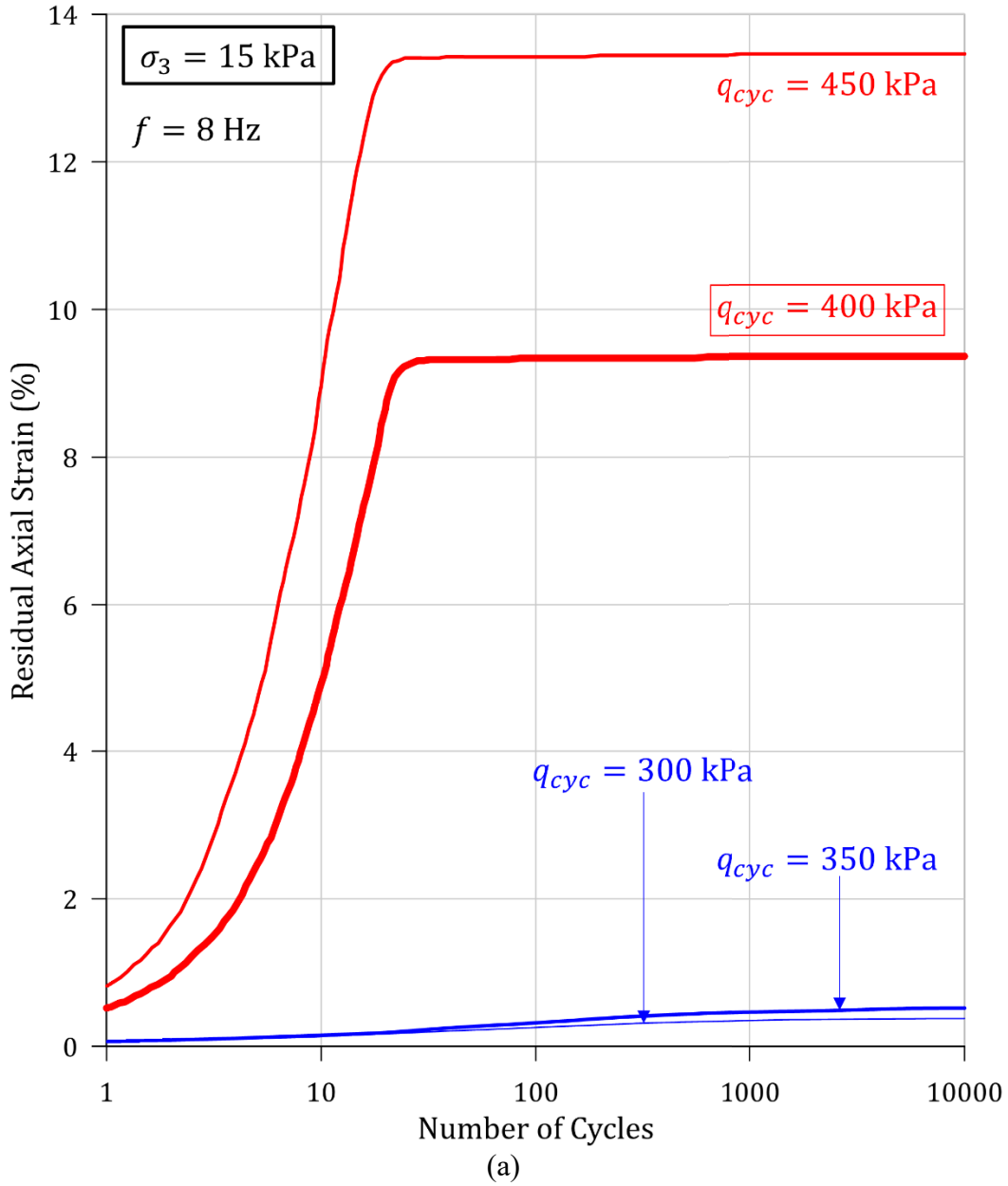
σ_3 = 15 kPa
f = 8 Hz
q_{cyc} = 450 kPa
q_{cyc} = 400 kPa
q_{cyc} = 300 kPa
q_{cyc} = 350 kPa
Residual Axial Strain (%)
Number of Cycles
0
2
4
6
8
10
12
14
1
10
100
1000
10000
(a)

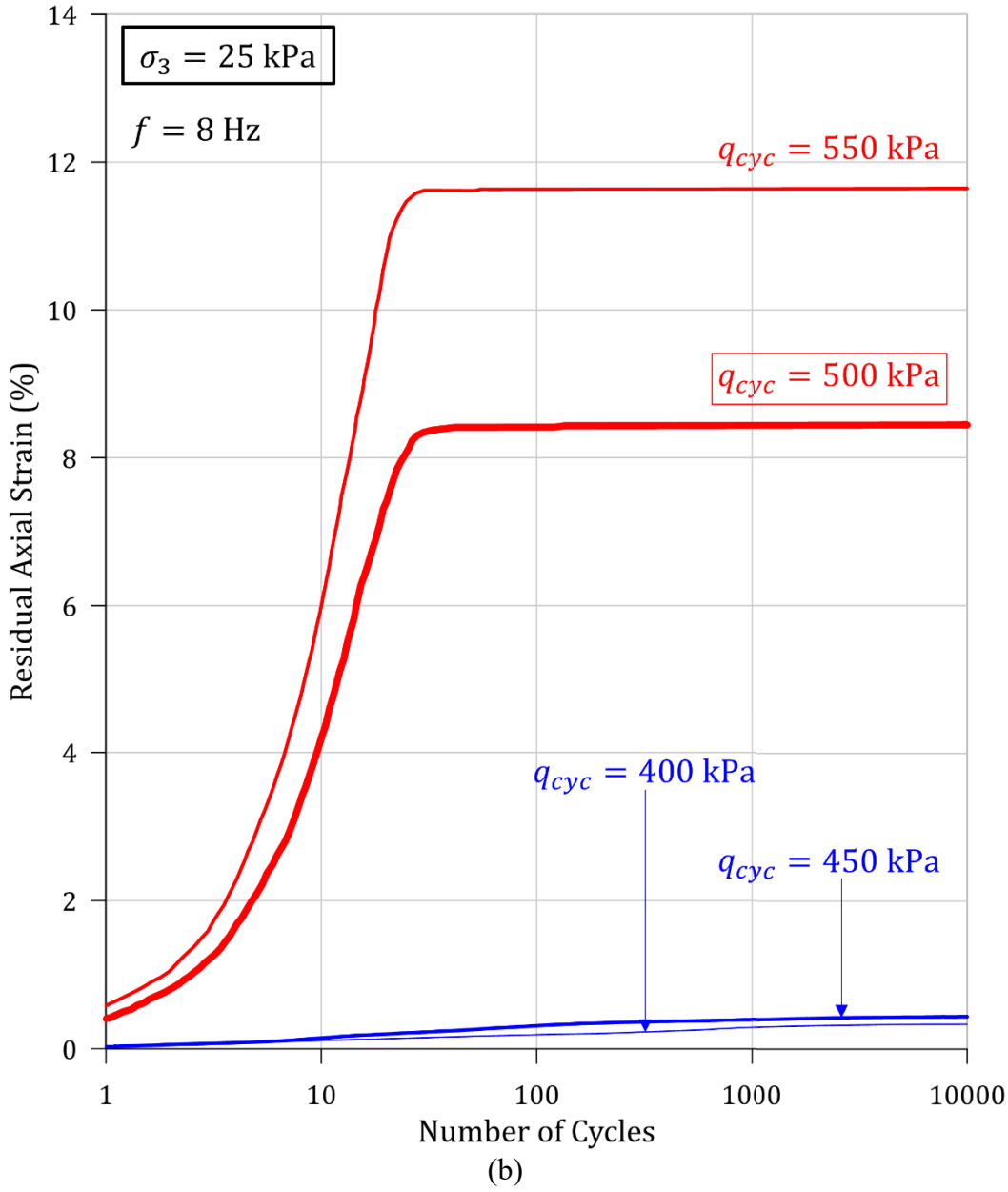
σ_3 = 25 kPa
f = 8 Hz
q_{cyc} = 550 kPa
q_{cyc} = 500 kPa
q_{cyc} = 400 kPa
q_{cyc} = 450 kPa
Residual Axial Strain (%)
Number of Cycles
0
2
4
6
8
10
12
14
1
10
100
1000
10000

(b)

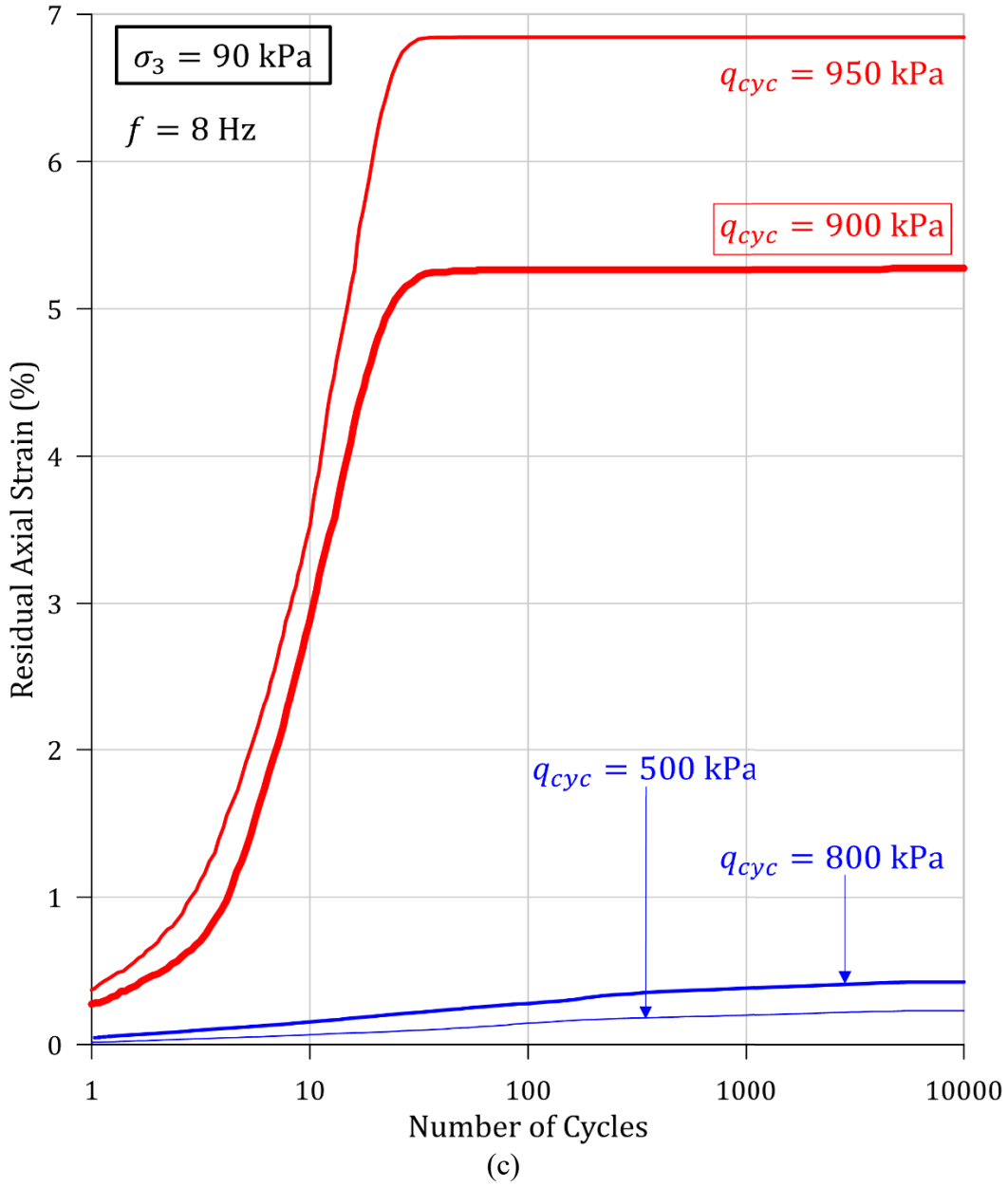
$\sigma_3 = 90$ kPa
$f = 8$ Hz
$q_{cyc} = 950$ kPa
$q_{cyc} = 900$ kPa
$q_{cyc} = 500$ kPa
$q_{cyc} = 800$ kPa
Residual Axial Strain (%)
Number of Cycles
0
1
2
3
4
5
6
7
1
10
100
1000
10000
(c)

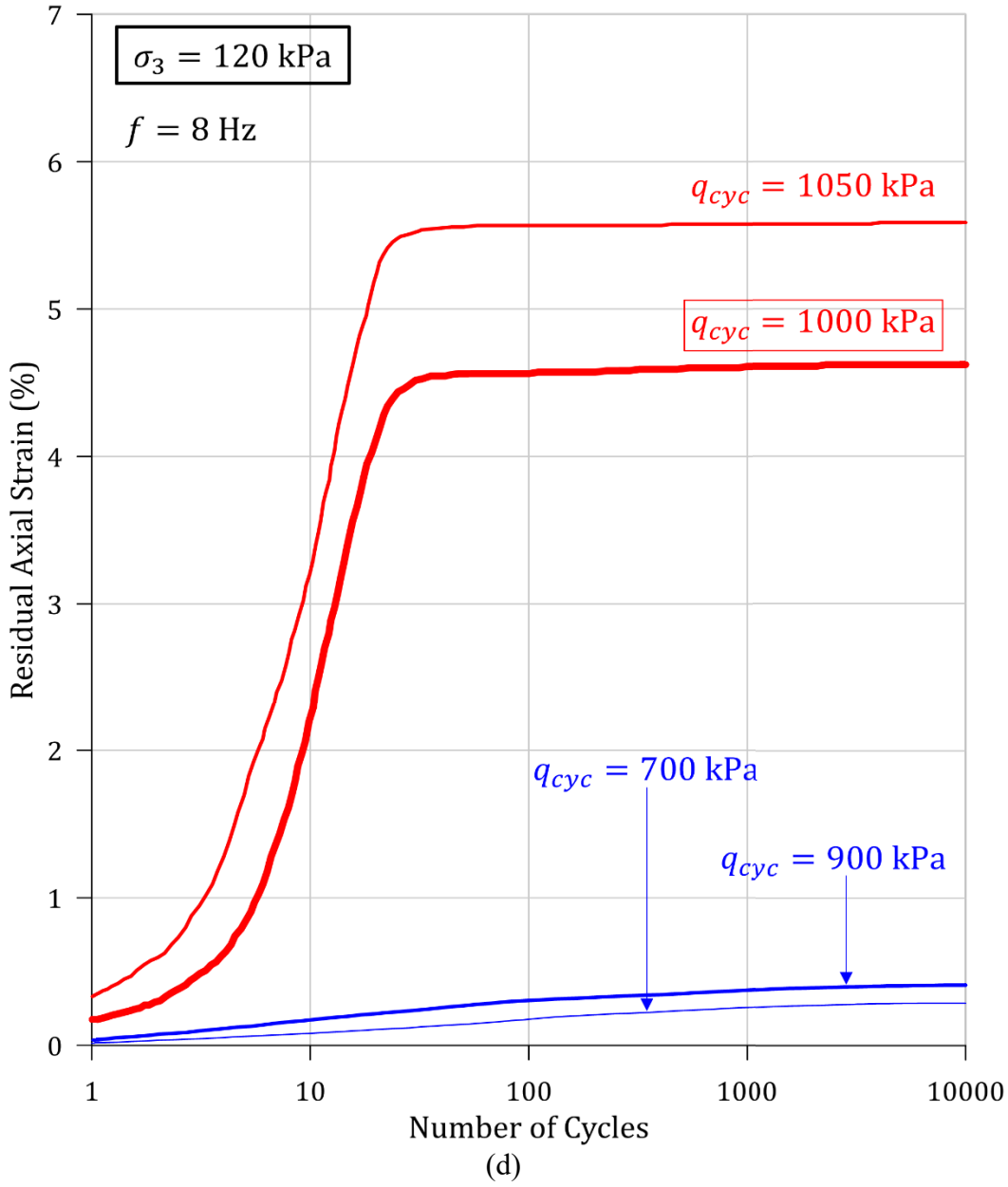

(d)

Figure 4.14. The residual axial strain evolution curves under different cyclic deviatoric stress amplitudes (q_{cyc}) and confining pressures (σ_3) of: (a) 15 kPa; (b) 25 kPa; (c) 90 kPa; and (d) 120 kPa.

The joint surfaces of the newly cast rock joints were scanned and digitised to obtain the initial JRC, which was measured to be JRC_o= 11.51. After completion of the cyclic loading, the rock joints were dismantled from the apparatus and re-scanned and digitised again to obtain the final JRC (JRC_f) values as reported in Figure 4.15. Upon visual inspection of the joint after cyclic loading, under lower cyclic deviatoric stresses (i.e. $q_{cyc} < q_c$), no visible damage to the asperities was observed in either half of the joint. As

a result, the difference between the initial and final JRC values was insignificant. However, when the cyclic deviatoric stress amplitudes exceeded the critical dynamic deviatoric stress threshold (i.e. $q_{cyc} \geq q_c$), substantial damage to the asperities of the rock joints was visually observed. Figure 4.16 presents samples of the damaged surfaces of the rock joints obtained at critical dynamic deviatoric stresses corresponding to the confining pressures of 25 kPa, 90 kPa and 150 kPa.

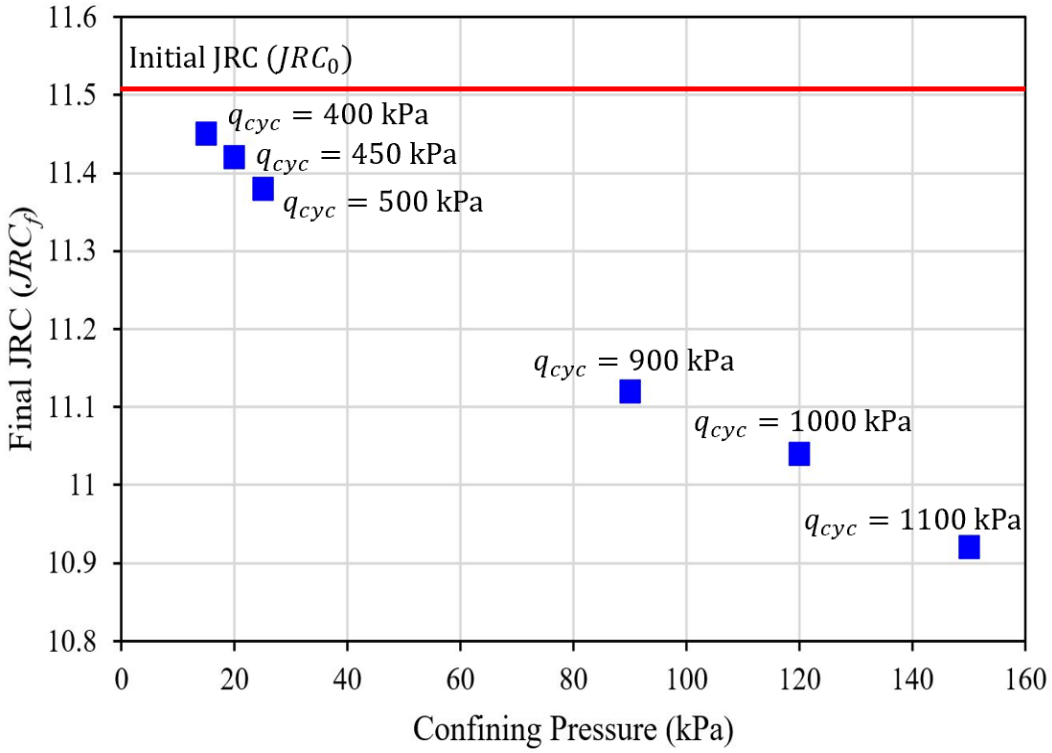

Figure 4.15. Variation of Final JRC values (JRC_f) of jointed rock samples subjected to critical dynamic stress (q_c) with confining pressure (σ_3).

(a)

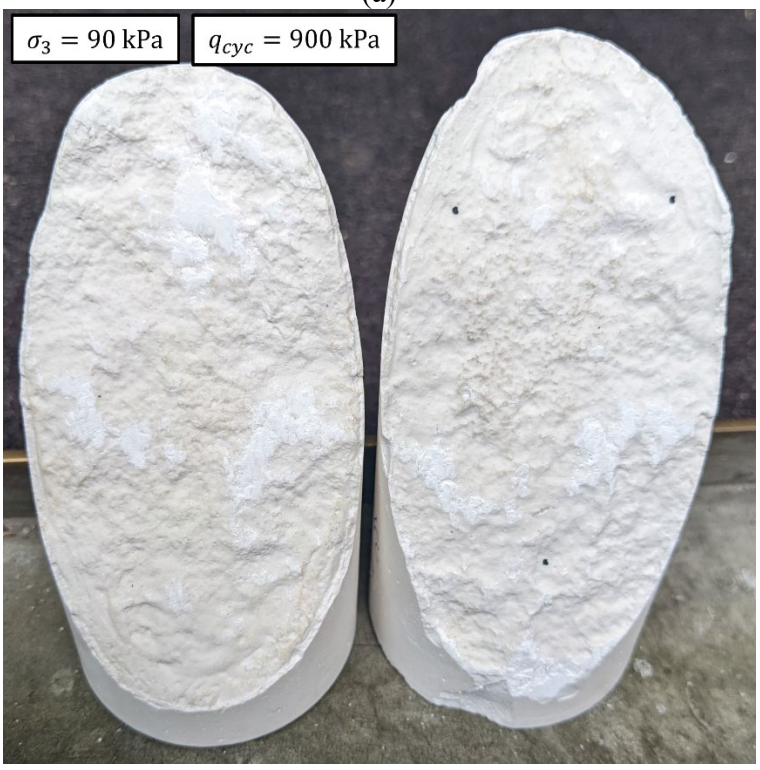

(b)

(c)

Figure 4.16. Samples of damaged surfaces of the jointed rock specimens at peak deviatoric stress amplitude at confining pressures (σ_3) of: (a) 25 kPa; (b) 90 kPa; and (c) 150 kPa.

According to Brady and Brown (1993), the deformation of a natural jointed rock mass occurs as a result of combined asperity sliding and asperity damage. From the mechanical perspective, asperity damage refers to the initiation and growth of micro-cracks within rock masses due to external loading, which may ultimately lead to the emergence of macro-fractures or visible fractures (Martin and Chandler, 1994). Moreover, the deformation behaviour of a natural rock joint is mainly dependent on the strength, size and shape of the asperities, the inclination of the joint and the applied stresses (Lee et al., 2001; Guo et al., 2015; Zhang et al., 2019). Therefore, when subjected to lower cyclic deviatoric stresses, micro-cracks would be generated on the asperities of the joint surface along with slight sliding of the asperities. However, these micro-cracks are unlikely to propagate into macro-cracks. On the other hand, when stresses exceed the critical dynamic deviatoric stress, formation of micro-cracks on the asperities is inevitable. These

micro-cracks would grow into macro-cracks, subsequently triggering macroscopic damage and excessive deformations of the rock joints, as also evident from Figures 4.14 and 4.16.

As evident from Figure 4.16, the damage sustained by the rock joints was predominantly localised to certain areas of the joint surface, possibly to areas with the highest asperities. Upon subjecting the rock joints to cyclic loading, the micro-cracks evolved into macro cracks, which consequently damaged the tips of the highest asperities on the joint surface. During this deformation process, the degraded materials accumulated on the valleys of the joint surface depending on the shear direction and formed into the gouge. According to Huang et al. (1993), this rubblised degraded material in the valleys of the joint surface usually becomes very firmly compacted and reattached to the joint surface, as also observed in the tested samples. Moreover, the surface of the rubblised asperity gouge and sheared-off asperity heads was smooth, as in a planar joint surface.

Figure 4.15 presents how the final JRC values under the critical dynamic deviatoric stresses varied with confining pressure. The ultimate residual axial strain (ε_{pu}) reported here is the cumulative residual axial strain attained by the rock joints upon the completion of cyclic loading. Referring to Table 4.1 and Figures 4.14 – 4.16, as the confining stress augmented, the critical dynamic deviatoric stress increased while the corresponding ultimate residual axial strain decreased. Simultaneously, there was an increase in damage to the asperities of the joint surface, which led to a subsequent reduction in the final JRC of the joint surface. Accordingly, under the effect of high confinement, deformation of the joint is restricted, and the cyclic stresses should be high enough to cause asperity damage and deformation of the joint. It should be noted that at such conditions, asperity damage will be dominated over asperity overriding.

4.3.5 Prediction of Cumulative Residual Axial Strain

Over the years, several empirical and analytical models have been proposed to predict the cyclic cumulative deformation behaviours of various geomaterials. Among them, the power equation proposed by Monismith et al. (1975) has been widely used with modifications to predict cumulative plastic deformation of various geomaterials. Referring to Figure 4.14, under lower cyclic deviatoric stresses (i.e., when $q_{cyc} < q_c$), the ultimate residual axial strains developed in the rock joints were insignificant in comparison to the strains incurred under higher cyclic deviatoric stresses (i.e., when $q_{cyc} \geq q_c$). Moreover, referring to Figure 4.14, the cumulative residual axial strain curves exhibited an upward trend as the cyclic deviatoric stress amplitude increased and confining stress diminished. Notably, the critical dynamic deviatoric stress is a function of joint properties such as joint inclination, roughness and strength that would influence the residual axial strains developed in the rock joint. Therefore, the number of cycles, applied cyclic deviatoric stress, confining stress and critical dynamic deviatoric stress were considered as independent parameters required for formulating an empirical relationship to predict residual axial strain (ε_p), as in Equation (4.4), based on the experimental results reported in Figure 4.14.

$$\varepsilon_p = \begin{cases} \alpha.\left(N^{\beta}\right).\tanh(\beta * N).\left[\dfrac{R_q}{(1+1/CSR)}\right]^{\lambda}, & q_{cyc} \geq q_c \\ 0, & q_{cyc} < q_c \end{cases} \tag{4.4a}$$

where,

$$R_q = \frac{q_{cyc}}{q_c} \tag{4.4b}$$

$$CSR = \frac{q_{cyc}}{2\sigma_3} \tag{4.4c}$$

$$q_c = Kq_{sp} \tag{4.4d}$$

where, N is the number of cycles, R_q is the dynamic deviatoric stress ratio, q_{cyc} is the applied cyclic deviatoric stress, q_c is the critical dynamic deviatoric stress, CSR is the cyclic stress ratio, σ_3 is the applied confining stress and q_{sp} is the peak deviatoric stress under static triaxial loading condition. In this study, the critical dynamic deviatoric stress determined from the cyclic triaxial experiments was correlated to the peak deviatoric stress under static loading via Equation (4.4d), where K was determined to be 0.68. Additionally, α, β and λ are empirical constants obtained based on data fitting exercise, which depend on joint characteristics such as joint roughness, inclination, and JCS. It should be noted that since the value of cyclic deviatoric stress amplitude for each loading cycle could slightly deviate from the target input value, particularly when the sample experience large deformations, a weighted average of cyclic deviatoric stress amplitude was used for each test as recommended by ASTM D5311-13 (2013) and reported in Equation (3.6).

In this study, the values of the empirical constants were obtained through a nonlinear regression analysis programmed in MATLAB using the Nonlinear Least Squares method and Trust-Region Algorithm as α = 7.843, β = 0.068 and λ = 5.488. Figure 4.17 presents the predicted residual axial strains from Equation (4.4) versus the laboratory measurements in the 3D space, while Figure 4.18 illustrates the same in the 2D space for the confining stresses of 25 kPa and 90 kPa as examples.

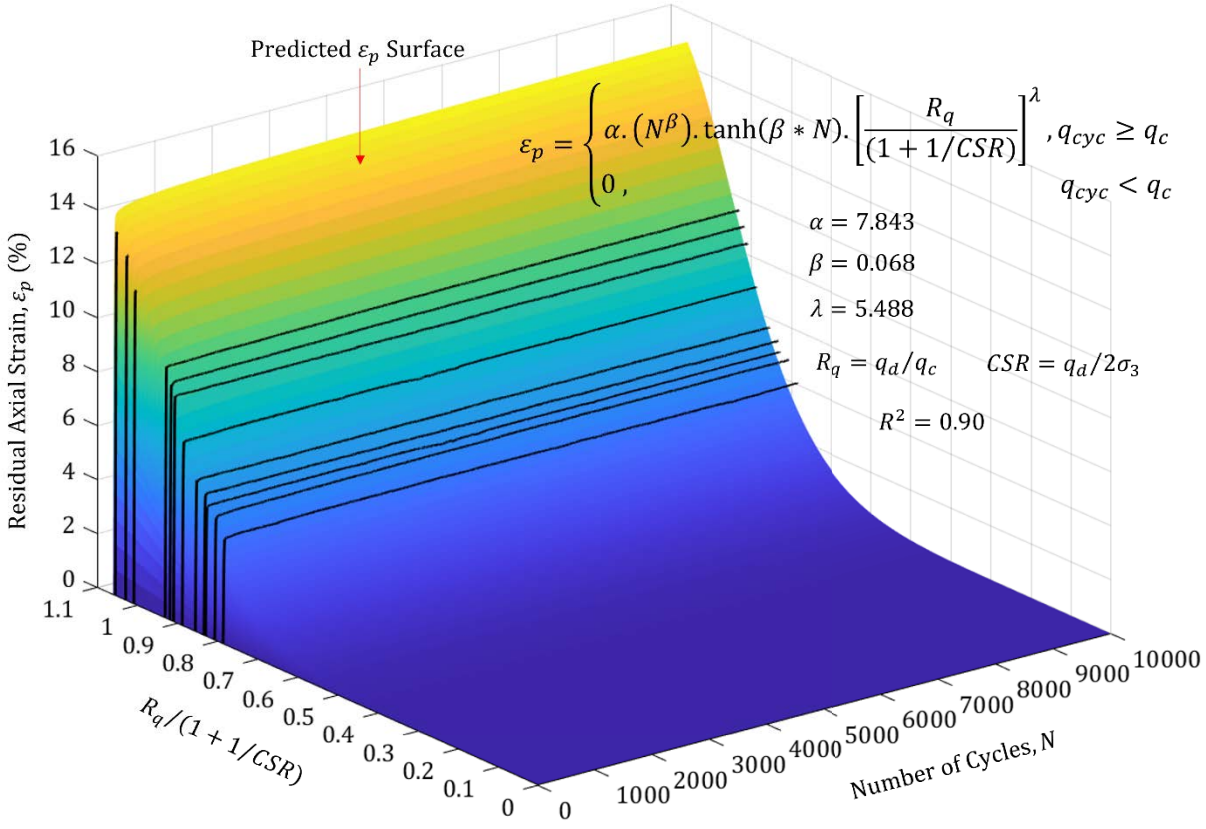

Figure 4.17. Variation of actual and predicted residual axial strain (ε_p) in the 3D space.

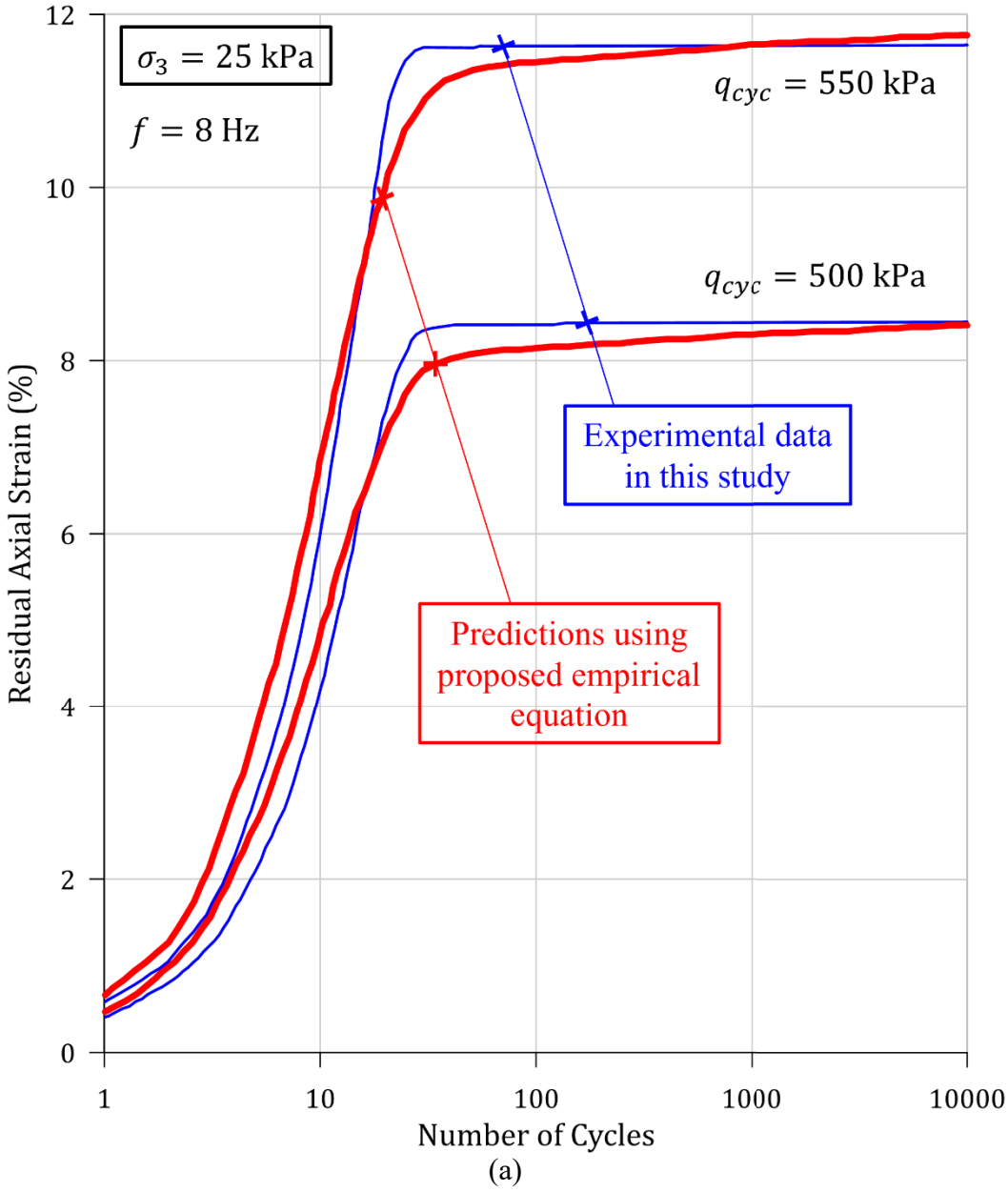
σ_3 = 25 kPa
f = 8 Hz
q_{cyc} = 550 kPa
q_{cyc} = 500 kPa
Experimental data in this study
Predictions using proposed empirical equation
Residual Axial Strain (%)
Number of Cycles
0
2
4
6
8
10
12
1
10
100
1000
10000
(a)

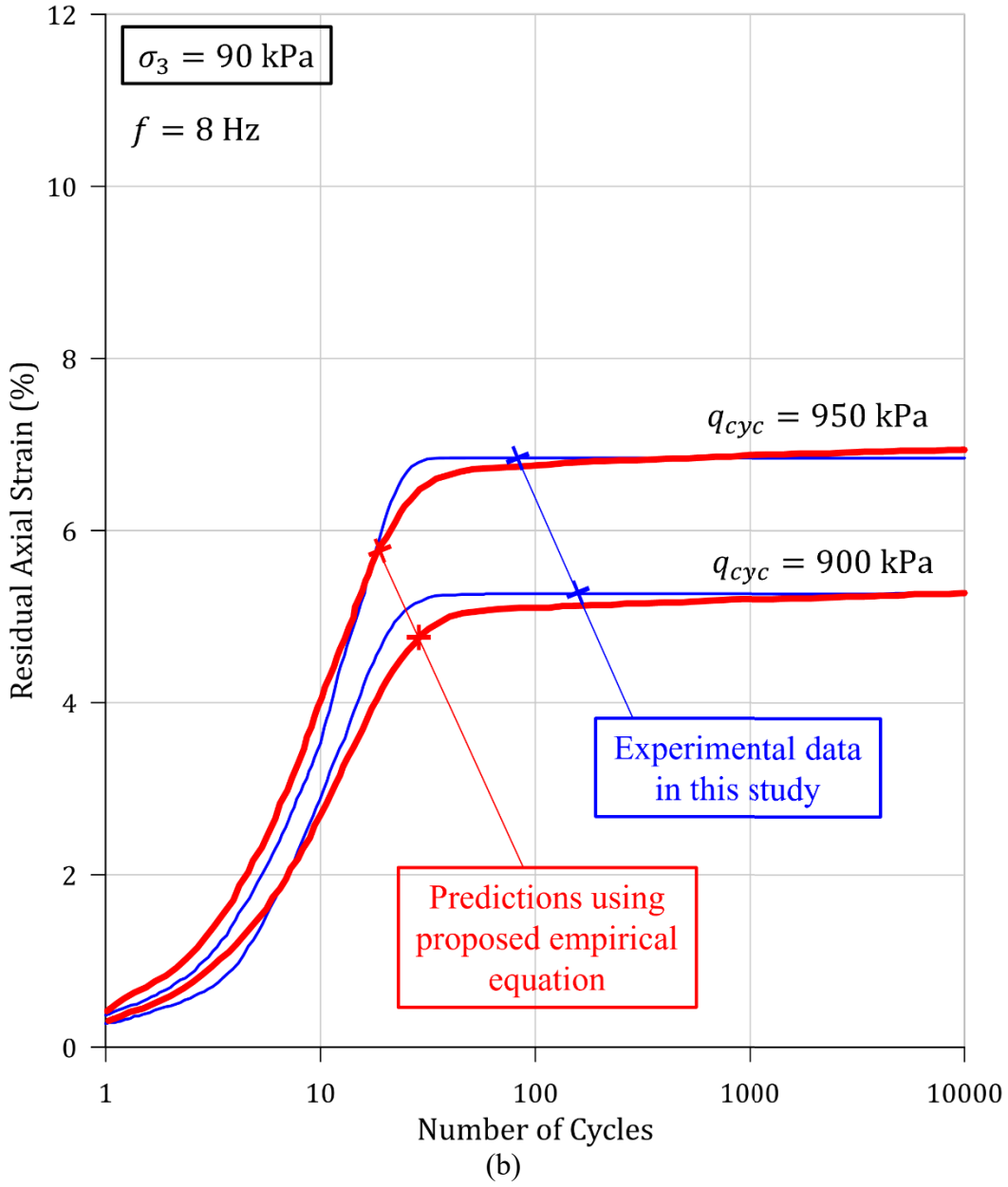

Figure 4.18. The predicted and experimentally obtained residual axial strain evolution curves under cyclic deviatoric stress amplitudes (q_{cyc}) exceeding the critical dynamic stress and confining pressures (σ_3) of: (a) 25 kPa; and (b) 90 kPa.

4.3.6 Resilient Modulus

The resilient modulus (M_R) is a parameter that can capture elastic deformation characteristics during the cyclic loading-unloading process. In fact, it specifically captures the unloading characteristics of the tested specimens related to the reversible axial strains recovered during the unloading process and is defined by Equation (3.7).

Figure 4.19 presents the variation of resilient moduli with the number of loading cycles for the confining stresses of 20 kPa, 90 kPa and 150 kPa and increasing cyclic deviatoric stress amplitudes. According to Figure 4.19, at lower cyclic deviatoric stresses (i.e., when $q_{cyc} < q_c$), the resilient moduli gradually degraded with increasing loading cycles, ultimately reaching a state of stabilisation. For cyclic deviatoric stresses exceeding the critical dynamic deviatoric stress (q_c), the degradation of the resilient moduli was quite rapid during the initial loading cycles, followed by a gradual slowing of the rate of degradation and eventually stabilised over the course of subsequent loading cycles. Comparable trends for the evolution of resilient moduli with the number of loading cycles were also reported by Fuenkajorn and Phueakphum (2010), Ma et al. (2013) and Wang et al. (2013) for intact rock samples and Liu et al. (2018b) and Zheng et al. (2020a) for jointed rock samples.

As evident in Figure 4.19, at lower cyclic deviatoric stresses, the slight degradation of resilient moduli during the initial loading cycles and the subsequent stabilisation during the rest of the loading cycles could be attributed to the formation of micro-fractures and slight asperity sliding, which did not amplify into macroscopic deformations or significant joint damage. When the applied cyclic stresses exceeded the critical dynamic deviatoric stress, the substantial degradation of the resilient moduli could be due to the amplification of micro-cracks into macro fractures accompanied by asperity sliding,

causing notable damage to the joint surface. Moreover, Figure 4.19 illustrates that the deterioration of the resilient moduli reduced at higher confining stresses. This behaviour could be attributed to greater restriction provided by increased confinement to the evolution of damage and asperity sliding in rock joints, as also reported by Liu et al. (2011).

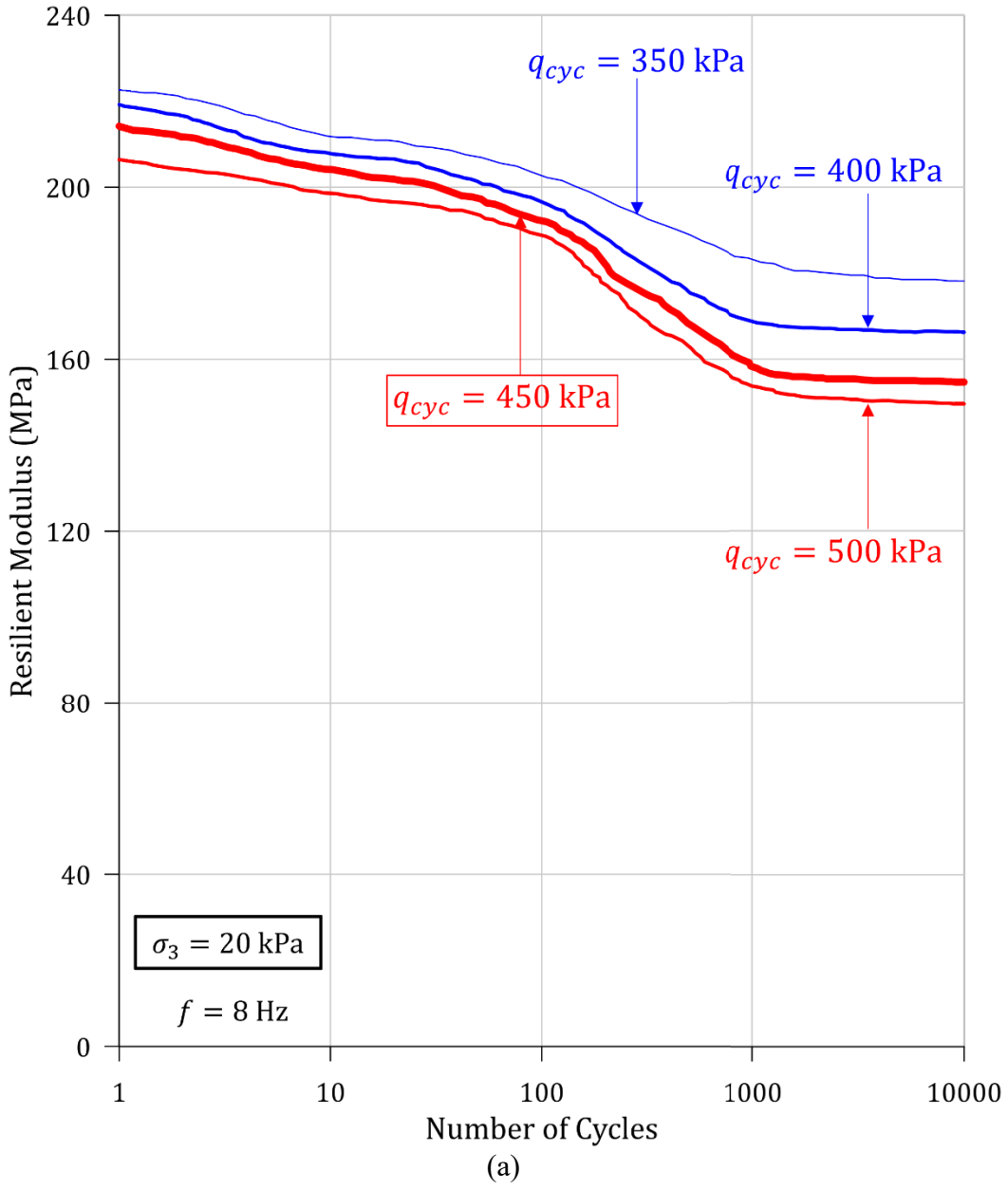

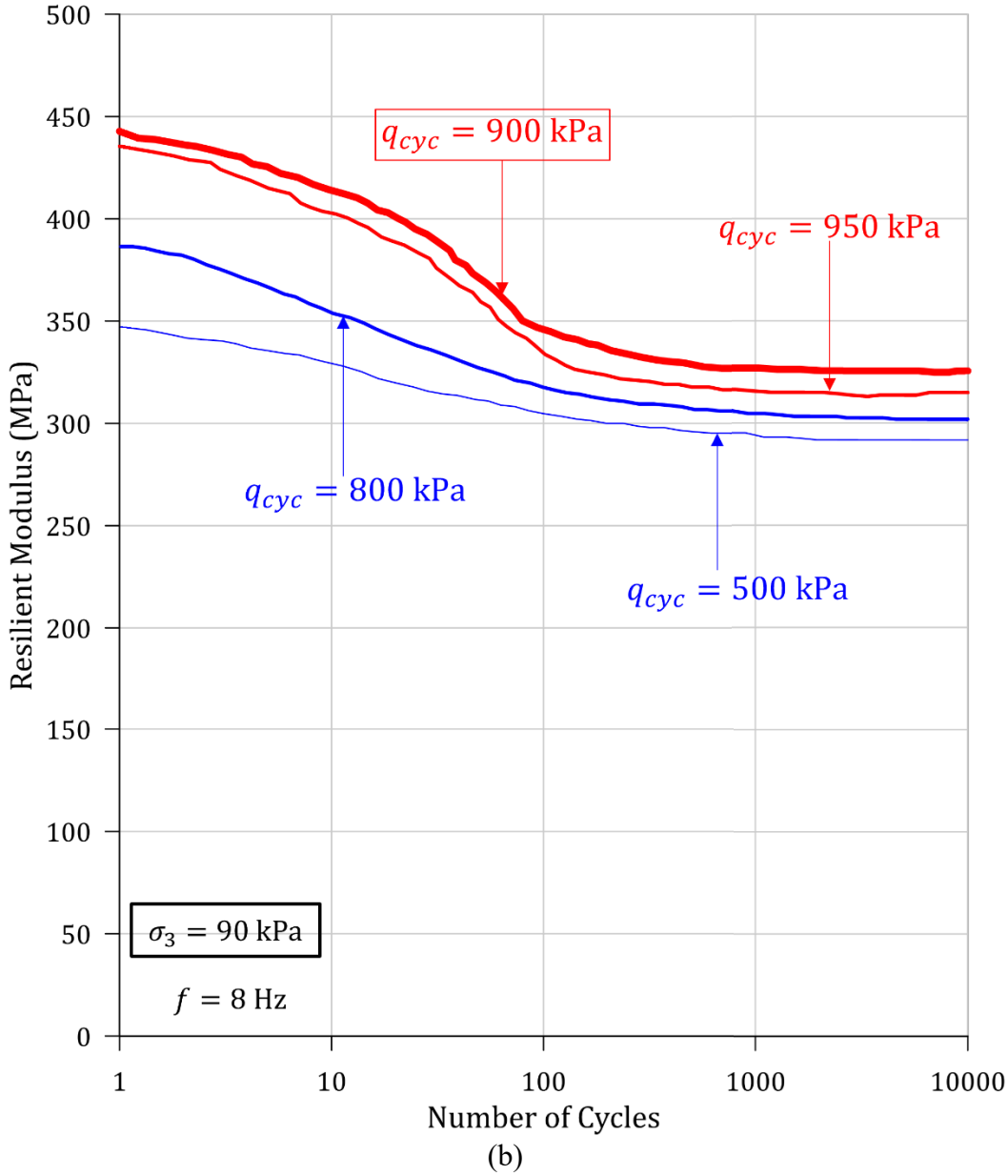
500
450
400
350
300
250
200
150
100
50
0
Resilient Modulus (MPa)
q_{cyc} = 900 kPa
q_{cyc} = 950 kPa
q_{cyc} = 800 kPa
q_{cyc} = 500 kPa
σ_3 = 90 kPa
f = 8 Hz
1
10
100
1000
10000
Number of Cycles
(b)

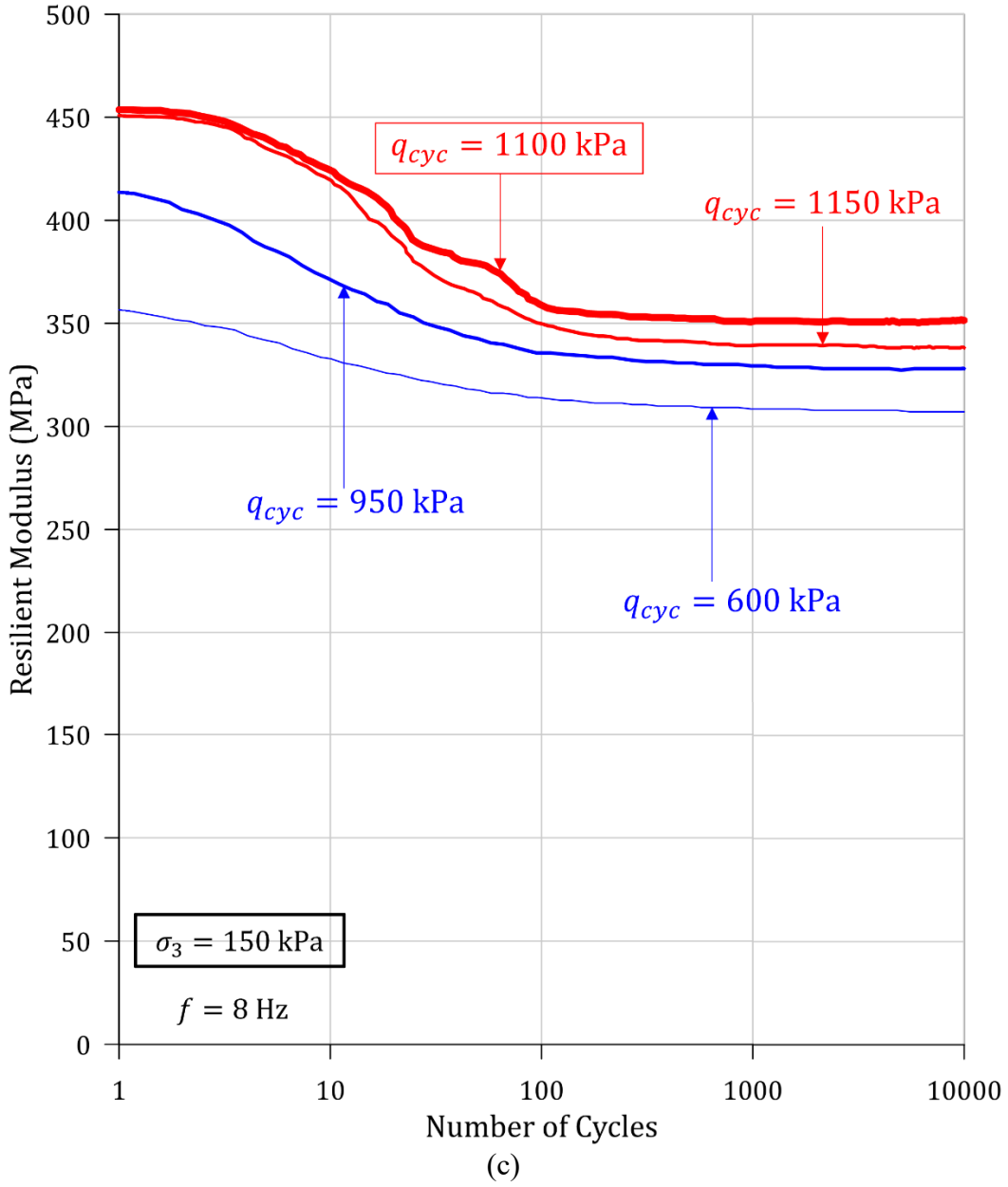

Figure 4.19. The resilient modulus evolution curves under different cyclic deviatoric stress amplitudes (q_{cyc}) and confining pressures (σ_3) of: (a) 20 kPa; (b) 90 kPa; and (c) 150 kPa.

4.3.7 Dynamic Energy Evolution and Damping Response

The deformation and failure mechanism of rock masses can be explained from the perspective of energy evolution based on energy theories and principles. For cyclic triaxial experiments, dissipated energy can be determined from the cyclic stress-strain response of the rock joints illustrated in Figures 4.6 – 4.8. As shown in Figure 2.8, the area of the hysteresis loop captures the energy dissipated from the rock joint in a given cycle. More precisely, the area of the hysteresis loops in the cyclic stress-strain curves provides the dissipated energy density. When it is multiplied by the sample volume, the dissipated energy during loading-unloading cycles can be determined. In this study, a MATLAB code was developed to calculate the area within the hysteresis loop in each cycle, adopting data collected from the cyclic triaxial tests.

Figure 4.20 presents how the dissipated energy density per load cycle varied with the number of loading cycles. As evident in Figure 4.20, at lower cyclic deviatoric stresses (i.e., when $q_{cyc} < q_c$), the dissipated energy density slightly increased and decreased promptly during the initial loading cycles and reached a steady state gradually. Referring to Figure 4.20, when the cyclic stresses exceeded the critical dynamic deviatoric stress (i.e., when $q_{cyc} \geq q_c$), the dissipated energy density escalated to an exorbitant value, followed by a dramatic decrease during the initial loading cycles and reached stabilisation gradually. Comparable trends for the evolution of dissipated energy with the number of loading cycles when $q_{cyc} < q_c$ were also stated by Momeni et al. (2015) and Yang et al. (2018b) for intact rock specimens, and Liu et al. (2017 & 2018b) for intermittently jointed rock samples. When $q_{cyc} \geq q_c$, comparable trends were also reported by Zhang et al. (2017) for intact red sandstone specimens.

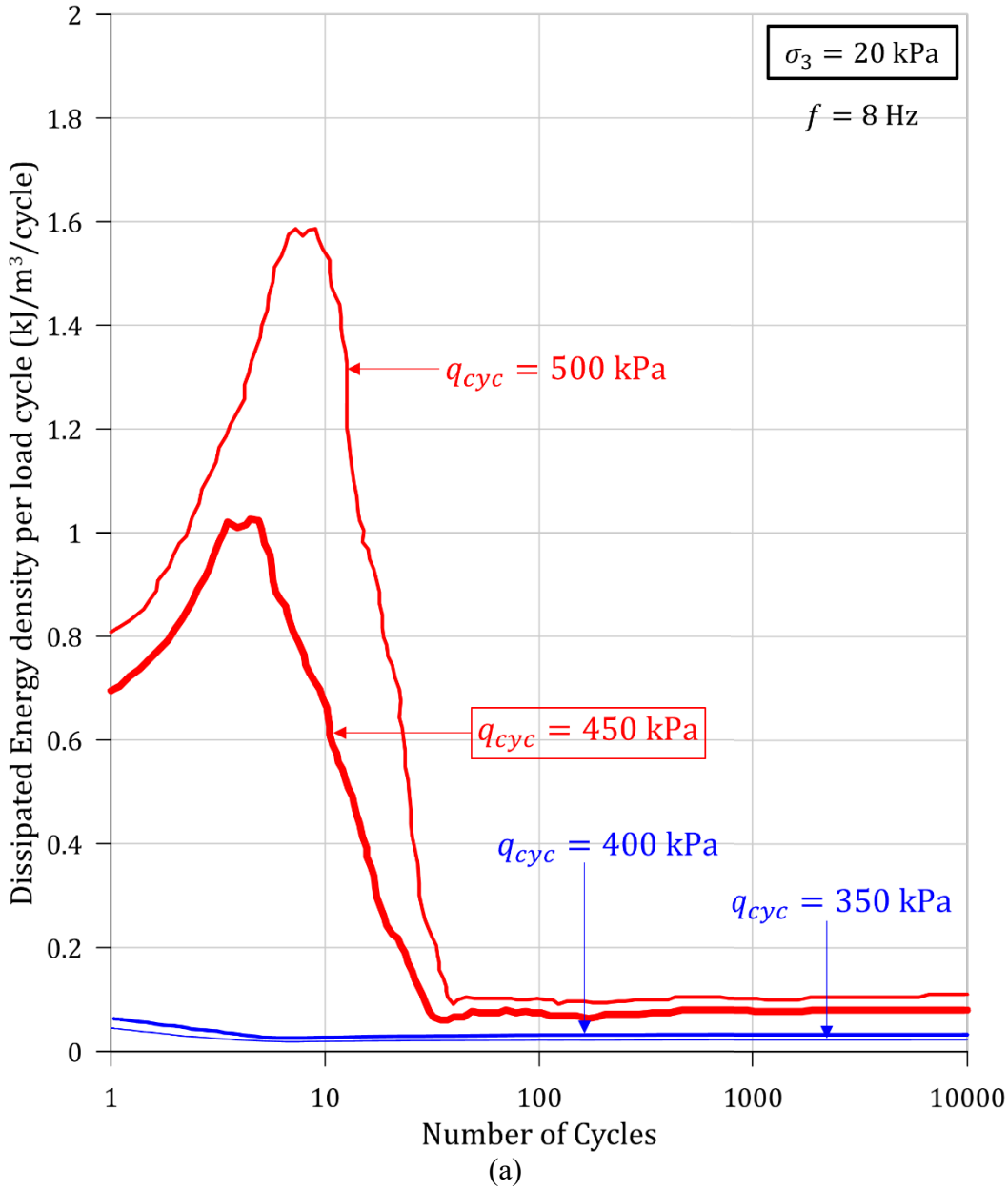
σ_3 = 20 kPa
f = 8 Hz
q_{cyc} = 500 kPa
q_{cyc} = 450 kPa
q_{cyc} = 400 kPa
q_{cyc} = 350 kPa
Dissipated Energy density per load cycle (kJ/m^3/cycle)
Number of Cycles
0
0.2
0.4
0.6
0.8
1
1.2
1.4
1.6
1.8
2
1
10
100
1000
10000
(a)

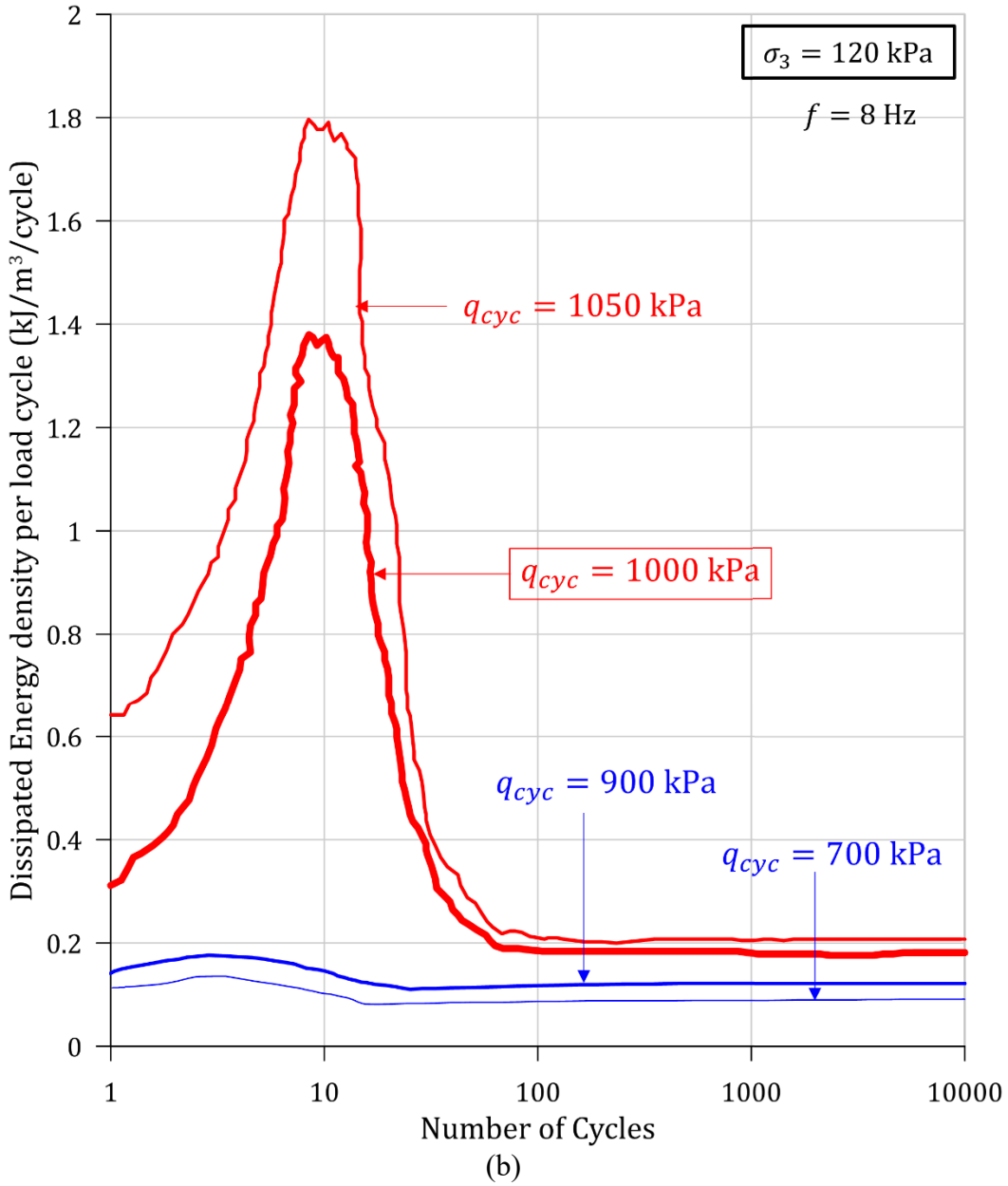
σ_3 = 120 kPa
f = 8 Hz
q_{cyc} = 1050 kPa
q_{cyc} = 1000 kPa
q_{cyc} = 900 kPa
q_{cyc} = 700 kPa
Dissipated Energy density per load cycle (kJ/m^3/cycle)
Number of Cycles
0
0.2
0.4
0.6
0.8
1
1.2
1.4
1.6
1.8
2
1
10
100
1000
10000
(b)

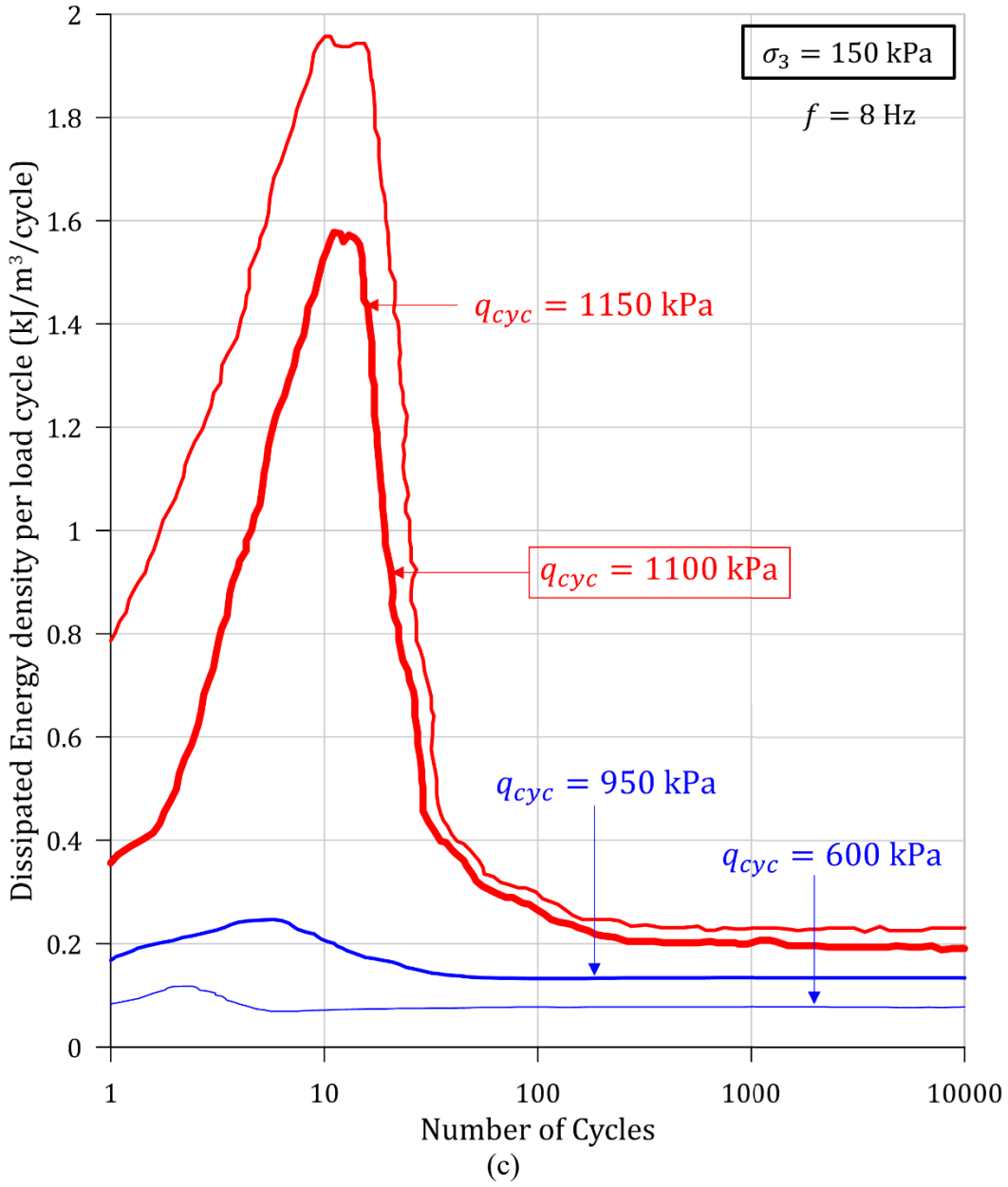

Figure 4.20. The evolution of dissipated energy at different cyclic deviatoric stress amplitudes (q_{cyc}) and under confining pressures (σ_3) of: (a) 20 kPa; (b) 120 kPa; and (c) 150 kPa.

Figure 4.21 illustrates how initial dissipated energy density per load cycle and steady-state dissipated energy density per load cycle values varied with applied cyclic deviatoric stress amplitudes for the confining stresses of 20 kPa and 120 kPa. The initial dissipated energy per load cycle (ΔE_{di}) and steady-state dissipated energy per load cycle (ΔE_{ds}) reported here are the calculated values of dissipated energy densities of the first loading cycle and final loading cycle, respectively. Here, the weighted average values of cyclic

deviatoric stress amplitudes, calculated using Equation (3.6), were used to plot results in Figure 4.21. Referring to Figures 4.20 and 21, both initial dissipated energy per load cycle and steady-state dissipated energy per load cycle values increased with cyclic deviatoric stress amplitude. However, the initial dissipated energy per load cycle values at cyclic stresses beyond the critical dynamic deviatoric stress threshold (i.e. $q_{cyc} \geq q_c$) were significantly larger than the corresponding values at lower cyclic deviatoric stresses (i.e. $q_{cyc} < q_c$).

As stated by Zhang et al. (2017), Song et al. (2020) and He et al. (2021b), the dissipated energy reflects work done on the initiation, propagation and coalescence of cracks in a rock mass exposed to loading-unloading conditions. i.e., dissipated energy causes irreversible material deterioration and plastic deformation of the rock joints. Accordingly, at lower cyclic deviatoric stresses, a substantial portion of the input energy was dissipated (as also explained by Liu et al. (2017)), causing some irreversible deformations during the initial loading cycles. As the dissipated energy under the applied cyclic stress was insufficient to amplify the micro-cracks into macro cracks, the dissipated energy progressively decreased and stabilised (see Figure 4.20), causing the irreversible deformation of the joint to progressively decrease and stabilise (see Figure 4.14). When the applied cyclic stress exceeded the critical dynamic deviatoric stress, a massive portion of the input energy was dissipated, which escalated during the initial loading cycles (see Figure 4.20). This energy dissipation caused the amplification of the micro-cracks into macro cracks, accompanied by significant asperity sliding, resulting in extensive irreversible degradation and deformation of the joint (see Figure 4.14). Since the cyclic loading application was continued even after the joint reached the ultimate residual deformation, the dissipated energy promptly decreased and stabilised (see Figure 4.20), causing the accumulated residual deformation of the joint to reach a steady state (see

Figure 4.14). i.e., the rock joints which underwent extensive deformation during the initial loading cycles regained stability and the capacity to accumulate energy causing the dissipated energy to decrease promptly, as also reported by Zhang et al. (2017). Nevertheless, plastic deformation and damage to the rock joint resulted in a decrease in the energy storage capacity, causing the percentage of dissipated energy to not revert to prior levels, as displayed in Figure 4.21.

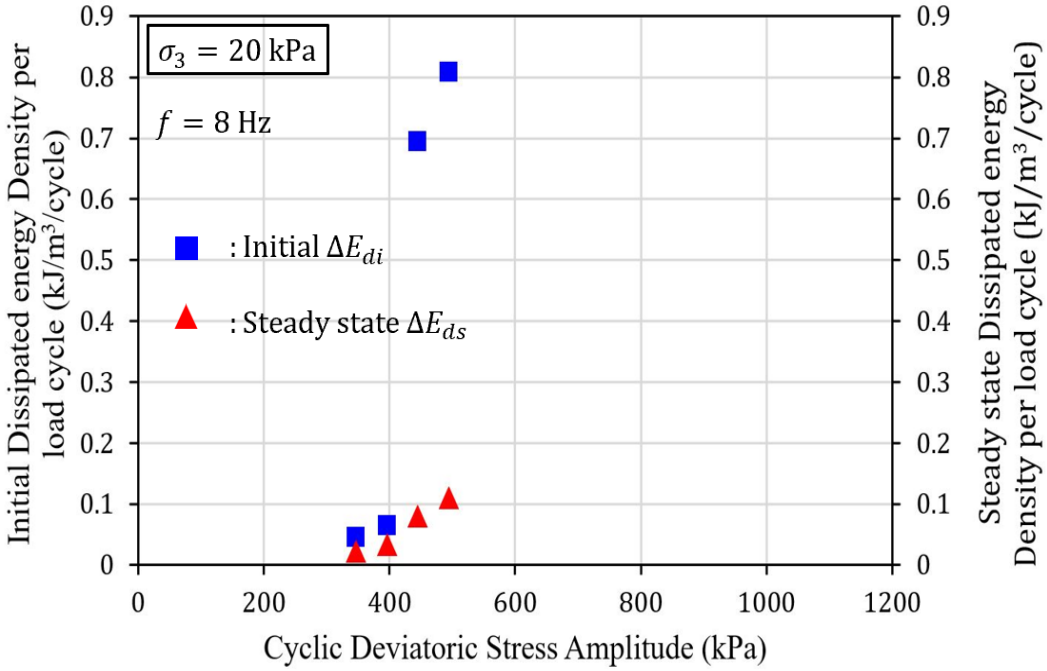

(a)

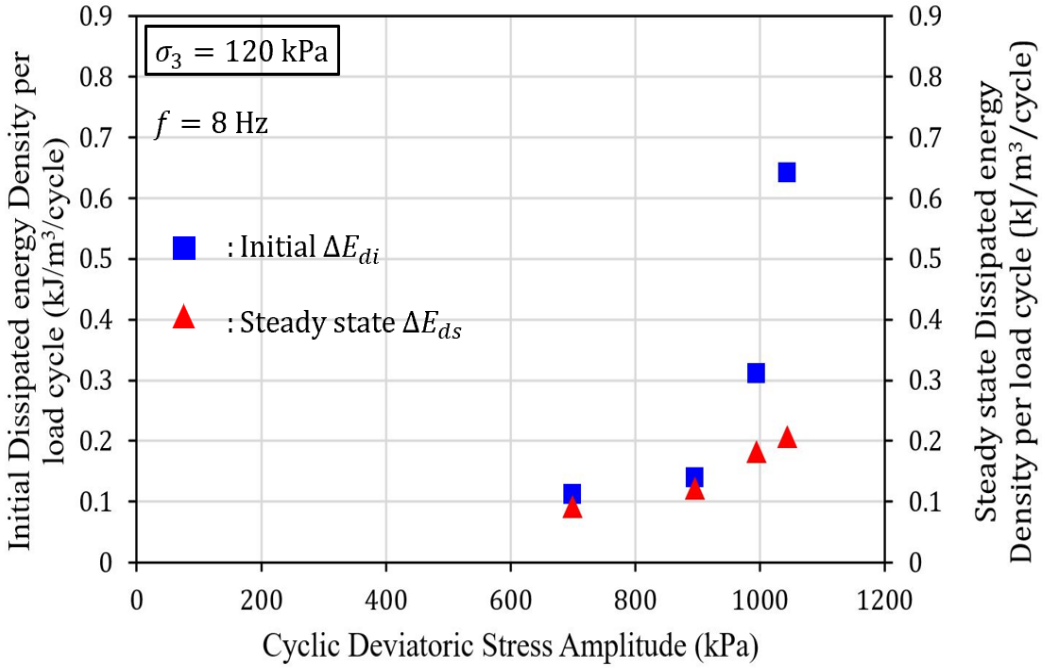

(b)

Figure 4.21. Variation of initial dissipated energy density and steady-state dissipated energy density per load cycle with cyclic deviatoric stress amplitude (q_{cyc}) at confining pressures (σ_3) of: (a) 20 kPa; and (b) 120 kPa.

The damping ratio for a given hysteresis loop in cyclic triaxial testing can be determined from Equation (2.2). Figure 4.22 presents how the damping ratio per load cycle values evolved with the number of cycles for various cyclic deviatoric stress amplitudes and confining stresses. As shown in Figure 4.22, the damping ratio decreased eminently during the initial loading cycles, then recovered slightly and stabilised with the progression of cyclic loading. The descent of the damping ratio during the initial loading cycles was more abrupt when the applied cyclic stresses exceeded the critical dynamic deviatoric stress (see Figure 4.22).

The initial damping ratio per load cycle (ξ_i) and steady-state damping ratio per load cycle (ξ_s) stated here are the calculated damping ratio values of the first loading cycle and final loading cycle, respectively. As evident from Figure 4.22, the initial damping ratio values increased when cyclic deviatoric stress amplitudes increased. Nevertheless, when the applied cyclic stresses surpassed the critical dynamic deviatoric stress, the initial damping

ratio values escalated notably. Referring to Figure 4.22, the values of the initial damping ratio were in the range of 40% - 80% when subjected to high cyclic stresses (i.e. $q_{cyc} \geq q_c$), whereas at low cyclic stresses (i.e. $q_{cyc} < q_c$), the initial damping ratio values were in the range of 5% - 35%. Nevertheless, the steady-state damping ratio values were below 12% under all the tested cyclic deviatoric stress amplitudes and confining stresses.

Accordingly, when lower cyclic stresses were applied (i.e. $q_{cyc} < q_c$), a significant portion of the input energy was dissipated (see Figure 4.20) than being stored as elastic energy during the initial loading cycles, resulting in some residual deformation of the joint and considerably higher damping ratios. Since the applied load was insufficient to cause macroscopic damage and residual deformation, the damping ratio decreased and reached a steady state. When the applied cyclic stresses exceeded the critical dynamic deviatoric stress (i.e. $q_{cyc} \geq q_c$), a significant portion of the input energy was dissipated (see Figure 4.20), allowing a minimum amount of stored elastic energy, resulting in macroscopic deformation of the joint and extensive damping ratios during the initial loading cycles, as illustrated in Figure 4.22. Under these higher cyclic stresses (i.e. $q_{cyc} \geq q_c$), as the cyclic loading continued, the accumulated residual axial deformation stabilised (see Figure 4.14) while the damping ratio decreased and stabilised with further loading.

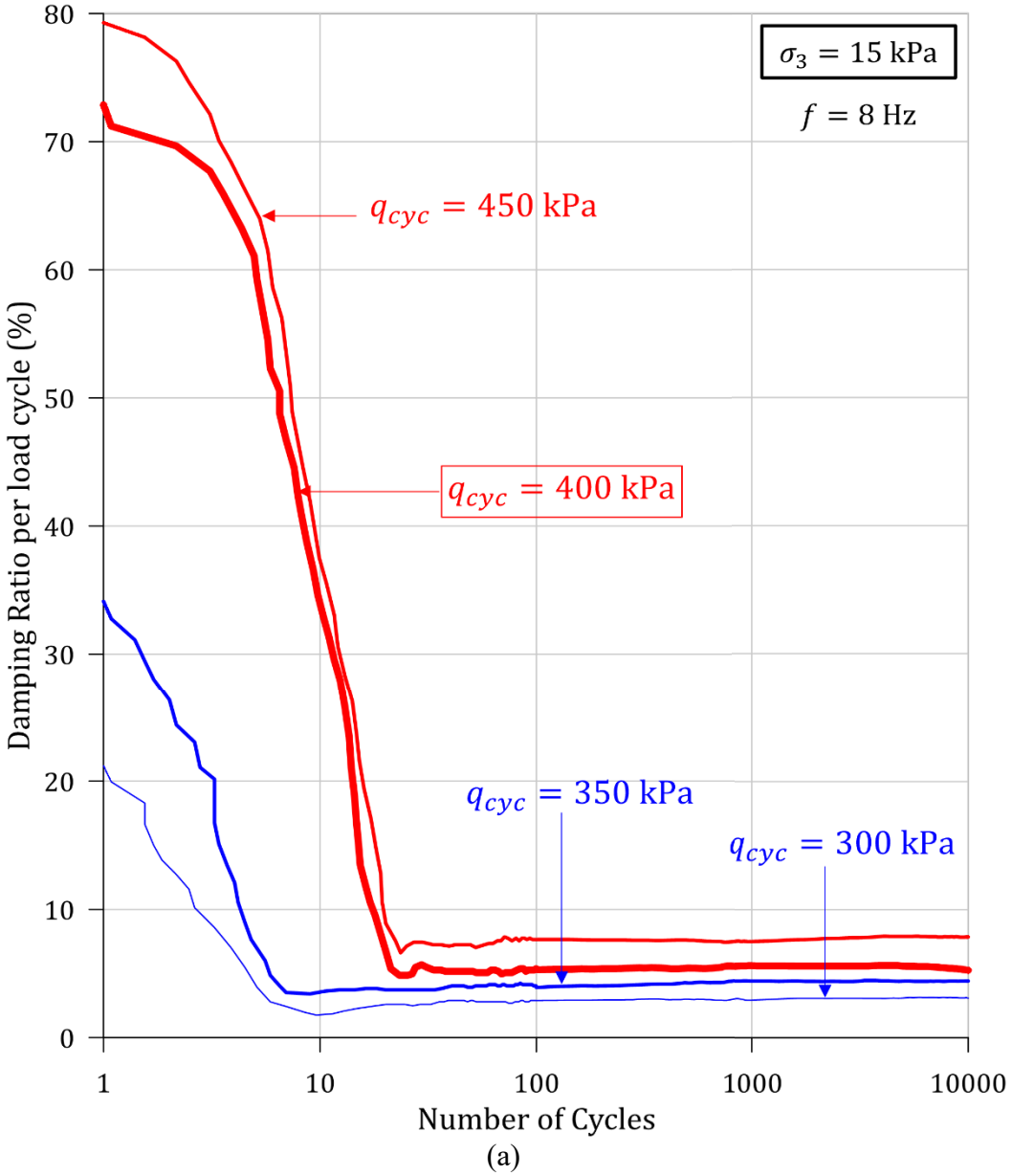
σ_3 = 15 kPa
f = 8 Hz
q_{cyc} = 450 kPa
q_{cyc} = 400 kPa
q_{cyc} = 350 kPa
q_{cyc} = 300 kPa
Damping Ratio per load cycle (%)
Number of Cycles
0
10
20
30
40
50
60
70
80
1
10
100
1000
10000
(a)

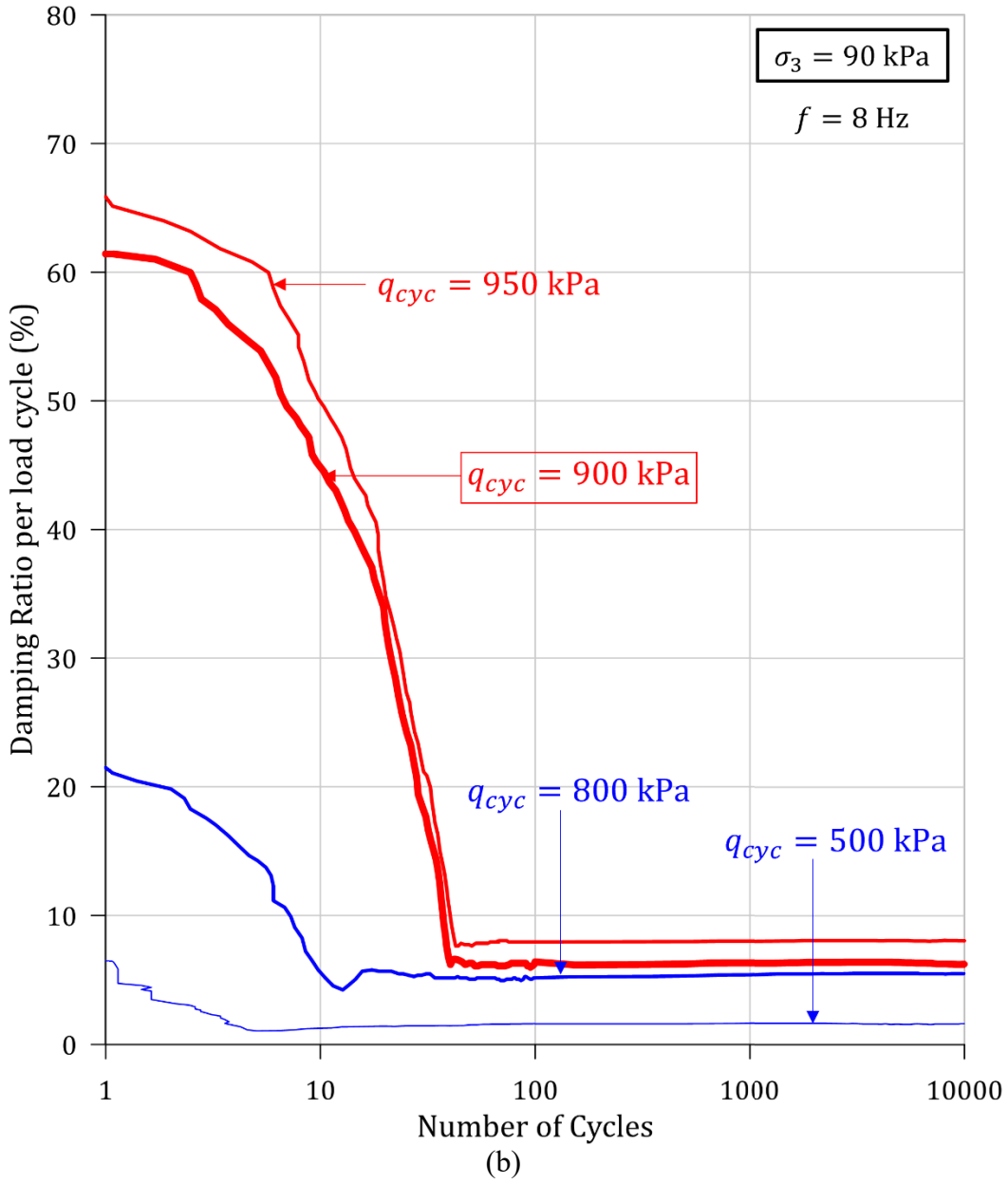
σ_3 = 90 kPa
f = 8 Hz
q_{cyc} = 950 kPa
q_{cyc} = 900 kPa
q_{cyc} = 800 kPa
q_{cyc} = 500 kPa
Damping Ratio per load cycle (%)
Number of Cycles
0
10
20
30
40
50
60
70
80
1
10
100
1000
10000
(b)

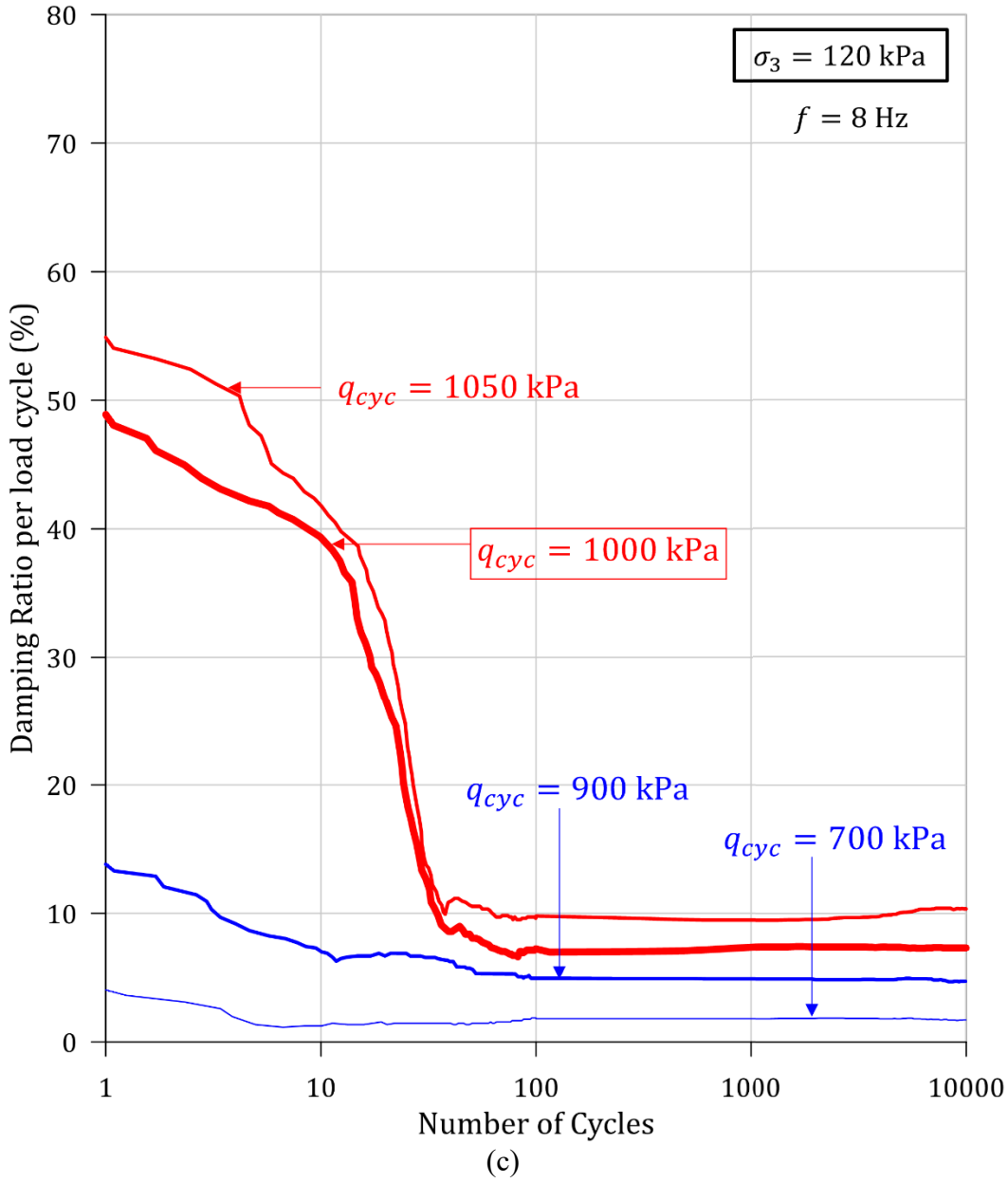

Figure 4.22. The evolution of damping ratio at different cyclic deviatoric stress amplitudes (q_{cyc}) under confining pressures (σ_3) of: (a) 15 kPa; (b) 90 kPa; and (c) 120 kPa.

4.4 Summary

This study explored the impact of confining stress and cyclic deviatoric stress amplitude below or in excess of the critical dynamic deviatoric stress on the deformation response and dynamic characteristics of jointed rocks under cyclic triaxial loading conditions. The results disclosed a critical dynamic deviatoric stress existed beyond which the yielding of the rock joint occurred. The ratio between critical dynamic deviatoric stress and the corresponding static peak deviatoric stress was in the range of 0.6 – 0.7, and the critical dynamic deviatoric stress increased with confining pressure. When the applied cyclic deviatoric stresses exceeded the critical dynamic deviatoric stress threshold, there was a substantial increase in the accumulated residual axial strain, damage to the asperities on the joint surface and degradation of the resilient moduli with increasing loading cycles. Moreover, the dissipated energy density and damping ratio per load cycle values were extensive during the initial loading cycles at cyclic deviatoric stresses in excess of the critical dynamic deviatoric stress threshold. An empirical relationship was proposed to predict the residual axial strain evolution with loading cycles of rock joints for cyclic deviatoric stress amplitudes in excess of the critical dynamic deviatoric stress.

Chapter 5: Stiffness and Damping Characteristics of Jointed Rocks Under Cyclic Triaxial Loading Subjected to Prolonged Cyclic Loading

5.1 General

Rock formations and rock structures are often exposed to repeated loads resulting from earthquakes, rock blasting, rock bursts, drilling and repeated wheel loading. Besides, it is well established that different materials exhibit different responses under cyclic loading conditions. For instance, some materials become stronger and more ductile under cyclic loading, while others become weaker and more brittle (Bagde and Petros 2005a). Moreover, fatigue is a well-known mechanism contributing to the weakening of various materials, including rocks, under prolonged cyclic stresses of lower magnitude than their monotonic strength (Attewell and Farmer 1973; Singh 1989). Thus, under prolonged cyclic loading, rock masses will inevitably be exposed to certain fatigue damage, deformation and a reduction in the long-term strength caused by the changes in the mechanical properties of the rock mass. The gradual deterioration of the rock may even result in instability and fatigue failure of the rock masses, leading to catastrophic accidents and disasters. Therefore, it is of great significance to explore the fatigue characteristics of rocks, to precisely assess the long-term stability and safety of rock engineering projects.

The fatigue behaviour and mechanical properties of intact rocks exposed to repeated loading have been investigated extensively. Burdine (1963), Attewell and Farmer (1973), Singh (1989) and Tien et al. (1990) were pioneers who employed uniaxial and triaxial cyclic loading experiments to analyse the fatigue behaviour of various intact rock types. Later Bagde and Petros (2005a & 2009), Xiao et al. (2010), Wang et al. (2013), Song et al. (2013), Fan et al. (2016), Voznesenskii et al. (2017), Yang et al. (2018b), Vaneghi et

al. (2020) and Liu et al. (2021a) explored the fatigue mechanism and the impact of various factors on the fatigue characteristics of various intact rocks subjected to repeated loading. Moreover, Xiao et al. (2010) and Yang et al. (2018b) developed fatigue damage variables to explain the fatigue damage evolution process in various intact rocks by analysing the experimental results.

Furthermore, it is well known that the dynamic response of geomaterials and their mechanical properties are dependent on the strain level (Wichtmann et al. 2017; Jia 2018). The mechanical properties, especially small strain parameters, are vital for the numerical analysis of geotechnical problems associated with designing new soil and rock structures exposed to vibration or cyclic fatigue loading. In particular, stiffness and damping parameters are two of the most critical dynamic mechanical properties that characterise the dynamic behaviour of rocks. Therefore, proper knowledge of the small-strain stiffness and damping parameters of rocks and their evolution with increasing strain levels is essential to predict more realistic responses to conduct rigorous dynamic stability and deformation analyses of rock structures. For instance, during the planning and design phases of novel surface and underground rail infrastructure projects, vibration analyses of the rail track structure, subgrade and adjacent structures are carried out to predict vibration levels. For such analyses, a broad understanding and precise quantification of dynamic characteristics such as small-strain stiffness and damping parameters of the rail subgrade is essential to predict the vibration levels accurately. Such knowledge is vital for proposing and executing cost-effective and efficient vibration control and attenuation measures during the construction phase of these projects rather than retroactively employing new vibration mitigation strategies post-construction while the railway lines would be in service.

Moreover, natural rock formations are heterogeneous and typically consist of discontinuities such as joints, fractures, faults and other planes of weaknesses, especially at shallow depths. The existence of such discontinuities substantially impacts the strength, deformability and overall stability of the rock masses (Belem et al. 2006; Xie et al. 1997; Huang et al. 1993). Therefore, some researchers have investigated a few of the fatigue and dynamic properties of jointed rocks subjected to cyclic loading for a relatively lower number of cycles. For example, Brown and Hudson (1973) conducted a preliminary experimental study to explore the fatigue failure mechanism and fatigue characteristics of jointed rocks by applying cyclic uniaxial compression loading on highly idealised block-jointed specimens. Later, Li et al. (2001b), Liu et al. (2018b), Lin et al. (2020), and He et al. (2021a) conducted cyclic uniaxial compression experiments on intermittent rock joints to investigate the impact of various cyclic loading parameters (i.e., cyclic deviatoric stress and frequency) and joint geometric configurations (i.e., joint density and inclination) on the fatigue deformation characteristics, fatigue energy and damage evolution and fatigue failure behaviour. Furthermore, Zheng et al. (2020b) evaluated fatigue and damage properties of jointed mudstone samples with various joint dip angles and loading frequencies under cyclic triaxial compression loading. Furthermore, Liu et al. (2018a) explored the shear mechanism for fatigue damage in jointed rocks by conducting cyclic direct shear experiments on rock joints with first-order and second-order triangular asperities.

Yet, there is a lack of experimental studies focussing on jointed rocks with continuous penetrating joints replicating a natural rough joint surface tested under cyclic triaxial conditions. In the meantime, a systematic study on the dynamic characteristics, such as small-strain stiffness and damping parameters, and analysis of their evolution with strain level of rock joints exposed to prolonged cyclic loading has not been conducted.

Therefore, this study experimentally investigates the fatigue response and dynamic properties of modelled rock joints with a natural replicated joint surface subjected to prolonged cyclic loading corresponding to train loading conditions. Indeed, this study delivers an important reference and quantifies variation of dynamic parameters such as stiffness and damping ratio with strain level under various confining stresses corresponding to the surface and underground railway conditions. The cyclic triaxial experiments were performed on jointed rock samples with a natural replicated joint surface inclined at a mean dip angle of 60^{o} under confining stresses in the range of 15 kPa – 300 kPa. The monotonic stress-strain response, cyclic stress-strain response, residual axial strain evolution, Young's moduli, resilient moduli and damping ratio variation with the strain level were analysed and discussed in detail.

5.2 Laboratory Investigation

5.2.1 Sample Preparation

A thorough laboratory experiment series was conducted to investigate the stiffness and damping characteristics of rock joints, utilising a set of modelled rock joints that featured a natural joint surface. The model rock joints were cast using a mixture of gypsum plaster ($CaSO_4.H_2O$ hemihydrates, 98%) and water mixed in a ratio of 3.5:1 by weight. The natural joint surface replicated in the model rock joints was obtained by splitting a sandstone block and copying the split rough rock surface to a mould-making rubber. Cylindrical hollow moulds made with acetal plastic and cylindrical silicon rubber moulds with each side of the natural joint surface were required to cast the model rock joints (see Figure 5.1(a)). The cylindrical jointed rock specimens had a diameter of 50mm and an overall height of 100mm (when both halves of the specimen were fully mated), with the

joint surface oriented at a mean dip angle of 60° (see Figure 5.1(b)). Further details on the sample preparation procedure were reported in Sections 3.2.1 and 4.2.1.

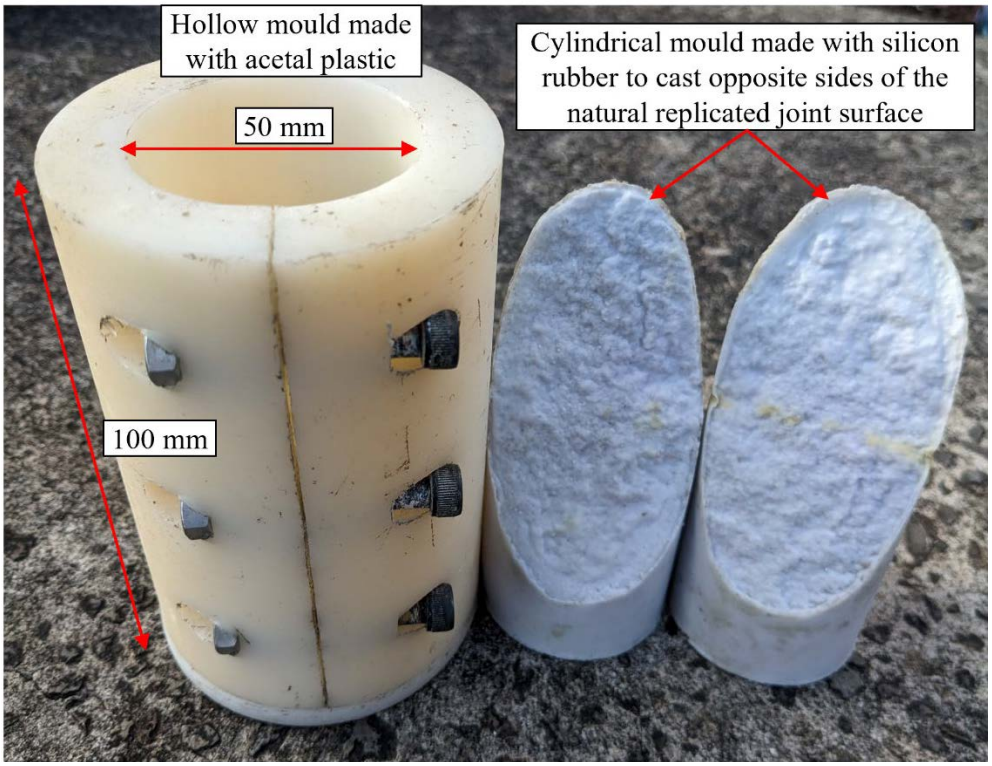

(a)

(b)

Figure 5.1. (a) The cylindrical hollow mould and rubber moulds of the two opposite sides of the natural replicated joint surface; and (b) The two opposite surfaces of a cast jointed rock specimen.

5.2.2 Testing Procedure

In this study, the triaxial setup was chosen for testing, and both cyclic and monotonic triaxial experiments were performed using the GDS ELDYN triaxial apparatus shown in Figures 3.2 and 4.2a. Further details on the test apparatus were reported in Sections 3.2.2 and 4.2.2.

Conventional monotonic triaxial experiments were conducted with a shearing rate of 0.05 mm/min in order to determine the friction angle and elastic moduli of the rock joints before and after subjecting them to cyclic loading. For the testing, eight levels of confining stresses (i.e., 15 kPa, 20 kPa, 25 kPa, 50 kPa, 90 kPa, 120 kPa, 150 kPa and 300 kPa) were selected and subjected to a cyclic deviatoric stress amplitude of 300 kPa. The confining stresses were determined by considering both surface and underground railway tracks resting on a rock subgrade. It should be noted that other researchers also adopted comparable confining stress ranges; for example, Ding et al. (2014) and Vergara et al. (2015) utilised confining pressures within the range of 100 kPa to 400 kPa when analysing the stability of railway tunnels, and Nie et al. (2020) and Wang and Zhuang (2021) employed confining stresses ranging from 15 kPa to 100 kPa when simulating railway subgrades under train loads. The cyclic deviatoric stress amplitude of 300 kPa was determined by performing elastic stress analysis of a moving train corresponding to a 40-ton axle load, employing the beam-on elastic foundation approach in conjunction with Boussinesq's solution. Moreover, comparable vertical stresses have been either measured or employed by previous researchers for cyclic testing, field measurements and numerical simulations of the formation layer of heavy haul train lines (Rose et al. 2004; Suiker et al. 2005; Leshchinsky and Ling 2013; Chen et al. 2019b; Arulrajah et al. 2020). The cyclic loading was applied up to 500,000 cycles simulating long-term service of the

rail track with a frequency of 8 Hz. Frequencies ranging from 5 Hz to 10 Hz have been employed by numerous researchers for cyclic loading experiments of the formation layer simulating loads from the heavy haul and high-speed trains (Suiker et al. 2005; Zhang et al. 2018a; Mohammadinia et al. 2020; Touqan et al. 2020; Naeini et al. 2021). The rock joints were subjected to cyclic loading in the form of a sinusoidal wave. The minimum deviatoric stress was kept at 20 kPa, while the maximum deviatoric stress was adjusted to achieve the desired target cyclic deviatoric stress amplitude.

5.3 Results and Discussion

5.3.1 Monotonic Stress-Strain Response

Conventional triaxial compression experiments were conducted on rock joints (i.e., on both new specimens and post-cyclic loading) to obtain the corresponding monotonic shear strength and Young's moduli values. Figures 5.2 and 5.3 present the monotonic deviatoric stress vs axial strain curves of the rock joints tested under various confining stresses pre and post-cyclic loading, respectively. Referring to Figures 5.2 and 5.3, the initial portion of the stress-strain curve was almost linear, exhibiting elastic behaviour until reaching the yield point beyond which the stress-strain response was elastoplastic, and the peak deviatoric stress point appeared in this elastoplastic region. Tables 5.1 and 5.2 report the peak deviatoric stresses pre and post-cyclic loading, respectively.

The mechanism of deformation can be considered to be dominated by sliding over the joint plane, as also reported by Yang et al. (1998), Fahimifar and Soroush (2005), and Chiu et al. (2013) for joint inclination angles as high as 50^{o}-75^{o}. In addition to sliding along the joint plane, asperity over-riding and asperity degradation accompanied by relocking of the broken and/or unbroken asperities during shearing could be the reason

behind several crests observed in the elastoplastic region of the monotonic stress-strain curve as also elaborated by Byerlee et al. (1970).

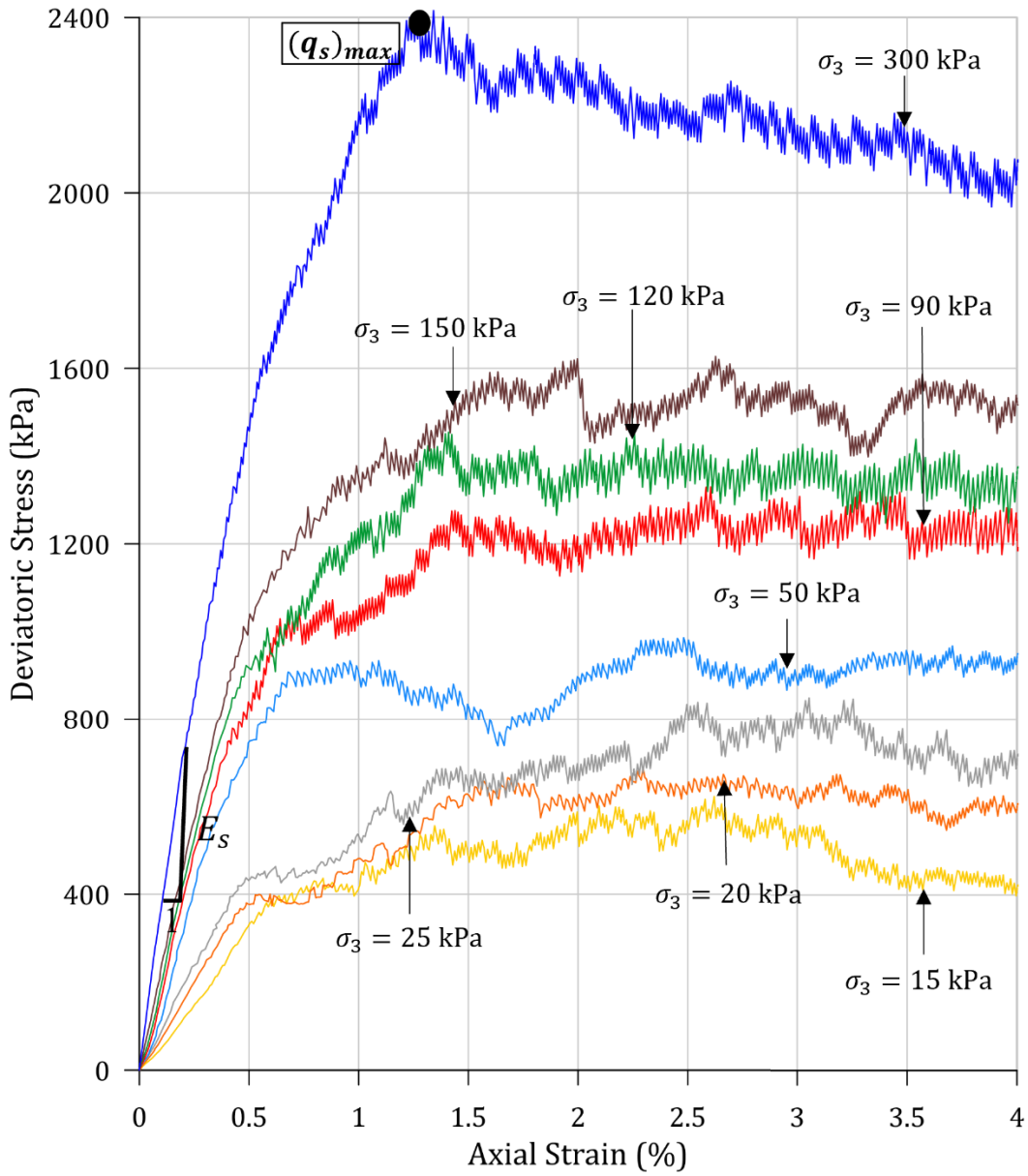

Figure 5.2. The monotonic stress-strain curves for jointed rock samples under the tested confining pressures pre-cyclic loading.

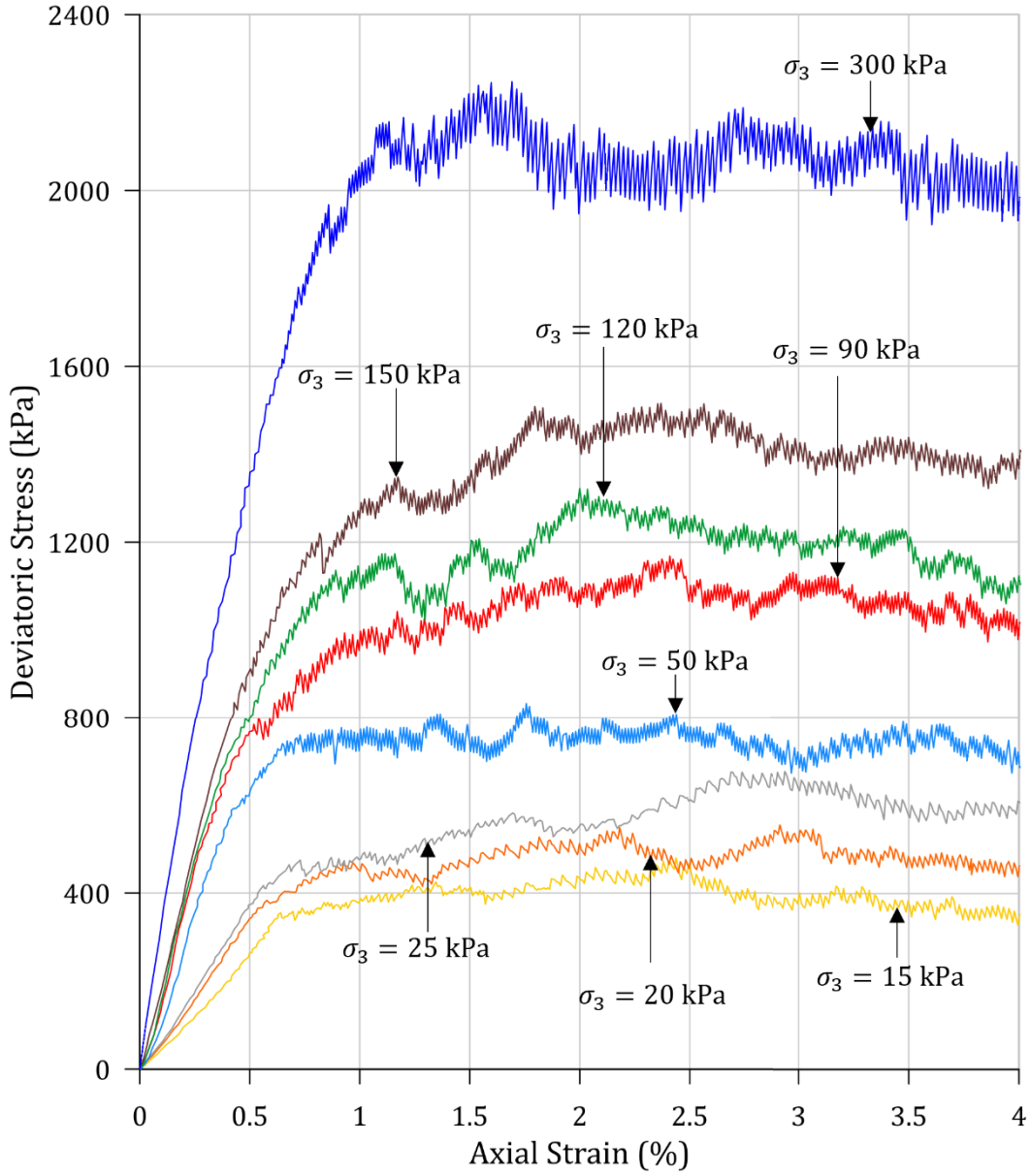

Figure 5.3. The monotonic stress-strain curves for jointed rock samples under the tested confining pressures post cyclic loading.

Moreover, it is clear from Figures 5.2 and 5.3 and Tables 5.1 and 5.2 that the measured peak deviatoric stresses of the rock joints increased with rising confining stress. Yet, the peak deviatoric stress values slightly decreased post-cyclic loading, which could be due to the formation of extra micro-cracks on the joint plane due to the repeated loading application prior to shearing the rock joint under monotonic loading.

Table 5.1. Results of jointed rock samples subjected to conventional monotonic triaxial tests before applying the cyclic loading.

Confining Pressure, σ_3 (kPa)	Monotonic Peak Deviator Stress, $(q_s)_{max}$ (kPa)	Monotonic Shear Strength, τ_s (kPa)	Young's Modulus, E_s (MPa)
15	601	260	66.51
20	687	297	82.45
25	801	347	95.16
50	977	423	153.07
90	1276	553	173.19
120	1439	623	187.98
150	1627	705	199.05
300	2416	1046	257.03

Table 5.2. Results of jointed rock samples subjected to conventional monotonic triaxial tests after applying the cyclic loading.

Confining Pressure, σ_3 (kPa)	Monotonic Peak Deviator Stress, $(q_s)_{max}$ (kPa)	Monotonic Shear Strength, τ_s (kPa)	Young's Modulus, E_s (MPa)
15	457	198	50.64
20	546	236	67.21
25	667	289	78.18
50	843	365	131.82
90	1153	499	149.43
120	1324	573	165.71
150	1509	653	177.16
300	2305	998	231.38

5.3.2 Cyclic Stress-Strain Response

Figure 5.4 demonstrates the cyclic deviatoric stress vs axial strain curves of the rock joints subjected to confining stresses of 15 kPa, 50 kPa, 120 kPa and 300 kPa, respectively. As displayed in Figure 5.4, the cyclic stress-strain behaviour of the rock joints was characterised by hysteresis loops formed through differing loading and unloading paths in each cycle of loading and unloading. Moreover, according to Figure 5.4, the hysteresis loops transitioned from sparse to dense as the cyclic loading progressed at all the adopted confining stresses. Indeed, these sparse to dense transitions were more evident at lower confining stresses of 15 kPa and 50 kPa (see Figures 5.4c & d). Accordingly, at higher confining stresses, the accumulated axial strain upon the completion of cyclic loading decreased.

As evident from Figure 5.4, during the initial loading cycles, the hysteresis loops were closed and nearly overlapped with each other, with a considerable residual axial strain. With increasing loading cycles, the loops tightly overlapped, with a decreasing residual axial strain accumulation. Consequently, the transition of hysteresis loops from sparse state to dense state reveals that during the initial loading cycles, the rock joints display viscoelastic plastic behaviour, while specimens exhibit nearly viscoelastic behaviour during the later loading cycles as a more stabilised joint condition and interlocking is reached.

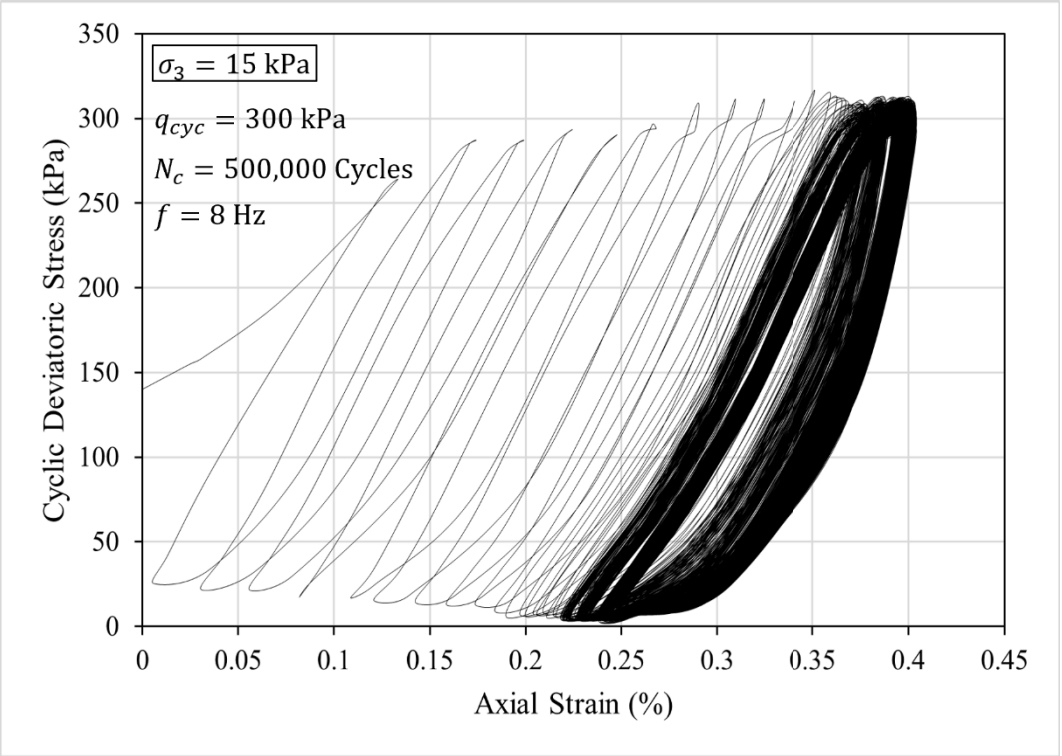
$\sigma_3 = 15$ kPa
$q_{cyc} = 300$ kPa
$N_c = 500{,}000$ Cycles
$f = 8$ Hz
Cyclic Deviatoric Stress (kPa)
Axial Strain (%)
0
50
100
150
200
250
300
350
0
0.05
0.1
0.15
0.2
0.25
0.3
0.35
0.4
0.45

(a)

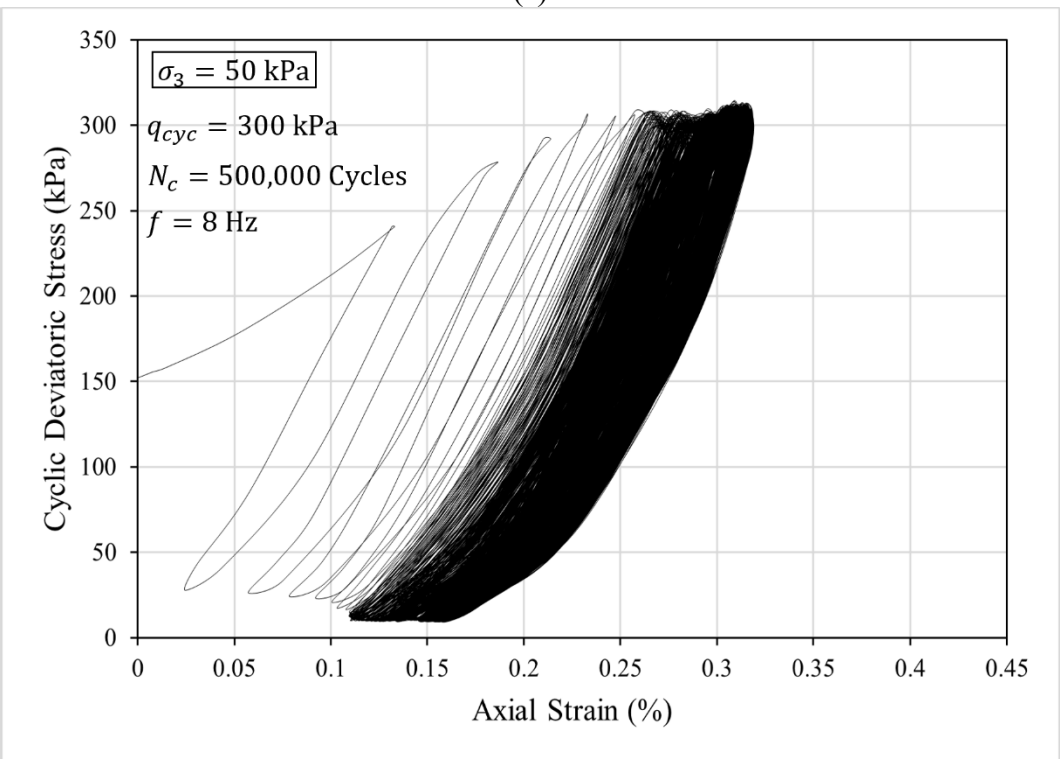
$\sigma_3 = 50$ kPa
$q_{cyc} = 300$ kPa
$N_c = 500{,}000$ Cycles
$f = 8$ Hz
Cyclic Deviatoric Stress (kPa)
Axial Strain (%)
0
50
100
150
200
250
300
350
0
0.05
0.1
0.15
0.2
0.25
0.3
0.35
0.4
0.45

(b)

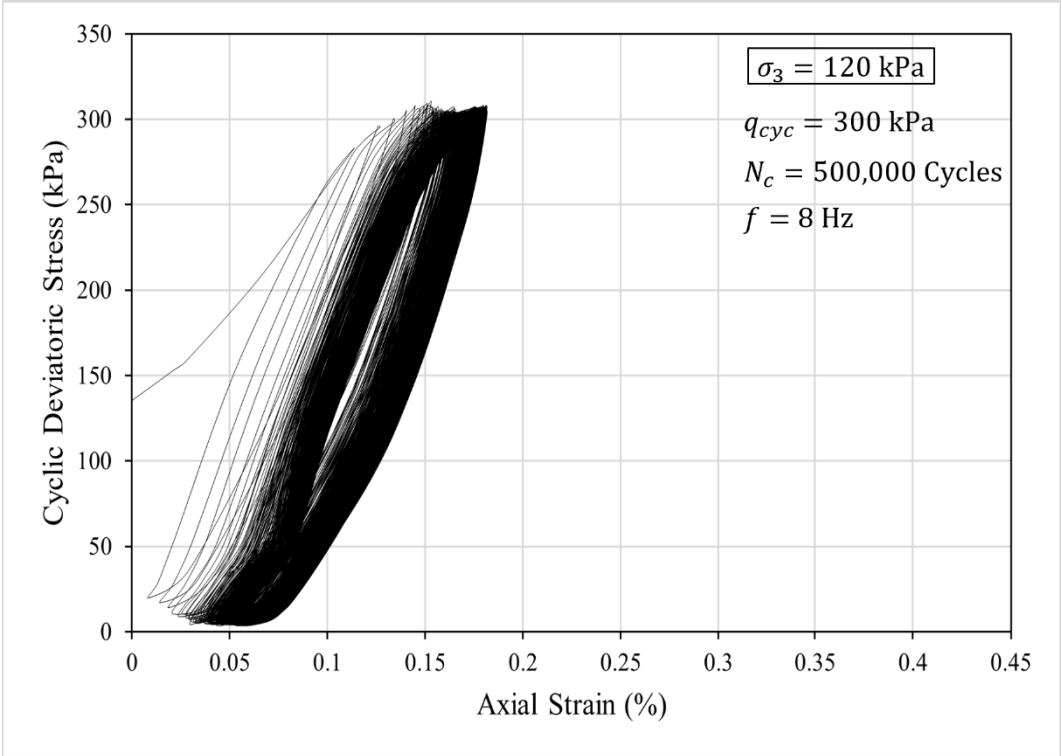

(c)

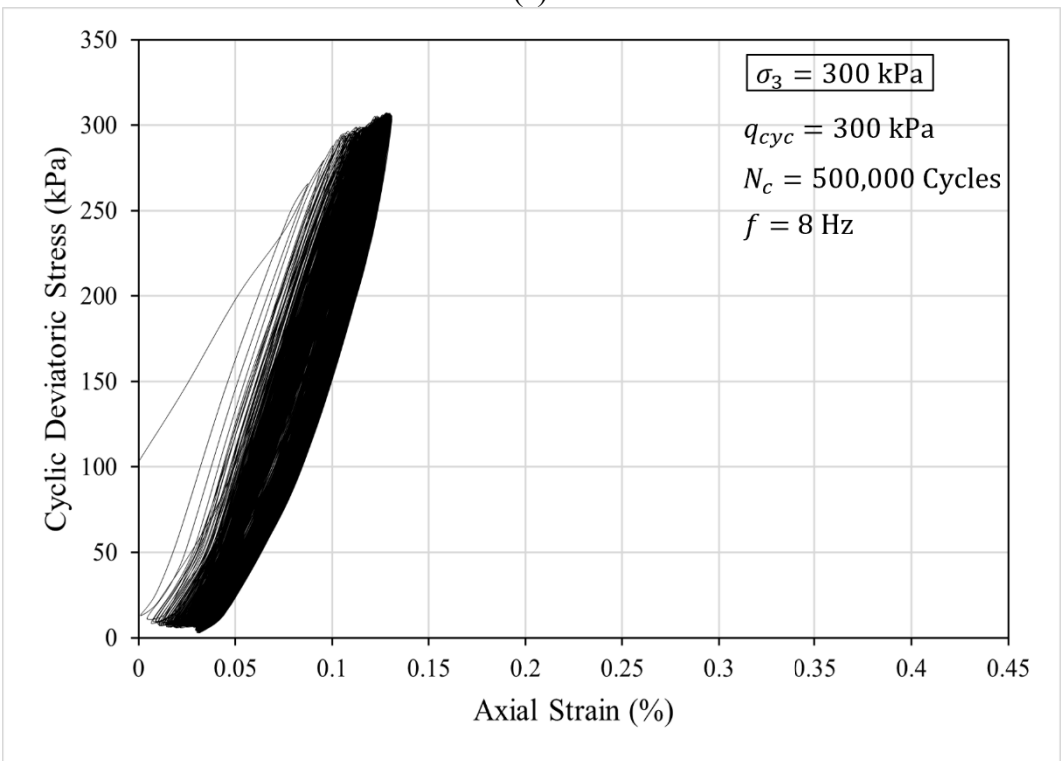

(d)

Figure 5.4. The cyclic stress-strain curves for jointed rock samples under confining pressures (σ_3) of: (a) 15 kPa; (b) 50 kPa; (c) 120 kPa and (d) 300 kPa.

5.3.3 Residual Axial Strain

Figure 5.5 shows how the cumulative residual axial strain of the rock joints varied with the number of loading cycles under the tested confining stresses. Referring to Figure 5.5, the cumulative residual axial strain swiftly increased during the initial loading cycles, and the accumulation of residual axial strain gradually reduced during the later cycles. Accordingly, the evolution of the cumulative residual axial strain can be presented with two development stages. i.e., the initial stage, in which major residual axial strain accumulation occurs rapidly, and the steady stage, in which the residual axial strain accumulation occurs very slowly. After the initial loading cycles (i.e., initial stage), the steady stage remains throughout the rest of the cyclic loading-unloading process giving no signs of accelerated increase of residual axial strain or failure of the rock joint even when the test was carried out for 500,000 cycles. This behaviour is also evident from the residual axial strain per cycle versus the number of cycles curves presented in Figure 5.6. As shown in Figure 5.6, the residual axial strain per cycle values were quite high during the initial loading cycles, and they decreased rapidly and reached a steady state with the progression of repeated loading.

According to Brady and Brown (1993), natural discontinuity behaviour is dominated by two mechanisms: sliding along the discontinuity surface and shearing through asperities. Moreover, the strength, size and shape of the asperities at the discontinuity surface, the inclination of the discontinuity, the presence of a gouge material, and applied stresses influence these mechanisms (Lee et al. 2001; Thirukumaran 2014; Zhang et al. 2019). Accordingly, the rapid residual axial strain development during the initial loading cycles can be due to the slight asperity overriding occurring due to the cyclic load application. Furthermore, the cumulative residual axial development reaching a steady state can be

attributed to the applied cyclic stresses not being sufficient to cause significant sliding or breakage of asperities producing extensive irreversible deformations in the rock joints.

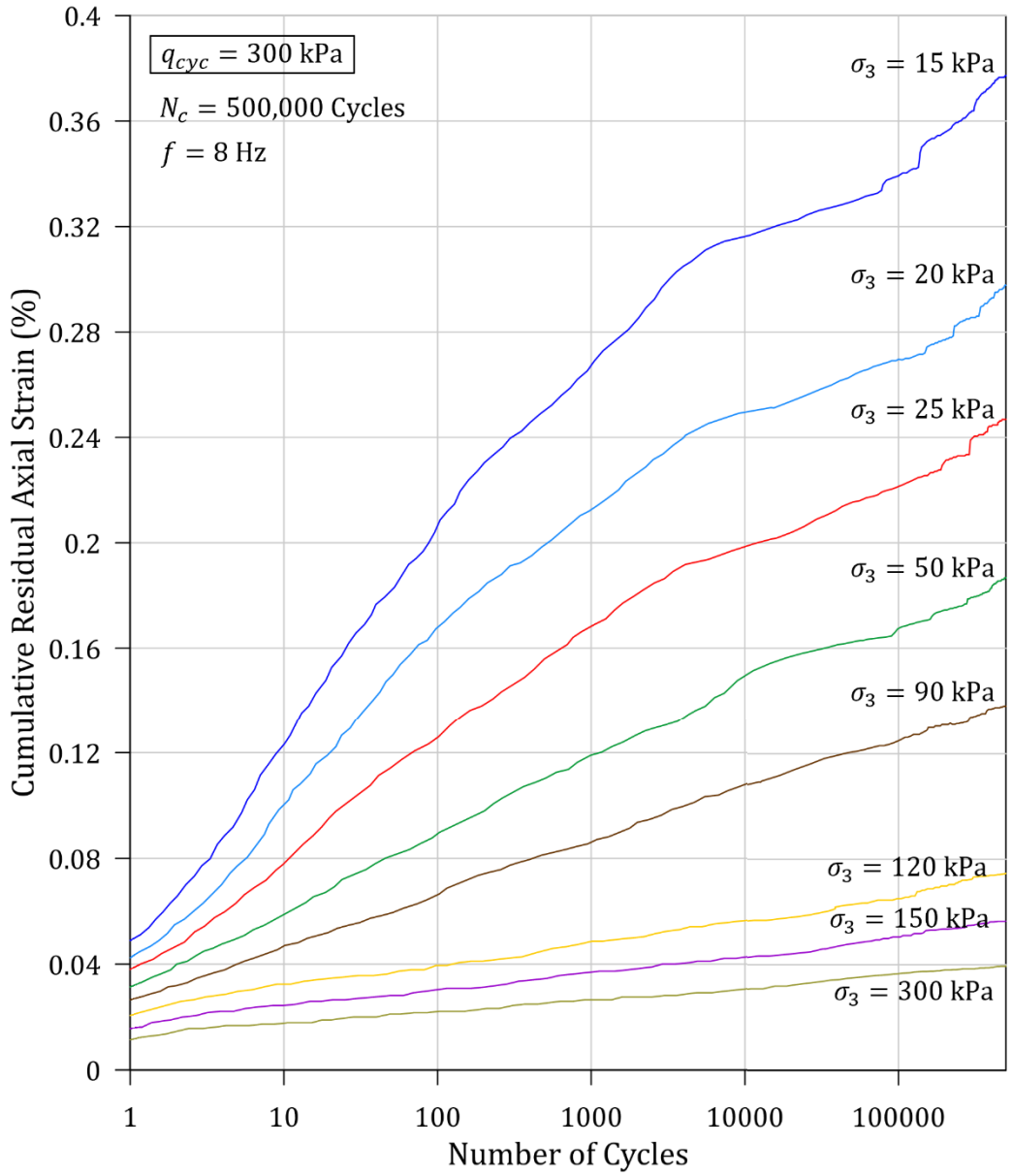

Figure 5.5. The evolution of cumulative residual axial strain with loading cycles under the tested confining pressures.

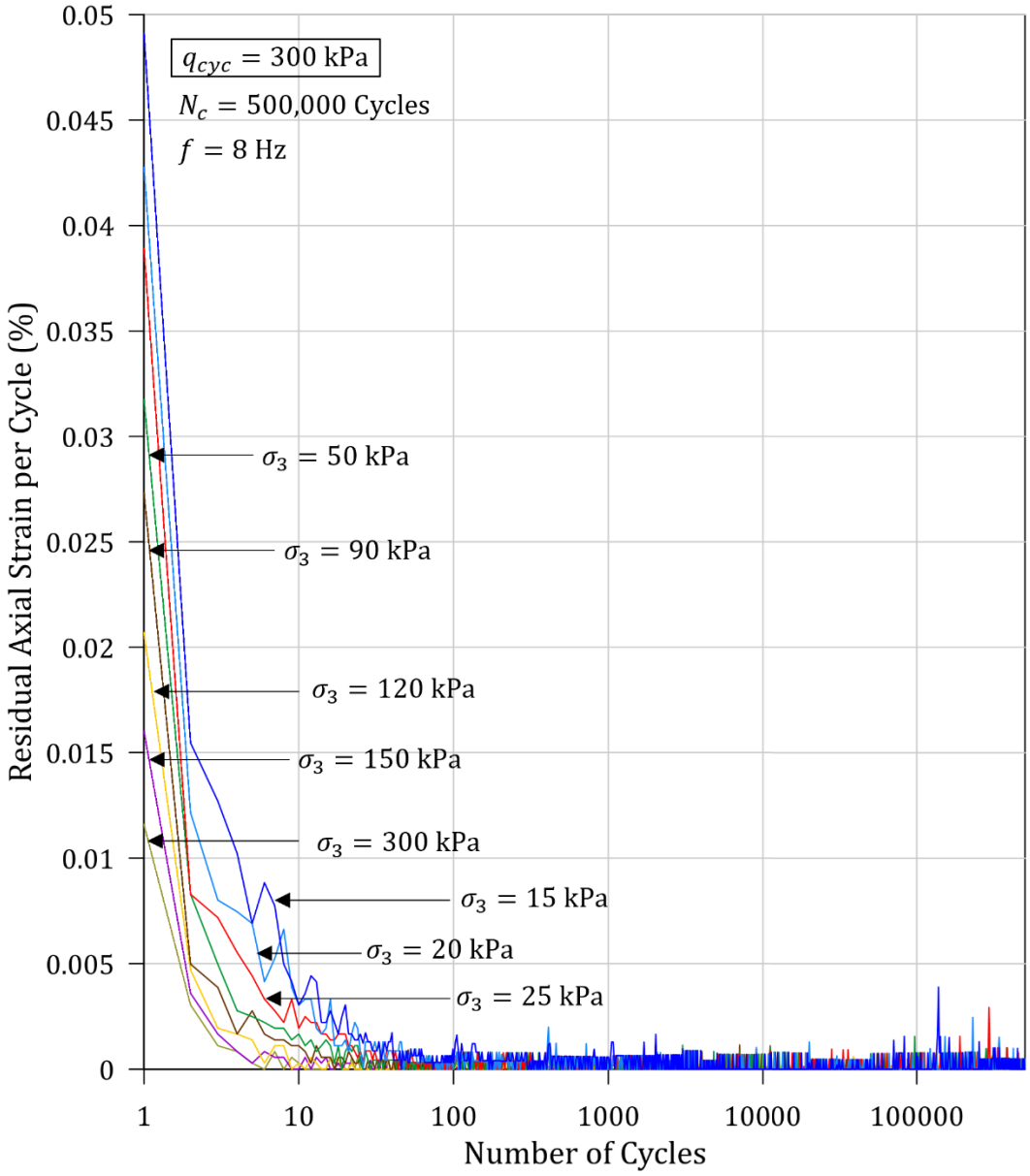

Figure 5.6. The residual axial strain per cycle vs the number of cycles curves under the tested confining pressures.

Moreover, as evident in Figures 5.5 and 5.6, the cumulative residual axial strain decreased as the confining stress increased. This behaviour can be attributed to the higher resistance the confining stress provides to sliding and shearing of joint asperities. Furthermore, at lower confining pressures, a sudden slight rise of residual axial strain could be observed at several locations of the curves (see Figures 5.5 and 5.6). This behaviour can be due to the sudden and slight sliding of asperities occurring due to applying the cyclic loads under low confinement for prolonged periods. Moreover, it can be observed that even after the

sudden slight rise of the residual axial strain, the cumulative residual axial strain stabilised again with no signs of abrupt increase in the axial deformation.

5.3.4 Deformation Moduli during monotonic and cyclic loading

Young's modulus is one of the parameters generally utilised to characterise the elastic deformation of loaded rock specimens (Brady and Brown 1993; Heap and Faulkner 2008). Referring to Figures 5.2 and 5.3, the stress-strain curves of jointed rocks under monotonic loading conditions consisted of an initial elastic stage in which the stress-strain response followed an almost linear growth relationship exhibiting elastic characteristics, signifying recoverable elastic deformation of the loaded rock joints. Accordingly, as suggested by Brady and Brown (1993), the average Young's modulus (E_{av}) was calculated from the average slope of the more-or-less straight portion of the deviatoric stress vs axial strain plots of rock joints obtained under conventional triaxial loading conditions (as shown in Figures 5.2 and 5.3). Figure 5.2 illustrates the calculation process of the average Young's modulus from the monotonic stress-strain curve, and the determined values of the average Young's moduli are listed in Tables 5.1 and 5.2.

Figure 5.7 illustrates how the average Young's moduli values of the rock joints pre and post-cyclic loading varied with applied confining stresses. As shown in Figure 5.7, the average Young's moduli under monotonic loading conditions demonstrated an upward trend with confining stress. Similar behaviour has been reported by Yang et al. (2012) for red sandstone specimens and Wu et al. (2019) for different rock types such as sandstone, gneiss, limestone and amphibolite. Moreover, as expected, Young's moduli values of the rock joints prior to applying the cyclic loading were higher than those of the samples after applying the cyclic load, as shown in Figure 5.7. The difference between Young's moduli values pre and post-cyclic loading was in the range of 15 – 25 MPa (i.e., 10 - 25%

reduction in Young's moduli of jointed rock as a result of 500,000 cycles of loading-unloading cycles).

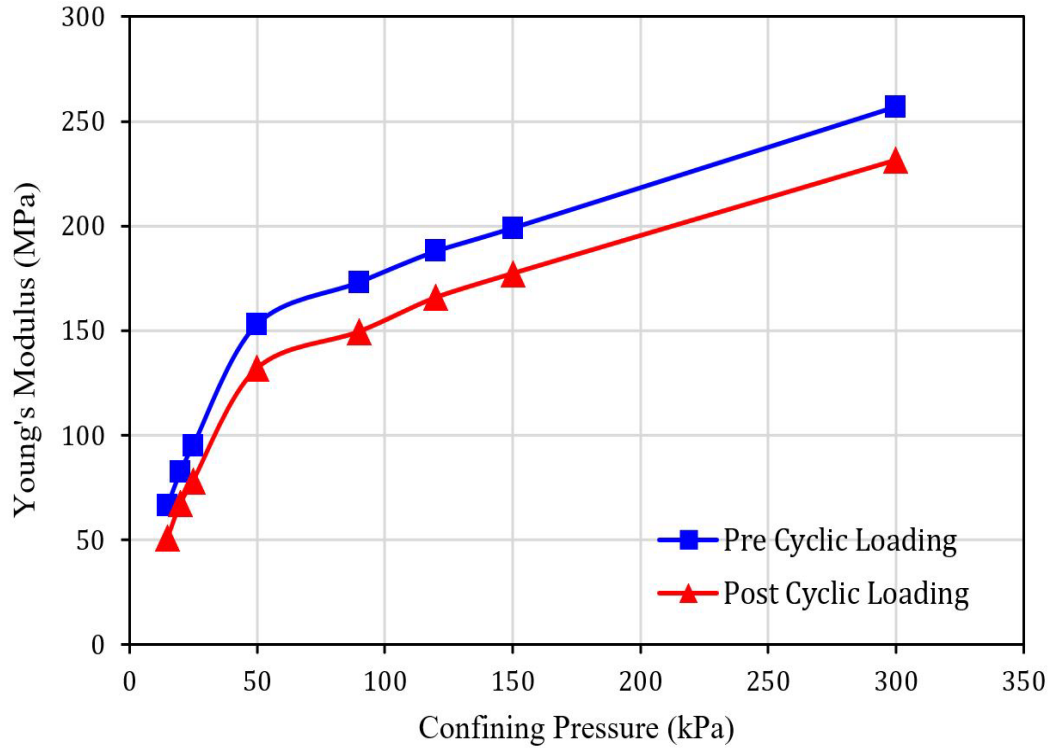

Figure 5.7. Variation of Average Young moduli before and after cyclic loading with confining pressure.

The resilient modulus is a parameter that is commonly employed to capture the elastic deformation characteristics during the cyclic loading-unloading process. In fact, it explicitly captures the unloading characteristics of the tested samples and depends on the axial strain recovered during the unloading process. Accordingly, the Resilient modulus (M_R) is defined by Equation (3.7).

Figure 5.8 illustrates how the resilient moduli values determined using Equation (3.7) varied with cumulative residual axial strain for the adopted confining stresses. As shown in Figure 5.8, the resilient moduli showed a downward trend with cumulative residual axial strain under all the confining pressures considered. Yet, the drop in resilient moduli during the initial residual axial strain development was higher. Comparable trends were

reported by Wang et al. (2013) for granite specimens, Chen et al. (2021) for solidified muddy soil, Akbarimehr and Fakharian (2021) for clay mixed with waste rubber and Golpazir et al. (2016) for polyurethane foam-sand mixtures.

Based on the studies by Bagde and Petros (2005a), Liu et al. (2012), and Ma et al. (2013), the downward trend in resilient moduli (i.e., stiffness degradation) with increasing loading cycles indicates progressive development of irreversible deformation of the rocks exposed to repeated loading. This observation is also supported by Wang et al. (2013), who noticed a one-to-one relationship between the deformation modulus and residual axial strain of rocks subjected to repeated loading. Accordingly, the initial rapid drop in resilient moduli can be due to the initial slight asperity overriding taking place due to the cyclic load application causing initial rapid residual axial strain development, as evident in Figures 5.5 and 5.6. Furthermore, with increasing loading cycles, the residual axial strain accumulates at a decreasing rate, as apparent in Figures 5.5 and 5.6, inducing a reduction in the resilient moduli degradation rate with further residual axial strain development (see Figure 5.8). Moreover, as shown in Figure 5.8, with increasing confining stress, the initial resilient moduli also increased, and the degradation of the resilient moduli with residual axial strain development decreased. This observation could be attributed to the higher resistance provided for the joint deformation by the higher confining stresses.

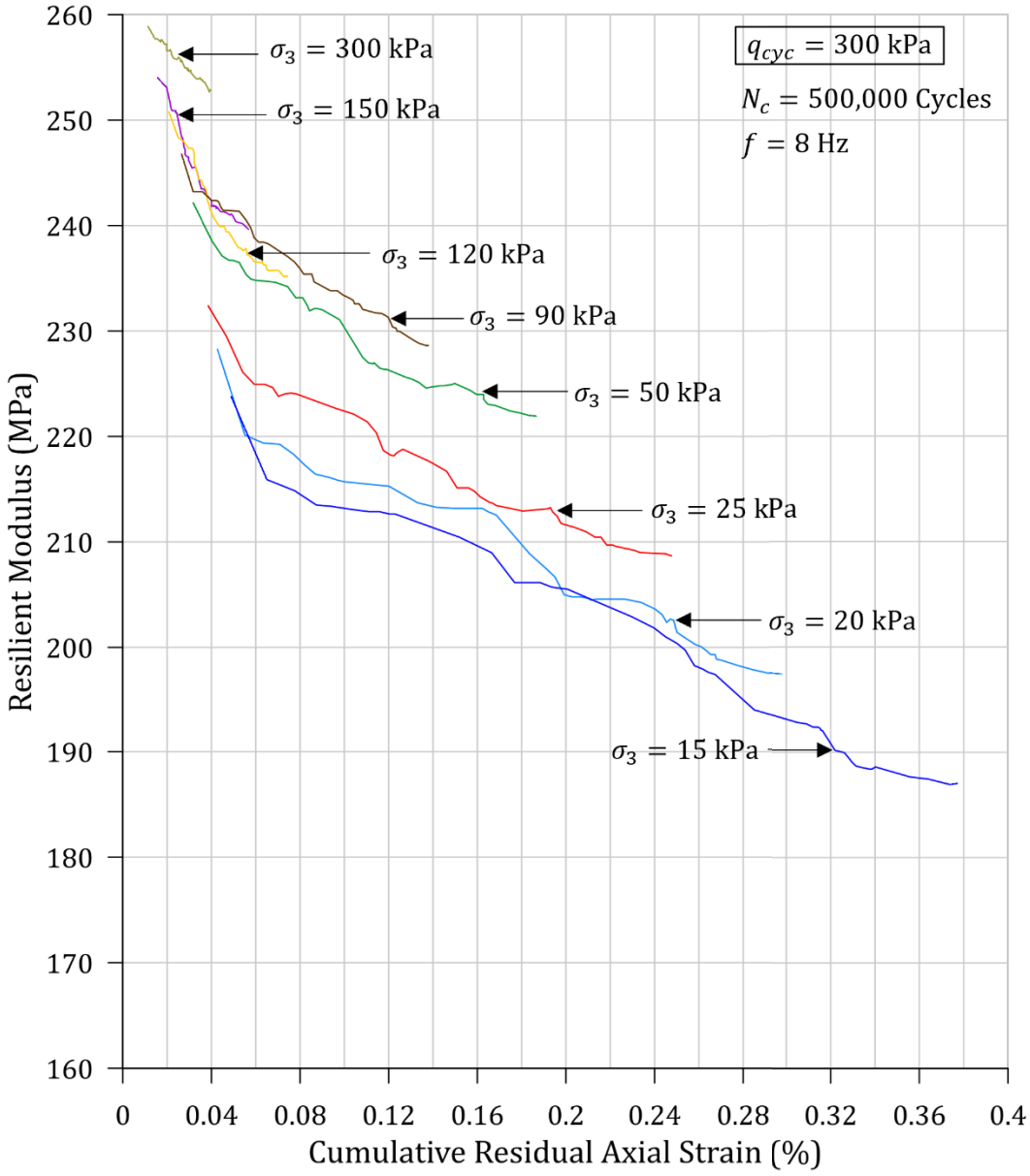

Figure 5.8. Degradation of resilient moduli with cumulative residual axial strain under the tested confining pressures.

The Ultimate resilient modulus (M_{RU}) reported here is determined for the last loading cycle. Figure 5.9 illustrates how the ultimate resilient moduli and Young's moduli (before applying cyclic loading) of the rock joints varied with the corresponding confining stress. Referring to Figure 5.9, both the ultimate resilient moduli and Young's moduli showed a nonlinear increase with confining pressure, as expected. Moreover, the ultimate resilient moduli values were quite higher than the corresponding Young's moduli values. This behaviour can be possibly due to the difference in strain level where resilient moduli

correspond to smaller strains developed during cyclic loading application (indeed, as a result of high-frequency cyclic loading, full deformation cannot be developed), while Young's moduli correspond to larger strains, fully developed under monotonic loading, as also explained by Fjaer (2009) and Wichtmann et al. (2017). Similar behaviour has been reported by Yang et al. (2015) for sandstone specimens and Wichtmann et al. (2017) for sands and gravels. Moreover, the difference between the ultimate resilient moduli and Young's moduli decreased with increasing confining stress, as also observed previously by Yang et al. (2015) for sandstone specimens.

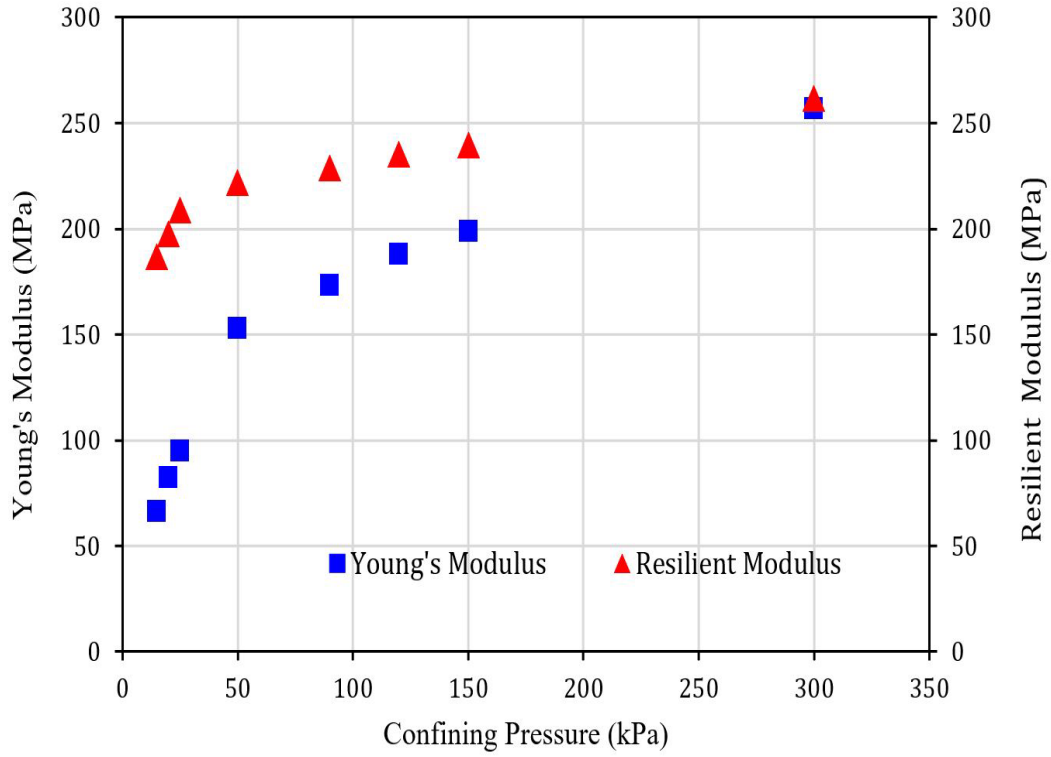

Figure 5.9. Variation of resilient moduli and Young's moduli under monotonic loading with confining pressure.

For the design of foundations exposed to dynamic loading, the small strain stiffness of the rock or soil formation is a key parameter. These small strain stiffness parameters are often determined from dynamic field tests via surface or borehole measurements of the wave velocities, which can be time-consuming and expensive. Therefore, several researchers have proposed empirical formulas or correlations to estimate cyclic stiffness

parameters from monotonic experiments. Referring to Figures 5.8 and 5.9, the resilient moduli showed a downward trend with residual axial strain and displayed an upward trend with the confining stress. Based on the experimental results, Equation (5.1) presents an empirical relationship to predict the ratio between resilient moduli (M_{RU}) and Young's moduli (E_s).

$$\frac{M_{RU}}{E_s} = \alpha * \frac{CSR^{\beta}}{{R_{\varepsilon_p}}^{\gamma}} \tag{5.1a}$$

$$CSR = \frac{q_{cyc}}{2\sigma_3} \tag{5.1b}$$

$$R_{\varepsilon_p} = \frac{\varepsilon_p}{(q_s)_{max}/E_s} \tag{5.1c}$$

where, E_s is the Young's modulus under monotonic loading, CSR is the cyclic stress ratio, q_{cyc} is the applied cyclic deviatoric stress, σ_3 is the applied confining pressure, R_{ε_p} is the normalised residual axial strain, ε_p is the measured residual axial strain and $(q_s)_{max}$ is the peak devitoric stress under monotonic loading condition. Furthermore, α, β and γ are empirical constants obtained based on data fitting exercise, which depend on joint characteristics such as joint roughness, joint inclination, and JCS. Through a nonlinear regression analysis programmed in MATLAB utilising the Nonlinear Least Squares method and Trust-Region Algorithm, the values of the empirical constants were determined to be α = 0.8937, β = 0.4737 and γ = 0.1042. Figure 5.10 compares the predictions obtained from Equation (5.1) with the laboratory measurements in the 3D space, and it is evident that the proposed empirical Equation provides reasonable predictions.

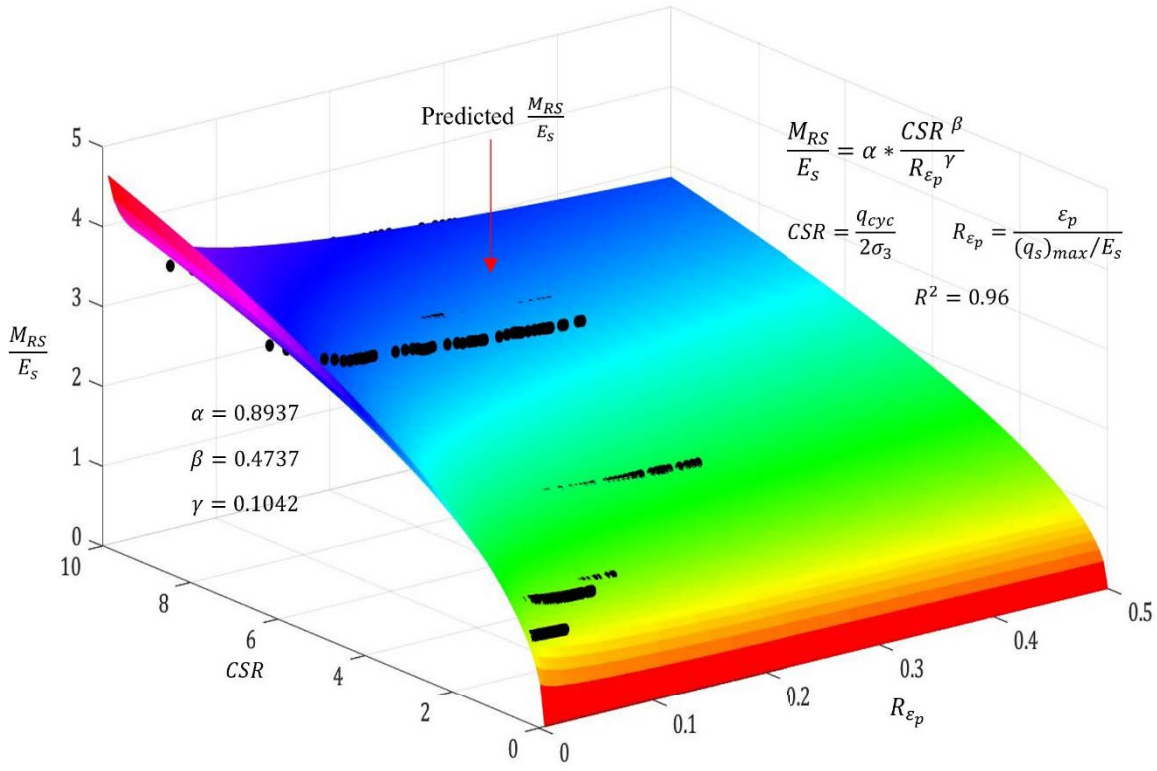

Figure 5.10. Variation of the actual and predicted ratio between resilient moduli and Young's moduli in the 3D space.

5.3.5 Damping Response

Damping is one of the important considerations when analysing the cyclic response of ground-structure systems. Researchers have used several parameters to quantify the damping characteristics of materials, and among them, the damping ratio is the most commonly used parameter. In accordance with ASTM D3999 (2013), the damping ratio for a given hysteresis loop under cyclic triaxial testing can be determined from Equation (2.2).

Figure 5.11 presents how the damping ratio per load cycle evolved with cumulative residual axial strain for the range of confining stresses used. Referring to Figure 5.11, the damping ratio per load cycle showed a rapid reduction initially, then slightly recovered and increased slowly with increasing cumulative residual axial strain. Similar behaviour

has been reported by Yang et al. (2020a) for granite and red sandstone specimens, Liu et al. (2021a) for dolomite specimens, Qin et al. (2021) for mudded intercalations, Akbarimehr and Fakharian (2021) for clay mixed with waste rubber and Golpazir et al. (2016) for polyurethane foam-sand mixtures.

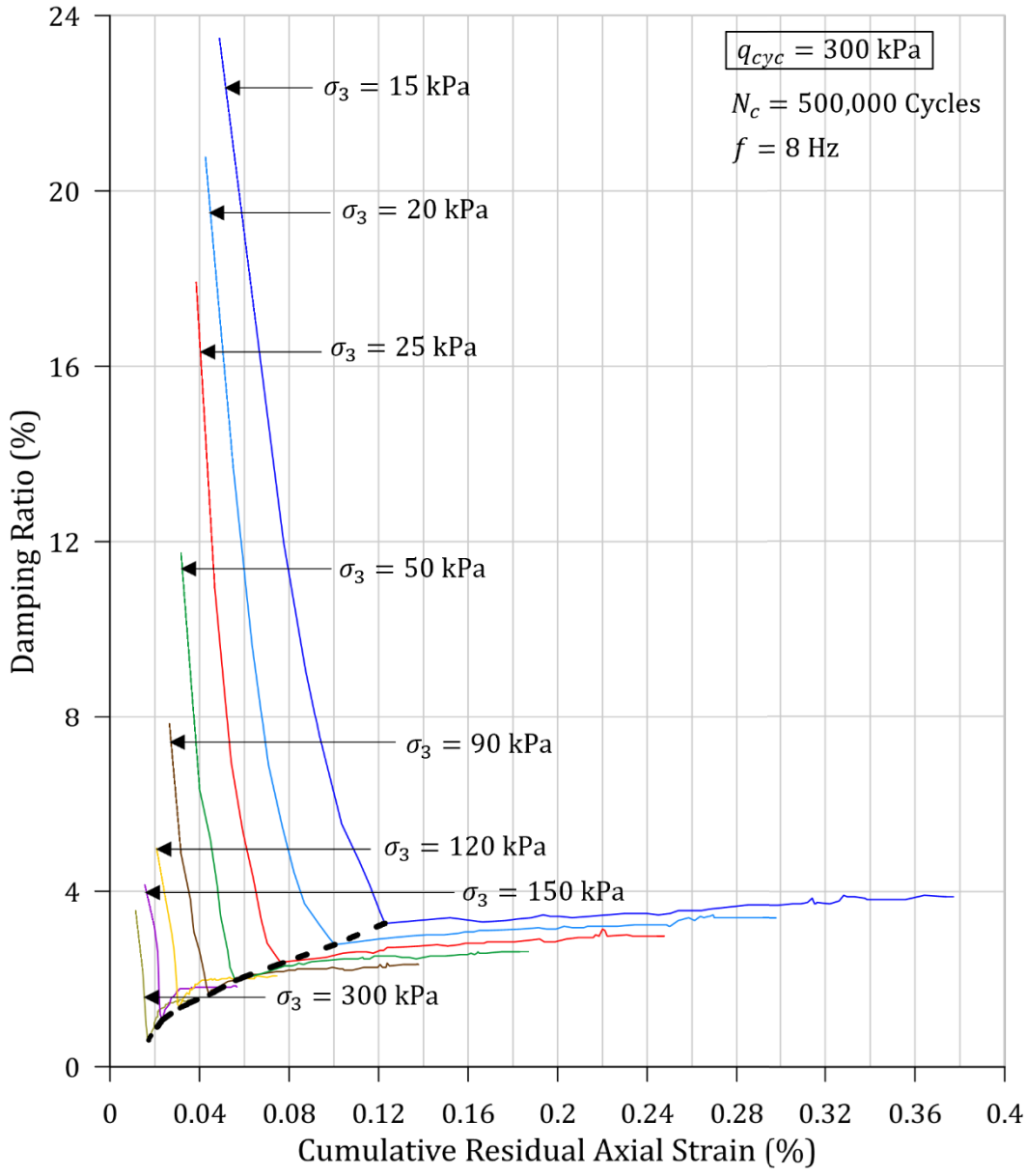

Figure 5.11. Evolution of damping ratio with cumulative residual axial strain under the tested confining pressures (bold dash line represents the line of minimum damping ratio).

Referring to the cumulative residual axial strain vs the number of cycles plots presented in Figure 5.5, the residual axial strain accumulation during the initial loading cycles was higher than the following loading cycles. This behaviour is also evident from the sparse hysteresis loops appearing during the initial loading cycles, as shown in Figure 5.4. Accordingly, a higher portion of the input energy will be dissipated during the initial loading cycles, while a lesser portion of the input energy being stored as elastic energy. This occurs as a result of the slight asperity overriding taking place due to the cyclic load application, resulting in a higher residual axial strain accumulation during the initial loading cycles. Therefore, the damping ratio per load cycle during the initial residual axial strain development will be higher. Moreover, with the progression of cyclic loading, the residual axial strain accumulation rate reduced, causing the dissipated energy to decrease promptly, which is reflected in the rapid decrement of the damping ratio with initial cumulative residual axial strain development, as shown in Figure 5.11. After reaching a minimum damping ratio, the damping ratio per load cycle started to increase at a very slow pace, as shown in Figure 5.11. Due to the prolonged application of the cyclic loading, the development of micro-cracks combined with asperity overriding may result in further accumulation of residual axial strain at a slower rate, which may also cause a slight increase in the energy dissipated as well as the damping ratio. Furthermore, referring to Figure 5.11, at high confining stresses, the damping ratio values of the rock joints reduced, possibly due to the higher resistance provided for the joint deformation leading to lower dissipated energy and, thus, higher accumulated elastic energy in the joint.

Moreover, referring to Figure 5.11, a critical dynamic residual axial strain $(\varepsilon_{1,p})_{critical}$ can be identified at which the damping ratio was the lowest and beyond which the damping ratio slightly increased. Figure 5.12 shows how the critical dynamic residual

axial strain values varied with confining stress. According to Figures 5.11 and 5.12, with rising confining stress, the corresponding critical dynamic residual axial strain nonlinearly decreased, possibly due to the constriction of the asperity overriding by higher confinement, causing slower development of initial residual axial strains. Equation (5.2) presents an empirical relationship between critical dynamic residual axial strain ($(\varepsilon_{1,p})_{critical}$) and cyclic stress ratio (CSR) developed based on the experimental results reported in Figures 5.11 and 5.12.

$$(\varepsilon_{1,p})_{critical} = \frac{\varepsilon_{cmax}}{1 + \frac{a}{CSR}} \tag{5.2}$$

where, CSR is defined in Equation (5.1b). ε_{cmax} captures the maximum critical dynamic residual axial strain when CSR is very large (i.e., $CSR \rightarrow \propto$) and a is an empirical constant obtained based on data fitting exercise. The values of ε_{cmax} and a determined through regression analysis were 0.2005% and 7.334, respectively. Figure 5.13 presents a comparison between the predictions obtained from Equation (5.2) and the laboratory measurements, and it is clearly apparent that the proposed empirical equation offers reasonable predictions.

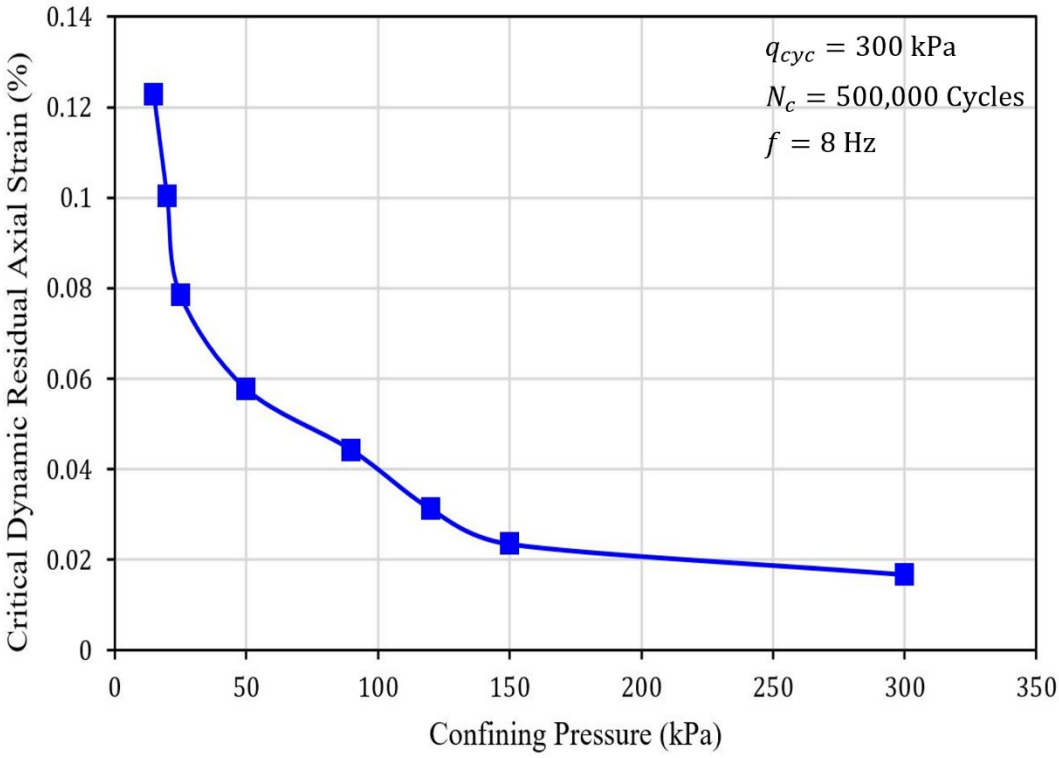

Figure 5.12. Variation of critical dynamic residual axial strain ($(\varepsilon_{1,p})_{critical}$) with confining pressure (σ_3).

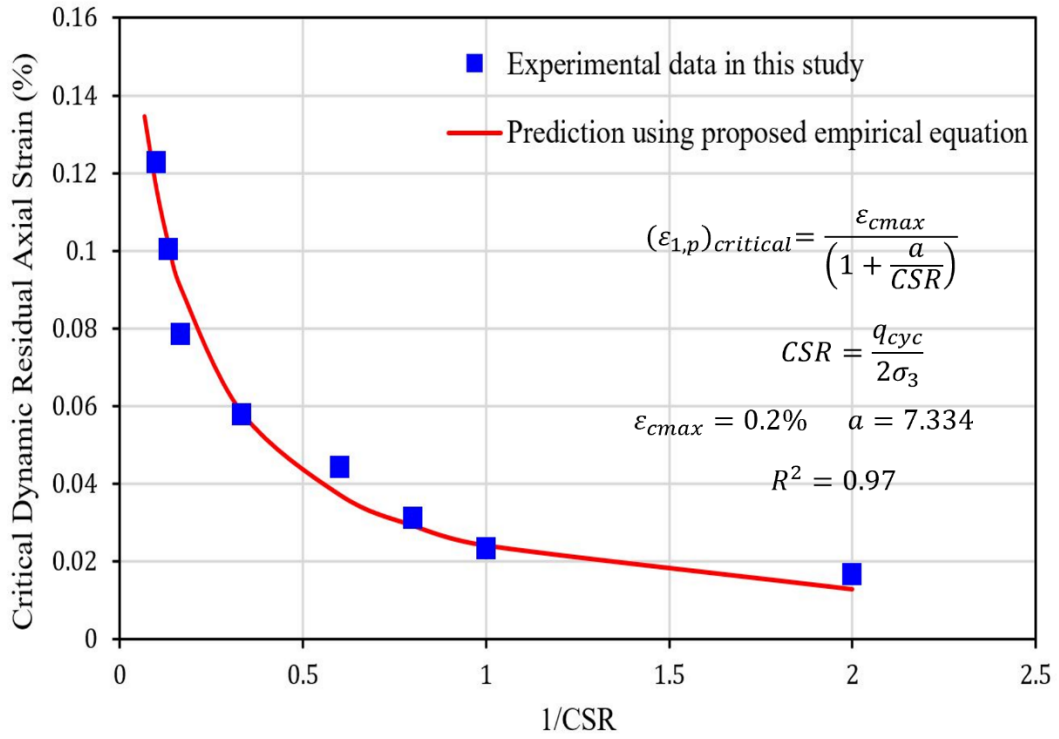

Figure 5.13. Variation of predicted and experimentally obtained critical dynamic residual axial strain ($(\varepsilon_{1,p})_{critical}$) with critical stress ratio (CSR).

5.4 Summary

In this study, the impact of confining stress on the fatigue characteristics of jointed rocks exposed to prolonged cyclic loading conditions was evaluated, with a focus on the variation of stiffness and damping parameters with the strain level. The results indicated that the residual axial strain accumulated swiftly during the initial loading cycles and slowly during the later loading cycles, with lower residual axial strain accumulation at higher confining stresses. The resilient moduli decreased with cumulative residual axial strain. But resilient moduli were higher than the corresponding Young's moduli, and both moduli increased with increasing confining stress. The damping ratio initially decreased rapidly and then increased slowly with cumulative residual axial strain. There existed a critical dynamic residual axial strain at which the damping ratio was the lowest and beyond which the damping ratio slightly increased. Empirical relationships were developed for the resilient moduli variation with cumulative residual axial strain and the correlation between critical dynamic residual axial strain and cyclic stress ratio.

Chapter 6: Conclusions and Recommendations

6.1 General

In many rock engineering projects, the rock masses are frequently exposed to repeated loads resulting from various geological processes and rock engineering applications, including earthquakes, mining operations, construction activities and traffic loading. In addition, natural rock masses are heterogeneous and often comprise discontinuities, such as joints, fractures and other planes of weakness, significantly impacting the strength and deformation characteristics of the rock mass, which may affect the overall stability of the rock engineering structures. In many countries, including Australia, the expansion of transportation infrastructure has become crucial due to the escalating population and demand for mobility. However, the highly populated coastal belt of Australia is characterised by rocky terrains featuring discontinuities such as joints, fractures, bedding planes and faults. Therefore, in order to extend rail transport infrastructure across these jointed rock formations, evaluating the dynamic behaviour of jointed rock masses subjected to repeated loads from train loading conditions is vital. Such evaluations are critical for the design and construction of rail transport infrastructure projects involving jointed rock masses.

This research study investigated the dynamic mechanical behaviour and the characteristics of jointed rock exposed to cyclic loading conditions. This study also analysed the effect of various cyclic loading conditions, including cyclic deviatoric stress, confining stress, the number of loading cycles corresponding to train loading conditions and the joint surface roughness on the dynamic response of jointed rocks exposed to repeated loading. Moreover, empirical relationships were proposed to predict crucial dynamic characteristics of rock joints that are essential for designing and analysing

structures on or near jointed rock formations exposed to repeated loading. Specific conclusions and observations for different aspects covered in this thesis are presented below.

6.2 Observations and Conclusions About Vibration Characteristics of Jointed Rocks

A series of cyclic triaxial experiments were conducted on modelled rock joints with planar (friction angle $\phi = 30^0$), sawtooth ($\phi = 58^0$) and natural replicated ($\phi = 51^0$) joint surfaces at various confining stresses (20 kPa - 150 kPa) and cyclic deviatoric stress amplitudes (220 kPa - 300 kPa) with a loading frequency of 8 Hz and subjected to 10,000 cycles. Analysis of the experiment results disclosed that under all the tested conditions, the cyclic stress-strain hysteresis loops of the rock joints transitioned from sparse to dense with increasing loading cycles. The residual axial strain accumulation with loading cycles illustrated an upward trend, particularly during the initial loading cycles. As the cyclic deviatoric stress increased and the confining stress decreased, the maximum residual axial strain gained by the rock joints increased. In addition, the maximum residual axial strain gained by planar joints was significantly higher than the sawtooth and natural replicated joints. The resilient moduli of rock joints exhibited a downward trend with the increasing number of cycles, particularly during the initial loading cycles. Moreover, lower cyclic deviatoric stress and higher confining stress resulted in higher resilient moduli for all three types of joints adopted. The dissipated energy and damping ratio demonstrated a sharp decrease within the initial cycles, then slightly increased and tended to stabilise with increasing loading cycles. A higher cyclic deviatoric stress and lower confining stress led to amplified dissipated energy and damping ratio values. Furthermore, the dissipated energy and damping ratio values of planar joints were considerably greater than the sawtooth and natural replicated joints. Moreover, empirical relationships for the steady-state resilient moduli and steady-state damping ratio were formulated using the

nonlinear regression analysis, which included the impact of cyclic deviatoric stress amplitude, confining stress, joint friction angle and shear strength.

The experimental observations in this study suggest that precise quantification of vibration characteristics such as dynamic stress-strain response, irreversible deformation evolution, stiffness degradation, and dissipated energy evolution, along with damping properties, is vital to carry out vibration analyses of rail structure, subgrade and nearby structures. This study provides an insight into vibration parameters that vary under various field conditions that are required, especially during the design phase of transport infrastructure projects. Instead of using simplified constant stiffness and damping parameters for jointed rock in vibration analyses, data from this study and proposed empirical relationships can be readily used by design engineers in their analyses to predict more realistic vibration responses. This can expedite the selection of vibration mitigation processes during the actual construction, which is more efficient and cost-effective, rather than retrofitting or adding new mitigation strategies post-construction while the railway lines would be in service.

6.3 Remarks About Cyclic Deformation and Critical Stress Amplitude of Jointed Rocks

Modelled rock joints featuring a natural replicated joint surface (with a JRC = 11.51 and ϕ = 51^{o}) were subjected to cyclic triaxial loading where the cyclic deviatoric stress amplitude was incrementally increased until the rock joint exhibited excessive deformation at various confining stresses (15 kPa - 150 kPa). The rock joints were subjected to 10,000 loading cycles at a loading frequency of 8 Hz. Analysis of the results disclosed a critical dynamic deviatoric stress existed beyond which the yielding of the rock joint occurred. The ratio between critical dynamic deviatoric stress and the static

peak deviatoric stress was in the range of 0.6 – 0.7. Moreover, the critical dynamic deviatoric stress increased as the confining stress increased. At cyclic stresses in excess of the critical dynamic deviatoric stress, the accumulated residual axial strains were extensively higher than those under lesser cyclic stresses. Furthermore, an empirical relationship was developed through nonlinear regression analysis for the evolution of cumulative residual axial strain with the number of cycles for cyclic stresses in excess of the critical dynamic deviatoric stress. Upon subjecting the rock joints to cyclic stresses exceeding the critical dynamic deviatoric stress threshold, considerable damage to the asperities was observed upon inspection of the joint surface after the cyclic loading. Conversely, lower cyclic stresses were found to cause no visible damage to the joint surface. The degradation of resilient moduli with the increasing number of cycles was quite rapid, especially during the initial loading cycles at cyclic stresses in excess of the critical dynamic deviatoric stress threshold. Furthermore, when the cyclic stress exceeded the critical dynamic deviatoric stress threshold, the initial dissipated energy and damping ratio values were significantly higher and displayed a dramatic decrease during the initial loading cycles. Subsequently, a slight recovery was observed, and the values gradually stabilised with further loading.

This study provides an important reference and quantifies variation of parameters such as permanent deformation, yielding stress, stiffness and damping ratio with field conditions. Design engineers can use the results of this study for more reliable predictions of the response of jointed rocks exposed to repeated loading and propose efficient and cost-effective solutions to curtail excessive deformations of structures built on or near jointed rock foundations exposed to repeated loading from machine foundations, railway, road traffic loads and rock cutting.

6.4 Concluding Remarks Regarding Stiffness and Damping Characteristics of Jointed Rocks Subjected to Prolonged Cyclic Loading

A series of cyclic triaxial experiments and conventional monotonic triaxial experiments were performed on rock joints with a natural replicated joint surface at various confining stresses (15 kPa - 300 kPa). The cyclic loading was applied up to 500,000 cycles with a cyclic deviatoric stress amplitude of 300 kPa and a frequency of 8 Hz. The analysis of the results indicated that the cyclic stress-strain hysteresis loops of the rock joints transitioned from sparse to dense with the increasing number of cycles. The monotonic peak deviatoric stress of the rock joints subjected to post-cyclic loading was slightly lower than those subjected to pre-cyclic loading. The cumulative residual axial strain rapidly increased during the initial loading cycles, and the accumulation of residual axial strain gradually decreased during the later loading cycles, giving no signs of failure. Moreover, higher confining stress resulted in lower accumulated residual axial strain. In addition, at lower confining pressures, a sudden slight rise of residual axial strain was observed at several locations of the cumulative residual axial strain curves. The resilient moduli showed a downward trend with cumulative residual axial strain. The resilient moduli of the rock joints were higher than Young's moduli values under all the adopted confining stresses. As the confining stress increased, both resilient moduli and Young's moduli increased, and the difference between the two moduli decreased. An empirical relationship for the resilient moduli variation with the cumulative residual axial strain was developed through nonlinear regression analysis. The damping ratio showed a rapid decrease initially and then increased slowly with cumulative residual axial strain. Higher confining stress corresponded to lower damping ratios. There existed a critical dynamic residual axial strain at which the damping ratio was the lowest and beyond which the damping ratio slightly increased. The corresponding critical dynamic residual axial strain also decreased

with increasing confining stress. An empirical relationship for the correlation between critical dynamic residual axial strain and cyclic stress ratio was proposed using nonlinear regression analysis.

This study provides an insight into fatigue characteristics of jointed rocks exposed to prolonged cyclic loadings, such as permanent deformation, stiffness and damping ratio and their variation with the strain level under various field conditions that are necessary during the design phase of transport infrastructure projects. Understanding the dynamic fatigue behaviour of jointed rocks at different strain levels can enhance the ability of design engineers to predict jointed rock response to prolonged cyclic loading more accurately, make informed decisions, and improve the safety of structures built on or near jointed rock formations. Moreover, thorough knowledge of the dynamic fatigue characteristics of jointed rocks could provide deeper insight into the underlying mechanics of jointed rock behaviour and contribute to the development of more reliable predictive models. These advancements could lead to the invention of more effective and efficient design solutions for rock engineering projects, thereby reducing the likelihood of unexpected behaviours during the construction and operation stages of these projects.

6.5 Recommendations for Future Work

The current study focussed on investigating the dynamic mechanical behaviour and the characteristics of rock joints subjected to cyclic triaxial loading conditions. Moreover, the effect of various cyclic loading conditions, including cyclic deviatoric stress amplitude, confining stress, number of loading cycles as well as the joint surface roughness on the dynamic response of jointed rocks subjected to repeated loading, were evaluated. To further expand this research study, the following recommendations can be made:

- Exploring the impact of loading frequency on the dynamic characteristics of jointed rocks under cyclic loading conditions.
- Evaluating the impact of joint inclination angle on the dynamic mechanical behaviour of jointed rocks subjected to repeated loading.
- Investigating the impact of joint roughness on the dynamic response of rock joints exposed to cyclic loading conditions by testing rock joints with different natural replicated joint surfaces.
- Assessing the impact of rock type on the dynamic behaviour of the jointed rocks by conducting experiments on model rock joints made with different gypsum plaster-to-water ratios.
- Examining the impact of the presence of an infill and its various properties on the dynamic rock joint behaviour under repeated loading.
- Developing a new constitutive model for the dynamic mechanical behaviour of jointed rocks under repeated loading conditions while capturing effects of joint type, roughness, inclination and degradation of asperities during loading.

References

Abdellah, W.R., Ali, M.A., Boghdady, G.Y. and Ibrahim, M.E., 2016. Evaluation of the effect of rock joints on the stability of underground tunnels. Journal of Civil Engineering and Architecture Research, 3(11), 1790-1799.

Akbarimehr, D. and Fakharian, K., 2021. Dynamic shear modulus and damping ratio of clay mixed with waste rubber using cyclic triaxial apparatus. Soil Dynamics and Earthquake Engineering, 140(1), 106435.

Arcos, R., Soares, P.J., Costa, P.A. and Godinho, L., 2021. An experimental/numerical hybrid methodology for the prediction of railway-induced ground-borne vibration on buildings to be constructed close to existing railway infrastructures: Numerical validation and parametric study. Soil Dynamics and Earthquake Engineering, 150(1), 106888.

Armand, G., Boulon, M., Papadopoulos, C., Basanou, M.E. and Vardoulakis, I.P., 2018, April. Mechanical behaviour of Dionysos marble smooth joints: I. Experiments. In Mechanics of jointed and faulted rock, Routledge, 159-164.

Arora, K., Chakraborty, T. and Rao, K.S., 2019. Experimental study on stiffness degradation of rock under uniaxial cyclic sinusoidal compression loading. Rock Mechanics and Rock Engineering, 52(1), 4785-4797.

Arulrajah, A., Naeini, M., Mohammadinia, A., Horpibulsuk, S. and Leong, M., 2020. Recovered plastic and demolition waste blends as railway capping materials. Transportation Geotechnics, 22(1), 100320.

Asadizadeh, M., Hossaini, M.F., Moosavi, M., Masoumi, H. and Ranjith, P.G., 2019. Mechanical characterisation of jointed rock-like material with non-persistent rough joints subjected to uniaxial compression. Engineering Geology, 260(1), 105224.

Ashmawy, A.K., Salgado, R., Guha, S. and Drnevich, V.P., 1995, April. Soil damping and its use in dynamic analyses. In: Third International conferences on recent advances in geotechnical earthquake engineering and soil dynamics, 9.

ASTM D3999-91(2003), Standard Test Methods for the Determination of the Modulus and Damping Properties of Soils Using the Cyclic Triaxial Apparatus, ASTM International, West Conshohocken, PA.

ASTM D5311-13 (2013), Standard test method for load controlled cyclic triaxial strength of soil. ASTM International,West Conshohocken, PA.

Atapour, H. and Moosavi, M., 2014. The influence of shearing velocity on shear behavior of artificial joints. Rock Mechanics and Rock Engineering, 47(1), 1745-1761.

Attewell, P.B. and Farmer, I.W., 1973, January. Fatigue behaviour of rock. In International Journal of Rock Mechanics and Mining Sciences & Geomechanics Abstracts, Pergamon, 10(1), 1-9.

Australian Bureau of Statistics, 2018. Population Projections 2017-2066, Australia, ABS, viewed on 24 March 2023, <https://www.abs. gov.au/statistics/people/population/ population-projections-australia/latest-release>.

Aygar, E.B. and Gokceoglu, C., 2021, August. Evaluation of collapse mechanism and portal interaction of a High-Speed Railway Tunnel (T29 Tunnel, Turkey). In IOP Conference Series: Earth and Environmental Science, 833(1), 012112.

Bagde, M.N. and Petroš, V., 2009. Fatigue and dynamic energy behaviour of rock subjected to cyclical loading. International Journal of Rock Mechanics and Mining Sciences, 46(1), 200-209.

Bagde, M.N. and Petroš, V., 2005a. Fatigue properties of intact sandstone samples subjected to dynamic uniaxial cyclical loading. International Journal of Rock Mechanics and Mining Sciences, 42(2), 237-250.

Bagde, M.N. and Petros, V., 2005b. Waveform effect on fatigue properties of intact sandstone in uniaxial cyclical loading. Rock mechanics and rock engineering, 38(3), 169-196.

Bahaaddini, M., Hagan, P.C., Mitra, R. and Khosravi, M.H., 2016. Experimental and numerical study of asperity degradation in the direct shear test. Engineering Geology, 204(1), 41-52.

Barton, N. and Choubey, V., 1977. The shear strength of rock joints in theory and practice. Rock mechanics, 10(1), 1-54.

Belem, T., Souley, M. and Homand, F., 2007. Modeling surface roughness degradation of rock joint wall during monotonic and cyclic shearing. Acta Geotechnica, 2(4), 227-248.

Bian, X., Jiang, H., Cheng, C., Chen, Y., Chen, R. and Jiang, J., 2014. Full-scale model testing on a ballastless high-speed railway under simulated train moving loads. Soil Dynamics and Earthquake Engineering, 66(1), 368-384.

Bieniawski, Z.T., 1967, October. Mechanism of brittle fracture of rock: part I—theory of the fracture process. In International Journal of Rock Mechanics and Mining Sciences & Geomechanics Abstracts,Pergamon, 4(4), 395-406.

Bie, P.F. and Liu, H.X., 2020. Influence of stress amplitude on the dynamic characteristics of phyllite samples under triaxial multi-stage cyclic loading. In IOP Conference Series: Earth and Environmental Science, 570(3), 032043.

Blewett, R.S., Kennett, B.L. and Huston, D.L., 2012. Australia in time and space. Shaping a nation: A geology of Australia, 47-117.

Booth, E., 2020. Australia's biggest rail infrastructure projects <https://infrastructuremagazine.com.au/2020/11/02/australias-biggest-rail-infrastructure-projects/>

Brady, B.H. and Brown, E.T., 1993. Rock mechanics: for underground mining. Springer science & business media.

Brotóns, V., Tomás, R., Ivorra, S.A.J.C. and Alarcón, J.C., 2013. Temperature influence on the physical and mechanical properties of a porous rock: San Julian's calcarenite. Engineering Geology, 167(1), 117-127.

Brown, E.T. and Hudson, J.A., 1973. Fatigue failure characteristics of some models of jointed rock. Earthquake Engineering & Structural Dynamics, 2(4), 379-386.

Bruneau, G., Tyler, D.B., Hadjigeorgiou, J. and Potvin, Y., 2003. Influence of faulting on a mine shaft—a case study: part I—Background and instrumentation. International Journal of Rock Mechanics and Mining Sciences, 40(1), 95-111.

Burdine, N.T., 1963. Rock failure under dynamic loading conditions. Society of Petroleum Engineers Journal, 3(1), 1-8.

Byerlee, J.D., 1970. The mechanics of stick-slip. Tectonophysics, 9(5), 475-486.

Cadoni, E., 2010. Dynamic characterization of orthogneiss rock subjected to intermediate and high strain rates in tension. Rock Mechanics and Rock Engineering, 43(6), 667-676.

Cai, X., Zhou, Z., Tan, L., Zang, H. and Song, Z., 2020. Fracture behavior and damage mechanisms of sandstone subjected to wetting-drying cycles. Engineering Fracture Mechanics, 234(1), 107109.

Cardani, G. and Meda, A., 2004. Marble behaviour under monotonic and cyclic loading in tension. Construction and Building Materials, 18(6), 419-424.

Cattaneo, S. and Labuz, J.F., 2001. Damage of marble from cyclic loading. Journal of materials in civil engineering, 13(6), 459-465.

Chai, J., 2021. Research on dynamic response characteristics for basement structure of heavy haul railway tunnel with defects. Mathematics, 9(22), 2893.

Cerfontaine, B. and Collin, F., 2018. Cyclic and fatigue behaviour of rock materials: review, interpretation and research perspectives. Rock Mechanics and Rock Engineering, 51(2), 391-414.

Chen, A., Cheng, F., Wu, D. and Tang, X., 2019a. Ground vibration propagation and attenuation of vibrating compaction. Journal of Vibroengineering, 21(5), 1342-1352.

Chen, T.C., Lin, M.L. and Hung, J.J., 2004a. Pseudostatic analysis of Tsao-Ling rockslide caused by Chi-Chi earthquake. Engineering Geology, 71(1-2), 31-47.

Chen, T.C., Yeung, M.R. and Mori, N., 2004b. Effect of water saturation on deterioration of welded tuff due to freeze-thaw action. Cold Regions Science and Technology, 38(2-3), 127-136.

Chen, W.B., Feng, W.Q., Yin, J.H., Borana, L. and Chen, R.P., 2019b. Characterization of permanent axial strain of granular materials subjected to cyclic loading based on shakedown theory. Construction and Building Materials, 198(1), 751-761.

Chen, X., He, P. and Qin, Z., 2019c. Strength Weakening and energy mechanism of rocks subjected to wet–dry cycles. Geotechnical and Geological Engineering, 37(1), 3915-3923.

Chen, X., Liao, Z. and Peng, X., 2012. Deformability characteristics of jointed rock masses under uniaxial compression. International Journal of Mining Science and Technology, 22(2), 213-221.

Chen, Y., Wu, H., Pu, H., Zhang, K., Ju, F., Wu, Y. and Liu, J., 2020. Investigations of damage characteristics in rock material subjected to the joint effect of cyclic loading and impact. Energies, 13(9), 2154.

Chen, Z., Xu, H., Cheng, M., Lu, H., Wang, Z. and Feng, P., 2021. Dynamic Triaxial Test and Microscopic Study of Solidified Muddy Soil with Different Mixing Ratios and Curing Ages. Frontiers in Materials, 8(1), 731449.

Chiu, C.C., Wang, T.T., Weng, M.C. and Huang, T.H., 2013. Modeling the anisotropic behavior of jointed rock mass using a modified smooth-joint model. International Journal of Rock Mechanics and Mining Sciences, 62(1), 14-22.

Clark, G. and Johnston, E.L., 2017. Australia state of the environment 2016: coasts, independent report to the Australian Government Minister for Environment and Energy. Australian Government Department of the Environment and Energy, Canberra.

Connolly, D., 2013. Ground borne vibrations from high-speed trains. PhD Thesis, The University of Edinburgh.

Costa, P.A., Calçada, R. and Cardoso, A.S., 2012. Track–ground vibrations induced by railway traffic: In-situ measurements and validation of a 2.5 D FEM-BEM model. Soil Dynamics and Earthquake Engineering, 32(1), 111-128.

Coviello, A., Lagioia, R. and Nova, R., 2005. On the measurement of the tensile strength of soft rocks. Rock Mechanics and Rock Engineering, 38(1), 251-273.

Craig, R.F., 2004. Craig's soil mechanics. CRC press.

Dai, J., Han, M. and Ang, K.K., 2019. Moving element analysis of partially filled freight trains subject to abrupt braking. International journal of mechanical sciences, 151(1), 85-94.

Das, B.M. and Ramana, G.V., 2011. Principles of Soil Dynamics, Cengage Learning.

Deloitte Access Economics, 2020. Value of Rail 2020, Australasian Railway Association.

Dexing, L., Enyuan, W., Xiangguo, K., Haishan, J., Dongming, W. and Muhammad, A., 2019. Damage precursor of construction rocks under uniaxial cyclic loading tests analyzed by acoustic emission. Construction and Building Materials, 206(1), 169-178.

Ding, Z.D., Du, Y.G., Huang, J. and Shi, C.H., 2014. Test study on dynamic deformation behavior of soft rock-concrete sample under cyclic loading. In Applied Mechanics and Materials. Trans Tech Publications Ltd, 501(1), 295-299.

Dos Santos, N.C., Barbosa, J., Calçada, R. and Delgado, R., 2017. Track-ground vibrations induced by railway traffic: experimental validation of a 3D numerical model. Soil Dynamics and Earthquake Engineering, 97(1), 324-344.

Duan, G., Li, J., Zhang, J., Assefa, E. and Sun, X., 2019. Mechanical properties and failure modes of rock specimens with specific joint geometries in triaxial unloading compressive test. Advances in Materials Science and Engineering, 2019(1), 1-14.

Duarte, M.L.M. and Filho, M.R., 2003. Perception Threshold of People Exposed to Sinusoidal Vibration. Proceedings of the Tenth International Congress on Sound and Vibration, 3791-3798.

Eberhardt, E., Stead, D. and Stimpson, B., 1999. Quantifying progressive pre-peak brittle fracture damage in rock during uniaxial compression. International Journal of Rock Mechanics and Mining Sciences, 36(3), 361-380.

Fahimifar, A. and Soroush, H., 2005. Effect of time on the stress–strain behaviour of a single rock joint. Bulletin of Engineering Geology and the Environment, 64(4), 383-396.

Fan, J., Chen, J., Jiang, D., Chemenda, A., Chen, J. and Ambre, J., 2017. Discontinuous cyclic loading tests of salt with acoustic emission monitoring. International Journal of Fatigue, 94(1), 140-144.

Fan, J., Chen, J., Jiang, D., Ren, S. and Wu, J., 2016. Fatigue properties of rock salt subjected to interval cyclic pressure. International Journal of Fatigue, 90(1), 109-115.

Fan, J., Jiang, D., Liu, W., Wu, F., Chen, J. and Daemen, J.J.K., 2019. Discontinuous fatigue of salt rock with low-stress intervals. International Journal of Rock Mechanics and Mining Sciences, 115(1), 77-86.

Fjær, E., 2009. Static and dynamic moduli of a weak sandstone. Geophysics, 74(2), WA103-WA112.

Fathi, A., Moradian, Z., Rivard, P. and Ballivy, G., 2016. Shear mechanism of rock joints under pre-peak cyclic loading condition. International Journal of Rock Mechanics and Mining Sciences, 83(1), 197-210.

Fuenkajorn, K. and Phueakphum, D., 2010. Effects of cyclic loading on mechanical properties of Maha Sarakham salt. Engineering Geology, 112(1-4), 43-52.

Gamage, R., 2000. Analytical and experimental modelling of coupled water and air flow through rock joints. PhD Thesis, The University of Wollongong.

Gatelier, N., Pellet, F. and Loret, B., 2002. Mechanical damage of an anisotropic porous rock in cyclic triaxial tests. International Journal of Rock Mechanics and Mining Sciences, 39(3), 335-354.

Ge, Y., Tang, H., Ez Eldin, M.A.M., Wang, L., Wu, Q. and Xiong, C., 2017. Evolution process of natural rock joint roughness during direct shear tests. International Journal of Geomechanics, 17(5), E4016013.

Golpazir, I., Ghalandarzadeh, A., Jafari, M.K. and Mahdavi, M., 2016. Dynamic properties of polyurethane foam-sand mixtures using cyclic triaxial tests. Construction and Building Materials, 118(1), 104-115.

Gong, F., Yan, J., Luo, S. and Li, X., 2019. Investigation on the linear energy storage and dissipation laws of rock materials under uniaxial compression. Rock Mechanics and Rock Engineering, 52(1), 4237-4255.

Gong, F.Q., Luo, S. and Yan, J.Y., 2018a. Energy storage and dissipation evolution process and characteristics of marble in three tension-type failure tests. Rock Mechanics and Rock Engineering, 51(1), 3613-3624.

Gong, L., Heitor, A. and Indraratna, B., 2018b. An approach to measure infill matric suction of irregular infilled rock joints under constant normal stiffness shearing. Journal of Rock Mechanics and Geotechnical Engineering, 10(4), 653-660.

Goodman, R.E., 1989. Introduction to rock mechanics, Wiley New York.

Graff, K.F., 2012. Wave motion in elastic solids. Courier Corporation.

Guo, S. and Qi, S., 2015. Numerical study on progressive failure of hard rock samples with an unfilled undulate joint. Engineering Geology, 193(1), 173-182.

Guo, Y., Yang, C. and Mao, H., 2012. Mechanical properties of Jintan mine rock salt under complex stress paths. International Journal of Rock Mechanics and Mining Sciences, 56(1), 54-61.

Guo, Y., Yang, C., Wang, L. and Xu, F., 2018. Effects of cyclic loading on the mechanical properties of mature bedding shale. Advances in Civil Engineering, 2018(1), 8985973.

Haggett, P., 2002. Encyclopedia of world geography, 17. Marshall Cavendish.

Haimson, B.C. and Kim, C.M., 1972. Mechanical behaviour of rock under cyclic fatigue. In: Proceedings of the 13th Symposium on Rock Mechanics, New York: ASCE, 845–863.

Han, G., Jing, H., Jiang, Y., Liu, R. and Wu, J., 2019. Effect of cyclic loading on the shear behaviours of both unfilled and infilled rough rock joints under constant normal stiffness conditions. Rock Mechanics and Rock Engineering, 53(1), 31-57.

He, G.C., Wu, W.Y., Wang, Y., Xue, Y.M., Dai, B. and Zhang, Z.J., 2021a. Fracture Characteristics and Fatigue Damage of Noncoplanar Fractured Rocklike Specimens under Uniaxial Graded Cyclic Loading and Unloading. Geofluids, 2021(1).

He, L., Zhao, Z., Liu, L. and Lu, X., 2022. Asperity Degradation Characteristics and Mechanical Behavior of Rock Joints Subjected to Pre-peak Cyclic Loading. Geotechnical and Geological Engineering, 40(2), 617-634.

He, M., Huang, B., Zhu, C., Chen, Y. and Li, N., 2018. Energy dissipation-based method for fatigue life prediction of rock salt. Rock Mechanics and Rock Engineering, 51(1), 1447-1455.

He, M., Li, N., Chen, Y. and Zhu, C., 2016. Strength and fatigue properties of sandstone under dynamic cyclic loading. Shock and Vibration, 2016(1), 9458582.

He, M., Li, N., Zhu, C., Chen, Y. and Wu, H., 2019. Experimental investigation and damage modeling of salt rock subjected to fatigue loading. International Journal of Rock Mechanics and Mining Sciences, 114(1), 17-23.

He, M.M., Zhang, Z.Q. and Li, N., 2021b. Experimental investigation and empirical model to determine the damping and shear stiffness properties of soft rock under multistage cyclic loading. Soil Dynamics and Earthquake Engineering, 147(1), 106818.

Heap, M.J. and Faulkner, D.R., 2008. Quantifying the evolution of static elastic properties as crystalline rock approaches failure. International Journal of Rock Mechanics and Mining Sciences, 45(4), 564-573.

Heap, M.J., Faulkner, D.R., Meredith, P.G. and Vinciguerra, S., 2010. Elastic moduli evolution and accompanying stress changes with increasing crack damage: implications for stress changes around fault zones and volcanoes during deformation. Geophysical Journal International, 183(1), 225-236.

Heap, M.J., Vinciguerra, S. and Meredith, P.G., 2009. The evolution of elastic moduli with increasing crack damage during cyclic stressing of a basalt from Mt. Etna volcano. Tectonophysics, 471(1-2), 153-160.

Hobbs, D., 1966, May. Scale model studies of strata movement around mine roadways. Apparatus, technique and some preliminary results. In International Journal of Rock Mechanics and Mining Sciences & Geomechanics Abstracts, Pergamon, 3(2), 101-112.

Holm, G., Andréasson, B., Bengtsson, P.E., Bodare, A. and Eriksson, H., 2002. Mitigation of track and ground vibrations by high-speed trains at Ledsgard, Sweden. Swedish Deep Stabilization Research Centre, Report, 10(1), 58-67.

Hossaini, K.A., Babanouri, N. and Nasab, S.K., 2014. The influence of asperity deformability on the mechanical behavior of rock joints. International Journal of Rock Mechanics and Mining Sciences, 70(1), 154-161.

Hou, D., Rong, G., Yang, J., Zhou, C., Peng, J. and Wang, X., 2016. A new shear strength criterion of rock joints based on cyclic shear experiment. European Journal of Environmental and Civil Engineering, 20(2), 180-198.

Huang T.H. and Doong Y.S., 1990. Anisotropic shear strength of rock joints. Proceedings of the International Symposium on Rock Joints, Loen, Norway, 211-218.

Huang, C.J., Yin, H.Y., Chen, C.Y., Yeh, C.H., Wang, C.L., 2007. Ground vibrations produced by rock motions and debris flows. Journal of Geophysical Research: Earth Surface, 112(1), F002014.

Huang, X., Haimson, B.C., Plesha, M.E. and Qiu, X., 1993, June. An investigation of the mechanics of rock joints—Part I. Laboratory investigation. In International journal of rock mechanics and mining sciences & geomechanics abstracts, Pergamon. 30(3), 257-269.

Hudson, J.A. and Harrison, J.P., 1997. Rock Engineering Mechanics- An Introduction to the Principles. Elsevier, Oxford.

Hungr, O. and Coates, D.F., 1978. Deformability of joints and its relation to rock foundation settlements. Canadian Geotechnical Journal, 15(2), 239-249.

Hutson, R.W. and Dowding, C.H., 1990, April. Joint asperity degradation during cyclic shear. In International Journal of Rock Mechanics and Mining Sciences & Geomechanics Abstracts, Pergamon. 27(2), 109-119.

Inland Rail, 2023. What is Inland Rail, Australian Rail Track Cooperation, viewed on 24 March 2023, < https://inlandrail.artc.com.au/what-is-inland-rail/>.

Indraratna, B., 1990. Development and applications of a synthetic material to simulate soft sedimentary rocks. Geotechnique, 40(2), 189-200.

Jafari, M.K., Hosseini, K.A., Pellet, F., Boulon, M. and Buzzi, O., 2003. Evaluation of shear strength of rock joints subjected to cyclic loading. Soil Dynamics and Earthquake Engineering, 23(7), 619-630.

Jafari, M.K., Pellet, F., Boulon, M. and Hosseini, K.A., 2004. Experimental study of mechanical behaviour of rock joints under cyclic loading. Rock Mechanics and Rock Engineering, 37(1), 3-23.

Jahanian, H. and Sadaghiani, M.H., 2015. Experimental study on the shear strength of sandy clay infilled regular rough rock joints. Rock Mechanics and Rock Engineering, 48(3), 907-922.

Jamal-Eddine, A.K., 2017. Sources of vibrations and their impact on the environment. PhD Thesis, Université Paris-Est.

Jayasinghe, B., Zhao, Z., Chee, A.G.T., Zhou, H. and Gui, Y., 2019. Attenuation of rock blasting induced ground vibration in rock-soil interface. Journal of Rock Mechanics and Geotechnical Engineering, 11(4), 770-778.

Jia, C., Xu, W., Wang, R., Wang, W., Zhang, J. and Yu, J., 2018. Characterisation of the deformation behavior of fine-grained sandstone by triaxial cyclic loading. Construction and Building Materials, 162(1), 113-123.

Jibson, R.W., Harp, E.L., Schulz, W. and Keefer, D.K., 2006. Large rock avalanches triggered by the M 7.9 Denali Fault, Alaska, earthquake of 3 November 2002. Engineering geology, 83(1-3), 144-160.

Jing, L., Stephansson, O. and Nordlund, E., 1993. Study of rock joints under cyclic loading conditions. Rock Mechanics and Rock Engineering, 26(1), 215-232.

Johnson, D., 2009. The geology of Australia. Cambridge University Press.

Johnston, I.W. and Choi, S.K., 1986. A synthetic soft rock for laboratory model studies. Geotechnique, 36(2), 251-263.

Jones, S., 2010. Ground vibration from underground railways: how simplifying assumptions limit prediction accuracy. PhD Thesis, University of Cambridge.

Khabbaz, H. and Fatahi, B., 2014. How to overcome geotechnical challenges in implementing high speed rail systems in Australia. Geotechnical Engineering Journal of the SEAGS & AGSSEA, 45(1).

Kulatilake, P.H.S.W., He, W., Um, J. and Wang, H., 1997. A physical model study of jointed rock mass strength under uniaxial compressive loading. International Journal of Rock Mechanics and Mining Sciences, 34(3-4), 165.e1-165.e15.

Kulatilake, P.H.S.W., Liang, J. and Gao, H., 2001. Experimental and numerical simulations of jointed rock block strength under uniaxial loading. Journal of Engineering Mechanics, 127(12), 1240-1247.

Kou, M., Liu, X., Tang, S. and Wang, Y., 2019. Experimental study of the prepeak cyclic shear mechanical behaviors of artificial rock joints with multiscale asperities. Soil Dynamics and Earthquake Engineering, 120(1), 58-74.

Kouroussis, G., Connolly, D.P. and Verlinden, O., 2014. Railway-induced ground vibrations–a review of vehicle effects. International Journal of Rail Transportation, 2(2), 69-110.

Kusumi, H., Nishida, K. and Teraoka, K., 2018. A formulation of shear strength for rock joints included two or three different asperities. In Mechanics of Jointed and Faulted Rock, Routledge, 235-239.

Lacy, H.S. and Gould, J.P., 1985. Settlement from pile driving in sands. In Vibration Problems in Geotechnical Engineering, ASCE, 152-173.

Ladanyi, B. and Archambault, G., 1969. Simulation of shear behavior of a jointed rock mass. In The 11th US Symposium on Rock Mechanics (USRMS). Berkeley, CA, 105-25.

Lanzo, G. and Vucetic, M., 1999. Effect of soil plasticity on damping ratio at small cyclic strains. Soils and Foundations, 39(4), 131-141.

Lee, H.S., Park, Y.J., Cho, T.F. and You, K.H., 2001. Influence of asperity degradation on the mechanical behavior of rough rock joints under cyclic shear loading. International journal of rock mechanics and mining sciences, 38(7), 967-980.

Leshchinsky, B. and Ling, H.I., 2013. Numerical modeling of behavior of railway ballasted structure with geocell confinement. Geotextiles and Geomembranes, 36(1), 33-43.

Liang, W., Zhang, C., Gao, H., Yang, X., Xu, S. and Zhao, Y., 2012. Experiments on mechanical properties of salt rocks under cyclic loading. Journal of Rock Mechanics and Geotechnical Engineering, 4(1), 54-61.

Li, B., Feng, Z., Wang, G. and Wang, W., 2016. Processes and behaviors of block topple avalanches resulting from carbonate slope failures due to underground mining. Environmental Earth Sciences, 75(1), 1-26.

Li, D.X., Wang, E.Y., Kong, X.G., Jia, H.S., Wang, D.M., Ali, M., 2019a. Damage precursor of construction rocks under uniaxial cyclic loading tests analysed by acoustic emission. Construction and Building Materials, 206(1), 169-178.

Li, J., Kaunda, R.B., Zhu, L., Zhou, K. and Gao, F., 2019b. Experimental study of the pore structure deterioration of sandstones under freeze-thaw cycles and chemical erosion. Advances in Civil Engineering, 2019(1), 9687843.

Li, N., Chen, W. and Zhang, P., 2001a. Strength properties of the jointed rock mass medium under dynamic cyclic loading. Progress in Natural Science, 11(3), 197-201.

Li, N., Chen, W., Zhang, P. and Swoboda, G., 2001b. The mechanical properties and a fatigue-damage model for jointed rock masses subjected to dynamic cyclical loading. International Journal of Rock Mechanics and Mining Sciences, 38(7), 1071-1079.

Li, T., Pei, X., Wang, D., Huang, R. and Tang, H., 2019c. Nonlinear behavior and damage model for fractured rock under cyclic loading based on energy dissipation principle. Engineering Fracture Mechanics, 206(1), 330-341.

Li, X. and He, S., 2009. Seismically induced slope instabilities and the corresponding treatments: the case of a road in the Wenchuan earthquake hit region. Journal of Mountain Science, 6(1), 96-100.

Li, X., Peng, K., Peng, J. and Hou, D., 2021. Experimental investigation of cyclic wetting-drying effect on mechanical behavior of a medium-grained sandstone. Engineering Geology, 293(1), 106335.

Li, Y., Oh, J., Mitra, R. and Hebblewhite, B., 2015. Experimental studies on the mechanical behaviour of rock joints with various openings. Rock Mechanics and Rock Engineering, 49(1), 837-853.

Lin, Q., Cao, P., Mao, S., Ou, C. and Cao, R., 2020. Fatigue behaviour and constitutive model of yellow sandstone containing pre-existing surface crack under uniaxial cyclic loading. Theoretical and Applied Fracture Mechanics, 109(1), 102776.

Liu, E. and He, S., 2012. Effects of cyclic dynamic loading on the mechanical properties of intact rock samples under confining pressure conditions. Engineering Geology, 125(1), 81-91.

Liu, E., He, S., Xue, X. and Xu, J., 2011. Dynamic properties of intact rock samples subjected to cyclic loading under confining pressure conditions. Rock mechanics and rock engineering, 44(5), 629-634.

Liu, E., Huang, R. and He, S., 2012. Effects of frequency on the dynamic properties of intact rock samples subjected to cyclic loading under confining pressure conditions. Rock mechanics and rock engineering, 45(1), 89-102.

Liu, H., Gao, K. and Zhu, X., 2021a. Experimental study on dynamic fatigue properties of dolomite samples under triaxial multi-level cyclic loading. Bulletin of Engineering Geology and the Environment, 80(1), 551-565.

Liu, J., Xie, H., Hou, Z., Yang, C. and Chen, L., 2014. Damage evolution of rock salt under cyclic loading in uniaxial tests. Acta Geotechnica, 9(1), 153-160.

Liu, M. and Liu, E., 2017. Dynamic mechanical properties of artificial jointed rock samples subjected to cyclic triaxial loading. International Journal of Rock Mechanics and Mining Sciences, 98(1), 54-66.

Liu, M., Liu, E., Feng, J., Zheng, Q., Fu, J. and Luo, W., 2021b, February. Dynamic mechanical properties of jointed soft rock samples subjected to cyclic triaxial loading: a FEM-DEM-based study. In IOP Conference Series: Earth and Environmental Science, IOP Publishing 676(1), 012066.

Liu, Q., Qian, Z. and Wu, Z., 2019. Micro/macro physical and mechanical variation of red sandstone subjected to cyclic heating and cooling: an experimental study. Bulletin of Engineering Geology and the Environment, 78(1), 1485-1499.

Liu, X.R., Kou, M.M., Lu, Y.M. and Liu, Y.Q., 2018a. An experimental investigation on the shear mechanism of fatigue damage in rock joints under pre-peak cyclic loading condition. International Journal of Fatigue, 106(1), 175-184.

Liu, X.S., Ning, J.G., Tan, Y.L. and Gu, Q.H., 2016. Damage constitutive model based on energy dissipation for intact rock subjected to cyclic loading. International journal of rock mechanics and mining sciences, 85(1), 27-32.

Liu, Y. and Dai, F., 2021. A review of experimental and theoretical research on the deformation and failure behavior of rocks subjected to cyclic loading. Journal of Rock Mechanics and Geotechnical Engineering, 13(5), 1203-1230.

Liu, Y., Dai, F., Dong, L., Xu, N. and Feng, P., 2018b. Experimental investigation on the fatigue mechanical properties of intermittently jointed rock models under cyclic uniaxial compression with different loading parameters. Rock Mechanics and Rock Engineering, 51(1), 47-68.

Liu, Y., Dai, F., Feng, P. and Xu, N.W., 2018c. Mechanical behavior of intermittent jointed rocks under random cyclic compression with different loading parameters. Soil Dynamics and Earthquake Engineering, 113(1), 12-24.

Liu, Y., Dai, F., Fan, P., Xu, N. and Dong, L., 2017. Experimental investigation of the influence of joint geometric configurations on the mechanical properties of intermittent jointed rock models under cyclic uniaxial compression. Rock Mechanics and Rock Engineering, 50(1), 1453-1471.

Lü, Q., Xiao, Z.P., Ji, J. and Zheng, J., 2017. Reliability based design optimization for a rock tunnel support system with multiple failure modes using response surface method. Tunnelling and Underground Space Technology, 70(1), 1-10.

Ma, L.J., Liu, X.Y., Wang, M.Y., Xu, H.F., Hua, R.P., Fan, P.X., Jiang, S.R., Wang, G.A. and Yi, Q.K., 2013. Experimental investigation of the mechanical properties of rock salt under triaxial cyclic loading. International Journal of Rock Mechanics and Mining Sciences, 62(1), 34-41.

Martin, C.D. and Chandler, N.A., 1994, December. The progressive fracture of Lac du Bonnet granite. In International journal of rock mechanics and mining sciences & geomechanics abstracts, Pergamon, 31(6), 643-659.

Meng, Q., Zhang, M., Han, L., Pu, H. and Nie, T., 2016. Effects of acoustic emission and energy evolution of rock specimens under the uniaxial cyclic loading and unloading compression. Rock Mechanics and Rock Engineering, 49(1), 3873-3886.

Mirzaghorbanali, A., Nemcik, J. and Aziz, N., 2014. Effects of cyclic loading on the shear behaviour of infilled rock joints under constant normal stiffness conditions. Rock mechanics and rock engineering, 47(4), 1373-1391.

Mohammadinia, A., Naeini, M., Arulrajah, A., Horpibulsuk, S. and Leong, M., 2020. Shakedown analysis of recycled materials as railway capping layer under cyclic loading. Soil Dynamics and Earthquake Engineering, 139(1), 106423.

Momeni, A., Karakus, M., Khanlari, G.R. and Heidari, M., 2015. Effects of cyclic loading on the mechanical properties of a granite. International Journal of Rock Mechanics and Mining Sciences, 77(1), 89-96.

Monismith, C.L., Ogawa, N. and Freeme, C.R., 1975. Permanent deformation characteristics of subgrade soils due to repeated loading. Transportation research record, (537).

Mostyn, G.R., Bagheripour, M.H., 1998. A new model material to simulate rock. In: Rossmanith P (ed) Proceedings of mechanics of jointed and faulted rock, 225–230.

Naeini, M., Mohammadinia, A., Arulrajah, A. and Horpibulsuk, S., 2021. Recycled glass blends with recycled concrete aggregates in sustainable railway geotechnics. Sustainability, 13(5), 2463.

National Freight and Supply Chain Strategy, 2019. Transport and Infrastructure Council, Commonwealth of Australia

Nejati, H.R. and Ghazvinian, A., 2014. Brittleness effect on rock fatigue damage evolution. Rock mechanics and rock engineering, 47(1), 1839-1848.

Ng, C.W.W., Liu, G.B. and Li, Q., 2013. Investigation of the long-term tunnel settlement mechanisms of the first metro line in Shanghai. Canadian Geotechnical Journal, 50(6), 674-684.

Nie, R., Li, Y., Leng, W., Mei, H., Dong, J. and Chen, X., 2020. Deformation characteristics of fine-grained soil under cyclic loading with intermittence. Acta Geotechnica, 15(1), 3041-3054.

Niktabar, S.M., Rao, K.S. and Shrivastava, A.K., 2017. Effect of rock joint roughness on its cyclic shear behavior. Journal of Rock Mechanics and Geotechnical Engineering, 9(6), 1071-1084.

Niu, W.J., Feng, X.T., Xiao, Y.X., Feng, G.L., Yao, Z.B. and Hu, L., 2021. Identification of potential high-stress hazards in deep-buried hard rock tunnel based on microseismic information: a case study. Bulletin of engineering geology and the Environment, 80, 1265-1285.

Peng, K., Zhou, J., Zou, Q. and Song, X., 2020. Effect of loading frequency on the deformation behaviours of sandstones subjected to cyclic loads and its underlying mechanism. International Journal of Fatigue, 131(1), 105349.

Peng, K., Zhou, J., Zou, Q., Zhang, J. and Wu, F., 2019. Effects of stress lower limit during cyclic loading and unloading on deformation characteristics of sandstones. Construction and Building Materials, 217(1), 202-215.

Petros, V., Bagde, M.N., Holub, K. and Michalcik, P., 2003. Comparison of changes in the strength and the deformation behaviour of rocks under static and dynamic loading. In: 10th Congress of the ISRM, Technology Roadmap for Rock Mechanics, Johannesburg, South Africa, 2(8-12), 899–902.

PLAXIS 3D Material Models Manual, 2022. Bentley Systems International Limited, Dublin.

Pola, A., Crosta, G.B., Fusi, N. and Castellanza, R., 2014. General characterization of the mechanical behaviour of different volcanic rocks with respect to alteration. Engineering Geology, 169(1), 1-13.

Prakash, S., 1981. Soil Dynamics. New York, McGraw Hill.

Premadasa, W.N., 2013. The influence of infill saturation on the shear strength of soil-infilled rock joints. Ph D Thesis, The University of Wollongong.

Prost, G.L., 1988, October. Jointing at rock contacts in cyclic loading. In International Journal of Rock Mechanics and Mining Sciences & Geomechanics Abstracts, Pergamon. 25(5), 263-272.

Qi, S., Xu, Q., Zhang, B., Zhou, Y., Lan, H. and Li, L., 2011. Source characteristics of long runout rock avalanches triggered by the 2008 Wenchuan earthquake, China. Journal of Asian Earth Sciences, 40(4), 896-906.

Qin, Y., Xu, X., Yan, C., Wen, L., Wang, Z. and Luo, Z., 2021. Dynamic damping ratio of mudded intercalations with small and medium strain during cyclic dynamic loading. Engineering Geology, 280(1), 105952.

Rainer, J.H., 1982. Effect of vibrations on historic buildings: An overview. Bulletin of the Association for Preservation Technology, 14(1), 2-10.

Rainer, J.H., Pernica, G., Maurenbrecher, A.H.P., Law, K.T. and Allen, D.E., 1988. Effect of train-induced vibrations on houses-a case study. In Symposium/workshop on serviceability of buildings (movements, deformations, vibrations), 603-14.

Ramamurthy, T., 2001. Shear strength response of some geological materials in triaxial compression. International Journal of Rock Mechanics and Mining Sciences, 38(5), 683-697.

Ray, S.K., Sarkar, M. and Singh, T.N., 1999. Effect of cyclic loading and strain rate on the mechanical behaviour of sandstone. International Journal of Rock Mechanics and Mining Sciences, 36(4), 543-549.

Ren, S.L., Tao, Z.G., He, M.C., Pang, S.H., Li, M.N. and Xu, H.T., 2020. Stability analysis of open-pit gold mine slopes and optimization of mining scheme in Inner Mongolia, China. Journal of Mountain Science, 17(12), 2997-3011.

Rose, J., Su, B. and Twehues, F., 2004. Comparisons of railroad track and substructure computer model predictive stress values and in-situ stress measurements. In Proceedings of the AREMA 2004 Annual Conference & Exposition, Nashville, TN.

Rosenblad, J.L., 1970. Geomechanical model study of the failure modes of jointed rock masses, PhD Thesis, University of Illinois at Urbana-Champaign.

Saucier, K.L., 1967. Development of material for modeling rock. U.S. Army Engineer Waterways Experiment Station (Vicksburg Mississippi.). Miscellaneous Paper, 6-93.

Scholz, C.H. and Koczynski, T.A., 1979. Dilatancy anisotropy and the response of rock to large cyclic loads. Journal of Geophysical Research: Solid Earth, 84(B10), 5525-5534.

Sheng, X., Jones, C.J.C. and Thompson, D.J., 2006. Prediction of ground vibration from trains using the wavenumber finite and boundary element methods. Journal of Sound and Vibration, 293(3-5), 575-586.

Shi, C.H., Lei, M.F. and Peng, L.M., 2014. Accumulated deformation behavior and computational model of water-rich mudstone under cyclic loading. Rock mechanics and rock engineering, 47(4), 1485-1491.

Singh, M., Rao, K.S. and Ramamurthy, T., 2002. Strength and deformational behaviour of a jointed rock mass. Rock Mechanics and Rock Engineering, 35(1), 45-64.

Singh, S.K., 1989. Fatigue and strain hardening behaviour of graywacke from the flagstaff formation, New South Wales. Engineering Geology, 26(2), 171-179.

Sinha, U.N. and Singh, B., 2000. Testing of rock joints filled with gouge using a triaxial apparatus. International Journal of Rock Mechanics and Mining Sciences, 37(6), 963-981.

Song, H., Zhang, H., Fu, D. and Zhang, Q., 2016. Experimental analysis and characterization of damage evolution in rock under cyclic loading. International Journal of Rock Mechanics and Mining Sciences, 88(1), 157-164.

Song, R., Yue-ming, B., Jing-Peng, Z., De-yi, J. and Chun-he, Y., 2013. Experimental investigation of the fatigue properties of salt rock. International Journal of Rock Mechanics and Mining Sciences, 64(1), 68-72.

Song, S., Liu, X., Tan, Y., Fan, D., Ma, Q. and Wang, H., 2020. Study on failure modes and energy evolution of coal-rock combination under cyclic loading. Shock and Vibration, 2020(1).

Srbulov, M., 2010. Ground vibration engineering: simplified analyses with case studies and examples, 12. Springer Science & Business Media.

Stiebel, D., Muller, R., Bongini, E., Ekbald, A., Coquel, G. and Alguacil, A.A., 2012. Definition of reference cases typical for hot spots in Europe with existing vibration problems. Rivas Project SCP0-GA-2010-265754. Deliverable D1. 5. Report to the EC.

Stimpson, B., 1970. Modelling materials for engineering rock mechanics. In International Journal of Rock Mechanics and Mining Sciences & Geomechanics Abstracts, Pergamon, 7(1), 77-121.

Suiker, A.S., Selig, E.T. and Frenkel, R., 2005. Static and cyclic triaxial testing of ballast and subballast. Journal of geotechnical and geoenvironmental engineering, 131(6), 771-782.

Sydney Metro, (2023). Sydney Metro Information and Plans, About Sydney Metro, viewed on 24 March 2023<https://www.sydneymetro.info/about>.

Taheri, A., Royle, A., Yang, Z. and Zhao, Y., 2016. Study on variations of peak strength of a sandstone during cyclic loading. Geomechanics and Geophysics for Geo-Energy and Geo-Resources, 2(1), 1-10.

Takarli, M., Prince, W. and Siddique, R., 2008. Damage in granite under heating/cooling cycles and water freeze–thaw condition. International Journal of Rock Mechanics and Mining Sciences, 45(7), 1164-1175.

Tan, X., Chen, W., Yang, J. and Cao, J., 2011. Laboratory investigations on the mechanical properties degradation of granite under freeze–thaw cycles. Cold Regions Science and Technology, 68(3), 130-138.

Thirukumaran, S., 2014. Shear strength of degradable rock joints. PhD Thesis, The University of Wollongong.

Tien, Y.M., Lee, D.H. and Juang, C.H., 1990. Strain, pore pressure and fatigue characteristics of sandstone under various load conditions. International Journal of Rock Mechanics and Mining Sciences & Geomechanics, 27(4), 283-289.

Touqan, M., Ahmed, A., El Naggar, H. and Stark, T., 2020. Static and cyclic characterization of fouled railroad sub-ballast layer behaviour. Soil Dynamics and Earthquake Engineering, 137(1), 106293.

Trimming, T.R., 2012. Derailing Powder River Basin coal exports: Legal mechanisms to regulate fugitive coal dust from rail transportation. Golden Gate University Environmental Law Journal, 6(1), 321.

Tse, R. and Cruden, D.M., 1979, October. Estimating joint roughness coefficients. In International journal of rock mechanics and mining sciences & geomechanics abstracts, Pergamon, 16(5), 303-307.

Vaneghi, R.G., Ferdosi, B., Okoth, A.D. and Kuek, B., 2018. Strength degradation of sandstone and granodiorite under uniaxial cyclic loading. Journal of Rock Mechanics and Geotechnical Engineering, 10(1), 117-126.

Vaneghi, R.G., Thoeni, K., Dyskin, A.V., Sharifzadeh, M. and Sarmadivaleh, M., 2020. Fatigue damage response of typical crystalline and granular rocks to uniaxial cyclic compression. International Journal of Fatigue, 138(1), 105667.

Vergara, M.R., Kudella, P. and Triantafyllidis, T., 2015. Large scale tests on jointed and bedded rocks under multi-stage triaxial compression and direct shear. Rock Mechanics and Rock Engineering, 48(1), 75-92.

Volberg, G., 1983. Propagation of ground vibrations near railway tracks. Journal of Sound and Vibration, 87(2), 371-376.

Voznesenskii, A.S., Krasilov, M.N., Kutkin, Y.O., Tavostin, M.N. and Osipov, Y.V., 2017. Features of interrelations between acoustic quality factor and strength of rock salt during fatigue cyclic loadings. International Journal of Fatigue, 97(1), 70-78.

Waltham, A.C. and Swift, G.M., 2004. Bearing capacity of rock over mined cavities in Nottingham. Engineering Geology, 75(1), 15-31.

Wang, H., He, M., Zhu, J., Guo, S., Chen, Y. and Li, N., 2021a. Experimental investigation of linear damping characteristics on granite and red sandstone under dynamic cyclic loading. European Journal of Environmental and Civil Engineering, 26(11), 5259-5278.

Wang, J., Li, J., Shi, Z. and Chen, J., 2022. Energy evolution and failure characteristics of red sandstone under discontinuous multilevel fatigue loading. International Journal of Fatigue, 160(1), 106830.

Wang, K. and Zhuang, Y., 2021. Characterizing the permanent deformation Response-Behavior of subgrade material under cyclic loading based on the shakedown theory. Construction and Building Materials, 311(1), 125325.

Wang, W.L., Wang, T.T., Su, J.J., Lin, C.H., Seng, C.R. and Huang, T.H., 2001. Assessment of damage in mountain tunnels due to the Taiwan Chi-Chi earthquake. Tunnelling and underground space technology, 16(3), 133-150.

Wang, W., Wang, M. and Liu, X., 2016. Study on mechanical features of Brazilian splitting fatigue tests of salt rock. Advances in Civil Engineering, 2016(1), 5436240.

Wang, Y., Hu, Y.Z. and Gao, S.H., 2021b. Dynamic mechanical behaviors of interbedded marble subjected to multi-level uniaxial compressive cyclic loading conditions: an insight into fracture evolution analysis. Engineering Fracture Mechanics, 241(1), 107410.

Wang, Y., Yi, Y.F., Li, C.H. and Han, J.Q., 2021c. Anisotropic fracture and energy characteristics of a Tibet marble exposed to multi-level constant-amplitude (MLCA) cyclic loads: a lab-scale testing. Engineering fracture mechanics, 244(1), 107550.

Wang, Z., Li, S., Qiao, L. and Zhao, J., 2013. Fatigue behavior of granite subjected to cyclic loading under triaxial compression condition. Rock Mechanics and Rock Engineering, 46(6), 1603-1615.

Wasantha, P.L.P., Ranjith, P.G. and Shao, S.S., 2014. Energy monitoring and analysis during deformation of bedded-sandstone: use of acoustic emission. Ultrasonics, 54(1), 217-226.

Wichtmann, T., Kimmig, I. and Triantafyllidis, T., 2017. On correlations between “dynamic” (small-strain) and “static” (large-strain) stiffness moduli–an experimental investigation on 19 sands and gravels. Soil Dynamics and Earthquake Engineering, 98(1), 72-83.

Wu, X., Jiang, Y., Guan, Z. and Gong, B., 2019. Influence of confining pressure-dependent Young’s modulus on the convergence of underground excavation. Tunnelling and Underground Space Technology, 83(1), 135-144.

Xiang, Z., Wang, H., Xu, W. and Xie, W.C., 2020. Experimental study on hydro-mechanical behaviour of anisotropic columnar jointed rock-like specimens. Rock Mechanics and Rock Engineering, 53(1), 5781-5794.

Xiao, J.Q., Ding, D.X., Jiang, F.L. and Xu, G., 2010. Fatigue damage variable and evolution of rock subjected to cyclic loading. International Journal of Rock Mechanics and Mining Sciences, 47(3), 461-468.

Xiao, J.Q., Ding, D.X., Xu, G. and Jiang, F.L., 2009. Inverted S-shaped model for nonlinear fatigue damage of rock. International journal of rock mechanics and mining sciences, 46(3), 643-648.

Xie, H., Wang, J.A. and Xie, W.H., 1997. Fractal effects of surface roughness on the mechanical behavior of rock joints. Chaos, Solitons & Fractals, 8(2), 221-252.

Xu, B., Liu, X., Zhou, X., Xie, Y., Suliman, L., Liu, X., Lin, G. and Huang, J., 2021a. Investigation on the macro-meso fatigue damage mechanism of rock joints with multiscale asperities under pre-peak cyclic shear loading. Soil Dynamics and Earthquake Engineering, 151(1), 106958.

Xu, H., Chen, C., Shao, Z., Wang, Z., Cai, L., Li, Z. and Xu, C., 2021b. Dynamic response of heavy-haul railway tunnels in fully weathered coastal red sandstone strata with base rock reinforcement: A numerical study. Journal of Coastal Research, 37(1), 191-202.

Yang, B., He, M. and Chen, Y., 2020a. Experimental study of nonlinear damping characteristics on granite and red sandstone under the multi-level cyclic loading-unloading triaxial compression. Arabian Journal of Geosciences, 13(2), 1-17.

Yang, S.Q., Huang, Y.H. and Tang, J.Z., 2020b. Mechanical, acoustic, and fracture behaviors of yellow sandstone specimens under triaxial monotonic and cyclic loading. International Journal of Rock Mechanics and Mining Sciences, 130(1), 104268.

Yang, S.Q., Jing, H.W. and Wang, S.Y., 2012. Experimental investigation on the strength, deformability, failure behavior and acoustic emission locations of red sandstone under triaxial compression. Rock mechanics and rock engineering, 45(4), 583-606.

Yang, S.Q., Ranjith, P.G., Huang, Y.H., Yin, P.F., Jing, H.W., Gui, Y.L. and Yu, Q.L., 2015. Experimental investigation on mechanical damage characteristics of sandstone under triaxial cyclic loading. Geophysical Journal International, 201(2), 662-682.

Yang, S.Q., Tian, W.L. and Ranjith, P.G., 2017. Experimental investigation on deformation failure characteristics of crystalline marble under triaxial cyclic loading. Rock Mechanics and Rock Engineering, 50(1), 2871-2889.

Yang, S.Q., Yang, J. and Xu, P., 2020c. Analysis on pre-peak deformation and energy dissipation characteristics of sandstone under triaxial cyclic loading. Geomechanics and Geophysics for Geo-Energy and Geo-Resources, 6(1), 1-15.

Yang, X., Wang, J., Hou, D., Zhu, C. and He, M., 2018a. Effect of dry-wet cycling on the mechanical properties of rocks: a laboratory-scale experimental study. Processes, 6(10), 199.

Yang, Y., Duan, H., Xing, L., Ning, S. and Lv, J., 2018b. Fatigue characteristics of limestone under triaxial compression with cyclic loading. Advances in Civil Engineering, 10(1), 1-12.

Yang, Y., Ju, Y., Li, F., Gao, F. and Sun, H., 2016. The fractal characteristics and energy mechanism of crack propagation in tight reservoir sandstone subjected to triaxial stresses. Journal of Natural Gas Science and Engineering, 32(1), 415-422.

Yang, Z.Y., Chen, J.M. and Huang, T.H., 1998. Effect of joint sets on the strength and deformation of rock mass models. International Journal of Rock Mechanics and Mining Sciences, 35(1), 75-84.

Yasuhara, K., Murakami, S., Toyota, N. and Hyde, A.F., 2001. Settlements in fine-grained soils under cyclic loading. Soils and foundations, 41(6), 25-36.

Yavuz, H., Demirdag, S. and Caran, S., 2010. Thermal effect on the physical properties of carbonate rocks. International Journal of Rock Mechanics and Mining Sciences, 47(1), 94-103.

Yin, Y., Sun, P., Zhang, M. and Li, B., 2011. Mechanism on apparent dip sliding of oblique inclined bedding rockslide at Jiweishan, Chongqing, China. Landslides, 8(1), 49-65.

Yoshinaka, R., Osada, M. and Tran, T.V., 1996, September. Deformation behaviour of soft rocks during consolidated-undrained cyclic triaxial testing. In International journal of rock mechanics and mining sciences & geomechanics abstracts, Pergamon, 33(6), 557-572.

Yu, D., Liu, E., Sun, P., Xing, H. and Zheng, Q., 2021. Dynamic mechanical properties and constitutive model for jointed mudstone samples subjected to cyclic loading. European Journal of Environmental and Civil Engineering, 26(14), 7240-7266.

Yu, J., Chen, X., Cai, Y.Y. and Li, H., 2016. Triaxial test research on mechanical properties and permeability of sandstone with a single joint filled with gypsum. KSCE Journal of Civil Engineering, 20(1), 2243-2252.

Zhang, C.L., Jiang, G.L., Su, L.J. and Liu, W.M., 2018a. Dynamic behaviour of weathered red mudstone in Sichuan (China) under triaxial cyclic loading. Journal of Mountain Science, 15(8), 1789-1806.

Zhang, H., Meng, X. and Yang, G., 2020. A study on mechanical properties and damage model of rock subjected to freeze-thaw cycles and confining pressure. Cold Regions Science and Technology, 174, 103056.

Zhang, J.C., Zhou, S.H., Xu, X.H. and Fang, L.G., 2013. Evolution of the elastic properties of a bedded argillite damaged in cyclic triaxial tests. International Journal of Rock Mechanics and Mining Sciences, 58(1), 103-110.

Zhang, M., Meng, Q. and Liu, S., 2017. Energy evolution characteristics and distribution laws of rock materials under triaxial cyclic loading and unloading compression. Advances in Materials Science and Engineering, 2017(1), 5471571.

Zhang, Q.B. and Zhao, J., 2014. A review of dynamic experimental techniques and mechanical behaviour of rock materials. Rock mechanics and rock engineering, 47(1), 1411-1478.

Zhang, X., Jiang, Q., Kulatilake, P.H.S.W., Xiong, F., Yao, C. and Tang, Z., 2019. Influence of asperity morphology on failure characteristics and shear strength properties of rock joints under direct shear tests. International Journal of Geomechanics, 19(2), 04018196.

Zhang, Z., Jiang, Q., Zhou, C. and Liu, X., 2014. Strength and failure characteristics of Jurassic Red-Bed sandstone under cyclic wetting–drying conditions. Geophysical Journal International, 198(2), 1034-1044.

Zhang, Z., Zeng, B., Dai, C. and He, W., 2018b. Study on structural service performance of heavy-haul railway tunnel with voided base. Advances in Civil Engineering, 2018(1), 3510979.

Zhao, B., Huang, T., Dongyan, L., Liu, D., Liu, Y. and Wang, X., 2020. Experimental study and damage model study of rock salt subjected to cyclic loading and cyclic creep. Advances in Civil Engineering, 2020(1), 8049626.

Zhao, K., Ma, H., Liang, X., Li, X., Liu, Y., Cai, R., Ye, L. and Yang, C., 2022a. Damage evaluation of rock salt under multilevel cyclic loading with constant stress intervals using AE monitoring and CT scanning. Journal of Petroleum Science and Engineering, 208(1), 109517.

Zhao, K., Ma, H., Zhou, J., Yin, H., Li, P., Zhao, A., Shi, X. and Yang, C., 2022b. Rock salt under cyclic loading with high-stress intervals. Rock Mechanics and Rock Engineering, 55(7), 4031-4049.

Zheng, B. and Qi, S., 2016. A new index to describe joint roughness coefficient (JRC) under cyclic shear. Engineering Geology, 212, 72-85.

Zheng, Q., Liu, E., Sun, P., Liu, M. and Yu, D., 2020a. Dynamic and damage properties of artificial jointed rock samples subjected to cyclic triaxial loading at various frequencies. International Journal of Rock Mechanics and Mining Sciences, 128(1), 104243.

Zheng, Q., Liu, E., Yu, D. and Liu, M., 2020b. Fatigue and damage properties of non-consecutive jointed mudstone samples subjected to cyclic triaxial loading. Bulletin of Engineering Geology and the Environment, 79(5), 2467-2481.

Zhenyu, T.A.O. and Haihong, M.O., 1990. An experimental study and analysis of the behaviour of rock under cyclic loading. Intl J of Rock Mech & Mining Sci & Geomechanics Abstracts, 27(1), 51-56.

Zhou, Y., Sheng, Q., Li, N. and Fu, X., 2019. Numerical investigation of the deformation properties of rock materials subjected to cyclic compression by the finite element method. Soil Dynamics and Earthquake Engineering, 126(1), 105795.

Zhou, Y., Sheng, Q., Li, N., Fu, X., Zhang, Z. and Gao, L., 2020. A constitutive model for rock materials subjected to triaxial cyclic compression. Mechanics of Materials, 144(1), 103341.

Zhou, Z.L., Wu, Z.B., Li, X.B. and Xiang, L.I., 2015. Mechanical behavior of red sandstone under cyclic point loading. Transactions of Nonferrous Metals Society of China, 25(8), 2708-2717.